The Dissertation Committee for Neil Behzad Fazel Certifies that this is the approved version of the following dissertation:

Quasi-monoenergetic laser-plasma acceleration of electrons beyond 1 GeV at the Texas Petawatt Laser

Committee:

Michael Downer, Supervisor

Michael Becker

Todd Ditmire

Manfred Fink

Gennady Shvets

Quasi-monoenergetic laser-plasma acceleration of electrons beyond 1 GeV at the Texas Petawatt Laser

by

Neil Behzad Fazel, MSPHY; MSCS

Dissertation

Presented to the Faculty of the Graduate School of

The University of Texas at Austin

in Partial Fulfillment

of the Requirements

for the Degree of

DOCTOR OF PHILOSOPHY

The University of Texas at Austin

August 2015

Dedication

To my parents

Acknowledgements

I would like to thank my advisor, Prof. Michael Downer, for giving me the opportunity to carry out the research that has been presented in this dissertation, for providing the funding, and for the supervision of the research. The doctoral research process is necessarily a long (and often winding) path. I am in particular grateful for Prof. Downer's insights at critical junctures on this path, and for his generousness with his time. The laser-plasma acceleration experiments discussed in this dissertation are a manifestation of the successful collaroborative efforts of a group of scientists that in addition to the author included postdocs and research scientists. I would like to thank in particular Xiaoming Wang and Rafal Zgadzaj, the postdocs in the Downer group, as well as Watson Henderson, the group research scientist. Their experience and particular skills were critical to the success of these experiments: Xiaoming's capability to distinguish the forest from the trees and focus on what was important, Rafal's precision as an experimentalist (as well as his pedagogic talent), and Watson's many experimental crisis management skills. Thanks are also due to the Texas Petawatt group, headed by Prof. Todd Ditmire, which provided the driving laser for all the experiments discussed in this dissertation. The members of the group included Michael Donovan, Gilliss Dyer, Erhard Gaul, Mikael Martinez, Hernan Quevedo, and Michael Spinks. Their collective efforts played a big role in the success of these experiments. The PIC simulations that guided the experiments, and helped us to interpret the results, were provided by the members of Prof. Shvets group. Thanks are due in particular to Austin Yi, Xi Zhang, and Vladimir Khudik. I would also like to warmly thank Marcel Reginatto at the Physikalisch-Technische Bundesanstalt in Germany for many fruitful discussions on the topic of spectroscopy and the design of spectrometers. Doctoral research often involves late-night

sessions designing the experiments and analyzing the data. I would like to thank Farbod Shafiei for the many interesting late-night discussions on all things related to physics and for sharing his insights as an experimentalist. I would also like to thank James Halligan for providing support, which included assistance in the purchasing of equipments.

Quasi-monoenergetic laser-plasma acceleration of electrons beyond 1 GeV at the Texas Petawatt Laser

Neil Behzad Fazel, Ph.D.

The University of Texas at Austin, 2015

Supervisor: Michael Downer

Laser-plasma accelerators first produced 1 GeV electrons with few percent energy spread and high beam quality in 2006. The goal of laser-plasma acceleration experiments conducted at the Texas Petawatt (TPW) laser starting in 2011 was to advance this energy frontier significantly while maintaining high electron beam quality. To maximize energy transfer from laser pulse to electrons, we adopted the strategy of lowering the plasma density so that accelerating electrons and the laser-driven plasma accelerating structure remained in phase over several centimeters, instead of only millimeters. This was only possible because pulses from the TPW laser uniquely have the power (~1 PW) and duration (150 fs) required to excite the plasma resonantly and nonlinearly, and thus to achieve the favorable blowout (bubble) regime, at electron densities as low as 10^{17} cm^{-3}.

In this dissertation I describe laser-plasma acceleration experiments driven by the TPW laser that successfully accelerated > 10^9 self-injected electrons (~1 nC) to > 1 GeV (> 10^8 self-injected electrons > 2 GeV) energy while maintaining < 5% energy spread and sub-milliradian divergence. These experiments have generated ~2 GeV electron bunches more consistently and in larger numbers than any laser-plasma accelerator in the world. I also describe single-shot diagnostic methods developed to characterize the divergence and energy spectrum of the electrons, and of the betatron x-rays they produced, despite low-repetition rate, significant pointing fluctuations, and electromagnetic pulse (EMP) background.

Betatron x-ray radiation originates from the transverse wiggling motion of accelerating electrons in the electrostatic field of a plasma bubble. It is useful as a broadband,

femtosecond x-ray source and as a diagnostic of transverse electron beam emittance. Experiments at the TPW laser yielded betatron x-rays that were brighter, more collimated and more energetic than in previous experiments. I describe in depth an x-ray spectrometer design and methodology that I developed for single-shot, spatially-resolved measurement of betatron x-ray spectra. X-rays were sampled through K-edge transmission filters distributed strategically on a planar detector, high-fidelity x-ray images were reconstructed, and iso-intensity contours subsequently defined. I demonstrate how x-ray spectra may be calculated on such contours and used to produce a 3D representation of the x-ray spectrum. This represents the first single-shot method for betatron x-ray spectroscopy offering spatial resolution over the entire range of the x-ray profile.

Table of Contents

List of Tables

List of Figures

Chapter 1 Introduction

In this chapter, the laser-wakefield acceleration of electrons is introduced. Its history, milestones, and some of the challenges will be presented.

In 1979, Tajima and Dawson proposed the visionary idea that it would be possible to accelerate electrons through the interaction of an intense electromagnetic wave with plasma during which electrons would be accelerated to GeV-level energies traversing through 1 cm of plasma at a density 10^{18} cm^{-3} [1]. The way they saw it, the passage of an intense laser pulse through *underdense* plasma, i.e., one where the natural frequency of oscillation, the *plasma frequency*, is lower than the frequency of the laser, would create a longitudinal electron density oscillation behind it through the interaction between the time-averaged electromagnetic radiation and the plasma electrons. This interaction, known as the *ponderomotive force* of the radiation on the charged particles, would push the negatively charged, therefore low-field seeking, electrons aside as it propagated through the plasma with the speed of light, producing a longitudinal wave in it wake. The positively charge ions, on the other hand, being more than 3 orders of magnitude heavier than the electrons, could be considered immobile in the timescale during which the pulse would propagate through the plasma. This would lead to the creation of a space charge on a microscopic scale inside the plasma, leading to the production of very large electric fields, or *wakefields*. This wave would move through the plasma with phase velocity equal to the group velocity of the electromagnetic radiation, and for a radiation pulse length equal to half the natural wavelength of the plasma oscillation, the interaction between the electromagnetic wave and plasma would be resonant. It is possible for wave-breaking electrons to become trapped inside the relativistically moving wakefield and accelerate due to the electrostatic force of the space charge. The acceleration would continue as long as the pulse energy remained available or *undepleted* and the motion of the trapped electrons and the wakefield remained in phase, during which time the electrons would gain a large amount of energy from the wakefield.

To put Tajima and Dawson's idea in perspective, it helps to consider acceleration in traditional radio frequency (RF) accelerators. In such devices, the accelerating particle

gains energy from the electric field inside an electromagnetic cavity. The maximum electric potential gradient is, however, limited to the range of 20-100 MV/m. Above such fields, structural breakdown of the RF cavity occurs. To reach high energies in traditional accelerators, therefore, requires that they instead be long. For example, at a field potential gradient of 20 MeV/m, 50 meters is required to reach 1 GeV in a linear accelerator, 2.5 km (SLAC) to reach 50 GeV, and 50 km to reach TeV energies required for modern particle physics experiments.

In contrast, plasma, being a fully ionized state of matter, where "maximum damage" has already taken place, can sustain very large acceleration gradients. As a result, a plasma accelerator cannot break down. The acceleration limit is, instead, determined by the breaking of a plasma wave as opposed to structural damage. To demonstrate, consider the following 1-dimensional case. In one dimension, the presence of a charge density wave ρ traveling in the z direction, resulting from a non-linear plasma density perturbation, itself created by a plane electromagnetic pulse propagating in the z direction, produces an electrostatic field $E(z)$ in the plasma, the magnitude of which may be determined by applying Gauss's law. Denoting by n_{e0} the unperturbed plasma density, and by δn_{e0} the amplitude of the density wave in the perturbed plasma with plasma frequency $\omega_p \approx k_p/c$ (where k_p is the plasma wave vector in 1D), the plasma density perturbation $\delta n_e(z)$ has the form

$$\delta n_e(z) = \delta n_{e0}\cos(k_p z) \approx n_{e0}\cos(k_p z)$$

($\delta n_{e0} \approx n_{e0}$ follows from the assumption that the perturbation is a non-linear one, i.e., approaches the wave-breaking limit.) Assuming a sinusoidal form for the resulting electric field having $\pi/2$ phase difference with the perturbation, i.e., $E(z) = E_{z0}\sin(k_p z)$, and using $\rho = e\,\delta n_e(z)$ for the charge density, Gauss's law becomes

$$\vec{\nabla}\cdot\vec{E} = \frac{\rho}{\varepsilon_0} \rightarrow \partial E_z/\partial z = \frac{e\,\delta n_e(z)}{\varepsilon_0} \rightarrow k_p E_{z0}\cos k_p z = \frac{e\,n_{e0}}{\varepsilon_0}\cos k_p z$$

This gives us a relation between the electric field, plasma wave vector, and unperturbed plasma density:

$$E_{z0}k_p = n_{e0}\, e/\varepsilon_0$$

Since the plasma wave is propagating behind the electromagnetic wave, its phase velocity is nearly the speed of light in the plasma medium. Using the relation $k_p \approx \omega_p/c$, where ω_p is the plasma frequency given (in SI units) by $\omega_p = \sqrt{n_{e0}e^2/(\varepsilon_0 m_e)}$, this relation can be written as:

$$E_{z0}k_p = \frac{n_{e0}e}{\varepsilon_0} \rightarrow E_{z0}\frac{1}{c}\sqrt{n_{e0}e^2/(\varepsilon_0 m_e)} = \frac{n_{e0}e}{\varepsilon_0}$$

Simplifying this, results in a relation between the electric field and the plasma density:

$$E_{z0} \approx c\sqrt{\frac{m_e n_{e0}}{\varepsilon_0}} = m_e c\omega_p/e$$

This is the accelerating field of the wakefield in 1 dimension near the wave-breaking limit. Using the notation E_{acc} and plugging in for the constants $m_e = 9.109 \times 10^{-31}$ kg , $\varepsilon_0 = 8.854 \times 10^{-12}$ F/m, and $c = 2.998 \times 10^8$ m/s, an equation relating the accelerating field of the wake to the plasma density in convenient units is obtained:

$$\boxed{E_{acc}(\mathrm{V/cm}) \approx 0.96\sqrt{n_{e0}(\mathrm{cm^{-3}})}} \qquad \textbf{Eq. 1.1}$$

At a plasma density of ~10^{18} cm^{-3}, for example, an electric field of ~10^9 V/cm is generated at the wave breaking limit. At such gradients, an electron acquires an energy of ~100 GeV in 1 meter of plasma in a laser-plasma accelerator (LPA), at least 3 orders of magnitude more energy than it would acquire in a conventional RF accelerator in the same distance.

The larger acceleration gradients of plasma accelerators translate to more compact accelerators. They also naturally produce shorter duration electron bunches. This is because for a wake structure of the order of 10 μm = 10^{-5} m, moving at a relativistic group velocity behind the laser pulse, the accelerated electron bunch duration is approximately 10^{-5} m / 3×10^8 m ~ 30 fs. This is shorter than the typical ps-duration electron bunches produced in RF accelerators and is another advantage of laser-plasma based accelerators. Smaller electron bunches, when used to create pulses of x-ray radiation, produce commensurately narrower, hence more broadband, bursts of x-ray radiation. Such femtosecond duration pulses enable the ultrafast imaging of physical

processes that evolve at similarly small timescales, for example, chemical reactions and atomic vibrations.

It took more than two decades following Tajima's and Dawson's idea before terawatt or higher power laser technology became available that could create charge density waves of large enough amplitude to create electric field of order GeV/m. It wasn't until 2004 that the production of high-quality electron bunches characterized by significant charge (100 pC) at high mean energy (100 MeV) with small energy spread (a few percent) and low divergence (a few milliradians) was achieved [2]–[4].

There are several limits to laser-plasma electron acceleration that determine the optimum design of the accelerator. Here I review them briefly, postponing the details until the following chapter. First, the laser pulse diffracts as it propagates through the plasma. This leads to the lowering of the laser intensity and the resulting weakening of the ponderomotive interaction between the laser and plasma. It is therefore necessary to *guide the laser beam*. This may be accomplished by using a preformed plasma channel, e.g., one created by a capillary discharge, or as was done in the experiments discussed in this dissertation, by relying on *relativistic self-focusing* of the laser pulse in plasma. In a plasma channel, the plasma density varies with distance from the channel axis; it is lowest on axis and highest near the channel boundary. Lower plasma density creates lower on-axis plasma frequency and higher on-axis index of refraction. Since the laser phase velocity ($v_{ph} = {}^{c}/_{n}$) is lower in regions with higher index of refraction, the laser pulse propagates more slowly near the axis than away from it. Consequently the curved (e.g., Gaussian) wave front flattens, reducing the diffraction. In relativistic self-focusing (RSF), the on-axis plasma frequency is lowered because of the increase in the relativistic mass of electrons oscillating at relativistic velocity in the intense laser field, rather than because of smaller electron density. RSF balances diffraction at a *critical power* P_{crit}, which is a function of the plasma density and laser frequency. When the laser power $P > P_{crit}$, the plasma focuses the pulse. For a fixed laser power and wavelength, there is an optimum range of densities in which RSF and diffraction are well balanced, and the laser pulse self-guides. At lower densities ($P << P_{crit}$), guiding is too weak to compensate

diffraction, whereas at higher densities ($P >> P_{crit}$), RSF becomes so strong that the pulse can filament and break up.

Dephasing of accelerating electrons from the plasma wave sets a second important limit to laser-plasma acceleration. When a wakefield is formed behind a guided laser pulse, it propagates with a phase velocity that matches the group velocity $v_g = d\omega/dk = nc$ of the laser pulse in plasma, where c is the speed of light in vacuum and n is the index of refraction of the plasma. Since $n < 1$ for underdense plasma, the group velocity of the laser pulse, and thus the phase velocity of the wake, is smaller than the speed of light in vacuum. When an electron trapped inside the wakefield accelerates, it can ultimately reach velocities that approach c, and exceed the speed of the accelerating structure in the plasma medium. As a result, the electron overtakes the wakefield and enters a decelerating region of its potential. When this happens, the electron and the wake are *dephased* and the electron loses energy back to the plasma. A goal of any laser wakefield experiment is to maximize the *dephasing length*, the distance over which the electron acquires energy from the wake and accelerates. As will be shown in the next chapter, the dephasing length increases as the plasma density is reduced. Hence by lowering the density it is possible to accelerate over longer distances and achieve a higher final energy. (It might be surprising that a reduction in plasma density can enhance the acceleration since, according to Eq. 1.1, the accelerating field scales as the square root of plasma density. However, it turns out that the gain in energy from an increase in the acceleration length following a reduction in plasma density more than compensates for the loss in energy as the result of a lower accelerating electric field.) The dephasing length also increases with the lowering of the laser wavelength. All things equal, a driving pulse with micron wavelength, as is the case with TPW laser, has longer dephasing length than one at 10 μm (CO_2 laser).

Loss of laser energy sets a third limit on laser-plasma acceleration. As the laser pulse propagates inside plasma, it transfers energy to the plasma via the ponderomotive force and stores it in the resulting wake that it creates. Some of this energy in then transferred from the electric field to electrons during the acceleration process. Therefore, as the electrons gain energy, the laser pulse loses energy. Ultimately the laser pulse becomes

depleted leading to a degradation of the accelerating structure. This phenomenon, *beam depletion*, is also a function of the plasma density and is slowed when the plasma density is lower. Lower plasma density therefore offers the twin advantage of increasing the dephasing length and reducing the beam depletion. All other factors being equal, one would like to conduct a wakefield experiment at the lowest density that still provides a significant advantage in accelerating gradient over conventional RF accelerators. However, as will be shown, lower plasma density increases the critical laser power required for relativistic self-focusing. For experiments conducted at the Texas Petawatt Laser, there is sufficient power available for relativistic self-focusing to take place even at densities as low as $\sim 1 \times 10^{17}$ cm^{-3}.

A fourth limit to the performance of wakefield accelerators is *injection* and *trapping* of electrons into the electrostatic field of the wake once it has been created. In most laser-plasma acceleration experiments, the leading edge of the drive laser pulse first fully ionizes a low-Z gas (e.g., hydrogen, helium), thereby creating plasma of uniform, constant background density n_{e0} in which its peak drives the wake. Often, however, these free electrons collectively form the wake structure without breaking off as particles and injecting into it. One way to inject electrons is by *ionization-induced injection* (I^3) [5]. In this process, an impurity gas of higher atomic number, typically oxygen or nitrogen, is mixed with the low-Z "carrier" gas. Along with the low-Z gas, the outer shell electrons of the impurity gas are ionized by the front edge of the laser pulse; the inner shell electrons, however, have larger ionization potential and require focused laser intensity before they are ionized. This occurs when the laser pulse relativistically self-focuses to the critical intensity required for the ionization of the inner-shell electrons of the impurity atoms, by which time the accelerating structure (the wake) has been created, and the inner-shell electrons, if trapped, will be accelerated. Another injection method, and the one primarily employed in the experiments described in this dissertation, is to have the plasma's own electrons inject into the accelerating structure. This approach, known as *self-injection*, requires the laser pulse to drive the plasma wake to a highly nonlinear, wave-breaking regime, which in turn requires a powerful, evolving laser pulse. For the same laser power, it is more difficult to self-inject electrons than it is by using an impurity via ionization-

induced injection, and it typically requires a higher plasma density. For this reason, the lowering of plasma density with the goal of increasing the dephasing length requires higher laser power to facilitate electron injection. As has been shown in the experiments discussed in this dissertation, given sufficient laser power, it is possible to self-inject at densities as low as 10^{17} cm^{-3}, twenty times lower than in any previous laser-plasma acceleration experiment. In addition to its simplicity, self-injection has the advantage over I^3 in that it can be spatially more localized, producing accelerated electrons with narrower divergence and energy spread. Nevertheless, with ionization-induced injection, divergence and energy spread can be reduced dramatically by confining the dopant gas to a region near the entrance of the interaction region using a two-stage gas cell design [6]. The first gas cell, comprising the injection stage, contains the impurity gas, is followed by a second gas cell, the acceleration stage, containing pure low-Z gas where the electrons injected in the previous stage are then accelerated. This suppresses continuous injection which would otherwise broaden the electron energy spectrum. It is also possible to temporally control the ionization-induced injection by tailoring the plasma density and laser parameters such that the laser pulse relativistically self-focuses and achieves the intensity required for the ionization of the inner-shell electrons of the impurity atoms only during a segment of its propagation through the plasma (denoted *mismatched propagation*), after which its intensity drops below the threshold level. Both spatial and temporal localization of injection are desired characteristics because they reduce the electron beam emittance.

A fifth, and final, limitation to the performance of laser-plasma accelerators is distortion of the accelerator structure by the electric field of the accelerated charge. This phenomenon is known as *beam loading* and is usually mitigated by lowering of the plasma density. Due to the extremely non-linear interaction between the laser and plasma, there is a small region in the parameter space of plasma density, laser pulse duration, spot size, and power, that is favorable to the injection and acceleration of electrons. A reduction in plasma density, for example, may be accompanied by a (perhaps unintended) change in laser pulse parameter, thus producing no injection. One challenge of the wakefield experiments conducted with the TPW laser is precisely the individual control

of experimental parameters. The resonant interaction between the laser pulse and plasma requires that the period of the plasma oscillations (Langmuir waves) match the duration of the laser pulse. A lowering of the plasma density to enhance the dephasing length, lower beam depletion, and mitigate beam loading, is accompanied by an increase in the period of the plasma oscillations, therefore requires a commensurately longer pulse duration for resonant laser-plasma interaction. For example, a plasma density of 5×10^{17} cm^{-3}, corresponding to a dephasing length of ~10 cm, requires a relatively long pulse duration of ~150 fs for resonant interaction.

In Table 1-1, some of the previous experiments in the laser-wakefield acceleration of electrons from the past decade are presented. The experimental parameters in these experiments span more than an order of magnitude in the case of plasma density and the power of the driving laser; these are accompanied by a 20-fold change in the maximum electron energy.

P_{laser} [TW]	n_e [$\times 10^{17}$ cm^{-3}]	L_{acc} [mm]	*Injection*	E_e [GeV]	*Electron Spectrum*	*Ref.*
12.5	200	2 (He)	self-injected	0.07	mono-energetic	Mangles *et al.* (2004) [2]
10	450	2.4 (He)	self-injected	0.086	mono-energetic	Geddes *et al.* (2004) [3]
30	200	3 (He)	self-injected	0.17	mono-energetic	Faure *et al.* (2004) [4]
40	43	33 (He)	self-injected	1	mono-energetic	Leemans *et al.* (2006) [7]
160	30	8 (He)	self-injected	0.72	mono-energetic	Froula *et al.* (2009) [8]
180	55	10 (He)	self-injected	0.80	mono-energetic	Kneip *et al.* (2009) [9]
110	15	13 (He 97%:CO_2 3%)	I^3	1.45	continuous	Clayton *et al.* (2010) [5]
60	57 25	1 (He 93%:O_2 7%) 3 (He)	I^3	0.80	mono-energetic	Liu *et al.* (2011) [6]
200	30	3 (He 99.5%:N_2 0.5%) 5 (He)	I^3	0.46	mono-energetic	Pollock *et al.* (2011) [10]

Table 1-1: Previous milestones in the laser-wakefield acceleration of electrons

The wakefield experiments driven by the TPW laser were different from previous experiments in the following key aspects:

- Lower plasma density (~10^{17} vs. 10^{19} cm^{-3}): lower density increases the distance over which electrons remain in phase with the accelerating structure of the plasma (the dephasing length L_{deph}), thus increasing the upper limit to the electron energy;
- Longer interaction length (~7-10 cm gas cell vs. < 1 cm jet): to exploit the longer dephasing length;

- Longer pulse duration, t_{pulse} (150 fs vs. < 60 fs): lower plasma density translates to lower plasma frequency, hence higher plasma period, requiring a commensurately longer pulse duration in order to excite plasma waves resonantly;
- Higher peak power (~ 1 PW vs. ~40 TW): to self-guide, to create nonlinearity required to access the blowout (bubble) regime, and trigger self-injection at low plasma density. Higher power at the same time as longer pulse duration requires more energetic laser pulse (~ 100 J vs. 10 J);
- Evolving bubble propagation vs. mode-matched bubble propagation: to self-inject electrons into the bubble. Our experiments also have the option of using ionization-induced injection, since lower density makes self-injection more difficult.

In this chapter, an overview of the laser-wakefield acceleration of electrons, together with some of the important experimental milestones, were presented. In the chapter that follows, important theoretical results having to do with the interaction between the laser pulse and the plasma will be introduced in more detail and, where necessary, derived. The theoretical discussion of the secondary x-rays produced by the accelerated electron will be postponed until Chapter 6.6.

Chapter 2 Physics of Laser-Plasma Acceleration

In this chapter, the main theoretical concepts needed to understand the parameter space of a laser-wakefield experiment are reviewed. Simple theoretical formulas are introduced and, where appropriate, derived. (A note regarding notation: where necessary, subscripts *p* and *laser* are used to distinguish between quantities relating to the plasma and laser, respectively. The speed of light in vacuum, the electron charge and mass, and the vacuum permittivity, are denoted by *c*, *e*, m_e, and ε_0, respectively. ω and *f* refer to the laser frequency, $\lambda_{0,laser}$ and λ_{laser} denote the laser wavelength in vacuum and in plasma, respectively; *k* is the laser wave number in plasma. n_e, ω_p, T_p, and λ_p denote the plasma density, frequency, period, and wavelength, respectively. *n* denotes the plasma index of refraction.)

The interaction between a laser pulse and a neutral gas leads to modification of both the pulse and the gas. In the spatial domain, the nonlinearity of the laser interaction with the medium gives rise to a laser-intensity dependent index of refraction for the plasma according to

$$n = n_0 + n_2 I \qquad \textbf{Eq. 2.1}$$

where $I = \frac{1}{2} n_0 \varepsilon_0 c E^2$ is the laser intensity and n_0 is the linear, or low-intensity, index of refraction. This is known as the *Kerr effect*. The nonlinear index of refraction, n_2, characterizes the nonlinearity of the medium and is related to its 3rd order susceptibility $\chi^{(3)}$ [11]:

$$n_2 = \frac{3}{2 n_0^2 \varepsilon_0 c} \chi^{(3)} \qquad \textbf{Eq. 2.2}$$

The intensity dependence of the index of refraction produces a higher value for *n* on axis, where the laser intensity is highest, than away from it. The on- vs. off-axis difference in the index of refraction causes the gas to act as a positive lens, focusing it towards the axis. This phenomenon, *self-focusing*, opposes the diffraction of the laser pulse, but is not by itself sufficient to guide it over distances of interest.

For high enough laser intensity, the interaction of the electromagnetic radiation with the gas leads to the ionization of the gas. To determine the intensity required for this, Coulomb's law, $E = \frac{q}{4\pi\varepsilon_0 r^2}$, may be applied to find the electric field of an electron at the characteristic atomic distance, i.e., the Bohr radius $a_0 = \frac{4\pi\varepsilon_0\hbar^2}{m_e e^2}$. Using $q = e$ and $r = a_0$, this characteristic atomic electric field is found to be $E_{atomic} = 5.14 \times 10^{11}$ V/m. Therefore a laser with intensity exceeding $I_{atomic} = \frac{1}{2} n_0 \varepsilon_0 c E_{atomic}^2 = 3.5 \times 10^{16}$ W/cm^2 will be sufficiently intense to overcome the attractive potential binding the electrons to the atoms and ionize it. When the laser is intense enough to ionize the gas and produce plasma, the interaction between the laser pulse and the plasma modifies the laser pulse in the spatial as well as the frequency domain. In the spatial domain, the interaction of a plasma of density n_e, with natural or *plasma frequency* ω_p given by

$$\omega_p = \frac{2\pi}{T_p} = \sqrt{\frac{n_e\, e^2}{m_e \varepsilon_0}} \qquad \textbf{Eq. 2.3}$$

with laser pulse of frequency *f* and vacuum wavelength $\lambda_{0,laser}$, where $f = \frac{\omega}{2\pi} = \frac{c}{\lambda_{0,laser}}$, induces an index of refraction *n* in the plasma. This may be found by using the dispersion relation for the laser propagation in plasma [12]

$$(ck)^2 = \left(\frac{2\pi c}{\lambda_{laser}}\right)^2 = \omega^2 - \omega_p^2 \qquad \textbf{Eq. 2.4}$$

Solving Eq. 2.4 for the laser wavelength gives

$$\lambda_{laser} = \frac{2\pi c}{\sqrt{\omega^2 - \omega_p^2}} = \frac{2\pi}{\omega} \frac{c}{\sqrt{1 - \frac{\omega_p^2}{\omega^2}}} \qquad \textbf{Eq. 2.5}$$

and by comparing Eq. 2.5 and $\lambda_{laser} = v_{ph,laser}/f = \frac{2\pi}{\omega}\frac{c}{n}$, where $v_{ph,laser}$ is the phase velocity of the laser propagation in plasma, the index of refraction is found:

$$n = \sqrt{1 - \frac{\omega_p^2}{\omega^2}} \qquad \textbf{Eq. 2.6}$$

Therefore, in the spatial domain, prior to the full ionization of the gas, an effect similar to the case when a laser interacts with neutral gas takes place. In this case, however, the relatively greater on-axis laser intensity produces a higher plasma density n_e near the

axis, i.e., $\frac{\partial n_e}{\partial r} < 0$. According to Eq. 2.3, this would make the plasma frequency larger near the axis. According to Eq. 2.6, the index of refraction of the plasma will then be smaller near the axis, i.e., $\frac{\partial n}{\partial r} > 0$. Therefore, the spatial effect of the plasma on the laser beam is initially similar to a negative lens, i.e., it defocuses the pulse. However, for a fully ionized gas, this defocusing effect disappears. If the laser has relativistic intensity, i.e., $a_0 \geq 1$, where $a_0 = \frac{e\,A_{laser}}{m_e c^2}$ is the laser strength parameter, Eq. 2.3 is replaced by the relativistic version

$$\omega_p = \frac{2\pi}{T_p} = \sqrt{\frac{n_e\, e^2}{\gamma m_e \varepsilon_0}} \qquad \textbf{Eq. 2.7}$$

where $\gamma = 1/\sqrt{1 - v_e^2/c^2}$ is the relativistic gamma factor for an electron of velocity $\vec{v}_e$. The closer an electron is to the peak intensity region of the laser pulse, the stronger its interaction with the laser and the larger its velocity and its relativistic gamma. This means that the plasma frequency is lower where the laser intensity is highest (near the axis) and, according to Eq. 2.6, the index of refraction is therefore higher, i.e., $\frac{\partial n}{\partial r} < 0$. The effect is similar to the Kerr effect for a non-plasma medium, i.e., the plasma medium acts as a positive lens to focus the pulse. This is *relativistic self-focusing* (RSF) and is one of the mechanisms to guide a laser pulse as it propagates in a plasma (the other being the use of a plasma channel). In addition to its role in guiding, RSF is also required to produce a nonlinear regime, known as the blow-out or *bubble* regime, where the laser intensity is sufficient to blow electrons out to produce a spherical cavitation conducive to efficient acceleration as well as self-injection [13]–[15]. RSF occurs when the laser power crosses a threshold level. The critical power, P_{crit}, required for relativistic self-focusing is given by [16]:

$$P_{crit} = 17 \times \left(\frac{\omega}{\omega_p}\right)^2 [\mathrm{GW}] = \frac{0.188}{n_e[10^{17}\mathrm{cm}^{-3}]\lambda^2[\mu\mathrm{m}]}[\mathrm{PW}] \qquad \textbf{Eq. 2.8}$$

For the TPW laser (λ_{TPW} = 1.057 μm), Eq. 2.8 indicates that for plasma density of ~$10^{17}\mathrm{cm}^{-3}$, the critical power required for RSF is ~0.2 PW. The inverse relationship between the plasma density and the critical power required for RSF indicates that at densities ~$10^{17}\mathrm{cm}^{-3}$, petawatt-class lasers are required for relativistic self-focusing and

the creation of a plasma bubble. The presence of a plasma bubble is required for self-injection. There is some evidence that when an idealized Gaussian laser pulse co-propagates quasi-statically with the plasma bubble it has created (known as *matched* propagation) the threshold for self-injection is related to the ratio P/P_{crit} of the laser power to the critical power required for RSF [8]. However, in the case of non-Gaussian focal profiles of first generation petawatt lasers, both the laser pulse and bubble evolve as they co-propagate. In fact, simulations indicate that it is this evolution of the plasma bubble that determines the dynamics of self-injection [17], [18] and in turn the electron beam characteristics such as its energy spread, angular divergence, and dark current.

The interaction of laser pulse with a gas medium also modifies the laser in the frequency domain. The front edge of the pulse ionizes the gas, so that a fixed point in the plasma becomes progressively more ionized as it encounters the increasing laser intensity of moving pulse; i.e., the plasma density increases with the rising edge of the pulse. This increase leads to an increase in the plasma frequency and a lowering of the index of refraction with the rising pulse. Consequently, the front regions of the pulse have lower phase velocity than parts of the pulse propagating inside fully ionized plasma. This leads to a compression of the pulse in the time domain and a lengthening in the frequency domain. Therefore the interaction of the pulse with the gas increases its bandwidth and produces a blue shift. On the hand, with a laser pulse of large enough intensity, a cavitation or bubble is produced behind the pulse, where all electrons have been blown out due the ponderomotive force of the laser pulse. A similar argument now applies to the falling edge of the laser pulse: it experiences the lower plasma density inside the cavitation, thus has smaller phase velocity. This causes the pulse to lengthen in time and shorten in the frequency domain, producing a red shift.

The laser-plasma interaction also modifies the laser's carrier wave. From Eq. 2.6, n < 1 for an underdense plasma, and it follows that the phase velocity

$$v_{ph,laser} = \frac{c}{n} \qquad \textbf{Eq. 2.9}$$

and the wavelength of a pulse's carrier wave

$$\lambda_{laser} = \frac{2\pi}{\omega} v_{ph,laser} = \frac{2\pi}{\omega}\frac{c}{n} = \frac{\lambda_{0,laser}}{n} \quad \textbf{Eq. 2.10}$$

both increase in plasma compared to their values in vacuum; however, the change is small for typical plasma densities. To determine its group velocity, $v_{g,laser} = \frac{d\omega}{dk}$ can be used:

$$v_{g,laser} = \frac{d\omega}{dk} = \left(\frac{dk}{d\omega}\right)^{-1} = c\sqrt{1 - \frac{\omega_p^2}{\omega^2}} = c\, n \quad \textbf{Eq. 2.11}$$

where $k = \omega\, n/c$ and Eq. 2.6 were used. Therefore the group velocity of the laser pulse in plasma is reduced relative to its value in vacuum. Since the disturbance created by the laser pulse in plasma propagates with the same phase velocity as the pulse's group velocity, i.e., $v_{ph,wake} = v_{g,laser}$, can write:

$$v_{ph,wake} = c\sqrt{1 - \frac{\omega_p^2}{\omega^2}} = c\, n \quad \textbf{Eq. 2.12}$$

Eq. 2.12 can then be used to find the plasma wavelength as

$$\lambda_p = \frac{2\pi}{\omega_p} \times v_{ph,wake} = \frac{2\pi}{\omega_p} \times c\, n \quad \textbf{Eq. 2.13}$$

Therefore the variation of the plasma wavelength with density is $\lambda_p \propto n_e^{-1/2}$. Since the wake moves with a phase velocity that is lower than *c*, whereas electrons can reach highly relativistic speeds in the accelerating structure of the wake, the electrons can in time overtake the wake to exit the region with attractive, hence accelerating, electric potential, and enter the region where the potential is repulsive and decelerating. The *dephasing length*, L_{deph}, the distance traversed by an electron before it enters the region with repulsive electric potential, is a distance over which the electron overtakes the wake by half a plasma wavelength due to the difference in velocity between the electron and the plasma wake; for highly relativistic electrons ($v_{e,z} \sim c$), this can be expressed as $L_{deph} - \frac{v_{ph,wake}}{c} L_{deph} = \frac{\lambda_p}{2}$. Solving for L_{deph}, and using Eq. 2.12, this becomes

$$L_{deph} = \frac{\lambda_p}{2} \times \frac{1}{1-n} \quad \textbf{Eq. 2.14}$$

For very underdense plasma ($\frac{\omega_p}{\omega} \ll 1$), Eq. 2.6 can be expanded to give $n \sim 1 - \frac{1}{2}\frac{\omega_p^2}{\omega^2}$; using this result in Eq. 2.14, with the help of Eq. 2.13, gives

$$L_{deph} \sim \lambda_p \times \frac{\omega^2}{\omega_p^2} \sim \frac{{\lambda_p}^3}{\lambda_{0,laser}^2} \qquad \textbf{Eq. 2.15}$$

The dephasing length therefore varies with the plasma density as $n_e^{-3/2}$. Given that the accelerating field (at wave breaking) varies as $n_e^{1/2}$ (Eq. 1.1), a reduction in plasma density still provides a net increase in the final electron energy, as the reduction in the accelerating gradient of the electric field is more than compensated by the increase in the maximum distance over which acceleration take place. Eq. 2.15 applies to the case of a linear wake. In the general case, however, the dephasing length also depends on the strength of the laser as indicated by its normalized vector potential a_0 (also known as the laser strength parameter):

$$a_0 = \frac{e\,A_{laser}}{m_e c^2} = 0.855 \times \sqrt{\lambda^2[\mu\text{m}]\, I[10^{18}\ \text{W/cm}^2]} \qquad \textbf{Eq. 2.16}$$

For example, in a nonlinear ($a_0 > 2$) 3D plasma, the dephasing length is [14]

$$L_{deph} \sim \frac{4}{3}\frac{1}{k_p}\frac{\omega^2}{\omega_p^2}\sqrt{a_0} \qquad \textbf{Eq. 2.17}$$

According to Eq. 2.17, for the same plasma density, the electron and the accelerating structure remain in phase longer the more intense the laser beam. The depletion length of the laser also varies with plasma density as $n_e^{-3/2}$ [19]:

$$L_{depl} \approx \frac{\omega^2}{\omega_p^2}\, cT_{pulse} \rightarrow L_{depl}[cm] < 3.4 \times 10^{27} \lambda^{-2}[\mu\text{m}]\, n_e^{-3/2}[\text{cm}^{-3}] \qquad \textbf{Eq. 2.18}$$

where the inequality in Eq. 2.18 resulted from imposing the condition $T_{pulse} < T_p \approx 10^{11} n_e^{-1/2}$ [cm^{-3}] [20], necessary to avoid catastrophic self-focusing that would lead to laser beam filamentation and breakup.

Plasma Density [$\times 10^{17}$ cm^{-3}]	ω_p [THz]	T_p [fs]	$n = \frac{v_{g,laser}}{c}$	λ_p [μm]	λ_{laser} [μm]	L_{deph} [mm]	L_{depl} [mm]	P_{crit} [TW]
100	180	35	0.994980	10.5	1.0623	1.0	1.0	1.7
30	98	64	0.998497	19.3	1.0586	6.4	5.8	5.7
5	40	157	0.999750	47.2	1.0573	94.2	86.0	34.4
4	36	176	0.999800	52.8	1.0572	131.7	120.2	43.0
3	31	203	0.999850	61.0	1.0572	202.8	185.1	57.3
2	25	249	0.999900	74.7	1.0571	372.7	340.2	86.0
1	18	352	0.999950	105.6	1.0571	1054.3	962.2	172.0

Table 2-1: Important parameters for the laser-wakefield acceleration of electrons for a range of plasma densities varying over two orders of magnitude, and laser wavelength in vacuum of $\lambda_{0,laser}$ = 1.057 μm.

In Table 2-1, the variation of plasma parameters (frequency, period, index of refraction, wavelength) as a function of the plasma density is shown together with acceleration parameters such as dephasing and depletion lengths, and the critical power required for relativistic self-focusing, for a laser pulse of wavelength $\lambda_{0,laser}$ = 1.057 μm (ω = 1783 THz), corresponding to the wavelength of the TPW laser. In the table, the plasma frequency (ω_p), plasma period (T_p), plasma index of refraction (*n)*, plasma wavelength (λ_p), laser wavelength in plasma (λ_{laser}), dephasing length (L_{deph}), and the critical power for relativistic self-focusing (P_{crit}) were calculated using Eq. 2.3, Eq. 2.6, Eq. 2.13, Eq. 2.10, Eq. 2.15, and Eq. 2.8, respectively. The depletion length, L_{depl}, was calculated according to Eq. 2.18 and represents an upper limit corresponding to $T_{pulse} = T_p$. As an example, according to Eq. 1.1, at a plasma density of 5×10^{17} cm^{-3}, the energy gain per centimeter for an electron would be approximately $\sqrt{5 \times 10^{17}}$ eV/cm ~ 0.7 GeV/cm. Given the dephasing length of ~9 cm, this would translate to a gain in the electron energy of $\gtrsim$ 6 GeV. A lowering of the plasma density (to increase the dephasing and depletion lengths), would increase the plasma wavelength and require an increase in the pulse duration to maintain resonant laser-plasma interaction. On the other hand, to maintain the pulse power while increasing its duration, would require a commensurate increase in the pulse energy, which would increase the likelihood of damage to optical components such as mirrors.

Perhaps the challenge of laser-wakefield experiments to accelerate self-injected electrons is in conducting the experiment in a region of the parameter space (plasma density, pulse energy, pulse duration, pulse focal profile) conducive to the experimental goals, while taking into account the limitations of the driving laser upstream, and the diagnostics systems downstream. In this chapter, important theoretical concepts having to do with the parameter space in laser-wakefield experiments driven by the TPW laser were presented. In the next chapter, the diagnostics of such experiments, in particular the constraints that needed to be met, will be reviewed.

Chapter 3 Diagnostics for Laser-Wakefield Experiments

3.1 Introduction

A number of constraints were taken into account when selecting diagnostics for the detection of electrons and x-rays in the laser-wakefield experiments driven by the TPW laser. The diagnostic decisions accommodated the repetition rate of the laser, the experimental time available, the reproducibility of the results, and the robustness of diagnostics to failure. In this chapter, the diagnostic challenges of these experiments, and the choices made in order to meet them, are discussed. Some aspects of the diagnostics, specific to the detection of x-rays produced in a GeV laser-plasma accelerator (LPA) driven by the TPW laser, will be deferred until Chapter 5.3 (Diagnostic Issues Specific to GeV LPAs).

3.2 Diagnostic Requirements and Options

Here it will be helpful to the reader to describe the typical chain of events taking place during a laser-wakefield experiment (see Figure 3.1):

1. Prior to the arrival of the high-energy laser pulse, referred to as a *system* shot, a low-energy *OPA* shot is used to focus the far field of the laser unto the entrance aperture of the gas cell. This is done by means of a deformable mirror (DFM) adaptive optics. Due to thermal lensing by optical components in the TPW laser, the actual far field focus location, as well as the mode, of the system shot may differ somewhat from that of the OPA shot. This introduces shot-to-shot variations into the driving pulse, impacting the extremely non-linear interaction between the laser and the plasma.
2. A few milliseconds prior to the system shot, a trigger arrives causing the helium source aperture into the gas cell to open, allowing sufficient time for the gas cell to uniformly fill up with gas. Prior adjustment of the backing pressure for the gas cell makes the setting of the gas cell pressure, hence plasma density, accurate to within 10%.
3. Immediately following a system shot, the TPW laser pulse propagates towards the gas cell filled with helium, enters the gas cell through its entrance aperture, converts the

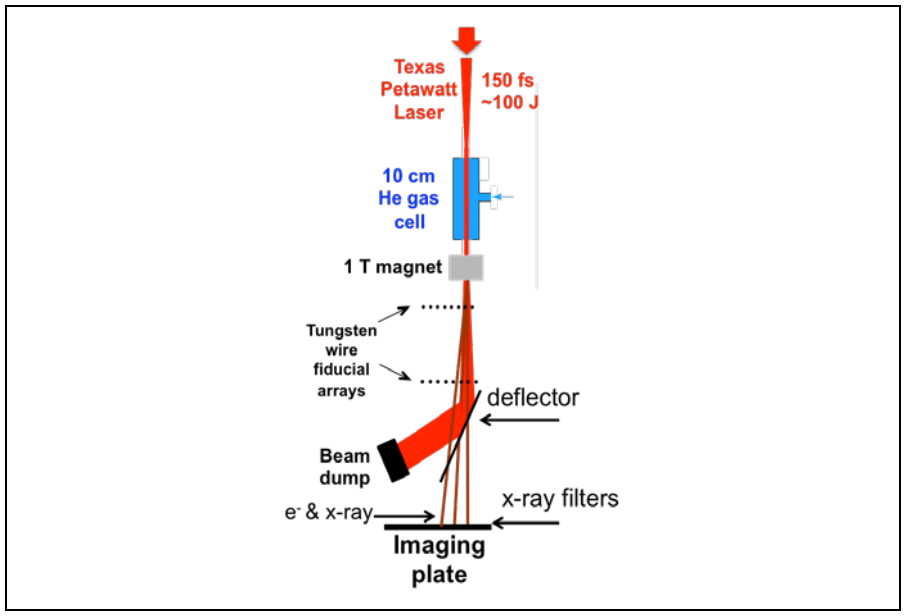

Figure 3.1: Schematic of the generic experimental setup for a laser-wakefield experiment

gas into plasma, self-focuses, and generates a non-linear plasma wake. The variability of the laser pulse parameters, the uncertainty in the plasma density, and the nonlinearity of the laser-plasma interaction, together create variability in the spectra and spatial distribution of the radiation produced during the interaction.

4. Provided that the laser intensity is high enough, a plasma bubble is formed, into which electrons get trapped and accelerated in the longitudinal field inside the bubble. The interaction between the laser and the plasma generates an electromagnetic pulse (EMP) that can affect the operation of nearby electronics.
5. As electrons accelerate inside the plasma bubble, they acquire relativistic speeds. They also oscillate in the transverse electrostatic field inside the bubble and produce radiation. Because the reference frame of the relativistic electrons is boosted with respect to the lab frame where the detectors are, the Lorentz-boosted radiation is in the x-ray part of the spectrum. This is the betatron radiation.
6. Accelerated electrons at various energies, as well as a broad spectrum of x-rays, leave the gas cell in a range of directions towards the detectors, at the far end of the diagnostic chamber. Before reaching the detectors, the electrons are deflected inside a magnetic spectrometer, with the lowest energy electrons suffering the largest deflection. The higher the electron energy, the closer it will be to the betatron radiation, which is detected on the same detector. In extreme cases (very high energy

electrons) it is possible therefore for the electron and x-ray signals to partially overlap.

7. Depending on the strength of the magnet used, there is a group of lower-energy electrons that do not make it to the end of the chamber. These electrons are detected closer to the magnet before entering the main diagnostic chamber.

Given the typical experimental scenario just described, the goals of the diagnostics with regard to the electrons and x-rays were the following:

1. Since the combination of the laser pulse parameter (mode, phase, duration, energy, spot size), and the plasma density, are not precisely reproducible, and the laser-plasma interaction takes place in the nonlinear regime, diagnostic methods are all single-shot, i.e., experimental results from each shot stand on their own. This requires that the detectors be sensitive enough to detect wakefield particles without the need for accumulation and averaging of signals.
2. To take advantage of the limited number of shots (100-150) available during the experimental run, diagnostics are capable of simultaneously detecting the presence and amount of all wakefield particles (e.g., electron charge and number of photons).
3. Diagnostics are capable of detecting the energy spectrum of all wakefield particles.
4. Detectors must have large active area size capable of detecting the spatial distribution (e.g., divergence) of the radiation in the presence of shot-to-shot pointing variation.
5. Be immune to EMP;

Given the relatively low repetition rate of the TPW laser, typically no more than 6 system shots per day, the limited time available for the experiments, typically a few weeks, and the single-shot nature of the experiment where no two shots produce similar results (this followed from the nonlinearity of the laser-plasma interaction) the strategy was adopted to prevent loss of data in the event of a diagnostic failure. Therefore, another diagnostic requirement was:

6. Incorporate built-in redundancy.

With these requirements in mind, diagnostics such as imaging plates (IP), radiochromic film (RCF), Lanex phosphor screens, plastic scintillator, and integrated current transformer (ICT) were considered. These are briefly discussed below.

1. Imaging Plate Detectors

Luminescence is non-thermal light emission (unlike the black body radiation). This can be in response to ionizing radiation such as charged particles or x-rays. The passage of charged particles, e.g., electrons, through matter leaves behind molecules in excited states. Some molecules release a fraction of about 3% of the excited energy as optical photons. This process, known as *scintillation*, is especially present in synthetic polymers having aromatic rings such polystyrene (PS) and polyvinyltoluene (PVT). When the excitation is by means of electrons or x-ray photons, and the de-excitation and accompanying release of radiation takes place with a long decay time (> 1 millisecond), the phenomenon is known as *phosphorescence* or afterglow. When photons are radiated with much smaller decay time, and have lower energy than the exciting photon, the phenomenon is known as *fluorescence*. Luminescent materials, whether phosphorescent, or (wavelength shifting) fluorescent, when synthetically made, are referred to as *phosphors*. Imaging plates (IPs) are a type of phosphor detectors displaying *photo-stimulated luminescence* (PSL). They are different in one crucial aspect from other luminescent materials: the requirement for optical (photo-) stimulation to release the energy stored by the primary ionizing radiation. As a result, imaging plates are in effect storage devices for energy deposited by ionizing radiation, making them flexible radiation detectors. This feature distinguishes them from other phosphor detectors, such as Lanex screens, where the emitted radiation must be imaged in real time. Compared to x-ray films, imaging plates have lower resolution (50-100 μm), but provide higher sensitivity and dynamic range [22]. As shown in Figure 3.2, IPs have a wide dynamic range of ~5 orders of magnitude and a response that varies linearly with dose over a greater range of values than in the case of x-ray films (where the response is S-shaped). As an example, when used to detect x-rays, the imaging plate response is linear for incident number of x-rays ranging from 8 to 4×10^4 x-ray photons per 100-μm pixel. In practice, however, the dynamic level of the IP is limited by the amplification limit of the photo-multiplier tube (PMT) in the read-out (scanner) system; this leads to the saturation of the read-out signal at high radiation dose levels. (This is further discussed in C.2.)

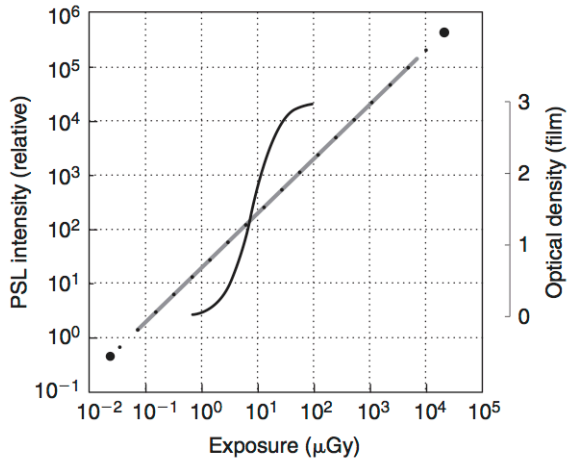

Figure 3.2: Imaging plates have higher dynamic range, and a linear response over a wider range of radiation doses than the x-ray film (S-shaped response) [23].

The standard imaging plate phosphor has the composition $BaF(Br_{0.85}I_{0.15}):Eu^{2+}$, in the form of clusters of small crystals of grain size ~5 μm, mixed with an organic binder, and uniformly coated on a plastic substrate [24]. The process for photo-stimulated luminescence, shown in Figure 3.3, starts with the ionization of europium (Eu) ions in phosphor crystals by incident radiation (x-rays, electrons) in the process $Eu^{2+} \rightarrow Eu^{3+} + e^{-}$ to create electron-hole pairs. These pairs are created in numbers proportional to the absorbed radiation energy. The electrons are then promoted from the valence band of the phosphor to the conduction band and are trapped in Br^{-} and F^{-} vacancies (crystal defects) that are intentionally manufactured into the crystal lattice. Known as color or *F* centers (*Farbezentrum*), electrons trapped in halogen ion vacancies, when irradiated during the read-out process by red laser light, are promoted to an excited state, then thermally excited into the conduction band. Recombination of the electrons with Eu^{3+} holes emits light as the result of the electron returning to the valence band; this luminescence, which is in the blue-violet part of the visible spectrum (photon energy of 3.2 eV, see Figure 3.3), is then collected by the light collection system of the imaging plate reader (scanner). The trapped electron may also be excited into the conduction band purely by thermal means, in a process known as *fading* and having exponential decay rate. The PSL response time is < 1 μs making it possible to read an imaging plate at speeds exceeding 5–10 μs per pixel.

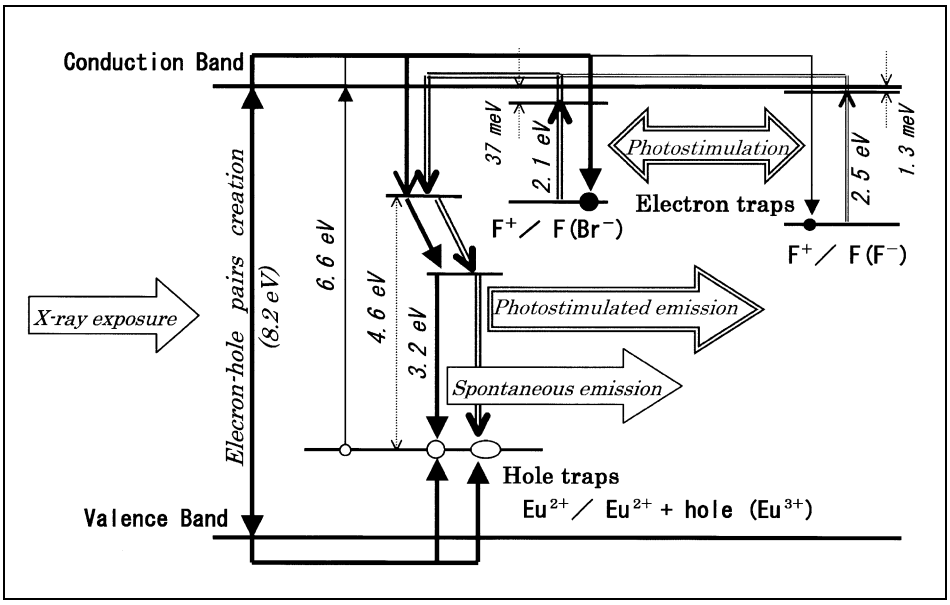

Figure 3.3: Energy diagram for photo-stimulated luminescence in BaFBr:Eu^{2+} [25]

2. Plastic Scintillators

There are two types of scintillators: organic and inorganic. Organic scintillators (e.g., polyvinyltoluene) can be liquid or plastic, have fast decay times (nanoseconds), and are relatively inexpensive; they have, however, lower light output (up to 10000 photons per MeV of deposited energy). Inorganic scintillators (e.g., CsI, Gd_2O_2S) are mostly in crystal form, have longer decay times (microseconds), and are relatively expensive, but produce up to 40000 photons per MeV of deposited energy. Experiments discussed in this dissertation confirmed that PVT-based plastic scintillators are appropriate for the detection of electrons, however produce insufficient amount of light for a reliable detection of x-rays. Even for electrons, the thickness of plastic scintillator required to produce a detectable amount of light (a few millimeters), comes at the price of lower resolution. This is because scintillation light is generated from all points in the path of the electrons as they traverse the scintillator; there is also scattering of the charged particles and light inside the scintillator. At higher energies scattering effects are reduced, but maintaining the depth of field for the light originating from different positions along the path of the electrons requires an increase in the f-number of the imaging optics, which itself reduces the amount of light. There is therefore a trade-off between resolution and sensitivity for scintillators, making the resolution of a scintillator-based detector lower than the 100- to 200-μm resolution obtained with imaging plates for similar sensitivity to

incident radiation. On the other hand, scintillator light may be imaged using a CCD in real time, without the need for a scanner read-out system. The vulnerability of CCDs to EMP can be significantly reduced by positioning the CCD far from the interaction chamber. The LPA experiments driven by the TPW laser indicated that scintillators are suitable as real-time diagnostics for detecting the presence, and the shape, of the magnetically deflected electron signal.

3. Scintillating Screens

Scintillating screen detectors (e.g., Lanex screens) are comprised of a layer of powdered rare earth phosphor (e.g., Gd_2O_2S + urethane binder) on a plastic substrate (e.g., polyethylene terephthalate), covered on both sides with a protective coating, e.g., cellulose acetate [26]. Originally used in medical x-ray radiography, these phosphorescent screens (scintillation decay time is 1 millisecond) are now routinely used in LPA experiments for the detection of relativistic electrons. Due to the smaller amount of scintillating material in the path of electrons, these detectors offer better resolution than plastic scintillators; this, however, comes at the prices of lower sensitivity. The response of scintillating screens to electron charge is linear over a wide range (from pC to tens of nC) [27] and is independent of electron energy above 3 MeV.

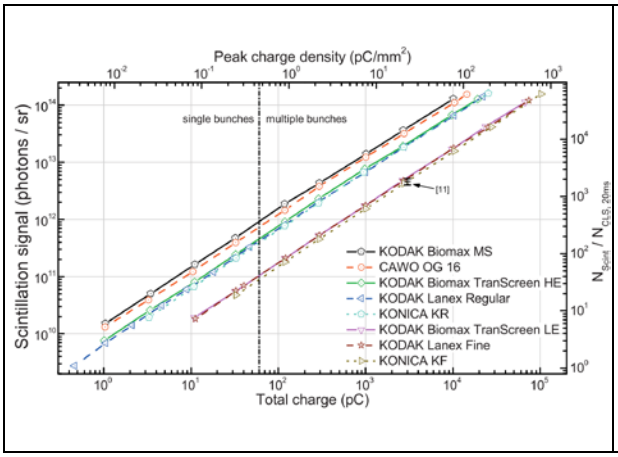

Figure 3.4: Lanex scintillation signal varies linearly with incident electron charge over a range of several orders of magnitude from pC to nC [27].

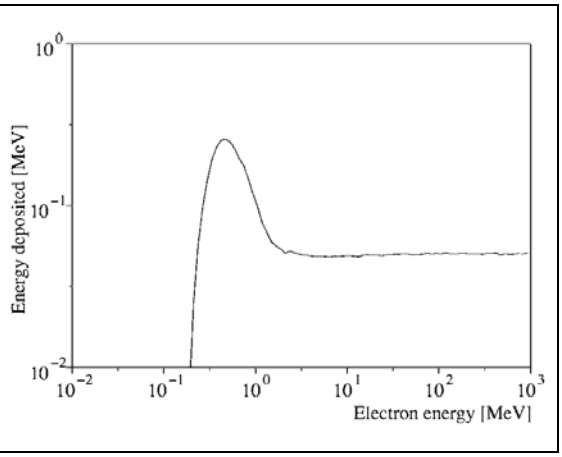

Figure 3.5: Energy deposited by electrons in Lanex screen is independent of incident electron energy above 3 MeV [28].

Unlike imaging plates, which store the radiation energy and require post-exposure processing using a specialized read-out system, the signal from a scintillating screen detector may be directly imaged onto a CCD and made available in real-time. These

detectors are also not susceptible to EMP as ICTs are. Together, these features make Lanex screens suitable as a charge diagnostic in LPA experiments, in particular in high-repetition rate environments where the scanning of imaging plates becomes impractical. Two types of scintillating screens are the Lanex Regular and Lanex Fine screens, both manufactured by Kodak. Lanex Regular screen is ~4 times more sensitive to electron charge and more appropriate for the measurement of weaker signals. By comparing Lanex and ICT measurements of the same charge for charges up to 100 pC/mm^2, Buck et al. [27] measured deviations from the expected linear relationship and attributed this to light output degradation due to saturation in the Lanex. Birks [29] attributed this saturation and the ensuing reduction in scintillation light yield to recombination and quenching effects among the excited molecules; the saturation effect is enhanced with the increasing density of the excited molecules. Fitting the Lanex charge density measurement ρ_{Lanex} to a Birks' law function, $\rho_{Lanex} = \rho_{ICT}/(1 + B\,\rho_{ICT})$, where the ICT charge density measurement ρ_{ICT} represents the correct (i.e. unaffected by saturation) measurement, and B is a constant, Buck et al. found that the Lanex Regular screen exhibits saturation at 44 ± 10 pC/mm^2. This makes the Lanex Regular screen susceptible to saturation, in particular near the peak of charge distribution. The less sensitive Lanex Fine screen saturates at > 100 pC/mm^2 and is better suited when high charge density is expected.

4. Single-CCD Lanex-Scintillator Detector

In the first round of laser-wakefield experiments covered by this dissertation (LWFA 1.5), a 4" x 4" plastic scintillator, with a thickness of 6 mm, was introduced as a diagnostic to detect the presence accelerated of electrons. The selected scintillator, EJ-260, emits in the green part of the visible spectrum, with an emission spectrum peaking at 490 nm (Figure 3.6). To detect the luminescence from this scintillator, a Basler scA640-70fm CCD camera was used. This camera has a quantum efficiency that is ~40% over

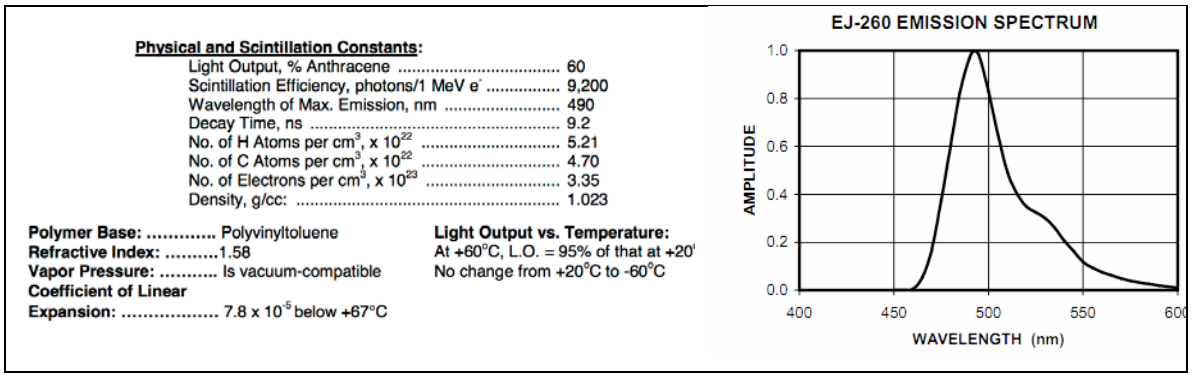

Figure 3.6: Physical properties of the EJ-260 plastic scintillator [Source: Eljen Technologies]

nearly the entire range of the EJ-260 emission spectrum, with the peak of the QE curve occurring very near to the peak of the scintillator emission spectrum (Figure 3.7). This matching of the emission spectrum and the QE curves ensured efficient detection of the luminescence from the plastic scintillator in response to the incident accelerated

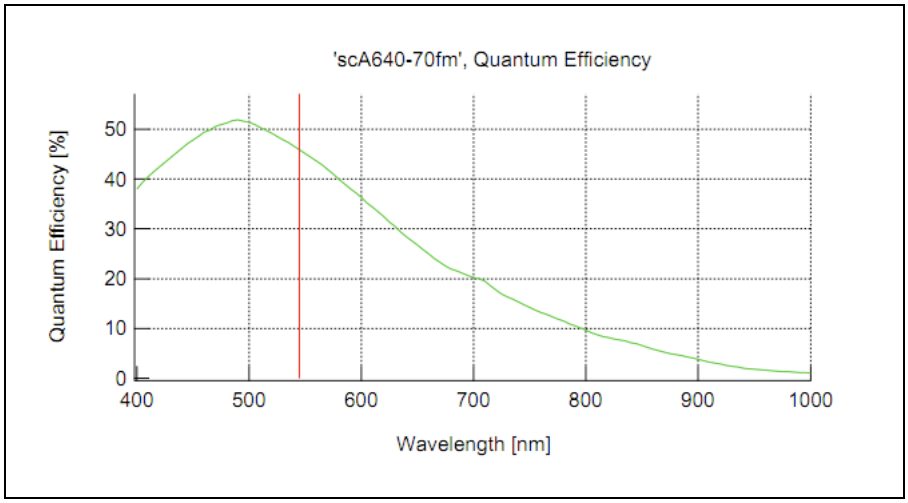

Figure 3.7: Absolute QE of the Basler scA640-70fm CCD camera [Source: Basler Corp.].

electrons. The energy deposited by an electron of energy E in passage through a scintillator of thickness δ is $\Delta E = E\left(1 - e^{-\delta/L_0}\right)$, where L_0 is the radiation length for the plastic scintillator (42.9 cm for the EJ-260 scintillator). Since the luminescence also scales linearly with incident charge, this diagnostic enables a comparison and ranking of laser-wakefield accelerated charge produced from different laser-plasma interactions. However, the plastic scintillator measurements are qualitative, under the assumption that the scintillator luminescence is a function of both incident charge and energy. Under the plausible scenario that the luminescence varied linearly with the energy deposited by the

electron in the scintillator, as well as with the electron charge, the presence of another detector to provide an independent, and commensurate, measurement of charge would enable a determination of the average energy of the electrons incident at any region on the combined diagnostic. Therefore it appeared that by measuring the luminescence of the plastic scintillator and relating it to the incident electron charge and deposited energy, and having an independent measurement of the incident electron charge, a diagnostic for the electron energy spectrum would result.

In the next two rounds of experiments (LWFA 2.0 and 3.0), in order to produce a more quantitative measurement of the accelerated electron charge, as well as its energy, a scintillating screen was introduced and a switch was made from the EJ-260 to the EJ-200 plastic scintillator. The luminescence from the combined diagnostic, the Kodak Lanex Regular scintillating screen and the EJ-200 plastic scintillator, was imaged onto a single color CCD in the geometry shown in Figure 3.8. The two scintillators are placed flush

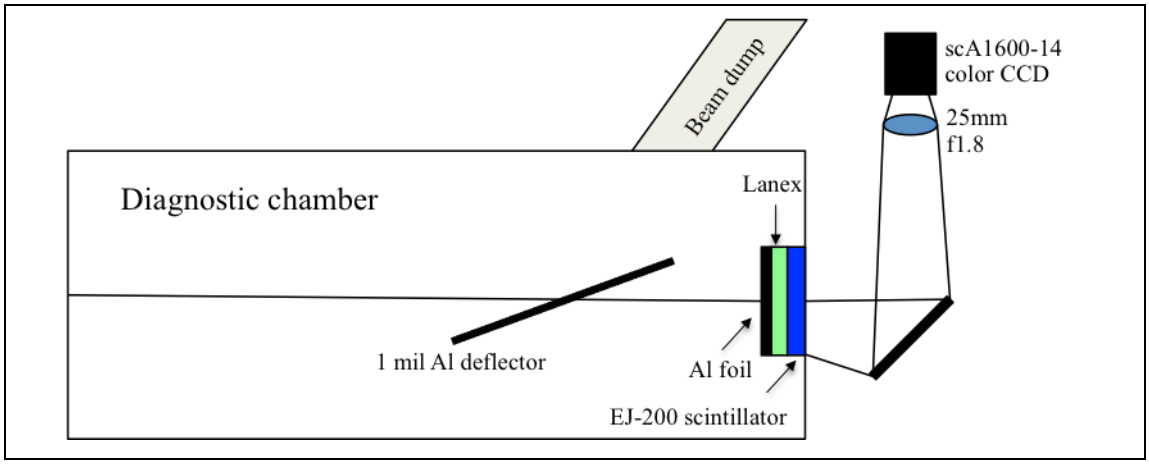

Figure 3.8: The schematic of the Lanex-scintillator double detector. Light from the Lanex screen (Kodak Lanex Regular[1]) and plastic scintillator (Eljen EJ-200[2]) reflects off a 3" broadband dielectric mirror (Thorlabs BB3-E02[3]), and is focused by a 25 mm focal length high resolution lens (Edmunds Optics #63-781[4]) onto a color CCD (Basler scA 1600-14fc[5]).

with one another, and positioned approximately at right angle to the incident electron

[1] http://www.carestream.com/lanex-screens.html
[2] http://www.eljentechnology.com/index.php/component/content/article/31-general/48-ej-200
[3] http://www.thorlabs.com/thorproduct.cfm?partnumber=BB3-E02
[4] http://www.edmundoptics.com/imaging/imaging-lenses/techspec-lenses/high-resolution-fixed-focal-length-lenses/63781
[5] http://www.baslerweb.com/products/scout.html?model=192

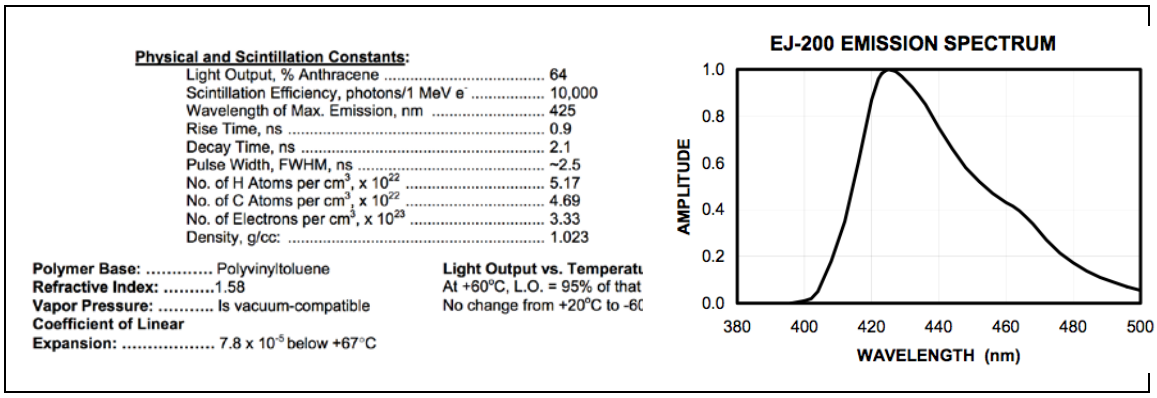

Figure 3.9: Physical properties of the EJ-200 plastic scintillator [Source: Eljen Technologies]

beam. This geometry ensures that the images produced by the Lanex and scintillator are commensurate, hence easier to compare. In addition, by minimizing the path of the electron through the scintillator, the scintillator thickness is matched to the depth of field, improving imaging resolution. The EJ-200 plastic scintillator was selected for the wavelength at which its emission spectrum peaks (425 nm, blue, Figure 3.9); it also has a high scintillation efficiency of 10000 photons per 1 MeV electron, a long optical attenuation length (~4 m) and fast response time (2–3 ns). The Lanex Regular, on the other hand, emits visible light sharply peaking at ~550 nm (green, Figure E-3). The peak emissions of the two detectors are well separated and detected by different color CCD channels; luminescence from the Lanex is primarily detected by the green channel; plastic scintillator radiation is detected by the blue channels. This allows efficient use of 2 of the 3 CCD channels.

The two major energy loss mechanisms for an electron in a scintillator are bremsstrahlung, and collisions (leading to ionizations and excitations); these mechanisms have different dependence on the incident particle energy. In the case of bremsstrahlung energy loss, the rate of energy loss (dE/dx) is proportional to the particle energy; for collisional energy loss, the rate of energy loss is proportional to the logarithm of particle energy. Energy loss dependence on the incident electron charge is linear in both cases. For a scintillator matrix material such as PVT, above a critical energy of ~242 MeV the rate for bremsstrahlung surpasses the rate for collisions and at 1 GeV bremsstrahlung dominates (the ratio of dE/dx for the two energy loss mechanisms is > 4). This suggests

that, all else being equal, the deposited energy per unit length, dE/dx, and the resulting luminescence, should vary linearly with incident particle energy, as well as with its charge. Given that the luminescence from the Lanex detector scales linearly with the incident electron charge (Figure 3.4), it was initially considered a diagnostic possibility to combine the measurements from the Lanex screen and the plastic scintillator detectors in order to detect the electron energy. This is because if the luminescence from the scintillator scaled linearly with the electron charge as well as deposited energy, it would appear that beginning with geometrically commensurate signals separately produced by the Lanex and scintillator detectors, it would be possible to divide the scintillator signal (proportional to energy times charge) by the Lanex signal (proportional to charge), to obtain a signal proportional to the electron energy at each point (pixel) on the signal image. In fact, energy loss by the incident particle should be considered separately from its conversion into scintillation light. This is because not all energy lost by the electron in the scintillator is re-absorbed and it is only the energy deposited and subsequently re-emitted by the scintillator in the visible part of the spectrum that contributes to the scintillator signal.

What happens is that the radiation energy re-emitted by the scintillator base material (e.g., PVT) is in the UV part of the spectrum; the base material is also relatively opaque to this radiation (i.e., has short absorption length). When one or more organic fluorescent agents, such as Anthracene ($C_{14}H_{10}$), are added to the PVT base as wavelength shifters, the UV scintillation light is absorbed and re-emitted by the fluorescent agent in the visible part of the spectrum, typically around 400 nm (Figure 3.10). Since not all energy deposited by the electron is re-emitted as luminescence in the visible part of the spectrum, the assumption of a linear relationship between the electron energy and measured luminescence is not valid. For this reason, the idea to combine the Lanex screen and the plastic scintillator detectors into an energy spectrum diagnostic for the electron proved not to be feasible. Nonetheless, this combination diagnostic does satisfy two of the diagnostic requirements described in 3.2. The luminescence from the Lanex detector, when separated from that of the scintillator, may be used as a charge diagnostic. This has been demonstrated in Appendix E. The combination of the Lanex and plastic

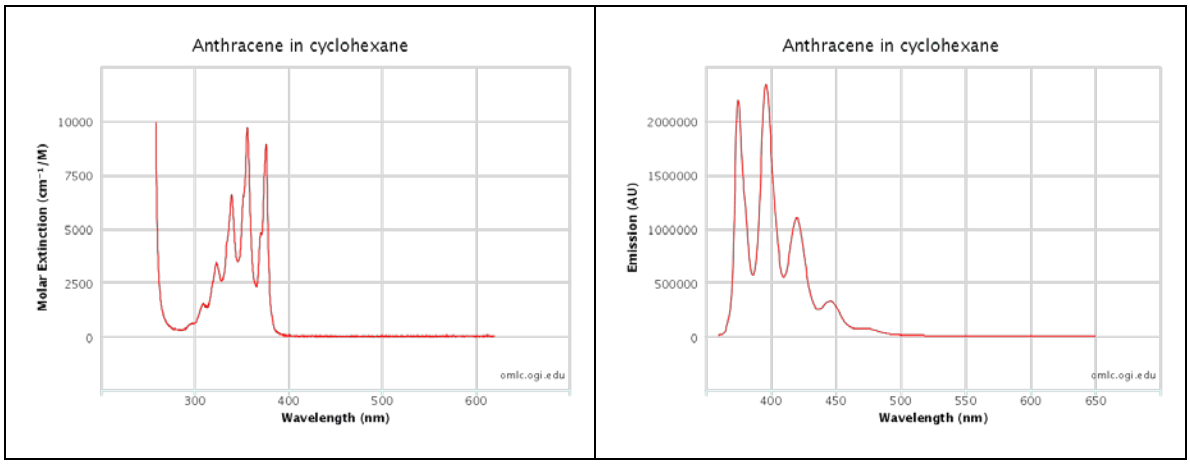

Figure 3.10: Absorption and emission spectra for the typical fluorescing material (Anthracene) added to the PVT base in order to shift a portion of the deposited and radiated energy from UV to visible.

scintillator measurements, taken together, provide a real-time diagnostic for the presence, shape, and approximate peak energy of the electron signal. Note that the light output of the scintillator is larger than that of the Lanex (by about a factor of 2), therefore the combination detector produces higher luminescence than the Lanex detector by itself. This is useful in cases where the Lanex signal by itself is too weak (due to low charge) to identify the presence of electrons.

3.3 Evolution of the Diagnostic Setup

Figure 3.11 shows the original conception for the diagnostic setup in the laser-wakefield experiments driven by the TPW laser. The top image shows three main components consisting of a round interaction chamber (left), a small round diagnostic chamber (middle), and a large diagnostic chamber (right). The laser pulse, arriving from the left, interacts with the helium gas in a gas cell of length ~7-10 cm (located at the center of the interaction chamber). The wakefield-accelerated electrons that are produced inside the gas cell exit through an aperture, in a cone of full angle < 2 mrad; this angle is determined by the launch angle of the electrons, and limited by the ~1-3 mm diameter of the aperture. All accelerated electrons pass through an integrated current transformer (ICT) and, in the absence of a deflecting magnet, propagate the ~2.7 m distance from the gas cell to the end of the diagnostic chamber and are detected by an imaging plate detector. The bottom image shows the same chambers but with the addition of a deflecting magnet of field strength 1.1 T at the center of the magnet. Trajectories for

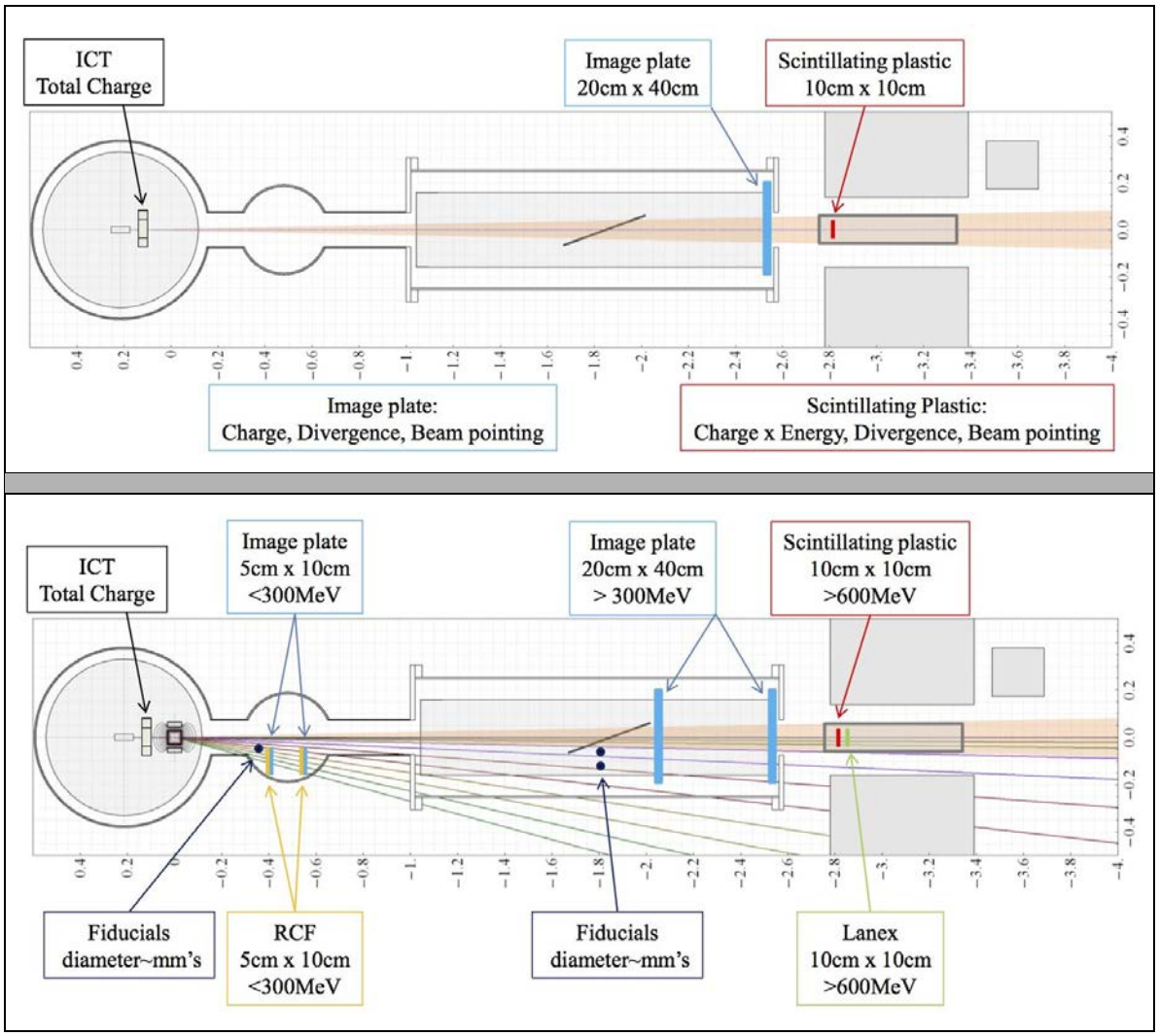

Figure 3.11: Top: Original conception of the interaction chamber (left) and the diagnostic chambers (middle and right). Bottom: Magnetic spectrometer showing electron trajectories corresponding to 85 MeV, 100 MeV, 120 MeV, 150 MeV, 200 MeV, 300 MeV, 500 MeV, 1 GeV, 2 GeV, and 4 GeV, as well as for undeflected electrons. [Image courtesy of Rafal Zgadzaj]

electrons having energies 85 MeV, 100 MeV, 120 MeV, 150 MeV, 200 MeV, 300 MeV, 500 MeV, 1 GeV, 2 GeV, and 4 GeV, as well as for undeflected electrons, are also shown. After passage through the ICT and the magnet, the electrons are deflected, with the lowest energy electrons suffering the largest deflection, therefore detected earlier along the longitudinal path. Electrons with energies in the range 100-200 MeV are detected in the small diagnostic chamber using small imaging plates or radiochromic films (RCF). Electrons with energies 200-300 MeV are prevented by the connecting tube between the small and large diagnostic chamber from entering the latter chamber; as a result they are not detected. Higher-energy electrons, with energies greater than 300-350

MeV are detected by imaging plates in the large diagnostic chamber. By positioning two longitudinally separated sets of fiducial wires in the path of electrons, the energy and the launch angle of the electrons corresponding to the shadow cast by a fiducial wire may be deconvolved by recovering the trajectory of electrons from the fiducial shadow to the fiducial wire that created it, then retracing the electron path through the field of the magnet and constraining it to cross the position of the x-ray source inside the gas cell. The position of the x-ray source (used as a proxy for the electron source) may be separately determined by using two shadows cast by fiducial wires in the betatron x-ray signal on the detector and triangulating each to the corresponding fiducial wire and finding the point where they intersect inside the gas cell. Alternatively, shadows of fiducials wire on two longitudinally separated imaging plates may be triangulated (shown on the bottom image). The former approach, requiring a single detector but using the position of the x-ray source for the recovery of the electron trajectory, was determined to be more accurate and used for experimental rounds 2-4.

In the round of the experiments that preceded the results presented in this dissertation, radiochromic film was employed to detect the electron signal. An electron impinging on a radiochromic film releases radiation energy that causes polymer chains to be formed in the film. The polymer density in a region of the film increases with amount of energy deposited, which itself increases with the number of electrons impinging on that region. The polymer absorbs red light. By scanning the film using a color scanner, and measuring the intensity of red light reflected from different regions on the film, the polymer density, and from that the deposited energy, can be determined. (It is possible to simulate the deposited energy for comparison with that estimated using red light intensity measured by the scanner.) After its first use, this detector was replaced in favor of other, more practical, diagnostics. The primary weakness of the radiochromic film is that it requires processing by means of a color scanner that requires a precise, and error-prone, calibration. It also is not very sensitive. In particular, it is not an optimal choice for the detection of the betatron radiation. Beginning with the first round of experiments covered by this dissertation (LWFA 1.5), an ICT detector was introduced into the small diagnostic chamber following the interaction chamber. These devices measure charge in a very fast

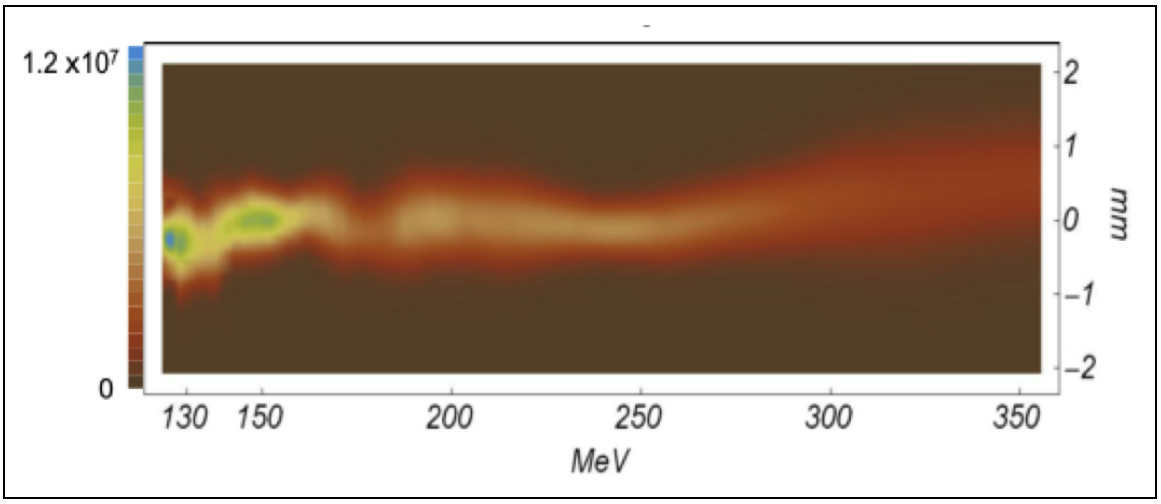

Figure 3.12: Electron signal detected on the Radiochromic film in the initial round of laser-wakefield experiments driven by the TPW laser (LWFA 1.0)

pulse by integrating over the current induced in the winding around an magnetic core, producing a signal with slower rise time which can be integrated over (Figure 3.13). They are capable of integrating over charge pulses with picosecond rise time and, in principle, can be used to measure the accelerated charge in a laser-wakefield experiment. They are, however, susceptible to the presence of electromagnetic pulse in the environment. After the initial deployment of the ICT device in the diagnostic chamber nearest to the interaction chamber, it was found that its signal was impacted by the EMP generated during the laser-plasma interaction. To remedy this, in the round of experiments that followed (LWFA 2.0), the ICT was shielded in order to protect it from EMP; this had mixed results. In the next round (LWFA 3.0), different cables were used to improve the impedance matching between the ICT and the oscilloscope. This seemed to have improved the quality of ICT data. However, the electron charge determined from the ICT seemed too large when compared to the imaging plate charge. Biased charged measurement by ICT due to its sensitivity to the presence of EMP in the environment is a known issue in laser-wakefield experiments [28], [30]. In LWFA 4.0, the ICT was not deployed.

In the first experimental round (LWFA 1.5), an EJ-260 plastic scintillator was rotated 18 degrees with respect to the normal as determined by the propagation direction of the laser (Figure 3.14), and imaged using a Basler scA640-70fm mono CCD, to detect the presence of high-energy electrons. The enclosure housing the plastic scintillator and the

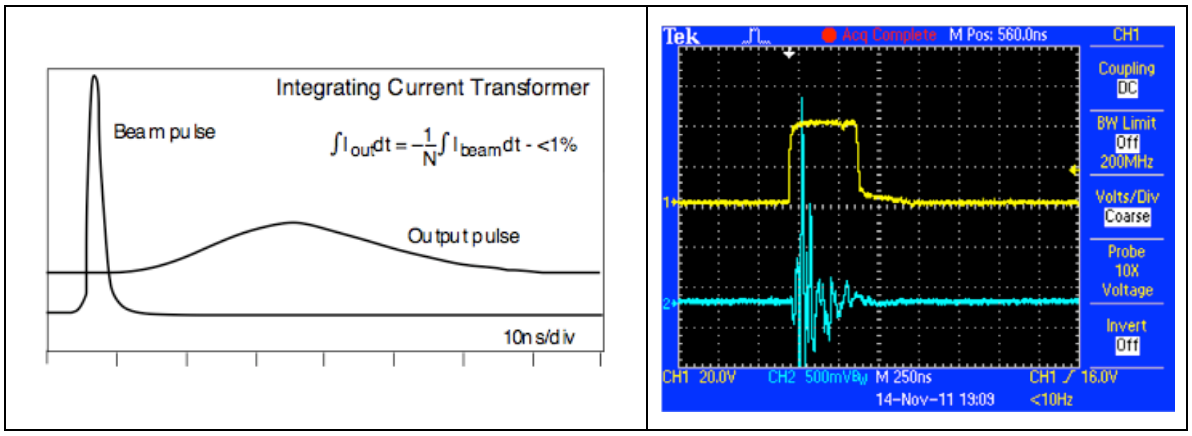

Figure 3.13: In response to a fast-rising pulse of charge, the ICT produces an output pulse with slower rise, which can be integrated over to determine the total charge (left). In the LPA experiments driven by the TPW laser, the ICT signal was impacted by the EMP from the laser-plasma interaction (right).

CCD was placed outside the large diagnostic chamber. In the following two rounds, an EJ-200 plastic scintillator, a Kodak Lanex Regular scintillating screen, together with a color CCD were used to detect the presence, as well as charge, of high-energy electrons (Figure 3.8). The Lanex screen and the plastic scintillator were both positioned inside the large diagnostic chamber and flush with its exit window in order to produce commensurate images from each detector. (An aluminum foil was used to prevent scintillation light from backscattering into the chamber.) The colors CCD and the flat

Figure 3.14: The enclosure housing the EJ-260 plastic scintillator (green) and the mono CCD used to image it was placed outside the large diagnostic chamber for the first experimental round (LWFA 1.5). See text for details.

reflecting mirror were positioned outside the large interaction chamber. In the final experimental round, the Lanex and scintillator diagnostics were not deployed. This was done to accommodate a parallel experiment that aimed to take advantage of the wakefield-accelerated electrons to produce muons by scattering electrons of GeV and

higher energies from a high-Z material (a block of tungsten) and pair production of the resulting bremsstrahlung photons.

3.4 The Magnetic Spectrometer

Charged particles deflect in the field of a magnet due to the Lorentz force. In the case of accelerated electrons, it is possible to determine their energy from their cumulative deflection in the plane of propagation and in the direction transverse to the direction of electron propagation in the absence of a magnet. This is discussed in detail in Chapter 4. However, accelerated electrons are launched into the field of a magnetic spectrometer in a range of directions and it is possible for electrons of different energies to arrive at the same position on the detector if they have the appropriate launch angles as they enter magnetic field. To accurately determine the energy of accelerated electrons using a magnetic spectrometer, a deconvolution of the electron energy from its launch angle is therefore required. This may be done using trajectory recovery. A variant of the two-screen technique ([5], [31]) was employed for this purpose. Instead of using two imaging plate detectors in the path of the particles, a single detector was used but thin wires were positioned in the paths of the particles to induce scattering in the particles on their way to the detector. The presence of these wires, referred to as fiducial wires, in the path of x-rays and electrons produces shadows in the both the x-ray and the electron signal

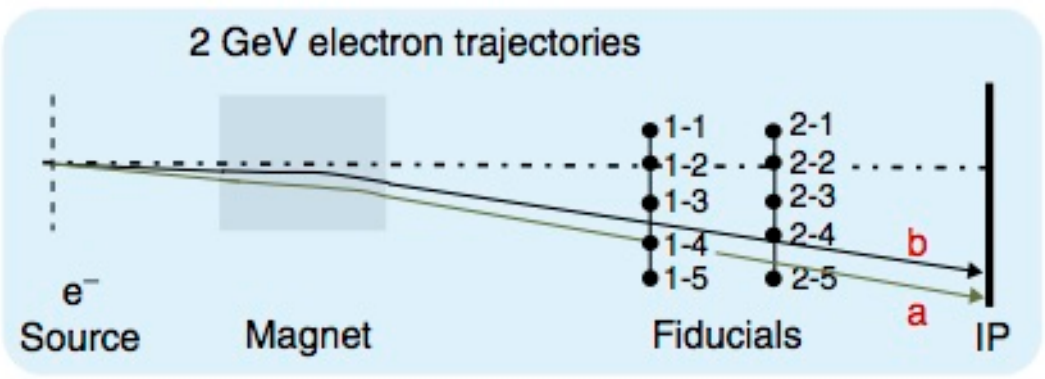

Figure 3.15: Two sets of fiducial wires were placed in the path of electrons and x-rays for the precise measurement of the accelerated electron energy. (A subset of the 8 wires used are shown in the figure.)

measured by the detector. As seen in Figure 3.15 (where only 5 of the 8 fiducial wires are shown), by triangulating the fiducial shadows on the x-ray signal back to the fiducial wires that created those shadows, the position of the x-ray source inside the gas cell may

be determined. Then by connecting the fiducial shadows for the electron signal back to the fiducial wires that created those shadows, then retracing the electron trajectory in the magnetic field back to the electron source position (using as proxy the x-ray source position from the previous step), the energy and the launch angle of the electrons corresponding to the recovered electron trajectory may be determined. Although electrons of different energies and launch angles may traverse the magnetic spectrometer to arrive at the same point on the detector, a set of 3 positions (fiducial shadow position on the detector, the position of the fiducial wire that created that shadow, and the x-ray source position in the gas cell) for magnetically deflected electrons of similar energy and launch angle, uniquely determines both the energy as well as the launch angle for the electrons that produced those shadows. (Note that using two sets of longitudinally separated fiducials, with wires on one rack appropriately offset with respect to those on the other, makes it possible to create shadows that are reasonably closely spaced on the detector without the need to position the fiducial wire too closely to each other on the same rack and risk scattering from multiple wires.) Having assigned energies to the positions on the detector (pixel numbers) corresponding to fiducial shadows, approximate formulas for the deflection of electrons in the magnetic spectrometer, as measured by their position on the detector, and as a function on their energy, can be used to perform a fit to the energy calibration results from fiducial triangulation. These formulas are derived in Chapter 4 (see Table 4-1 for a summary), where it is also shown that they are accurate to ~1% for electrons having energies greater than a few hundreds of MeV. In general, they have one free parameter, x_∞, representing the unobserved position of undeflected electrons on the detector, and determined during the fitting process. Although the formulas are derived assuming a vanishingly small electron launch angle, the fact that the data they are fit to (fiducial calibration data for the electron energy corresponding to fiducial shadows) do not make this assumption, in effect embeds in the free parameter any deviation from the assumption of vanishingly small electron launch angle.

To maximize the resolution of the magnetic spectrometer, GEANT4 simulations were performed to determine the optimum thickness and material for the fiducials. The criterion used was that for electron energies of interest ($\gtrsim$ 1 GeV), as well as for x-rays,

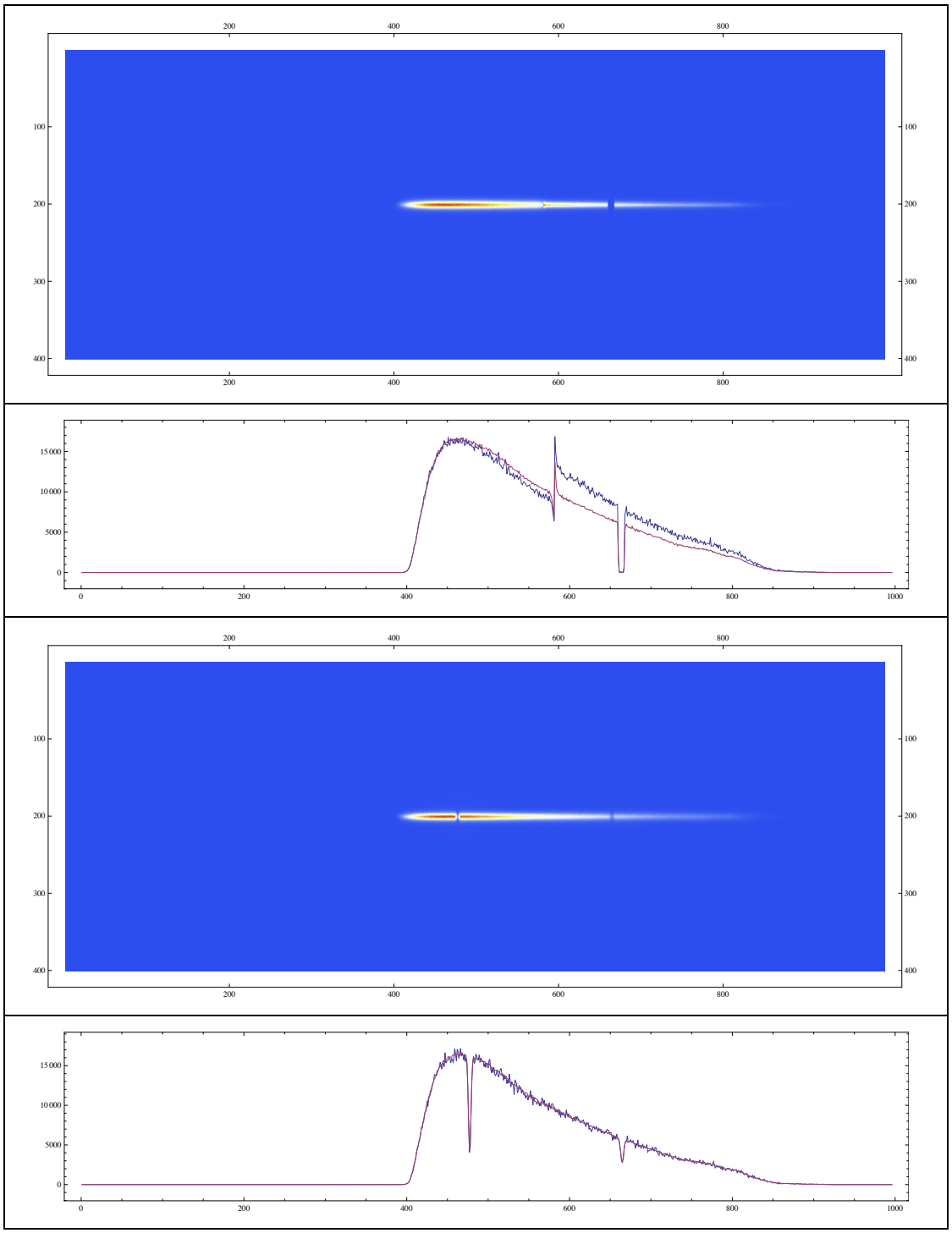

Figure 3.16: GEANT4 simulation results used to select the optimum fiducial diameter: (a) simulated electron distribution on the imaging plate using 1/64" (15.625 mil) tungsten fiducials; (b) horizontal lineout of the image in (a); (c) same as (a) with 5-mil tungsten fiducials; (d) horizontal lineout of the image in (c).

the width of the shadows produced should be comparable or smaller than the resolution of the imaging plate detectors. The depth of the shadows should also be large enough to provide high contrast. First a set of GEANT4 simulations were done to determine, in an

iterative approach, the electron energy spectrum and angular distribution that would reproduce the electron signal on the detector for a selected shot from the first experimental round discussed in this dissertation (LWFA 1.5). The accuracy of the iteratively obtained energy and angle distributions for the electrons was confirmed by using them as input to a simulation that replicated the geometry of the diagnostic chamber in round 1 experiments and accurately reproduced the electron signal detected on the high sensitivity image plate. The energy and angle distributions for this shot were then used to determine the optimum parameters for the fiducial wires. Figure 3.16 shows the simulated electron signal using the electron energy spectrum and angular distributions obtained for shot 3033. Tungsten was found to be an appropriate material due to the high-contrast shadows it creates for both x-rays and electrons. GEANT4 simulations indicated that in the case of GeV electrons, the sharply bounded shadows were due to the scattering of the low-divergence electron beam by the tungsten wires, whereas in the case of x-rays, shadows were primarily the result of absorption by the wires. To determine the optimum fiducial thickness, different diameters for the fiducial were simulated. The upper panels in the figure show the simulated electron signal, and its horizontal lineout, when tungsten fiducials of diameter 1/64" were placed in the path of the electron for the simulation. The lower panels show the same images but using tungsten fiducial wire of 0.005" diameter. Since the simulations used actual (hence realistic) energy and angular distributions for the electrons, and the simulated resolution and contrast of the fiducial shadows from the much thinner diameter for tungsten fiducial matched the requirements, the fiducial wire thickness of 0.005" was chosen for use in the magnetic spectrometer. To create two sets of shadows for electrons of given energy and launch angle, the fiducials were vertically positioned on two racks longitudinally separated by 20", with the fiducial rack closest to the end of the diagnostic chamber placed at a distance of 36.75" from the detector that was positioned there. On each rack, a set of 8 fiducial wires was positioned at distances chosen to produce shadows for a large range of electron energies. A 5 × 5 cm permanent dipole magnet with field strength of 1.1 T at its center was used. The magnet, having a fringe-free effective field of 1.48 T for 5 cm (alternatively fringe-free field of 1.10 T for effective distance of 6.7 cm) was positioned in the interaction chamber such that the direction of the magnetic field would produce deflection in the plane perpendicular to the

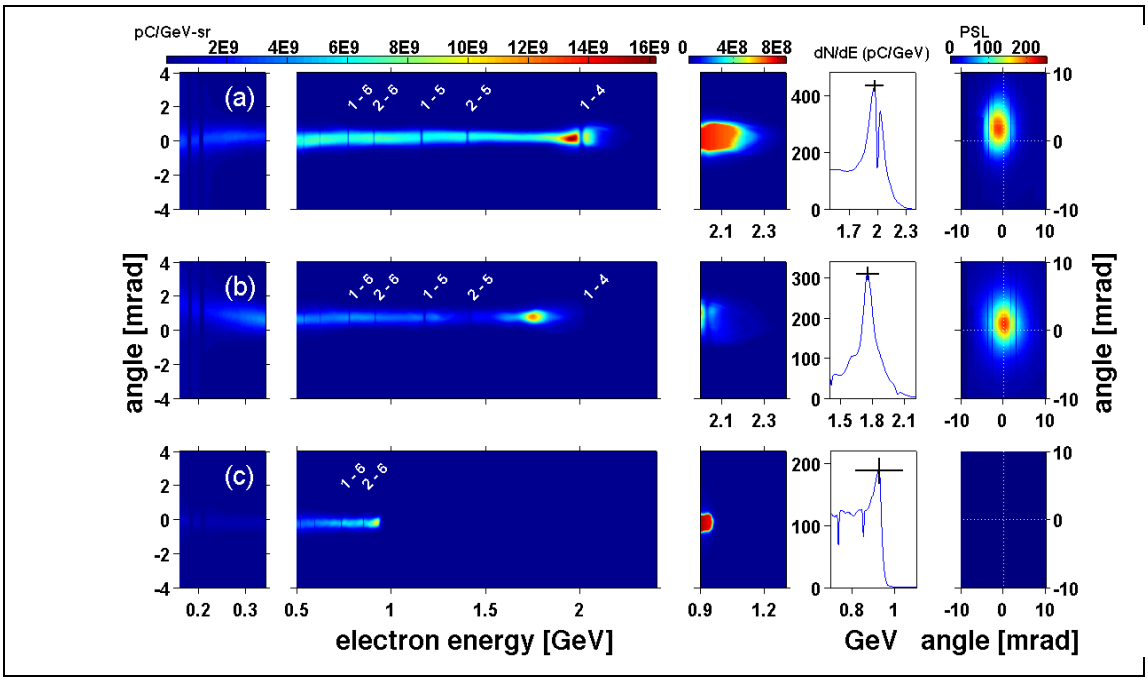

Figure 3.17: Sample electron spectrum and x-ray profile from the LWFA 2.0 experiment [32]

fiducial wires and to the right of the axis chamber for electrons as they traversed the magnetic spectrometer (see Figure 4.1). The IP detector was place 2.46 cm downstream from the magnet. On both fiducial racks, a fiducial wire (labeled 1-1 and 2-1 for the fiducial on the rack closest and farthest in relation to the gas cell, respectively) was positioned such that its transverse position coincided with the chamber axis. Another pair (labeled 1-2 and 2-2) was positioned 0.300" to the left of the chamber axis, when looking away from the gas cell in the direction of the detector. Electrons, deflected in the opposite direction, would clear these two fiducial wires but x-rays would produce shadows when scattered by these wires. On the fiducial rack nearest to the source, the remaining 6 fiducials were positioned at distances 0.330", 0.630", 0.960", 1.356", 1.871", and 2.592" from the chamber axis (direction of the laser beam alignment), and labeled 1-3, 1-4, 1-5, 1-6, 1-7, and 1-8, respectively. On the fiducial rack nearest to the detector, the remaining 6 fiducials were positioned at distances 0.300", 0.700", 1.140", 1.668", 2.354", and 3.315" from the chamber axis and labeled 2-3, 2-4, 2-5, 2-6, 2-7, and 2-8, respectively. Compared to the two-screen method cited previously, the fiducial wire method did not suffer from additional scattering of the electrons as they passed through the first detector. This enabled the transverse position of the x-ray (and electron) source to be determined to an accuracy of ±75 μm; the longitudinal position was determined to an accuracy of ±1 cm

[32]. Accurate measurement of the source position, when used to triangulate the fiducial shadows produced by the electrons on the detector, led to a resolution for the magnetic spectrometer of ±5% and enabled the electron energy to be determined to an accuracy of ±100 MeV at 2 GeV (Figure 3.17). As just described, each measurement of the magnetically deflected accelerated electrons typically produces a number of fiducial shadows for the electrons on the detector; the position of these shadows on the detector, following triangulation, yields a set of corresponding electron energies. These energy vs. position data may then be used as a dataset to fit approximate formulas that will be derived in the next chapter, to obtain a free parameter, the position on the detector corresponding to undeflected electrons, and used as a reference point to easily convert the electron deflection in the magnetic spectrometer to its energy. These formulas are less accurate than the method that uses shadows produced by fiducial wires to recover electron and x-ray trajectories, because of the assumption of a vanishingly small launch angle for the electron (see Figure 4.10 for a comparison), however they may be used to determine the electron energy for all positions on the detector in a programmatic, hence nearly real-time, approach (e.g., using ImageJ scripts).

In this chapter, the diagnostic aspects of laser-wakefield experiments were discussed, with emphasis on the diagnostic requirements of experiments driven by the TPW laser. In the next chapter, the spectroscopy of relativistic electrons in a GeV LPA will be reviewed and all necessary formulas for relating the observed electron deflection in the magnetic spectrometer to the electron energy will be derived. Spectroscopy of the x-ray radiation from a GeV LPA will be discussed in Chapter 5.

Chapter 4 Spectroscopy of Relativistic Electrons in a GeV LPA

4.1 Introduction

In this chapter, the equations governing the motion of an electron in a magnetic spectrometer are derived, then adapted to the parameters of the 4 rounds of experiments covered by this dissertation to obtain simple engineering-type formulas. In contrast to the method using fiducial wires and the triangulation of their shadows on the detector, discussed in 3.4, these equations are derived assuming a vanishingly small launch angle for the electron. They have the advantage, over the triangulation method, that they can be programmatically implemented and used to determine the electron energy spectrum and charge distribution in a nearly real-time manner. When used together with an accurate estimate of the betatron x-ray center on the detector, these formula yield results that are typically within 5% of the values from the fiducial shadow triangulation method.

The transverse deflection of an electron in the magnetic spectrometer has two components:

1. Deflection of the electron between entry into, and exit from, the magnet, due to the Lorentz force of the magnetic field on the charged particle;
2. Deflection of the electron between exit from the magnet and arrival at the detector, due to transverse velocity acquired during passage through the magnetic field.

Each component is derived separately, then the two are added to find the total transverse deflection of the electron in the magnetic field. Due to the relativistic energies of the laser-wakefield accelerated electrons, it is possible to derive approximate expressions for the electron energy in terms of its deflection at the detector that are accurate to < 1%.

4.2 Deflection of Relativistic Electrons in the Magnetic Spectrometer

A right-handed coordinate system $(\hat{\imath}, \hat{\jmath}, \hat{k})$ is used, where the field direction of the deflecting magnet (for now assumed uniform and with no edge effect) determines the $-\hat{\jmath}$

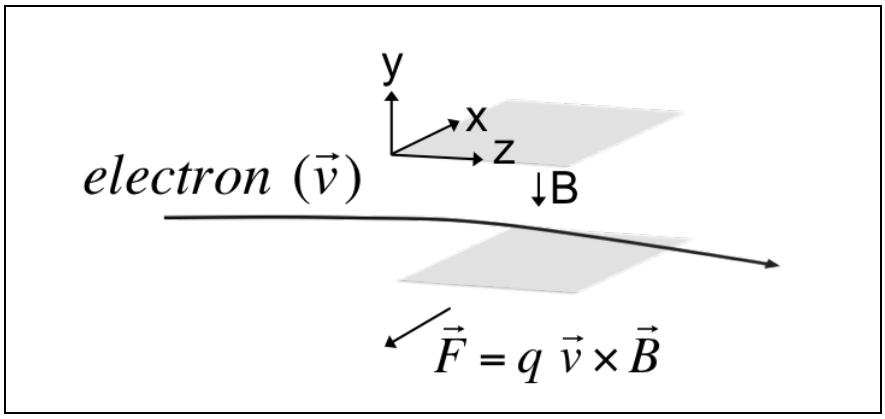

Figure 4.1: The path of an electron through the magnet, and the coordinate system used

direction, and the electron trajectory as it exits the gas cell (assumed co-linear with the laser propagation direction and the diagnostic chamber axis), determines the $\hat{k}$ axis. Then the field of the magnet, $\vec{B}$, the electron velocity as it enters the magnetic field, $\vec{v}_0$, and electron velocity inside the magnetic field, $\vec{v}(t)$, are:

$$\vec{B} = -B\,\hat{\jmath}$$

$$\vec{v}_0 = v_0\,\hat{k}$$

$$\vec{v}(t) = v_0(-\sin\omega t\,\hat{\imath} + \cos\omega t\,\hat{k})$$

where $\omega = \frac{|q|B}{\gamma m}$ is the relativistic Larmor frequency for the motion of a particle of charge q, mass m, and relativistic gamma γ, in magnetic field of amplitude B. The displacement of the charged particle inside the magnet is:

$$\Delta\vec{r}_M(t) = \int_{t_i}^{t} \vec{v}(t')\,dt' = \int_{t_i}^{t} v_0\big(\cos\omega t\,\hat{k} - \sin\omega t\,\hat{\imath}\big)\,dt' = \frac{v_0}{\omega}\big[\sin\omega t'\,\hat{k} + \cos\omega t'\,\hat{\imath}\big]_0^t$$

$$= \frac{v_0}{\omega}\{(\cos\omega t - 1)\,\hat{\imath} + \sin\omega t\,\hat{k}\}$$

The electron enters the magnet at $t = 0$ and exits the magnetic field at $t = t_f$. To find t_f, note that for an electron trajectory entering on one side of the magnet and exiting from the opposite (i.e., no side exit), the distance traversed in the $\hat{k}$ direction equals the length of the magnet L_M:

$$L_M = \vec{r}(t_f)\cdot\hat{k} = \frac{v_0}{\omega}\sin\omega t_f \longrightarrow t_f = \frac{1}{\omega}\sin^{-1}\frac{L_M\omega}{v_0}$$

The total displacement of the electron inside the magnet is:

$$\Delta\vec{r}_M(t_f) = \Delta x_M\hat{\imath} + \Delta z_M\hat{k} = \frac{v_0}{\omega}\big(\cos\omega t_f - 1\big)\,\hat{\imath} + \frac{v_0}{\omega}\sin\omega t_f\,\hat{k}$$

where

$$\Delta x_M = \frac{v_0}{\omega}\left\{\cos\left(\sin^{-1}\frac{L_M\omega}{v_0}\right)-1\right\} = \frac{v_0}{\omega}\left(\sqrt{1-\frac{L_M^2\omega^2}{v_0^2}}-1\right) = \frac{1}{\omega}\left(\sqrt{v_0^2-L_M^2\omega^2}-v_0\right)$$

The longitudinal and transverse displacements of the electron in the magnetic field is

$$\boxed{\begin{aligned}\Delta x_M &= \frac{1}{\omega}\left(\sqrt{v_0^2-L_M^2\omega^2}-v_0\right)\\ \Delta z_M &= L_M\end{aligned}} \qquad \textbf{Eq. 4.1}$$

The terminal velocity of the electron as it exits the magnet is:

$$\vec{v}(t_f) = v_0\left(-\sin\omega t_f\,\hat{\imath}+\cos\omega t_f\,\hat{k}\right) = v_0\left\{-\sin\left(\sin^{-1}\frac{L_M\omega}{v_0}\right)\hat{\imath}+\cos\left(\sin^{-1}\frac{L_M\omega}{v_0}\right)\hat{k}\right\}$$

$$= v_0\left(\sqrt{1-\frac{L_M^2\omega^2}{v_0^2}}\,\hat{k}-\frac{L_M\omega}{v_0}\hat{\imath}\right) = -L_M\omega\,\hat{\imath}+\sqrt{v_0^2-L_M^2\omega^2}\,\hat{k}$$

$$= v_i(t_f)\hat{\imath}+v_k(t_f)\hat{k}$$

The displacement of the electron between the magnet and the detector is

$$\Delta\vec{r}_{MD} = \Delta x_{MD}\hat{\imath}\ +\ \Delta z_{MD}\hat{k}\ = v_i(t_f)\times\frac{L_{MD}}{v_k(t_f)}\hat{\imath}+L_{MD}\hat{k} = -\frac{L_M\omega L_{MD}}{\sqrt{v_0^2-L_M^2\omega^2}}\hat{\imath}+L_{MD}\hat{k}$$

The displacement of the electron in the longitudinal and transverse direction, between magnet exit and arrival at the detector is

$$\boxed{\begin{aligned}\Delta x_{MD} &= -\frac{L_M\omega L_{MD}}{\sqrt{v_0^2-L_M^2\omega^2}}\\ \Delta z_{MD} &= L_{MD}\end{aligned}} \qquad \textbf{Eq. 4.2}$$

4.3 Determination of Electron Energy from its Deflection in the Spectrometer

The total electron deflection in the magnetic spectrometer is a function of the electron energy (mainly through its dependence on ω, but also on v_0) and is the sum of deflection in the magnetic field, Eq. 4.1, and drift between the magnet exit and the detector at the end of the diagnostic chamber, Eq. 4.2:

$$\boxed{\Delta x(E) = \Delta x_M(E)+\Delta x_{MD}(E) = \frac{1}{\omega(E)}\left(\sqrt{v_0^2-L_M^2\omega^2}-v_0\right)-\frac{L_M\omega L_{MD}}{\sqrt{v_0^2-L_M^2\omega^2}}} \qquad \textbf{Eq. 4.3}$$

This expression may be significantly simplified by writing it as follows:

$$\Delta x = \Delta x_M + \Delta x_{MD} = \frac{v_0}{\omega}\left(\sqrt{1-\frac{L_M^2\omega^2}{v_0^2}}-1\right)-\frac{L_M\omega L_{MD}}{v_0\sqrt{1-\frac{L_M^2\omega^2}{v_0^2}}} \qquad \textbf{Eq. 4.4}$$

The expression $\frac{L_M^2\omega^2}{v_0^2}$ is small; to determine its magnitude, v_0 and ω are needed. The electron mass, is $m_e = 0.511\ MeV/c^2$, therefore $m_e c^2 = 511{\times}10^{-6}\ GeV$. The relativistic gamma factor γ may be written as:

$$E_e[GeV] = \gamma m_e c^2 \longrightarrow \gamma = \frac{E_e[GeV]}{m_e c^2} = \frac{E_e[GeV]}{511{\times}10^{-6}} \qquad \textbf{Eq. 4.5}$$

Using the relativistic gamma factor $\gamma = 1/\sqrt{1-\beta^2}$ (where $\beta = v/c$) in Eq. 4.5, yields

$$1/\sqrt{1-\beta^2} = \frac{E_e[GeV]}{511{\times}10^{-6}}$$

Solving for β, yields a relation for v_0:

$$v_0 = \beta c = c\sqrt{1-\left(\frac{511{\times}10^{-6}}{E_e[GeV]}\right)^2} \qquad \textbf{Eq. 4.6}$$

The electron Larmor frequency for $q = e$ is:

$$\omega = \frac{|e|B}{\gamma m_e} = \frac{|e|B}{m_e}\frac{511{\times}10^{-6}}{E_e[GeV]} \qquad \textbf{Eq. 4.7}$$

Using Eq. 4.6 and Eq. 4.7, $\frac{L_M^2\omega^2}{v_0^2}$ may be written as:

$$\frac{L_M^2\omega^2}{v_0^2} = \frac{L_M^2}{c^2} \times \left(\frac{|e|B}{m_e}\frac{511{\times}10^{-6}}{E_e[GeV]}\right)^2 \Bigg/ \left(1-\left(\frac{511{\times}10^{-6}}{E_e[GeV]}\right)^2\right) \qquad \textbf{Eq. 4.8}$$

Using $L_M = 0.05\ m,\ B_{nominal} = 1.1\ T,\ B_{effective} = 1.4819\ T,\ c = 3{\times}10^8\ m/s, e = 1.602{\times}10^{-19}\ C,\ m_e = 9.11{\times}10^{-31}\ kg$, the behavior of $\frac{L_M^2\omega^2}{v_0^2}$, Eq. 4.8, as function of energy is plotted between 0.3-2.5 GeV. The small magnitude of $\frac{L_M^2\omega^2}{v_0^2}$ at energies greater than 0.3 GeV (~0.35 GeV is smallest energy detected by the magnetic spectrometer), makes an accurate (to better than 1%) approximation of Δy, Eq. 4.4, possible, using Taylor expansion of the types $(1-\alpha)^\beta \cong 1-\beta\alpha$, for $\alpha \ll 1$ and $\beta = \left(\frac{1}{2}, -\frac{1}{2}\right)$:

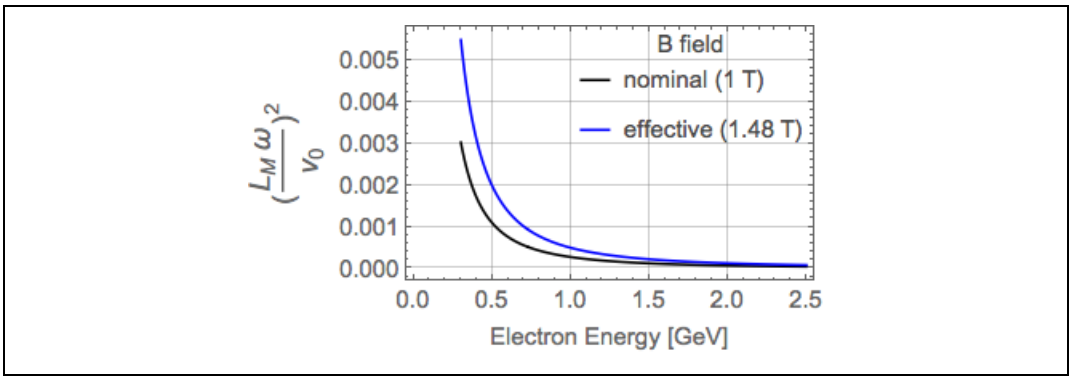

Figure 4.2: Behavior of term used for Taylor expansion of electron deflection in the magnetic spectrometer

$$\Delta x \cong \frac{v_0}{\omega}\left\{\left(1-\frac{1}{2}\frac{L_M^2\omega^2}{v_0^2}\right)-1\right\}-\left\{\frac{L_M\omega L_{MD}}{v_0}\left(1+\frac{1}{2}\frac{L_M^2\omega^2}{v_0^2}\right)\right\}$$
$$= -\frac{1}{2}\frac{L_M^2\omega}{v_0}-\left\{\frac{L_M\omega L_{MD}}{v_0}\left(1+\frac{1}{2}\frac{L_M^2\omega^2}{v_0^2}\right)\right\} \qquad \textbf{Eq. 4.9}$$

The 2nd term inside parenthesis in Eq. 4.9 may also be ignored (it is of the order of 0.001), giving

$$\Delta x \cong -\frac{1}{2}\frac{L_M^2\omega}{v_0}-\frac{L_M\omega L_{MD}}{v_0} = -\frac{\omega}{v_0}L_M\left(\frac{L_M}{2}+L_{MD}\right) \qquad \textbf{Eq. 4.10}$$

Using Eq. 4.7 for ω, and noting that $v_0 = c\sqrt{1-\left(\frac{511\times10^{-6}}{E_e[GeV]}\right)^2} \cong c$, the electron energy may be linked to the electron deflection at the detector using Eq. 4.10:

$$\Delta x \cong -\left(\frac{|e|B}{m_e}\frac{511\times10^{-6}}{E_e[GeV]}\right)\frac{L_M}{c}\left(\frac{L_M}{2}+L_{MD}\right)$$

Solving for E_e, and using $|\Delta x| = -\Delta x$ for $\Delta x < 0$, yields:

$$\boxed{E_e[GeV] \cong \frac{L_M}{c}\left(\frac{|e|B}{m_e}\frac{511\times10^{-6}}{|\Delta x|}\right)\left(\frac{L_M}{2}+L_{MD}\right)} \qquad \textbf{Eq. 4.11}$$

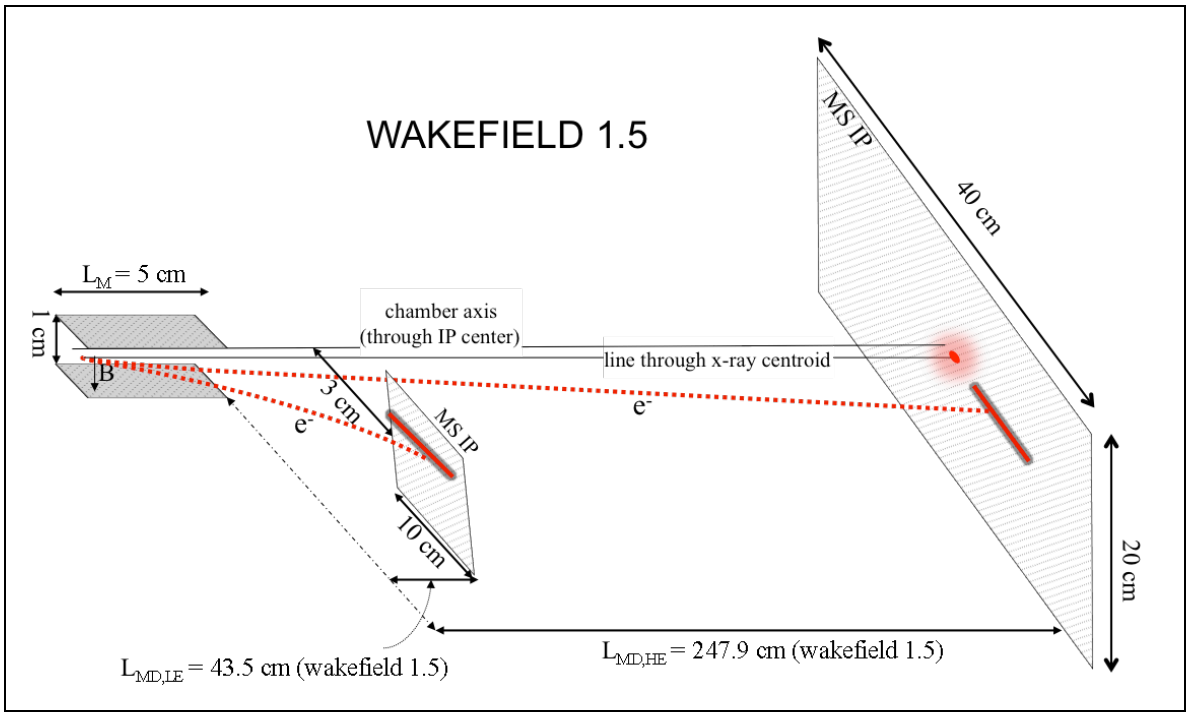

Figure 4.3: The magnetic spectrometer showing the position of the imaging plates with respect to the magnet for LWFA 1.5 experiment (drawings not to scale)

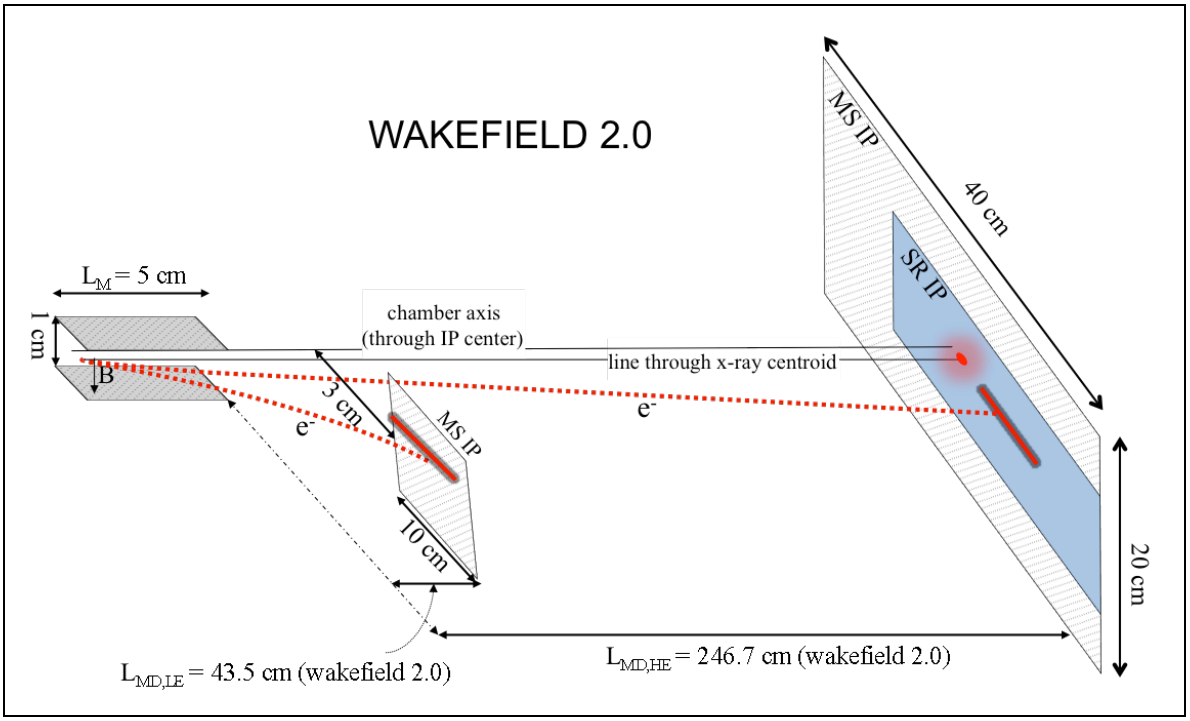

Figure 4.4: The magnetic spectrometer showing the position of the imaging plates with respect to the magnet for LWFA 2.0 experiment (drawings not to scale)

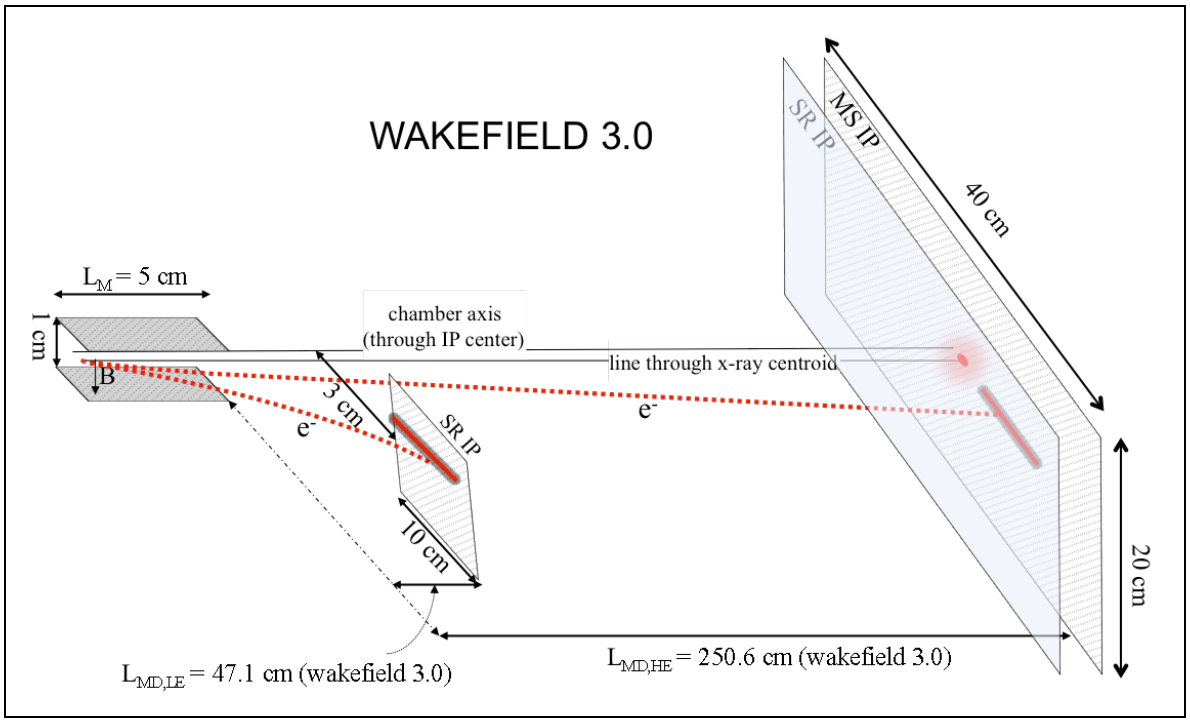

Figure 4.5: The magnetic spectrometer showing the position of the imaging plates with respect to the magnet for LWFA 3.0 experiment (drawings not to scale)

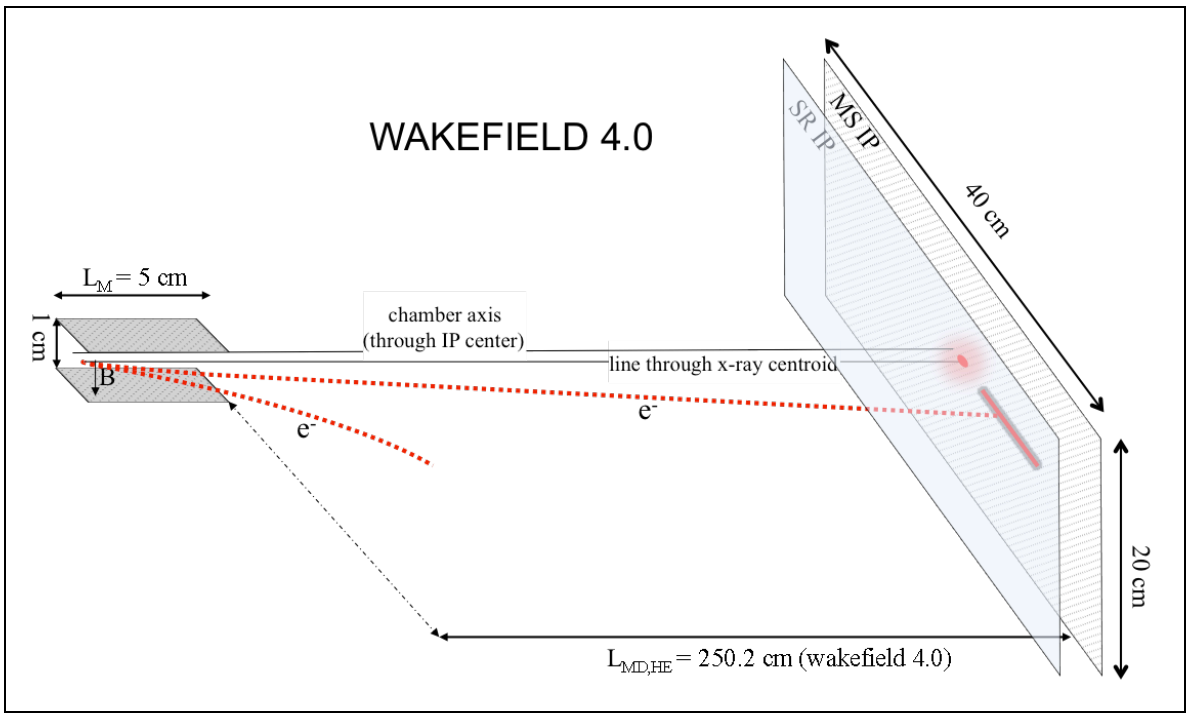

Figure 4.6: The magnetic spectrometer showing the position of the imaging plates with respect to the magnet for LWFA 4.0 experiment (drawings not to scale)

Figure 4.3-Figure 4.6 show the imaging plates used in the wakefield experiments and their positions with respect to the magnet. Using $L_{MD,HE}$ (indicated on the images) for the separation between the magnet exit edge and the far IPs used for high energy (HE) electrons, and using the parameters $L_M = 0.05\ m, B_{effective} = 1.4819\ T, c = 3\times 10^8\ m/s, e = 1.602\times10^{-19}\ C, m_e = 9.11\times10^{-31}\ kg$, a relation for the electron energy as a function of it deflection as measured on the far IP is obtained :

$$E_{e,HE}[GeV] \cong \frac{C_{HE,wakefield}\times10^{-4}}{|\Delta x_{HE}\ [m]|}$$

$C_{HE,1.5} = 556.217$
$C_{HE,2.0} = 553.598$
$C_{HE,3.0} = 562.188$
$C_{HE,4.0} = 561.326$

Eq. 4.12

The subscript *HE* denotes *high energy* and $\Delta x_{HE}\ [m]$ in Eq. 4.12 refers to the deflection of the electrons with respect to the line through the x-ray center (geometric or peak intensity), measured on the high energy (far) imaging plate. The subscript *wakefield* refers to one of the 4 experimental rounds. Similarly, for the near IP, used for low energy electrons (LE), using $L_{MD,LE}$ (indicated on the images) yields:

$$E_{e,LE}[GeV] \cong \frac{C_{LE,wakefield}\times10^{-4}}{|\Delta x_{LE}\ [m]|}$$

$C_{LE,2.0} = 102.180$
$C_{LE,3.0} = 110.253$

Eq. 4.13

The subscript *LE* denotes *low energy* and $\Delta x_{LE}\ [m]$ in Eq. 4.13 refers to the deflection of the electrons with respect to the line through the x-ray center, measured on the low energy (near) imaging plate.

The energy calculated using Eq. 4.12 slightly *underestimates* the energy calculated by solving Eq. 4.3; however, as shown in Figure 4.7, the approximate formula is remarkably accurate; the plots of electron energy vs. electron deflection virtually overlap up to a large deflection of 2000 pixels (left image), which corresponds to ~280 MeV using Eq. 4.12; even at energies as low as 300 MeV, the error is only -0.4% (right image). At energies ~1 GeV and higher the error approaches -0.1%.

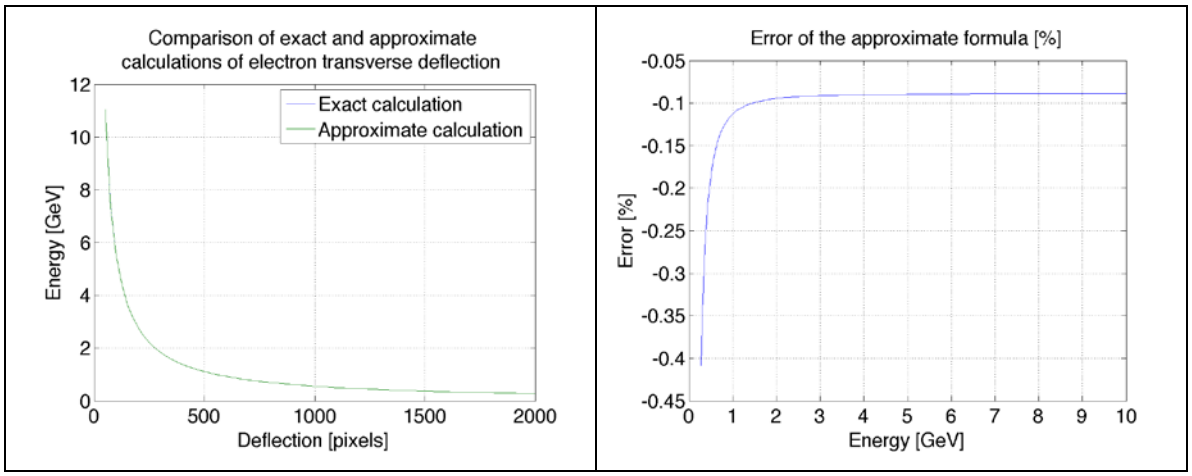

Figure 4.7: Comparison of exact (**Eq. 4.3**) and approximate (**Eq. 4.11**) formulas for electron energy vs. deflection in the magnetic spectrometer; the approximate formula underestimates the energy by ~0.1 % at E > 1 GeV.

To measure Δx for an electron experimentally, note that $\Delta x = 0$ corresponds to an undeflected electron (i.e., having infinite energy). A proxy for the position on the detector where undeflected electrons would arrive is the center of the betatron x-ray radiation (see Figure 4.6). By measuring the deflection of an electron with respect to the line perpendicular to the imaging plate and through the x-ray center (geometric or peak intensity), Δx may be measured, and from that the electron energy is obtained using Eq. 4.12 and Eq. 4.13.

4.4 Application to Imaging Plate Detectors

The relationships derived in the preceding chapter will now be applied to the imaging plate detectors used in all experimental rounds.

1. High-Energy Electron IP Detectors

$|\Delta x_{HE}\ [m]|$ in Eq. 4.12 may be written as $\Delta x_{HE}\ [pixels]\times 10^4 \left(\frac{100}{pixel\ size\ [\mu m]}\right)$ to express it in terms of the electron's horizontal pixel coordinate on a detector of known pixel size (resolution):

$$E_{e,HE}[GeV] \cong \frac{C_{HE,wakefield}}{\Delta x_{HE}\ [pixels]}\left(\frac{100}{pixel\ size\ [\mu m]}\right)$$

Electron energy as a function of deflection on IP, in pixels, for 40 cm by 20 cm IPs (LWFA 1.5, 2.0, 3.0, and 4.0) **Eq. 4.14**

$\Delta x_{HE}\ [pixels]$ is the electron deflection, in pixels, with respect to the position of the x-ray center (geometric or peak intensity), measured on the high-energy electron detector.

For example, for 100-μm and 50-μm resolution detectors (e.g., Fujifilm imaging plate of type BAS-MS and BAS-SR, respectively), the electron energy as a function of deflection in the magnetic spectrometer is in pixels:

$$E_{e,HEMS}[GeV] \cong \frac{C_{HE,wakefield}}{\Delta x_{HEMS}\,[pixels]} = \frac{C_{HE,wakefield}}{x_{HEMS}\,[pixels] - x_{\infty,MS}[pixel]}$$

Electron energy as a function of deflection on IP, in pixels, for 4000 × 2000 MS IP (LWFA 1.5, 2.0, 3.0, and 4.0) **Eq. 4.15**

$$E_{e,HESR}[GeV] \cong \frac{2\,C_{HE,wakefield}}{\Delta x_{HESR}\,[pixels]} = \frac{2\,C_{HE,wakefield}}{x_{HESR}\,[pixels] - x_{\infty,SR}[pixel]}$$

Electron energy as a function of deflection on IP, in pixels, for 8000 × 4000 SR IP (LWFA 3.0, and 4.0) **Eq. 4.16**

The constant $C_{HE,wakefield}$ is provided in Eq. 4.12 for each of the 4 experimental rounds. The subscript HEMS (HESR) in Δx_{HEMS} (Δx_{HESR}) indicates that the measurement is on the MS (SR) imaging plate. Eq. 4.15 is applicable to shots where a 4000×2000 pixel BAS-MS IP was used as the primary diagnostic for electrons and x-rays. For redundancy and to increase resolution, beginning with the LWFA 2.0 experiment, an SR imaging plate was added to the electron and x-ray diagnostics. For the LWFA 2.0 experiment, the SR IP was 30 cm by 10 cm, i.e., 6000×2000 pixels (Figure 4.8) and was positioned behind the MS IP. In LWFA 3.0 and 4.0 experiments, the high energy IPs were both 40 cm by 20 cm; in most cases the MS IP was placed in front of the SR IP and served as the primary detector for the x-ray due its higher sensitivity. Exceptions were shots during the LWFA 4.0 experiment devoted to the x-ray source size measurement, where the SR IP was the primary detector and was placed in front of the MS IP.

There are two ways of determining the x_∞ to use in Eq. 4.15 and Eq. 4.16. One is to use the position of the x-ray center (geometric or peak intensity) on the primary IP used for high-energy electron. Another is to use the infinite energy pixel determined by fitting Eq. 4.15 and Eq. 4.16 to the energy vs. deflection calibrations performed using fiducial shadow triangulation measurements (3.4) and finding the pixel for which the denominator vanishes. (The latter method is more accurate as it also takes the electron launch angle into account.) When the MS IP was the primary detector, the x-ray center was more accurately determined on the MS IP (due to its higher contrast) for use in Eq. 4.15, then

converted for use in Eq. 4.16. When the MS and SR IP were the same size (i.e., 4000×2000 pixel MS vs. 8000×4000 pixel SR), the conversion is straightforward. Since the SR pixel size is half the MS pixel size, the deflection on the MS IP times 2 converts it to the deflection on the SR IP. Using $\Delta x_{\infty,SR}\ [pixels] = 2\ \Delta x_{\infty,MS}\ [pixels]$ in Eq. 4.16 converts it to Eq. 4.15, therefore Eq. 4.15 is valid for both MS and SR IPs as longs they are of the same size and electron deflection is measured on the MS IP. This was the case for the LWFA 3.0 and 4.0 diagnostics.

In LWFA 2.0, the 6000×2000 pixel SR IP (50-μm pixel size) was smaller than the 4000×2000 pixel MS IP (100-μm pixel size). The positioning of the LWFA 2.0 imaging plates with respect to one another is shown in Figure 4.8:

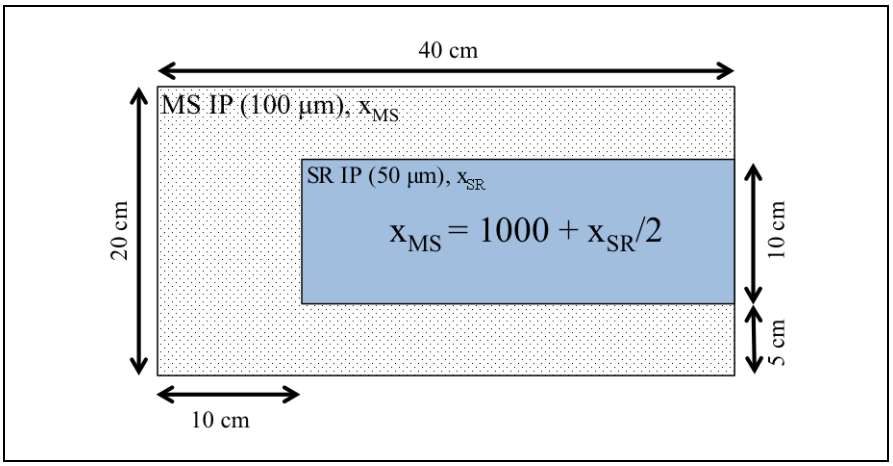

Figure 4.8: The positioning of MS and SR imaging plates for the LWFA 2.0 experiment

In order to convert electron deflection measured on the MS IP to deflection on the SR IP, the configuration shown in the figure was used to relate the deflections as follows. The left edge of the SR IP (pixel 0) was offset of 1000 pixels (10 cm) on the MS IP; therefore given the 2:1 pixel size ratio between MS and SR IPs, $x_{\infty,MS}\ [pixels] = 1000 + \frac{x_{\infty,SR}\ [pixels]}{2}$ and

$$x_{\infty,SR}\ [pixels] = 2\ x_{\infty,MS}\ [pixels] - 2000 \qquad \textbf{Eq. 4.17}$$

Plugging Eq. 4.17 into Eq. 4.16 gives:

$$E_{e,HESR}[GeV] \cong \frac{2\ C_{HE,wakefield}}{x_{HESR}\ [pixels] - 2\ x_{\infty,MS}\ [pixels] + \ 2000}$$

Electron energy as a function of deflection on IP, in pixels, for 6000 × 2000 SR IP (LWFA 2.0)

Eq. 4.18

There are two scenarios where the SR IP data are used but the additional resolution compared to the MS IP is not required. One is in the set of shots in LWFA 4.0 where the SR IP was deployed as the primary diagnostic in order to use its higher resolution to enable the measurement of the x-ray source size; this resolution is not required for the measurement of the electron charge or spectrum. The 2nd scenario is when commensurate regions on the MS and SR IPs, corresponding to a region of interest (e.g., an ImageJ selection) created on one of the IPs, are to be compared. In both scenarios, a *reduced-size* SR image is used by combining 4 SR pixels into 1 reduced-SR pixel as shown in Figure 4.9:

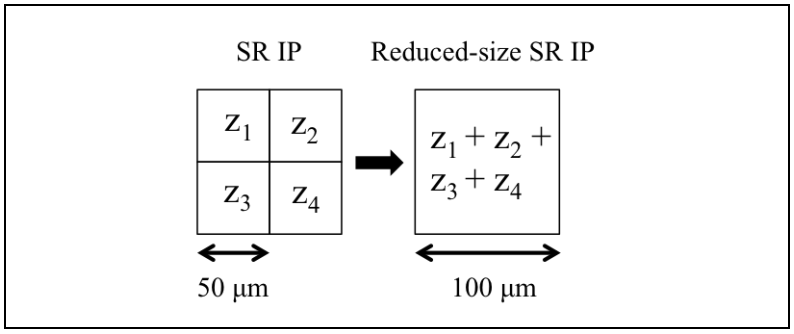

Figure 4.9: Conversion of SR IP pixel values to produce a reduced-size SR IP

The size reduction may be done in ImageJ using *Image* → *Adjust* → *Size...* followed by *Process* → *Math* → *Multiply...*, to reduce the size 50% in each dimension to create a reduced-size SR image of pixel size 100-μm, by replacing each adjacent 4 pixels with a single pixel having value equal to the sum of the 4 original pixels. For LWFA 2.0 SR imaging plate data, the left edge of the SR IP (pixel 0) still has offset of 1000 pixels on the MS IP; however, following size reduction, the pixel size ratio between MS and reduced-size SR IPs is 1:1, therefore $x_{\infty,MS}\ [pixels] = 1000 + \ x_{\infty,Reduced\ SR}\ [pixels]$, giving

$$x_{\infty,Reduced\ SR}\ [pixels] = x_{\infty,MS}\ [pixels] - \ 1000$$

Eq. 4.19

Plugging Eq. 4.19 into Eq. 4.14 gives:

$$E_{e,HESR}[GeV] \cong \frac{C_{HE,wakefield}}{x_{HESR}\,[pixels] - x_{\infty,MS}\,[pixels] + 1000}$$

Electron energy as a function of deflection on IP, in pixels, for 3000 × 1000 reduced-size SR IP (LWFA 2.0) **Eq. 4.20**

For LWFA 3.0 and 4.0 SR IP data, size reduction makes them geometrically equivalent to MS data; hence Eq. 4.15 may used:

$$E_{e,HESR}[GeV] \cong \frac{C_{HE,wakefield}}{x_{HESR}\,[pixels] - x_{\infty,MS}[pixel]}$$

Electron energy as a function of deflection on IP, in pixels, for 4000 × 2000 reduced-size SR IP (wakefield3.0, and 4.0) **Eq. 4.21**

2. Low-Energy Electron IP Detectors

For low-energy electrons detected on the imaging plate nearest to the magnet, Eq. 4.13 may be written as

$$E_{e,LE}[GeV] \cong \frac{C_{LE,wakefield}}{\Delta x_{LE}\,[pixels]}\left(\frac{100}{pixel\ size\ [\mu m]}\right)$$

Electron energy as a function of deflection on IP, in pixels, for 10 cm by 10 cm IPs (LWFA 1.5, 2.0, 3.0) **Eq. 4.22**

to express the electron energy in terms of its deflection on the IP. Referring to Figure 4.6 the left edge of the IP (pixel 0) is at 3 cm offset from the chamber axis. This is equivalent to $300 \times \left(\frac{100}{pixel\ size\ [\mu m]}\right)$ pixels. Δx is measured with respect to the line through the x-ray center (representing undeflected electrons). For an x-ray center position measured on the far MS IP with respect to IP center (chamber axis), one can write

$$\Delta x_{LEMS} = 300 + x_{LEMS}\,[pixels] - x_{\infty,MS}[pixel]$$

$$\Delta x_{LESR} = 600 + x_{LESR}\,[pixels] - 2\,x_{\infty,MS}[pixel] \quad \textbf{Eq. 4.23}$$

Plugging these into Eq. 4.22 yields the electron energy on the MS or SR IP nearest to the magnet:

$$E_{e,LEMS}[GeV] \cong \frac{C_{LE,wakefield}}{300 + x_{LEMS}\,[pixels] - x_{\infty,MS}[pixel]}$$

Electron energy as a function of deflection on IP, in pixels, for 1000 × 1000 MS IP (LWFA 1.5 and 2.0) **Eq. 4.24**

$$E_{e,LESR}[GeV] \cong \frac{2\,C_{LE,wakefield}}{600 + x_{LESR}\,[pixels] - 2\,x_{\infty,MS}[pixel]}$$

Electron energy as a function of deflection on IP, in pixels, for 1000 × 1000 SR IP (LWFA 3.0) **Eq. 4.25**

The formulas derived in this appendix are summarized in :

Electron Energy vs. Deflection Formula	***Detector***	***Used in Experiment***
$E_{e,HEMS}[GeV] \cong \frac{C_{HE,wakefield}}{x_{HEMS}\,[pixels] - x_{\infty,MS}[pixel]}$	4000 × 2000 BAS-MS IP	LWFA 1.5, 2.0, 3.0, and 4.0
$E_{e,HESR}[GeV] \cong \frac{2\,C_{HE,wakefield}}{x_{HESR}\,[pixels] - x_{\infty,SR}[pixel]}$	8000 × 4000 BAS-SR IP	LWFA 3.0 and 4.0
$E_{e,HESR}[GeV] \cong \frac{2\,C_{HE,wakefield}}{x_{HESR}\,[pixels] - 2\,x_{\infty,MS}\,[pixels] + 2000}$	6000 × 2000 BAS-SR IP	LWFA 2.0
$E_{e,HESR}[GeV] \cong \frac{C_{HE,wakefield}}{x_{HESR}\,[pixels] - x_{\infty,MS}\,[pixels] + 1000}$	3000 × 1000 reduced-size BAS-SR IP	LWFA 2.0
$E_{e,HESR}[GeV] \cong \frac{C_{HE,wakefield}}{x_{HESR}\,[pixels] - x_{\infty,MS}[pixel]}$	4000 × 2000 reduced-size BAS-SR IP	LWFA 3.0 and 4.0
$E_{e,LEMS}[GeV] \cong \frac{C_{LE,wakefield}}{300 + x_{LEMS}\,[pixels] - x_{\infty,MS}[pixel]}$	1000 × 1000 BAS-MS IP	LWFA 1.5 and 2.0
$E_{e,LESR}[GeV] \cong \frac{2\,C_{LE,wakefield}}{600 + x_{LESR}\,[pixels] - 2\,x_{\infty,MS}[pixel]}$	1000 × 1000 BAS-SR IP	LWFA 3.0

Table 4-1: Summary of formulas used to calculate energy from the electron deflection in the magnetic spectrometer

The constants $C_{HE,wakefield}$ and $C_{LE,wakefield}$, incorporating the parameters of the magnetic spectrometer, are provided in Eq. 4.12 and Eq. 4.13 for the different experimental rounds.

3. Calculation of dQ/dE and $d^2Q/(dE\,d\Omega)$

The variation of electron charge with energy, dQ/dE, required to determine the electron energy spectrum and the peak of the charge distribution (e.g., see Figure 6.12), may be expressed using the chain rule for derivatives in terms of the electron deflection in the magnetic spectrometer:

$$\frac{dQ}{dE} = \frac{dQ}{dx}\,\frac{dx}{dE} \qquad \textbf{Eq. 4.26}$$

where x denotes the absolute deflection of electron in the magnetic spectrometer in meters. For a detector with resolution of 100 μm (MS imaging plate), $x = N{\times}10^{-4}$, where N is electron deflection at the detector in pixels; plugging in, Eq. 4.26 becomes

$$\frac{dQ}{dE} = \frac{dQ}{dN}\,\frac{dN}{dE} \qquad \textbf{Eq. 4.27}$$

Noting that $N = \Delta x\ [pixels]$, the formulas derived in 4.4 relating Δx to E may used. In all cases, we derived $E = \frac{C}{N}$, where C was a constant specific to the detector. Writing it as $N = \frac{C}{E}$, Eq. 4.27 may be written as

$$\frac{dQ}{dE} = \frac{dQ}{dN}\frac{d}{dE}\left(\frac{C}{E}\right) = -\frac{dQ}{dN}\frac{C}{E^2} \qquad \textbf{Eq. 4.28}$$

Eliminating E in Eq. 4.28 using $N = \frac{C}{E}$, gives

$$\boxed{\frac{dQ}{dE} = -\frac{dQ}{dN}\frac{N^2}{C}} \qquad \textbf{Eq. 4.29}$$

dQ/dN is the charge in one column of the region of interest, e.g., one pixel or one column of pixels on the image. For any IP detector, by using its corresponding value for C from 4.4, $\frac{dQ}{dE}$ for that detector may be derived.

As an example, for electrons detected on the high energy (far) MS IP used in all experiments, from Eq. 4.15 and Eq. 4.12 we have $E_{e,HEMS}[GeV] \cong \frac{553.598}{\Delta x_{HEMS}\,[pixels]}$. Noting that C = 553.598 and $N = \Delta x_{HEMS}\ [pixels]$, Eq. 4.29 may be written as:

$$\boxed{\frac{dQ}{dE} = -\frac{dQ}{dN}\frac{(\Delta x_{HEMS}\ [pixels])^2}{553.598}} \qquad \textbf{Eq. 4.30}$$

where $\Delta x_{HEMS}\ [pixels] = x_{HEMS}\ [pixels] - x_{\infty,MS}[pixel]$.

As another example, for the electrons detected on the low-energy (near) SR IP, from Eq. 4.22 and Eq. 4.13 we have $E_{e,LE}[GeV] \cong \frac{202.140}{\Delta x_{LESR}\,[pixels]}$. Noting that $C = 202.140$ and $N = \Delta x_{LESR}\ [pixels]$, Eq. 4.29 may be written as:

$$\boxed{\frac{dQ}{dE} = -\frac{dQ}{dN}\frac{(\Delta x_{LESR}\ [pixels])^2}{202.140}} \qquad \textbf{Eq. 4.31}$$

where $\Delta x_{LESR}\ [pixels]_{HEMS}$ is given in Eq. 4.23.

The differential charge per unit energy and solid angle, $\frac{d^2Q}{dE\ d\Omega}$, may also be derived from Eq. 4.29 noting that $d\Omega$ refers to the solid angle corresponding to a pixel on a imaging plate:

$$d\Omega = \frac{pixel\ area}{(pixel\ to\ source\ distance)^2}$$

Dividing dQ/dE by $d\Omega$ gives the electron energy spectrum in terms of the charge per unit energy per unit solid angle:

$$\boxed{\frac{d^2Q}{dE\ d\Omega} = -\frac{dQ}{dN}\frac{N^2}{C} \times \frac{(pixel\ to\ source\ distance)^2}{pixel\ area}} \qquad \textbf{Eq. 4.32}$$

As charged particles, electrons deflect in the magnetic spectrometer, and the deflection may be measured with respect to the position of x-rays, which traverse the spectrometer undeflected. N in Eq. 4.29 represents the deflection, in pixels, of the electron at the detector, with respect to the position of the undeflected particle (center of betatron x-rays). For an image where the x-ray center is at pixel N_β, a rectangular region of interest (ROI) with its nearest edge perpendicular to the plane of deflection positioned at position N_0, and the electron offset with respect to N_0 designated as N_{offset}, we can write

$$N = N_{offset} + N_0 - N_\beta$$

Throughout this chapter, it has been assumed that the electron launch angle is vanishingly small. This is not generally the case and introduces an additional error into the calculations. To determine the magnitude of this error, a comparison of the electron energy spectrum was done for a shot from the 4th experimental round (8269) using the method described in this chapter and the method using the triangulation of fiducial shadows (3.4). The results are shown in Figure 4.10. The top panel displays the electron charge distribution (dQ/dE) in absolute units as a function of the electron energy. The bottom panel shows the same function, in arbitrary units, determined using the fiducial shadow triangulation method. The important features in the 2 spectra, notably the position of the fiducial shadows and the peaks, all nearly line up in this example. This suggests that the assumption of vanishingly small angle, is acceptable given the computational advantages that it provides.

In the chapter, the deflection of electrons in a magnetic spectrometer was reviewed and approximate formulas, accurate to ~1% for relativistic electrons, were derived. These formulas have the feature that they may be programmatically implemented to enable the rapid calculation of the electron energy spectrum. In the next chapter, the spectroscopy of

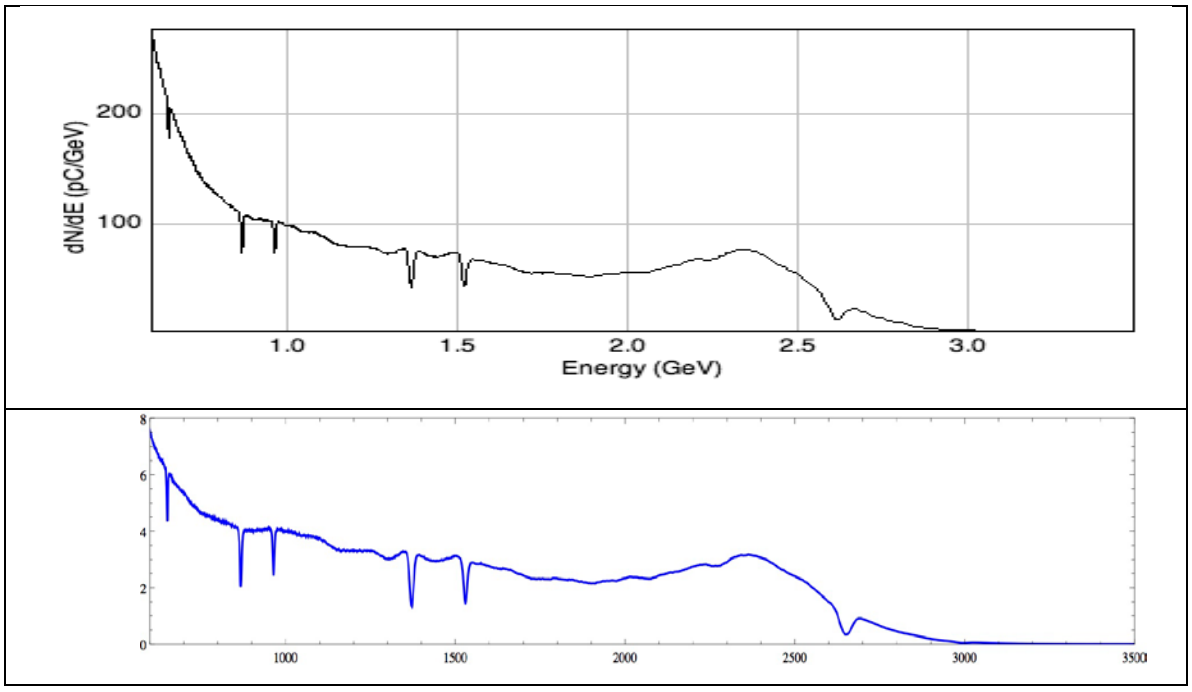

Figure 4.10: Comparison of electron spectra (for shot 8269) obtained using the method assuming vanishingly small launch angle (top) and the method using triangulation of fiducial shadows (bottom).

betatron x-rays that are produced, when accelerated electrons oscillate inside the relativistically boosted frame of reference of the plasma bubble, are discussed. The diagnostic challenges specific to x-rays produced by electrons accelerated to GeV energies required the development of a new diagnostic approach and a methodology for the analysis of the x-ray radiation data obtained in a GeV LPA.

Chapter 5 Spectroscopy of Betatron X-ray Radiation from a GeV LPA

5.1 Introduction

In this chapter, the spectroscopy of x-rays using filters is introduced and the methodology developed for the single-shot, spatially resolved spectroscopy of betatron x-ray radiation from GeV LPAs over the full angular range of the x-ray profile is presented. This includes the design of a single-shot x-ray detector that is robust to variations in the x-ray beam pointing direction, an algorithm for low-artifact reconstruction of the incident x-ray profile from the filtered x-ray data, a method for self-consistent sampling of the filtered x-ray data, and a reconstruction of the spectrum in 3D as a function of photon energy and angle. The techniques discussed in this chapter will later be used in the analysis of x-ray data when experimental results are presented (Chapter 6). There the x-ray beam observables (divergence, photon number, and critical energy), together with the electron beam charge, are used to compute effective values for the acceleration parameters (the electron energy, its oscillation amplitude, and the number of oscillations), and investigate their mutual consistency.

One of the hallmarks of the laser-wakefield acceleration of electrons is the generation of x-ray radiation as a byproduct of the acceleration mechanism. This *betatron* radiation is broadband, multi-keV, and ultrafast (tens of femto-seconds in duration), making it suitable for the investigation of fundamental physical processes evolving at similarly short time scales, as well as for radiography of dense matter opaque to low energy x-rays, e.g., warm dense matter (WDM), phase contrast imaging of objects not visible to absorption radiography, and x-ray absorption spectroscopy of surfaces (EXAFS). At the same time, the betatron radiation may be used as a diagnostic tool for the laser-plasma accelerator (LPA) itself. For example, by measuring the x-ray spectrum, it is possible to determine the electron beam rms transverse size σ_x and from that the electron beam emittance $\epsilon \approx \gamma\sigma_x\sigma_\theta$ [33]; the spatial profile of the x-ray may be used to study the physics of electron injection, e.g., the evolution of the angular momentum [34].

The spectrum of the betatron radiation varies with angle [35]. In addition, the divergence of this radiation scales inversely with the square root of the accelerated electron energy. For GeV-accelerated electrons, this has the consequence that the FWHM of the x-ray profile is typically $\lesssim$ 6 mrad wide; even at a distance of 2.7 m from the x-ray source, this translates to a FWHM diameter of ~1.6 cm, with much of the variation in the spectrum occurring within this diameter, making it challenging to use differential filters because of the difficulty to guarantee that the spectra of the photons incident on the two filters in a differential filter are identical; this is especially the case given that multiple filters are required to obtain the spectrum with sufficient resolution and for practical reasons (e.g., to avoid edge effects) there is a lower limit on the size of the individual filters. Even more challenging is to obtain sufficient number of data points from a single shot to reconstruct the spectrum over a wide range of angles. Such spatially resolved spectra provide information about the dynamics of accelerating structures; this information is integrated over when the spectra are presented as a function of energy alone.

5.2 Spectroscopy of X-rays using Filters

Attenuation though filters is perhaps the earliest method used in the spectroscopy of x-rays [36]. For a mono-energetic beam of x-rays of energy $E = \hbar\omega$ incident on a layer of filter of some material of thickness x, the relation between the incident and emerging intensities is described by the *Beer–Lambert law*:

$$I(x) = I_0 e^{-\mu(E)x} \qquad \textbf{Eq. 5.1}$$

where $\mu(E)$, in inverse units of length, is the material- and energy-dependent *attenuation coefficient* for the filter; it is determined by the cross sections for the various processes in which the photon participates, and has the form $\mu(E) = \frac{N_A}{A}\sum_i \sigma_i$, where σ_i are the cross sections for processes that absorb the photon (photoelectric effect and pair production) or scatter it (Compton effect). (Note that attenuation tables from sources such as NIST XAAMDI[6] and FFAST[7] databases provide the ratio μ/ρ, i.e., the ratio of the attenuation and mass density; this ratio is referred to as the *mass attenuation* and typically has units cm^2/g. Then the thickness x in Eq. 5.1 is replaced by the *mass thickness*, i.e., the product

[6] http://www.nist.gov/pml/data/xraycoef/index.cfm
[7] http://www.nist.gov/pml/data/ffast/index.cfm

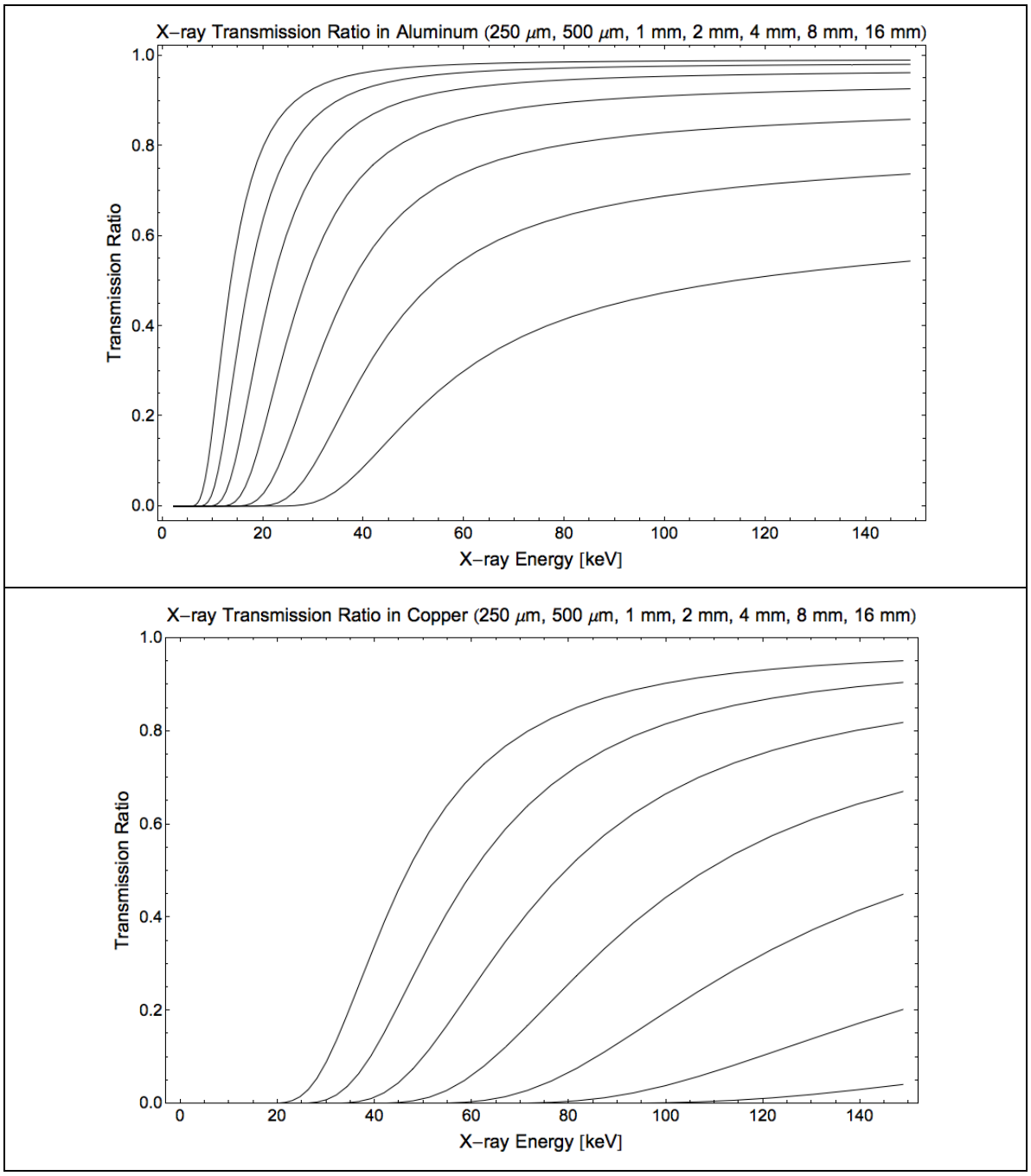

Figure 5.1: Transmission ratios for Al (top) and Cu (bottom), for 250 μm, 500 μm, 1 mm, 2 mm, 4 mm, 8 mm, 16 mm. In each case, the upper-most curve corresponds to the smallest thickness.

of mass density and actual thickness, in units of g/cm^2; Eq. 5.1 then becomes $I(x) = I_0 e^{-\frac{\mu(E)}{\rho} x\rho}$.) To determine the energy of a mono-energetic beam of x-rays, one could a) select as x-ray filter a material of known type and thickness (typically aluminum or copper, see Figure 5.1), b) use Eq. 5.1 to calculate the *transmission ratio*

$T(E,x) = I(E,x)/I_0$ for the filter, c) experimentally determine the transmission ratio through the filter, d) then determine the energy of the x-ray beam by looking up the transmission ratio on the graph. Aluminum has good resolution at energies < 40 keV; at higher energies, where aluminum's transmission ratio flattens, copper offers better resolution.

Spectroscopy of X-rays using Differential Filters

Most of the time, however, the x-ray beam is not mono-energetic and looking up the measured transmission ratio on the transmission ratio curve produces an energy that depends on the overlap of the x-ray spectrum and the transmission curve and is not necessarily indicative of the energy at which the spectrum peaks. For any radiation detector, the detector reading is the convolution of the spectrum $S(E)$ and the detector response function, where in the case of an x-ray filter detector, the response function is the product of the filter transmission function and the response function of the detector, e.g., that of an imaging plate. (Note that $dN(E) = S(E)d(E)$ is the number of photons in the energy bandwidth E to $E + dE$.) For an x-ray beam transmitted through a filter of thickness x with transmission function $T(E,x)$, and detected on detector with response function $R(E)$, the convolution integral is

$$TS = \int_0^\infty S(E)T(E,x)R(E)d\,(E) \qquad \textbf{Eq. 5.2}$$

where TS is the transmitted signal, e.g., PSL for an imaging plate, and has dependence on both the filter material and its thickness x. The task is then to find $S(E)$ knowing $R(E), T(E,x)$ and the detector reading $TS(x)$, i.e., to solve an integral equation of the first kind. This is an inverse problem and the uniqueness of the solution is not guaranteed. One way of tackling Eq. 5.2, however, is by using two filters and differencing the signals. (See [37], [38] for other approaches.) For filters with transmission functions $T_1(E,x)$ and $T_2(E,x)$, the differential transmitted signal can be written as

$$\Delta TS = TS_1 - TS_2 = C\int_0^\infty S(E)\,(T_1(E,x) - T_2(E,x))\,R(E)\,d\,(E) \qquad \textbf{Eq. 5.3}$$

where C is a geometric constant that, for example, can be used to express the spectrum at number of photons per unit energy per pixel, or per unit energy per unit solid angle. The

part of the integrand in Eq. 5.3 multiplying the filter transmission and detector response functions is known as the *residual sensitivity* function:

$$ResSen(E) = (T_1(E,x) - T_2(E,x))\, R(E) \qquad \textbf{Eq. 5.4}$$

When the residual sensitivity function is narrow enough (ideally a delta function) that the spectrum may be considered constant over its width, one may invert the integral and determine for $S(E_{avg})$ as the ratio of the differenced transmitted signal, ΔTS, and the area under the residual sensitivity curve for the two filters:

$$S(E_{avg}) = [d\,N(E)/dE]_{E=E_{avg}} = \frac{\Delta TS}{C\int_0^\infty (T_1(E,x) - T_2(E,x))\, R(E)\, d\,(E)} \qquad \textbf{Eq. 5.5}$$

E_{avg} denotes the average energy of the residual sensitivity function viewed as distribution over energy E, i.e.

$$E_{avg} = \frac{\int_0^\infty E \times ResSen(E)\, d\,(E)}{\int_0^\infty ResSen(E)\, d\,(E)} \qquad \textbf{Eq. 5.6}$$

where the dependence of the residual sensitivity $ResSen(E)$ on the two filter types and thicknesses is implicit.

Eq. 5.5 gives the number of photons in the spectrum per unit energy at energy E_{avg}. An alternative way of expressing the spectrum is per unit of bandwidth. Rewriting Eq. 5.3 as

$$\Delta TS = TS_1 - TS_2 = C\int_0^\infty [0.1\%\; E\; S(E)]\, \frac{(T_1(E,x) - T_2(E,x))\, R(E)}{0.1\%\; E}\, d\,(E) \qquad \textbf{Eq. 5.7}$$

and assuming that the *residual sensitivity per 0.1% bandwidth*

$$ResSen_{PUBW}(E) = \frac{(T_1(E,x) - T_2(E,x))\, R(E)}{0.1\%\; E} \qquad \textbf{Eq. 5.8}$$

is narrow and the spectrum per unit bandwidth is may be considered constant over its distribution, then

$$[0.1\%\; E\; S(E)]_{E_{avg}} = \left[\frac{dN}{dE/0.1\%\; E}\right]_{E_{avg}} = \frac{\Delta TS}{C\int_0^\infty \frac{(T_1(E,x) - T_2(E,x))\, R(E)}{0.1\%\; E}\, d\,(E)} \qquad \textbf{Eq. 5.9}$$

The FWHM of the residual sensitivity, Eq. 5.4, or residual sensitivity per 0.1% bandwidth, Eq. 5.8, is taken to represent the range of uncertainty in E_{avg}, i.e., $E = E_{avg} \pm \delta E$, where $\delta E = 0.5 \times E_{FWHM}$.

To illustrate, Figure 5.2 shows, on the left, the sensitivity to x-rays for two types of imaging plate detectors (Fujifilm BAS-MS and BAS-SR) on Fuji FLA-7000 scanner [39]. This corresponds to the detector response function $R(E)$. The transmission functions, $T_{Al}(E, x = 0.25\ \text{mm})$ and $T_{Al}(E, x = 0.5\ \text{mm})$, for two thicknesses of aluminum (0.25 mm and 0.50 mm), and shown in the top panel of Figure 5.1, are then used to calculate the residual sensitivity per 0.1% of bandwidth, according to Eq. 5.8. The right panel in Figure 5.2 shows the result for the MS (higher sensitivity) and SR (higher resolution) imaging plate. The residual sensitivities in this case are relatively peaked; this, however, is not in general the case. The residual sensitivity, using the MS IP as detector, has an average energy of 18.6 keV with a FWHM of 11.0 keV; as a result, the point on the spectrum calculated according to Eq. 5.9 corresponds to $E_{avg} \pm \delta E = (18.6 \pm 5.5)$ keV.

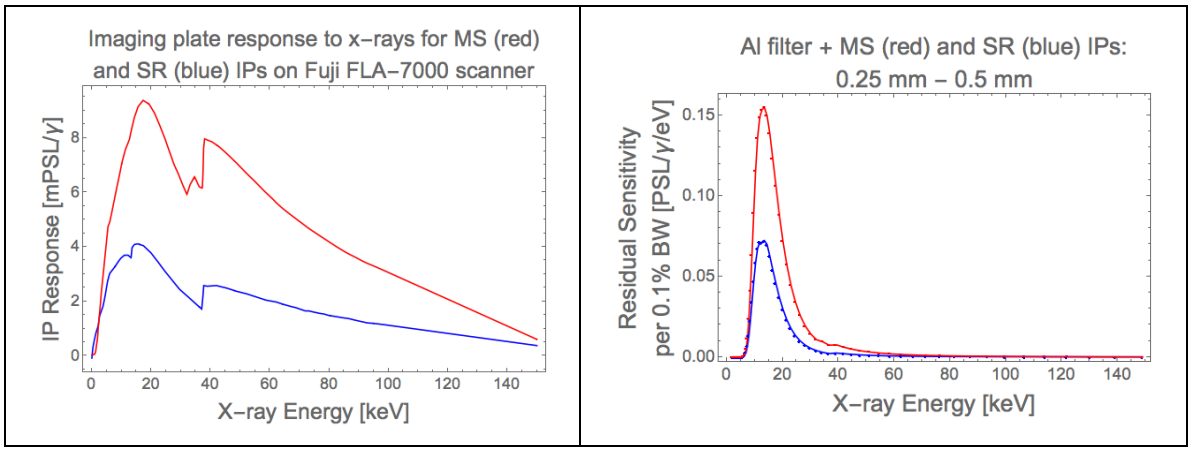

Figure 5.2: Left: detector response (sensitivity) to x-rays for two types of imaging plate detectors [36]. Right: residual sensitivity (**Eq. 5.8**) for aluminum (of thickness 0.25 mm and 0.5 mm) for two types of IP detectors

Spectroscopy of X-rays using K-edge (Ross) Filters

The FWHM of the residual sensitivity function for a pair of differential filters (Eq. 5.4 or Eq. 5.8) determines δE, the error in the energy E_{avg} associated with that filter pair, and the horizontal error bars in the x-ray spectrum. In order to improve the accuracy of the

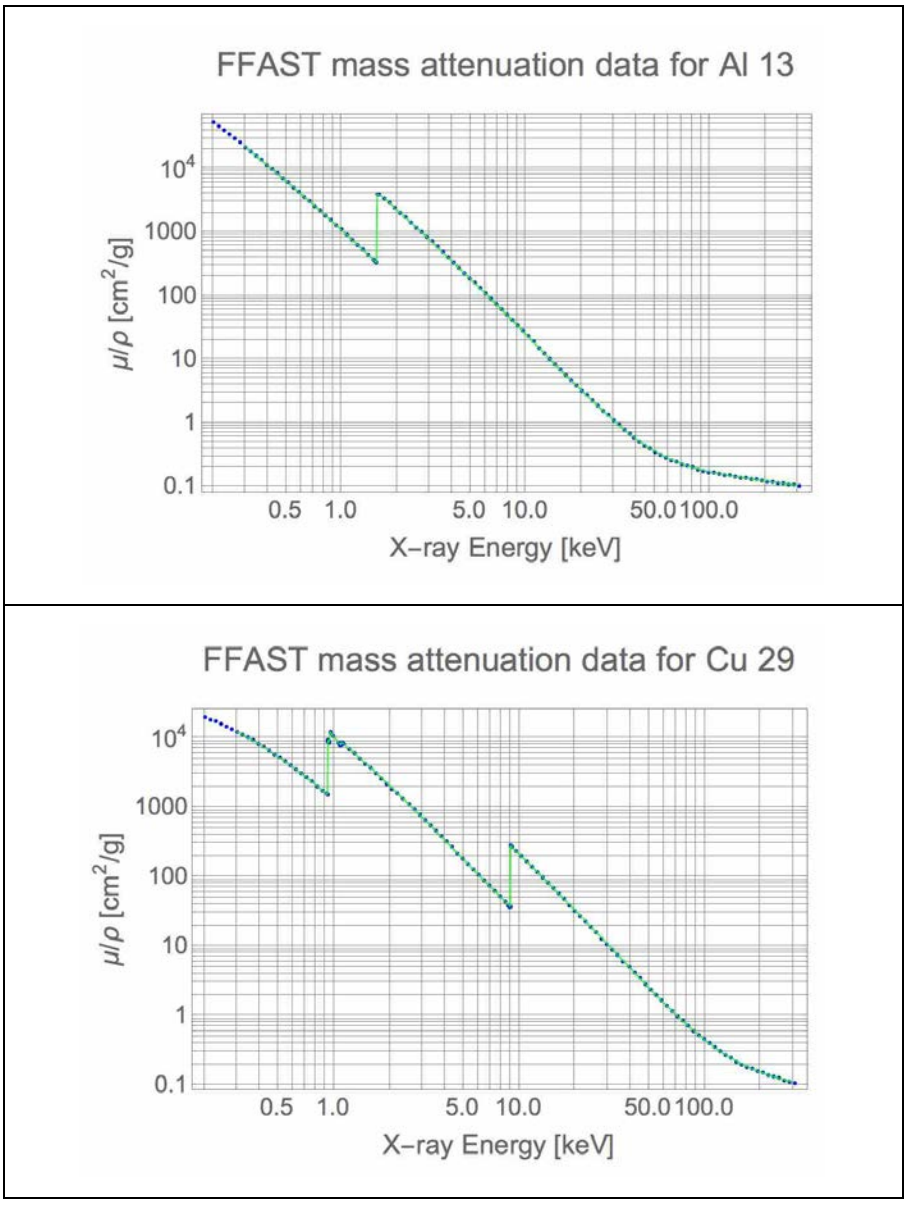

Figure 5.3: Mass attenuation plots for aluminum and copper showing the K-edge energies

differential filtering by minimizing δE, a type of differential filter known as K-edge filter (also known as Ross filter) can be used. The term *K-edge* refers to the x-ray energy at which a sharp rise in the mass attenuation, together with a sharp drop in the transmitted intensity (Eq. 5.1), occurs. At the K-edge value, the energy of the x-ray photon incident on an atom matches the energy required for the ionization of the innermost shell (K shell) electron of an atom and the resulting resonant condition leads to the large absorption of the x-rays by the absorbing material. Mass attenuations for Al and Cu as a function of energy are shown in Figure 5.3. For aluminum, the sharp drop indicative of the K-edge is

at 1.55960 keV; for copper it is at 8.97890 keV. K-edge filters are differential filters where each pair of filters is carefully selected (by selecting each element and it thickness) such that the residual sensitivity function (Eq. 5.4 or Eq. 5.8) for the pair is significant for the energies between the K-edges of the two filters, and largely vanishes elsewhere. For filters k and $k+1$, having K-edges at energies E_k and E_{k+1}, where $E_k < E_{k+1}$, the residual sensitivity per unit bandwidth (similar relations obtain in the per unit energy case) is ideally chosen such that:

$$ResSen_{PUBW,k}(E) = \begin{cases} f(E) & E_k \le E \le E_{k+1} \\ 0 & E < E_k, E > E_{k+1} \end{cases}$$

Then the differential transmitted signal for a Ross filter Eq. 5.7 may be written as

$$\Delta TS_k = TS_k - TS_{k+1} = C \int_{E_k}^{E_{k+1}} [0.1\%\ E\ S(E)]\ \frac{(T_k(E,x) - T_{k+1}(E,x))\ R(E)}{0.1\%\ E}\ d\,(E) \quad \textbf{Eq. 5.10}$$

Eq. 5.9, for the spectrum per unit bandwidth, becomes

$$[0.1\%\ E\ S(E)]_{E_{avg,k}} = \left[\frac{dN}{dE/0.1\%\ E}\right]_{E_{avg,k}} = \frac{\Delta TS_k}{C \int_{E_k}^{E_{k+1}} \frac{(T_k(E,x) - T_{k+1}(E,x))\ R(E)}{0.1\%\ E}\ d\,(E)} \quad \textbf{Eq. 5.11}$$

Sometimes it is possible to choose the filters in a K-edge pair such that the residual sensitivity is constant between the K-edge energies and vanishes in the region outside those energies. In such cases, one may write:

$$[0.1\%\ E\ S(E)]_{E_{avg,k}} = \frac{\Delta TS_k}{C\ ResSen_{PUBW,k}\ \Delta E_k}$$

where $ResSen_{PUBW,k}$ is the constant residual sensitivity (per unit bandwidth) for the Ross filter pair k, and $\Delta E_k = E_{k+1} - E_k$ is the energy difference between K-edges. In practice, selection of filters with constant residual sensitivity is difficult; the integral in Eq. 5.11 is then numerically evaluated between the bounds determined by the K-edges energies.

5.3 Diagnostic Issues Specific to GeV LPAs

Spectroscopy of x-rays from the wakefield experiments driven by the TPW laser was required to accommodate the following constraints:

1. *Small average FWHM of x-ray profile*: The divergence of the betatron x-ray beam decreases with increasing electron energy (Eq. 6.4). For example, the average FWHM of the x-ray profiles in the LWFA 4.0 experiment was ~5.9 mrad with respect to the

x-ray source. At a distance of ~2.7 m from the source, this span of ~1.6 cm (Figure 5.4) is comparable to the dimensions of a CCD chip:

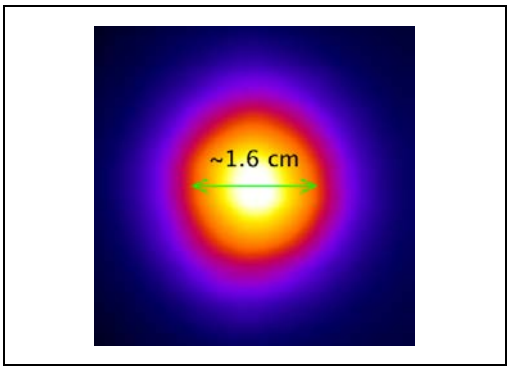

Figure 5.4: FWHM of x-ray profile (LWFA 4.0)

With a stable x-ray beam one could attempt to detect the x-ray using an x-ray CCD; however the other constraint was:

2. *Large shot-to-shot pointing variability for the x-ray beam*: Figure 5.5 shows the range of motion of the betatron x-ray beam on the imaging plate detector. (These images do not correspond to consecutive shots.) The center of the x-ray beam had a range of motion of 1.8 cm (6.6 mrad) horizontally and 3.5 cm (12.8 mrad) vertically during the LWFA 4.0 experiment.

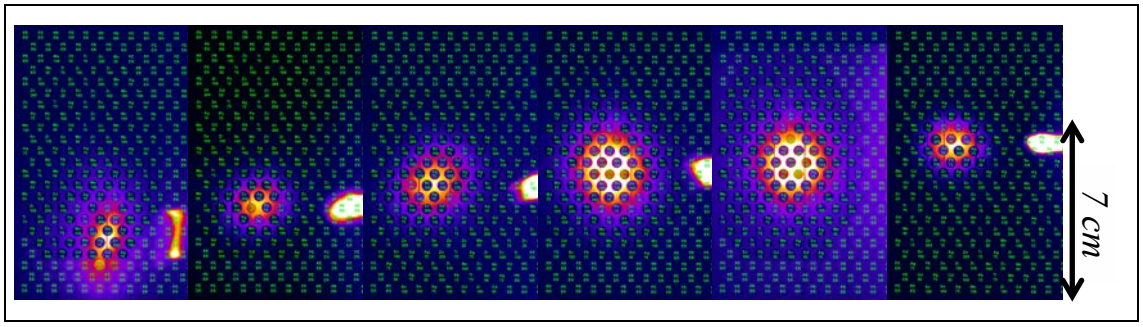

Figure 5.5: Range of motion for the betatron x-ray beam in the LWFA 4.0 experiment

It follows that the x-ray beam would not necessarily remain aligned with a CCD detector from one shot to the next. With a high repetition laser system, one could still attempt many shots and use the measurements from those in which the x-ray beam and the detector were well aligned. However, another constraint in the experiment was the:

3. *Low repetition rate*: With a repetition rate of ~6 shots/day, shots could not be "wasted" due to the wrong alignment between the x-ray beam and the detector.

A well-designed detection system for the x-rays in these experiments would therefore need to minimize the possibility of loss of data due to lack of alignment between detector and the direction of radiation propagation. This made the x-ray CCD, the preferred detector for betatron x-rays in high repetition rate environments [40]–[42], not viable as a detector for x-rays from the GeV accelerator driven by the TPW laser. The low repetition rate also made the use of crystal x-ray spectrometers impractical. In such spectrometers, the spectrum is measured at different wavelengths on the spectrum by rotating the crystal such that the Bragg condition, $n\lambda = 2dsin\theta$, is satisfied for a particular x-ray wavelength λ at a particular angle θ. To measure the spectrum at N points, it is necessary to rotate the crystal N times, i.e., during N shots. However, the x-ray spectrum changes from shot to shot, making shot-to-shot comparisons unreliable. (More on this in following sections.) If the spectrum did not change from shot to shot, with a sufficiently large crystal it would be possible to detect a large part of the x-ray beam, however there is the need for maintaining x-ray beam alignment with the detector from shot to shot and at present the degree of x-ray beam variability poses the same challenge to crystal x-ray spectrometry that is does to x-ray CCD spectrometry.

The conclusion was that for a method of x-ray spectrometry to be successful with betatron radiation from a GeV LPA driven by the TPW laser, it would need to accommodate a low-repetition, single-shot environment with high variability of the x-ray beam direction. It was determined that the use of differential filters, together with imaging plates, were most likely to satisfy these criteria.

5.4 Differential Filter Design for the LWFA 3.0 Experiment

X-ray radiation from the betatron oscillation of accelerated electrons is broadband. Spectroscopy of the betatron radiation therefore requires the use of several pairs of differential filters, each pair having a residual sensitivity $ResSen_k(E)$ and $E_{avg,k}$. A well-selected set of differential filters made up of N pairs will yield N points on the x-ray spectrum which may be used to reconstruct the spectrum. The requirement in selecting the set of filter pairs is that the set of $\{E_{avg,k}\}$, for all k, together span the spectrum with sufficient resolution, providing the coverage needed for the reconstruction.

In the 3rd experimental round covered by this dissertation, preparations were made to determine the spectrum of the betatron radiation. For the first iteration of this initial attempt, a simple symmetric step geometry (0.5 mm → 1 mm → 2 mm → 1mm → 0.5 mm) was used to make 0.4 cm × 1.5 cm filters of 3 thicknesses on a 2 cm × 1.5 cm copper mask. From a single material of 3 thicknesses, 3 residual sensitivities may be computed, in this case corresponding to transitions from 0 mm (only IP cover) to 0.5 mm, 0.5 mm to 1 mm, and 1 mm to 2 mm filters. Figure 5.6 shows the residual sensitivities per 0.1% BW, computed taking into account the additional material for the IP cover used to shield the IP detector from ambient light. The IP cover was from aluminum, 0.012" in thickness, and the x-ray beam was always attenuated by this material before reaching the IP detector. The residual sensitivities can then be used in Eq. 5.9 for the spectrum in per

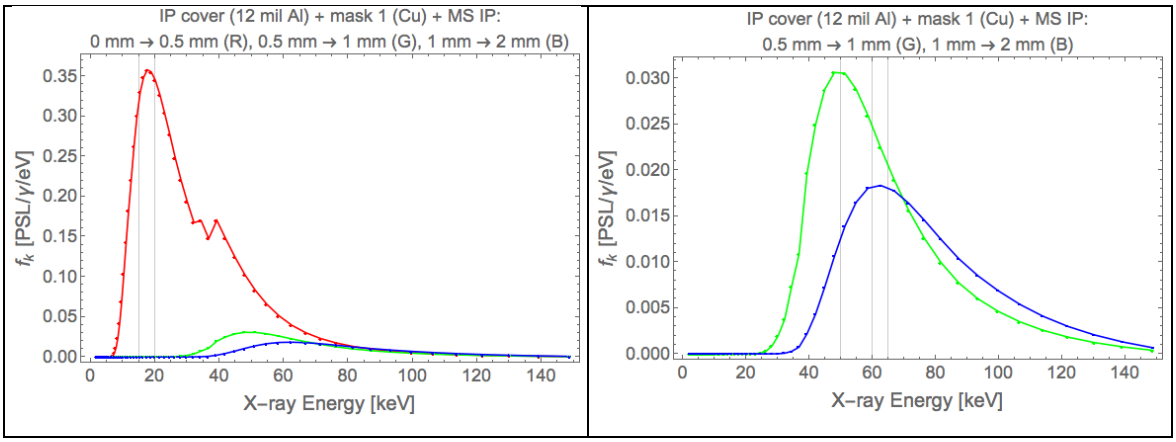

Figure 5.6: Residual sensitivities corresponding to filters on mask 1 (copper of thicknesses 0.5 mm, 1 mm, and 2 mm (right image shows the green and blue curves from the left image)

unit bandwidth units to obtain 3 spectral data points. The average and HWHM energies ($E_{avg} \pm \delta E$) from the residual sensitivities in Figure 5.6 are at 24 ± 12 keV (red curve), 57 ± 18 keV (green curve), and 62 ± 30 keV (blue curve), Figure 5.7 shows the imaging plate measurements for 3 shots from this round. It may be seen that depending on where the x-ray landed, the filter position could coincide with the x-ray profile (right panel), or mostly or partially miss it (left and middle panels). This was an issue due to the variable

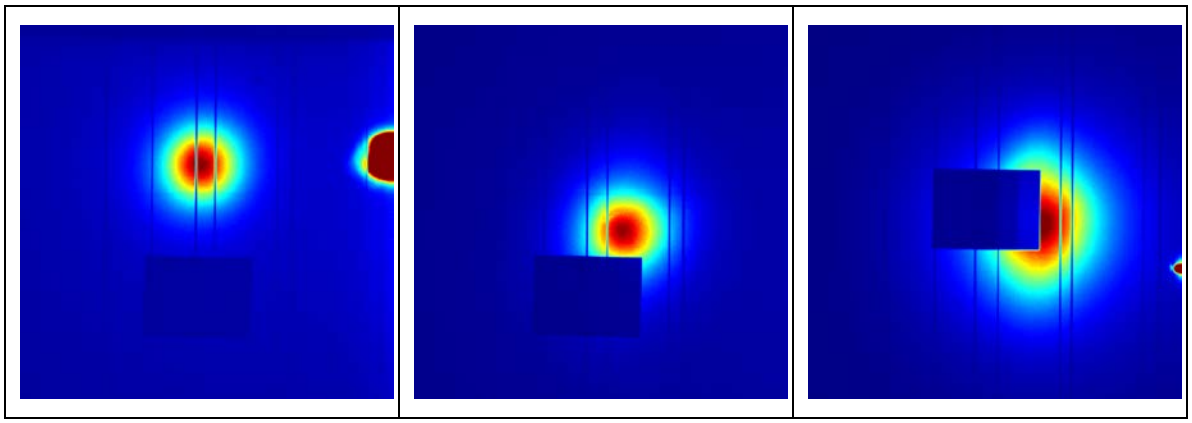

Figure 5.7: First attempt to measure betatron x-ray spectrum used small copper mask (aka mask 1) in 3 thicknesses

pointing direction of the x-ray beam. This variability is quantified in Figure 5.8, where the X and Y coordinates of the peak x-ray position across all shots in this round have been histogrammed. The X and Y coordinates had a range of 200 and 250 pixels, respectively, on the high sensitivity imaging plate (MS IP with 100-μm pixel size). When the x-ray filters and x-ray beam were well-aligned, the large attenuation produced by this filter

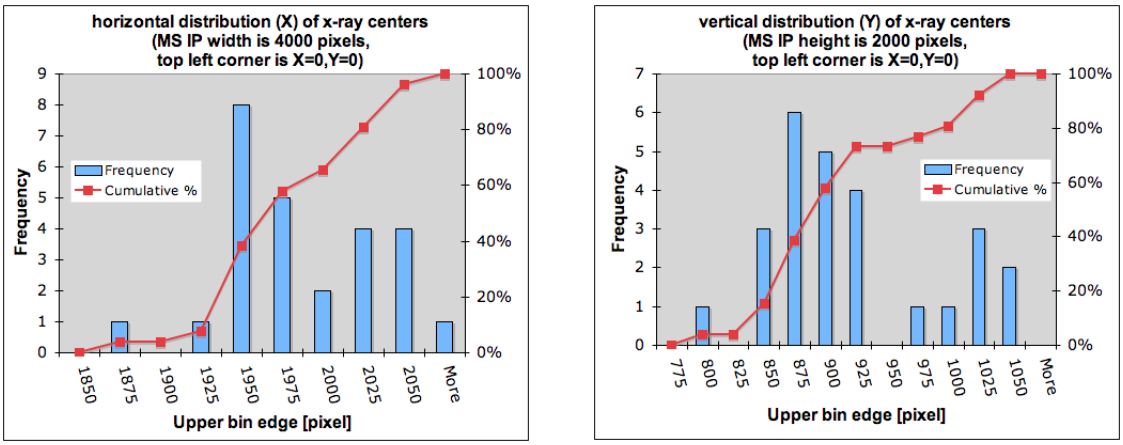

Figure 5.8: Histograms of the coordinates of the x-ray peak intensity pixel on the detector in the 3rd experimental round. The X coordinate had a 20 mm range (200 pixels on the MS IP) [left]. The Y coordinate had a 25 mm range (250 pixels on the MS IP) [right].

mask indicated the need for less attenuating filters, i.e., material with lower atomic number (Z) and/or of smaller thickness.

For the next iteration, a larger filter mask (mask 2), in separate aluminum and copper versions, each incorporating filters in 4 thicknesses and in a symmetrical step geometry (0.25 mm → 0.5 mm → 1 mm → 2 mm → 1mm → 0.5 mm → 0.25 mm) was deployed.

As seen in Figure 5.1, the aluminum version of this set of filters can resolve the spectrum at energies approximately in the range 10-20 keV; below this range, aluminum blocks nearly all x-rays; above this range, it becomes nearly transparent. The set of copper filters have resolution for x-rays at energies > 30 keV. Each filter mask had the geometry shown in Figure 5.9, where the filter thickness starts at 0.25 mm on either size, then doubles at each step to become 2 mm in the center. A filter mask could be used by itself to measure the residual sensitivity corresponding to different thicknesses of same material (Al or Cu), each pair of thicknesses yielding a data point with relatively large energy error bar due to the large FWHM of the residual sensitivities. It was soon realized that differencing of spectra filtered using different materials (Al and Cu) yielded more spaced out data points providing better spectral coverage. To increase the number of filter combinations, the aluminum and copper masks were combined in 3 geometries, either without overlap (combination 1) or overlain with offset (combinations 2 and 3). Figure 5.10 shows the Al and Cu masks arranged in combination 3. This combination yields a larger number of

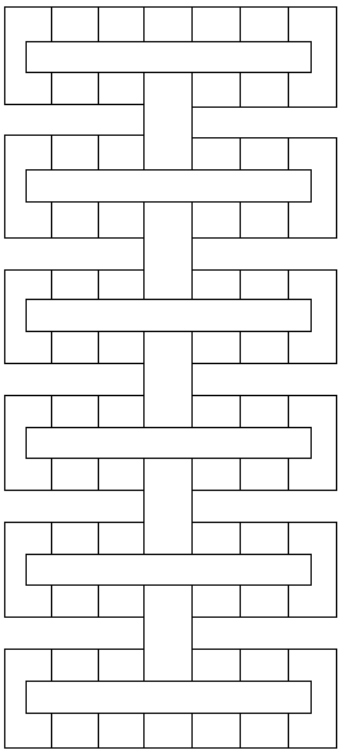

Figure 5.9: Filter design used for Al and Cu in LWFA 3.0 experiment. From left to right, the thickness changes in steps (0.25 mm → 0.5 mm → 1 mm → 2 mm → 1mm → 0.5 mm → 0.25 mm)

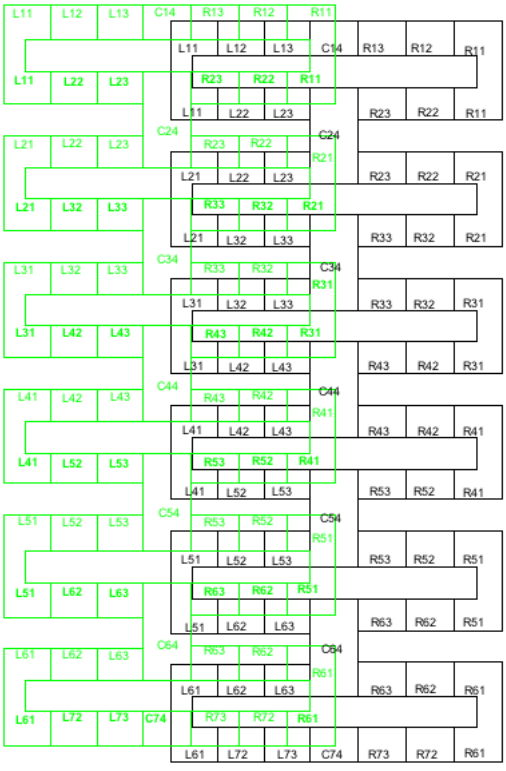

Figure 5.10: One of the 3 arrangements used to combine various thicknesses of Al and Cu to produce a richer set of residual sensitivities

filter combinations, producing a set of 16 residual sensitivities representing energies from ~20 keV to ~70 keV. To combine a pair of filter measurements from different regions of the x-ray profile, one needs to ensure that the same x-ray spectrum is incident on both filters. The use of a transmittance map [43], whereby the ratio of the filtered and reconstructed x-ray profiles is used for this purpose, was found to be inadequate due to the energy dependence of the detector response to x-rays and the fact that the spectrum appeared to change significantly in scale and shape on different regions of the mask. Equalization of pixel values on the filtered x-ray image to the peak pixel value, as is accomplished using a transmittance map, is appropriate when the detector response function is not a function of energy. When the detector is more sensitive to x-rays in one part of the spectrum than in others, pixel value equalization in effect assumes that the spectra incident at two separate pixels on the detector are scaled versions of one another, i.e., the spectrum changes merely by a factor. In fact, different frequencies on the spectrum scale differently when moving from one pixel to another (not necessarily

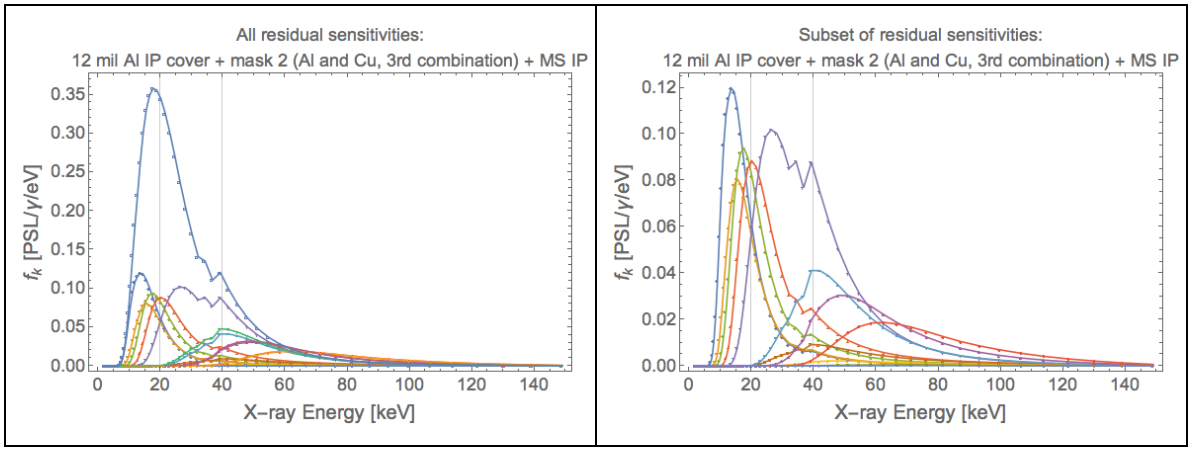

Figure 5.11: Left: all residual sensitivities corresponding to differential filter in **Figure 5.9**, in Al and Cu versions, combined in the arrangement shown in **Figure 5.10**. Right: a subset of the residual sensitivities shown in the image on the left.

contiguous) pixel. This is especially the case in GeV LPAs, as the x-ray divergence is smaller (Eq. 5.13) making the spectrum change with pixel location more important. This led to a search for a consistent method for sampling of filtered x-ray data, which led to the use of iso-intensity contours, described in 5.7.2; on such contours, the x-ray spectrum is assumed to be constant and filtered measurements on the intersection of the filter and the contour would be appropriate for the calculation of residual sensitivities. The use of such contours, however, required

1. A preprocessing of the filter x-ray profile, in which all image pixels representing filtered or scattered x-ray radiation are removed (replaced by NaN in ImageJ).
2. A reconstruction of the unfiltered x-ray profile.

The preprocessing task of pixel removal was found to require significant effort, especially when masks were overlain (combinations 2 or 3). Manual sampling of filter data is slow and limits the number of x-ray measurements that can be processed. Therefore the use of iso-intensity contours also requires

3. Knowledge of all x-ray filter boundaries, in order to programmatically sample filter data on a large number of contours.

Determination of filter boundaries, on the other hand, is tedious, when done for many x-ray measurements from multiple laser shots, especially where filter masks are overlain (e.g., see Figure 5.12 for filter boundaries determined for shot 5862 in LWFA 3.0 where

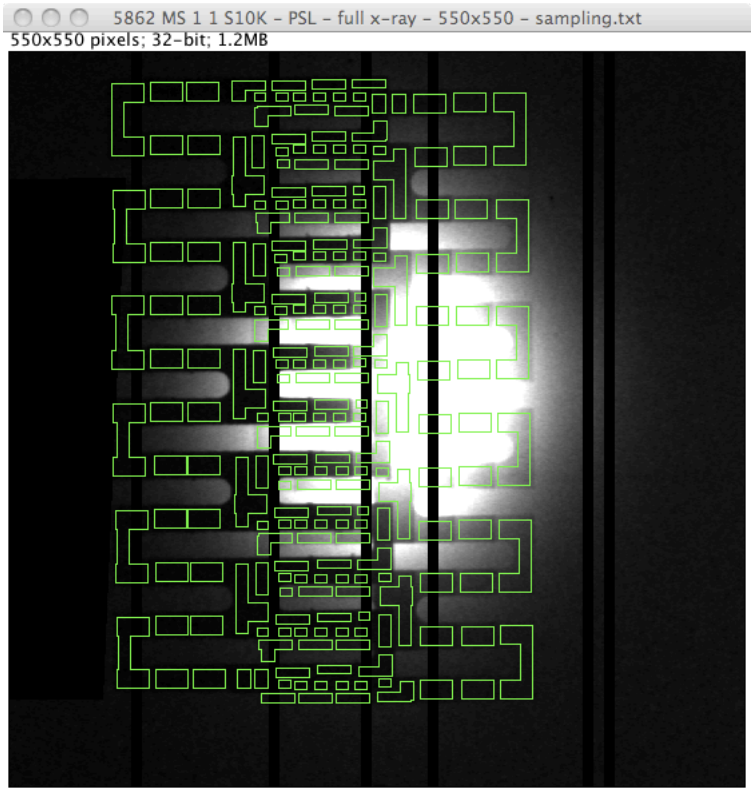

Figure 5.12: Cu (left) and Al (right) x-ray filters (each having 4 different thicknesses) overlain according to the configuration shown in **Figure 5.10**, with the distinct filter boundaries indicated in green. This configuration yields a larger set of differenced spectra, hence spectral data points, but is not optimal from an image reconstruction and data sampling standpoint.

the Al and Cu Type II masks are used in combination 3). To use iso-intensity contours for multiple betatron x-ray measurements, the filter design therefore needed to

incorporate the need for x-ray profile preprocessing, filter boundary determination, and accurate x-ray profile reconstruction.

In addition to the design of the filter masks, another shortcoming of the x-ray diagnostics in this round was the attenuation created in the x-ray beam by the 0.012" Al IP protective cover which protected the IP from ambient light and prevented it erasure. The attenuation produced by the IP cover, negligible for relativistic electrons, is > 50% for x-ray photons with energies $\lesssim$ 14.5 keV. When the thickness of the Al laser beam deflector is taken into account (0.001" at 23.53° offset to perpendicular), the attenuation is > 50% for x-ray photons with energies $\lesssim$ 16 keV.

The insights gained from this experimental round regarding the design of the filter mask for x-ray diagnostics, were incorporated into the design of x-ray filter for the following round.

5.5 Ross Filter Design for the LWFA 4.0 Experiment: Part I

The initial experience with the design of x-ray filters for the spectroscopy of the betatron radiation during the 3rd experimental round, taught us the following:

1. The differenced spectra should provide coverage of the x-ray spectrum using simple arrangement of filters.
2. The FWHM of the difference spectra should be minimized in order reduce the energy error bars.
3. The attenuation due to the IP protective cover should be minimized in order to enable the detection of the low-energy tail of the x-ray spectrum.
4. X-ray filter mask should be robust to the variations in the x-ray beam pointing direction.
5. Mask design should incorporate the needs for x-ray profile preprocessing and reconstruction.
6. The design should incorporate the need for filter boundary determination across a large number of shots and small, but not negligible changes, in the relative transverse positioning of the x-ray source and the filter mask from shot to shot.

These criteria were applied to the design of the K-edge (Ross) filters in the 4th experimental round.

Note on Sources of X-ray Attenuation Data

The two major sources of x-ray attenuation data are NIST FFAST[8] and XAAMDI[9] databases. XAAMDI database, calculated using the same theoretical framework as the NIST XCOM[10] database, differs from the one used for the FFAST database. The differences between data retrieved from these sources can be significant (> 50%) at lower energies (< 4 keV) for Z ~ 30 or Z > 60, in particular near the K-edges. According to NIST[11], FFAST data "was produced for x-ray diffraction, interferometry, crystallography, and related areas". XAAMDI and XCOM databases were produced for dosimetric purposes and are therefore more appropriate for x-ray spectroscopy. However, FFAST data was chosen for its granularity. In the design of the Ross filter, an attempt was made to avoid using elements for which databases have discrepancies. The K-edge energies for the elements used in the Ross filter are all $\gtrsim$ 5 keV therefore avoiding the

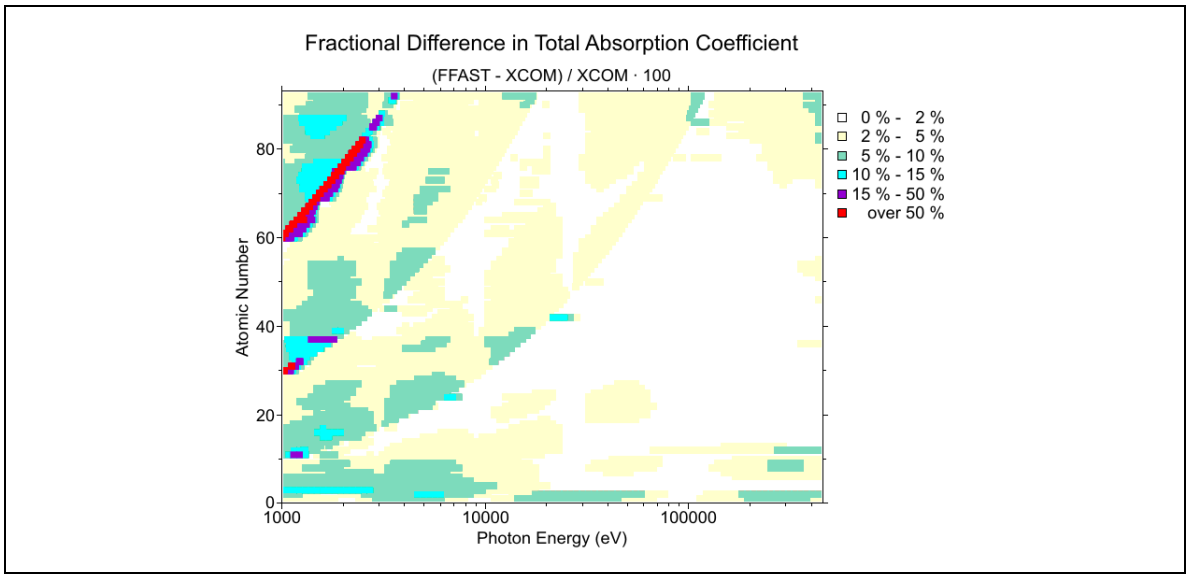

Figure 5.13: Differences between x-ray attenuation data calculated using FFAST and XCOM methodologies for different energies and atomic numbers

[8] http://www.nist.gov/pml/data/ffast/index.cfm
[9] http://www.nist.gov/pml/data/xraycoef/index.cfm
[10] http://www.nist.gov/pml/data/xcom/index.cfm
[11] http://physics.nist.gov/PhysRefData/XrayNoteB.html

regions with largest discrepancies. At higher energies, $\gtrsim$ 21 keV, for Z=41 (niobium), the difference can be 10-15%. This element was not used.

5.5.1 Design of the Ross Filter

The important criteria for the design of the Ross filters used for the spectroscopy of betatron x-ray radiation may be divided into the categories of spectrum coverage, cost, fabrication, profile reconstruction, and contour coverage:

Spectrum Coverage

1. The energy bins for the Ross pairs should span the spectrum from ~5 keV to ~80 keV.
2. A balance is required between resolution (number of bins, or filter pairs) and S/N. (Too many bins increase resolution but reduce S/N.)
3. Prefer better resolution in the 10-30 keV region; this is the energy range where the peak of the spectrum and the critical energy are expected to be (based on round 3 results).

Cost

1. To minimize costs, use inexpensive elements (i.e., filter materials) where possible.
2. To minimize costs, use foil thicknesses that are available off-the-shelf, instead of custom-rolled foils.
3. Share filters between different (neighboring) bins if possible.
4. Smaller filters and square filters are more expensive. Opt for round filters; filter size needs to balance cost and the need to reconstruct the x-ray profile. (Smaller filters produce smaller gaps in the x-ray profile, making reconstruction more accurate.)

Fabrication

1. Square vs. circular filters: the former have lower tolerance (also see cost).
2. Filter size: smaller filters are harder to make and deploy, but provide better spatial resolution.

X-ray Profile Reconstruction

1. Square filters produce images that are easier to reconstruct
2. Smaller filters produce images that are easier to reconstruct
3. Regular geometry grid of filters easier to reconstruct than packed hexagonal

Contour Coverage of Filters

1. Smaller filters increase the number of filters crossed by a contour, but are more costly to make.
2. More closely packed filters increase coverage. Opt for hexagonal packing (shift every 2nd row by half a filter diameter.
3. The x-ray pointing stability must be considered (see 5.3); this requires filter area larger than the size of x-ray profile. Also, since the range of motion of the x-ray beam center in the 3rd round was greater in the vertical than in the horizontal direction (25 mm vs. 20 mm), choose mask taller than wide.

Trade-offs

1. The smaller the filter the better the spatial resolution, and the more accurate the reconstruction of the x-ray profile; however, smaller filters are more costly. In addition, the fabrication of the filter pockets becomes more difficult and expensive.
2. Closely packed filters increase coverage but make reconstruction more difficult.

The critical aspects of a Ross bin design are spectral resolution and cost. One data point corresponds to one energy bin, and two filters are required having K-edges which bound the bin on the energy scale. To increase the resolution, more bins, hence more filters are required.

The Ross filter array selected for the spectroscopy of the betatron radiation consists the 7 pairs of differential filters, which together covered the spectrum in the spectral range $\gtrsim$ 7 keV to ~70 keV (bin midpoints). The elements used, and their K-edge energies are provided in Table 5-1. Note that the materials chosen are, except for gadolinium, moderately priced. (All x-ray filters were purchased from the Goodfellow Corporation.) These elements were then combined in pairs (Table 5-2), which together provide the best resolution at ~20 keV. In order to achieve residual sensitivities that vanished beyond the

Element	Symbol	Atomic No.	K-edge [keV]	Mass Density [g/cm^3]
Titanium	Ti	22	4.9664	4.540
Copper	Cu	29	8.9789	8.960
Zinc	Zn	30	9.6586	7.133
Zirconium	Zr	40	17.9976	6.506
Molybdenum	Mo	42	19.9995	10.22
Silver	Ag	47	25.5140	10.50
Tin	Sn	50	29.2001	7.310
Gadolinium	Gd	64	50.2391	7.900
Lead	Pb	82	88.0045	11.35

Table 5-1: Material used in the Ross filter for the LWFA 4.0 experiment and relevant physical properties

boundary of the K-edges (a requirement for Ross filters), while at the same time minimizing costs, the filters in each pair combined one element having available off-the-shelf thickness (element A), with copper of sufficient off-the-shelf thickness (element B). In each case of each pair (representing an energy bin), the selection of all filter thicknesses, such that the residual sensitivity was adequate between the K-edges and

Pair	Bin Boundaries		Filter 1				Filter 2			
			Element A		Element B		Element A		Element B	
	E_1 [keV]	E_2 [keV]	Type	Thickness [μm]	Type	Thickness [μm]	Type	Thickness [μm]	Type	Thickness [μm]
1	4.9664	9.6586	Ti	75	NA	NA	Zn	20	NA	NA
2	9.6586	17.9976	Zn	200	NA	NA	Zr	100	NA	NA
3	17.9976	19.9995	Zr	100	NA	NA	Mo	55	NA	NA
4	19.9995	25.5140	Mo	100	Cu	40	Ag	75	Cu	34
5	25.5140	29.2001	Ag	75	Cu	34	Sn	100	Cu	30
6	29.2001	50.2391	Sn	100	Cu	30	Gd	50	Cu	25
7	50.2391	88.0045	Gd	50	Cu	25	Pb	15	Cu	34

Table 5-2: Structure of the 7-bin Ross pair used in LWFA 4.0

vanished outside, was an optimization problem requiring considerable effort. To more accurately determine the residual sensitivity plots for the differential filters in Table 5-2, a switch was made from the imaging plate calibrations for x-rays in [39] (Figure 5.2, left), used for the analysis of the x-ray measurements in the previous experimental round, to a more recent calibration [44] shown in Figure 5.14, where the solid red lines represent the sensitivity of the high-sensitivity (MS) and high-resolution (SR) imaging plate detectors. Compared to the curves in Figure 5.2, the more recent calibration lowers the sensitivity for both types of imaging plates. In addition to the scaling down of sensitivity curves, in the case of the high-sensitivity IP (the main detector for betatron x-rays) the

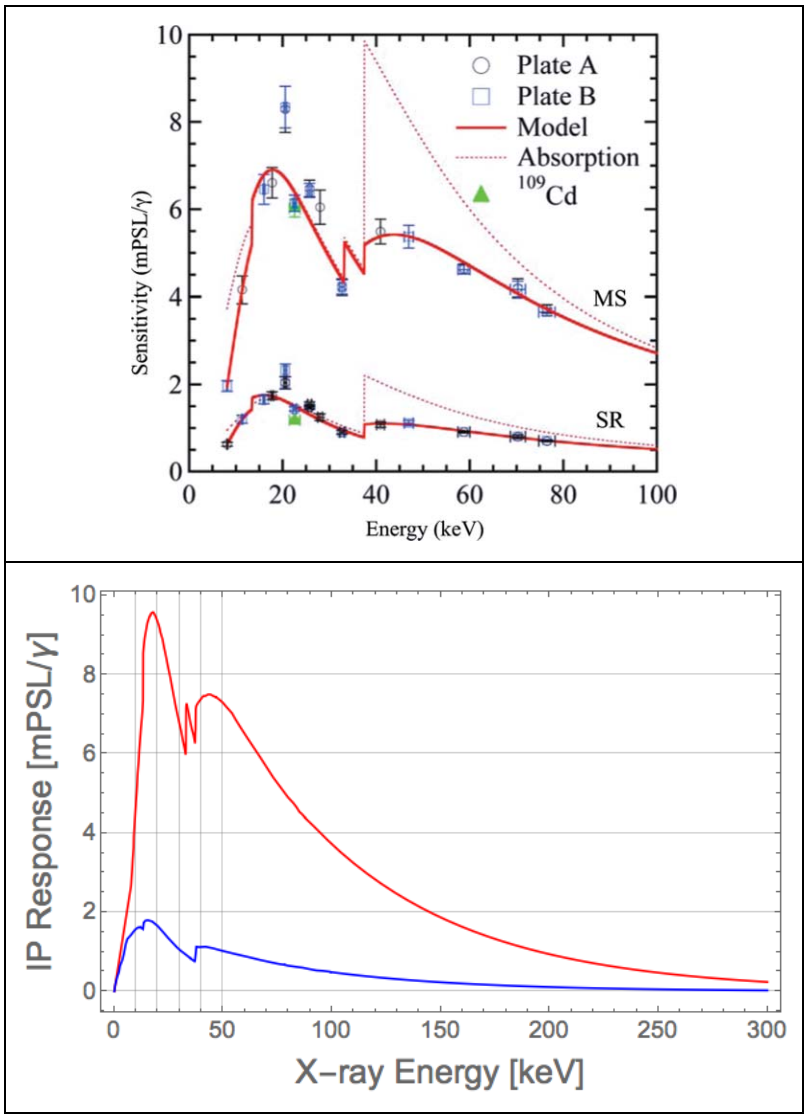

Figure 5.14: Imaging plate response to x-rays used to calculate the residual sensitivities in **Figure 5.15**; see text for details.

sensitivity in the 30-40 keV region (where there are 2 K-edges in the sensitivity curve) also differs in shape between the two calibrations. To calculate the residual sensitivities, the IP sensitivities were digitized. This had already been done for the MS and SR IP sensitivity curves in [39], but was repeated only for the MS IP sensitivity in [44]. The SR sensitivities were sufficiently similar in shape that it was possible to use the ratio of sensitivities at 13.474 keV from the 2 different calibrations (this ratio was 1.75/4), to scale the old digitized calibration down to obtain the new one for the SR IP without the need for re-digitization. Since the MS (SR) imaging plates have 100 μm (50 μm) pixel

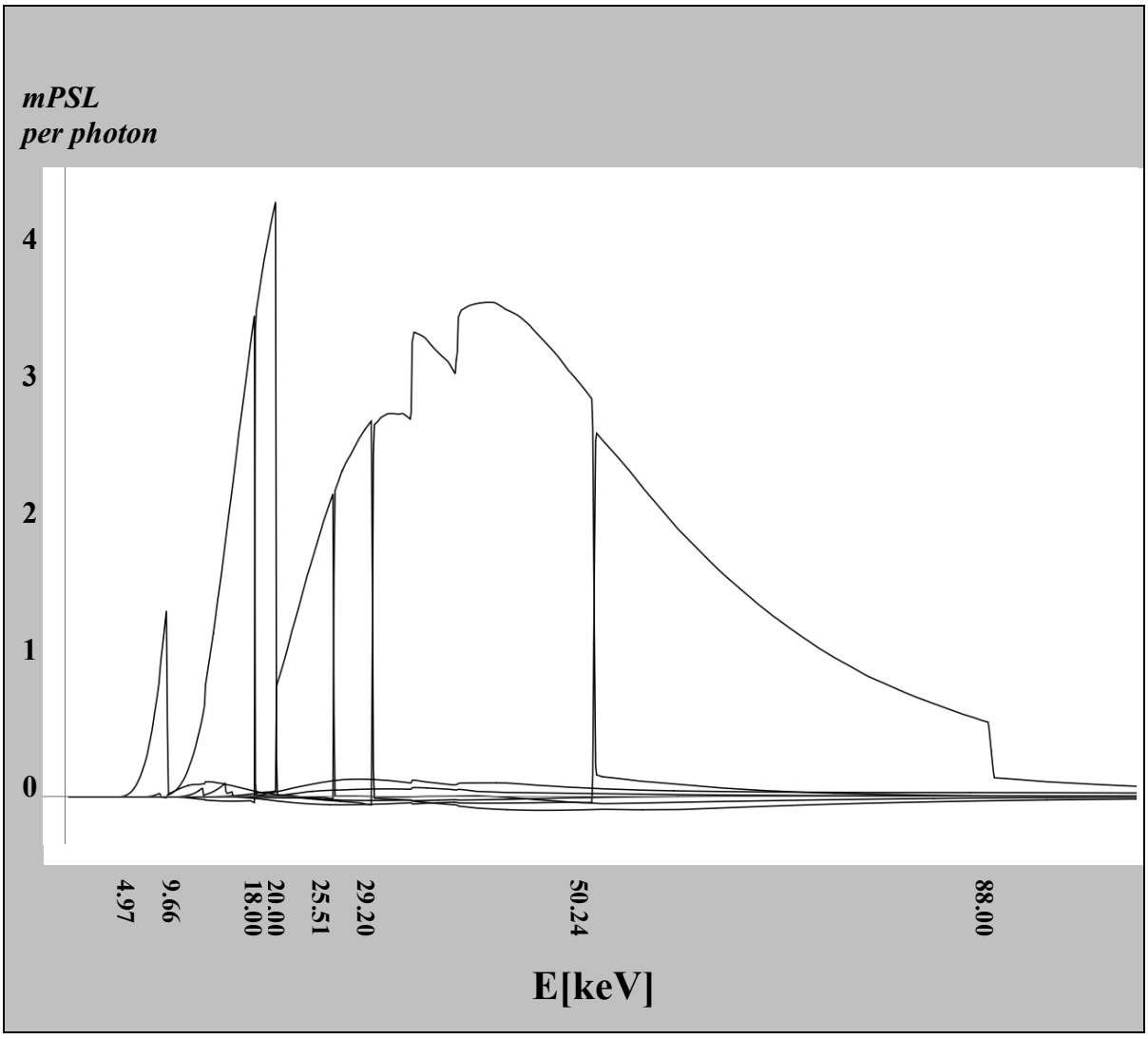

Figure 5.15: Residual sensitivity plot for the K-edge (Ross) filters used in the LWFA 4.0 experiment (**Table 5-2**)

size, they were always scanned using a 100 μm (50 μm) step size (i.e., scanner resolution setting, see Appendix C). The calibrations in [44] were, however, performed using a 50 μm step size for both types of imaging plates. This meant that the new calibrations for the MS IP would need to be adjusted to take into account the differing step sizes used for the calibration and for the read-out during the experiment. Fortunately, sensitivity multipliers had also been provided in [44] for conversion between the different step sizes. This multiplier (1.38) was applied to the digitized MS IP sensitivity. The resulting curves, extrapolated to 300 keV, are shown in the bottom image of Figure 5.14. In nearly all of the cases, the red curve (for the MS IP) represents the response function of the IP detector (*R(E)* in Eq. 5.11). (The blue curve is for the SR IP; this detector was used as the primary

detector for x-ray spectroscopy only once.) The residual sensitivities for the 7 Ross filter pairs in Table 5-2 are shown in Figure 5.15. The K-edges of elements A in the table determine the boundaries of the energy bins in the residual sensitivity plot. Elements B ensure that outside these boundaries, the residual sensitivity for the pair either vanishes or become relatively small.

5.5.2 Filter Design Validation using Phantom Spectrum

It is possible to increase resolution of the Ross filter array by increasing the number of filter pairs. This has the side effect of making the energy bins for the K-edge filters narrower and, for each affected bin, would lead to a reduction in the number of photons whose energies would fall within that bin's energy boundaries. In other words, the signal from the bin would be reduced, at the same time that the signal contributed by the region outside the bins (see Figure 5.15) could increase. An enhancement in the resolution of a K-edge filter is therefore accompanied by a reduction in the S/N ratio and for a Ross filter design to be successful it is necessary to address both resolution and S/N. To confirm that the design of the Ross filter had adequate S/N, it was tested using a representative spectrum from the LWFA 3.0 experiment. The chosen spectrum (for shot 5671, Figure 6.26) was determined using differential filter analysis described in 5.2. It was

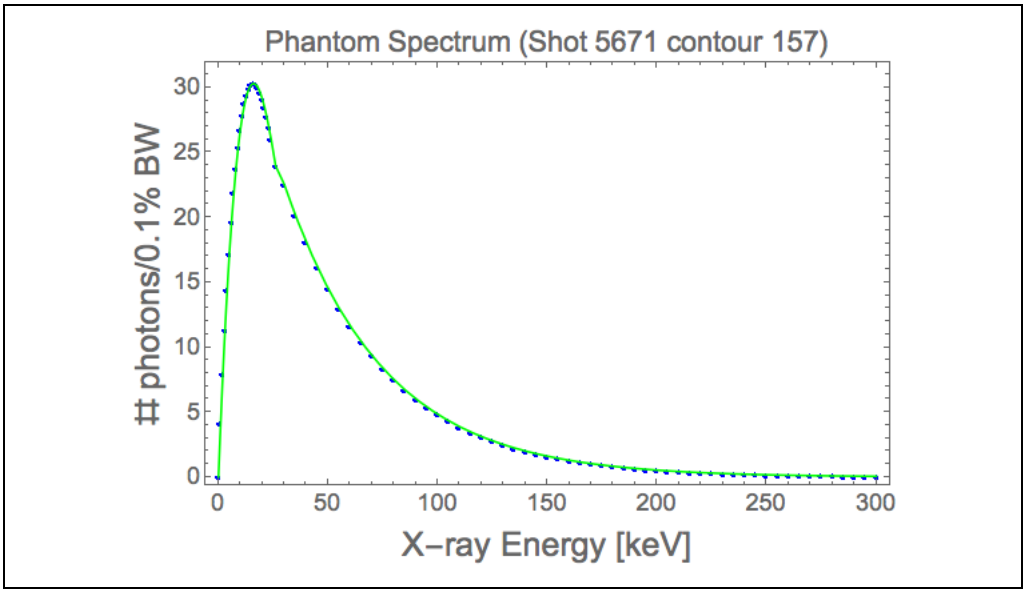

Figure 5.16: The phantom spectrum used to determine the error for the Ross filter design in **Table 5-2**

then interpolated (Figure 5.16) and the resulting spectrum, denoted by $S(E)$, convolved with the residual sensitivities for the filters used in the Ross filter design (Figure 5.15) according to the convolution integral in Eq. 5.10. The convolution was done separately for each Ross filter pair, and in each case the bin boundaries (K-edge energies) given in Table 5-2 determined the limits of the convolution integral. This gave the differential transmitted signal for each of the 7 bins. In addition, the integral was numerically evaluated in the regions outside the K-edges and the following figure of merit was calculated:

$$\chi_k = \frac{\left|\int_0^{E_k} S(E)(T_k(E) - T_{k+1}(E))\, R(E)\, d\,E\right| + \left|\int_{E_k}^{\infty} S(E)(T_k(E) - T_{k+1}(E))\, R(E)\, d\,E\right|}{\left|\int_0^{E_k} S(E)(T_k(E) - T_{k+1}(E))\, R(E)\, d\,E\right| + \int_{E_k}^{E_{k+1}} S(E)(T_k(E) - T_{k+1}(E))\, R(E)\, d\,E + \left|\int_{E_k}^{\infty} (T_k(E) - T_{k+1}(E))\, R(E)\, d\,E\right|}$$

Figure 5.17: Expression for the figure of merit for a Ross filter having k-edges at E_k and E_{k+1}

The numerator in this ratio is the area under the residual sensitivity plot for filter pair k in the region between its K-edges. (Note that the transmission function $T_k(E)$ is implicitly dependent on the thickness of filter k.) The denominator has 3 components; together they represent the area between the K-edges and outside it on each side (the tail areas). Absolute value of the integrals for the areas outside the K-edge regions has been used because these integrals, although small, can become negative. For an ideal K-edge filter, the area in the tails of the residual sensitivity plot vanishes and this ratio equals 1. For a non-ideal filter, the ratio quantifies the departure of that filter from the ideal case and

Pair	E_1 [keV]	E_2 [keV]	$\int_{E_k}^{E_{k+1}}$	$\left\|\int_{E_0}^{E_k}\right\| + \left\|\int_{E_k}^{E_\infty}\right\|$	$\left\|\int_{E_0}^{E_k}\right\| + \int_{E_k}^{E_{k+1}} + \left\|\int_{E_k}^{E_\infty}\right\|$	$\frac{\left\|\int_{E_0}^{E_k}\right\| + \left\|\int_{E_k}^{E_\infty}\right\|}{\left\|\int_{E_0}^{E_k}\right\| + \int_{E_k}^{E_{k+1}} + \left\|\int_{E_k}^{E_\infty}\right\|}$
1	4.9664	9.6586	12.27	1.65	13.92	11.9%
2	9.6586	17.9976	23.17	2.32	25.49	9.1%
3	17.9976	19.9995	12.58	1.37	13.95	9.8%
4	19.9995	25.5140	9.52	0.35	9.87	3.5%
5	25.5140	29.2001	7.76	1.13	8.89	12.7%
6	29.2001	50.2391	31.47	0.58	32.05	1.8%
7	50.2391	88.0045	8.70	1.23	9.93	12.4%

Table 5-3: Figure of merit calculations for the Ross filters in **Table 5-2**

gives an indication of the filter error. Table 5-3 shows the calculation steps for the figure of merit for the Ross filter array used in LWFA 4.0. (Note that the cut-off energy of 300 MeV has been used.) The tail region represents an area as small as $\lesssim$ 2% (for bin 6) and

not exceeding $\lesssim 12.7\%$ (for bin 5). These figures of merit can be used to estimate the error in the integrated residual sensitivity (denominator of Eq. 5.11), denoted as $\delta(\int ResSen(E)dE)$ in propagation of error formula used to calculate the error in the spectrum (see Eq. F-8).

5.6 Ross Filter Design for the LWFA 4.0 Experiment: Part II

The first part of the redesign of the x-ray detector for the 4th experimental round, addressed the first 2 requirements laid out in 5.5. The remaining criteria, having to do with the optimization of the imaging plate protective cover and the mask used to house the x-ray filters, are discussed in the following sections.

5.6.1 Optimization of the Imaging Plate Cover

To minimize the scattering and energy loss of laser-wakefield-generated radiation before reaching the detector, the layer of material protecting the imaging plate from background radiation and ambient light (the IP cover) would need to be of a thin, low-Z material. It should also work well with both of x-rays and electrons. In each case, the IP cover would act as an attenuator of the incoming radiation in its path to the detector. However, relativistic electrons scatter minimally passing throw thin layers of low-Z material, so an IP cover that works well with x-rays, will also be appropriate for electron electrons.

In the case of x-rays, the region of the IP cover exposed to radiation also needed to house the Ross filters. The material used for the cover therefore had to satisfy the following requirements:

1. Low absorption for betatron x-rays
2. Opaque to visible light
3. Low outgassing down to a few millitorrs
4. Precision machinable to allow the creation of pockets to house the filters
5. Can withstand high radiation dose (from electrons and x-rays)

Several candidate materials were considered for the IP cover, including polyoxymethylene (a thermoplastic sold under brand name Delrin), polyimide plastics (e.g., Vespel, manufactured by DuPont, and its cheaper version, Plavis), and polyether ether ketone (a thermoplastic known as PEEK). PEEK and Vespel both have very low

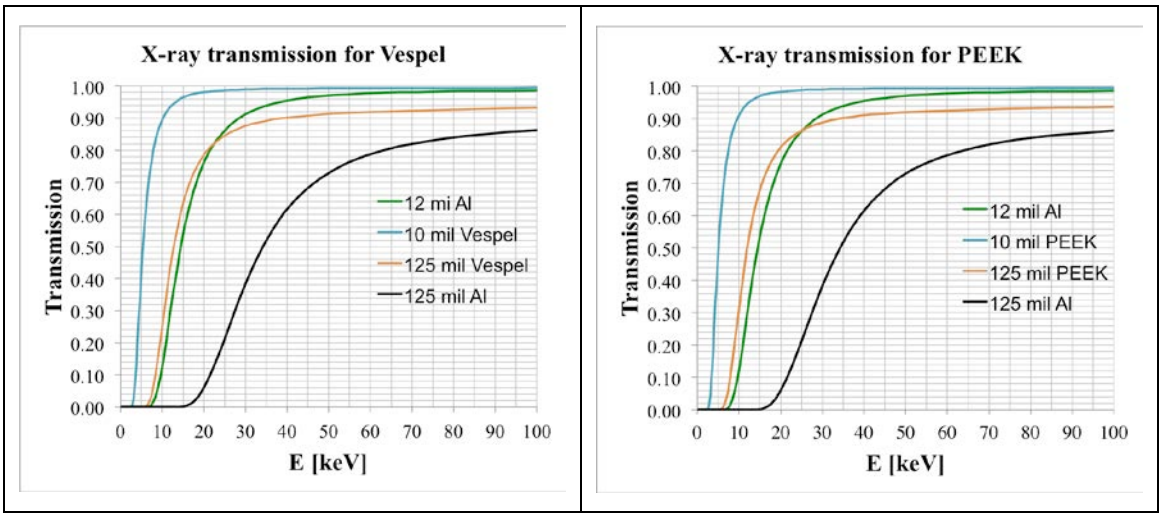

Figure 5.18: Comparison of two candidate materials (Vespel and PEEK) for the imaging plate detector cover which would also house the Ross x-ray filters

attenuation for x-rays; PEEK was selected for its lower cost compared to Vespel. The design of the filter mask involved two separate thicknesses, one for the thicker region external to the pockets (the mask thickness), and another for the substrate at the bottom of the filter pockets that would be machined into the mask. A thickness of 0.010"-0.012" was found to be adequate for the substrate, making it minimally absorptive of x-rays and structurally robust; a thickness of 0.125" was used for the external region. Figure 5.18 shows the transmission of x-rays at energies 0-100 keV through polymers (Vespel and PEEK) for both thicknesses and compares that with 12-mil (the thickness of the Al IP cover used prior to LWFA 4.0 experiment) and 125-mil aluminum. The transmission ratios $T(E,x) = I(E,x)/I_0$ were calculated using Eq. 5.1, where the mass attenuation was calculated using data from the NIST FFAST database, and the chemical formula ($(C_{26}H_{14}N_2O_5)_n$) and mass density (1.43 g/cm^3) for Vespel and the chemical formula ($(C_{19}H_{12}O_5)_n$) and mass density (1.31 g/cm^3) for "natural" or "unfilled" PEEK (i.e., with no carbon filling). As shown in Figure 5.18, at the thinner thickness (10-mil), polymers have better transmission for x-rays at all energies < 100 keV and are therefore more suitable than aluminum for the material that would be placed between the x-ray filters and the imaging plate detector (i.e., the filter pocket substrate). The thicker polymer used for the regions outside the filters pockets also has significantly better transmission than its aluminum counterpart (125 mil) at all energies and even compares favorably with the thinner aluminum at lower energies. The superior transmission of polymers, of either

thickness, in the region of interest for the spectroscopy of betatron radiation (i.e., where the critical energy is) makes polymers excellent candidates for the design of the IP cover. Note that to create filter pockets in aluminum, the region external to the pockets would have to be much thicker than 0.012" and closer to 0.125", for which aluminum attenuates much more strongly than polymers. Comparing PEEK to Vespel, PEEK has ~10% higher

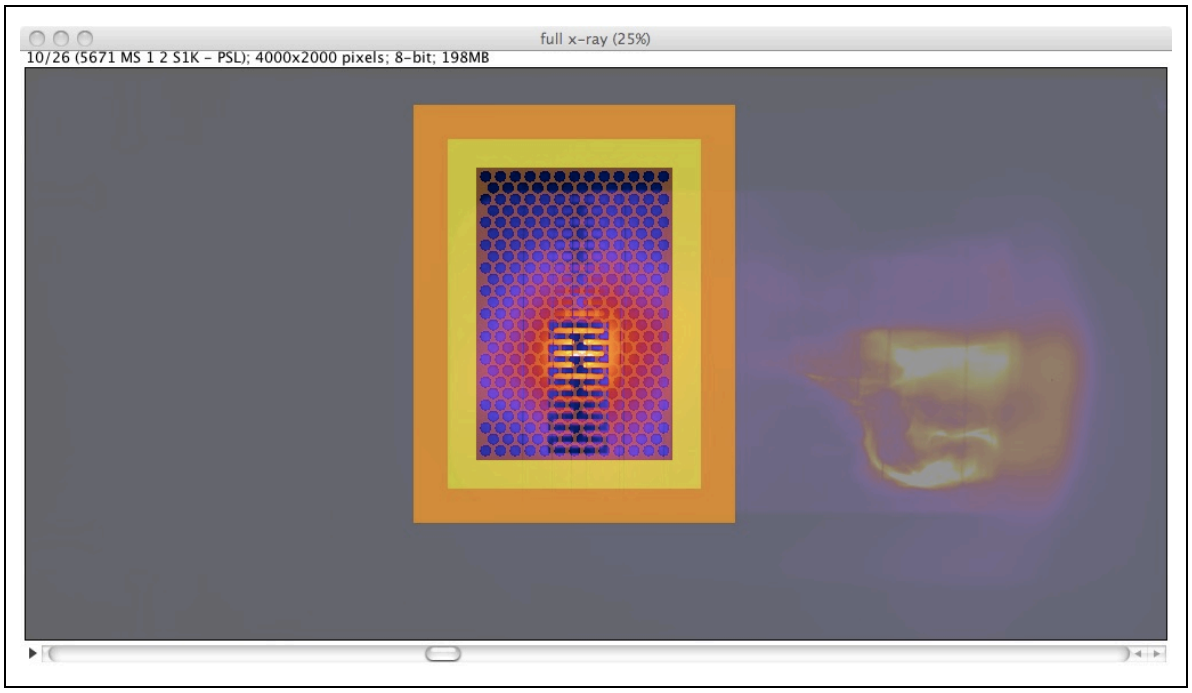

Figure 5.19: Simulation of the full IP cover used for the 4th round of experiments, including the PEEK layer used in the x-ray region and 0.012" aluminum layer used in the electron region, using the x-ray and electron signal for shot 5671 from the previous round

transmission below 10 keV and is therefore more suitable for detecting low-energy x-rays. High-energy behavior is similar for both polymers.

To summarize, the redesigned IP cover incorporate the following features:

- PEEK layer used for x-ray detection only
- PEEK layer in contact with IP detector to minimize scattering effects
- PEEK layer has vertical and horizontal degree of freedom (1 cm) by means of slots
- PEEK layer extends over Al layer for light-tightness

These features are seen in Figure 5.19, where the new design is validated using simulation by overlaying it with the IP measurement for a shot (5671) from the 3rd round of experiments. Two distinct regions are seen on the IP cover. The gray region indicates an aluminum layer of thickness 0.012" from which a rectangular region has been

removed for the insertion of the PEEK mask. The aluminum region mainly interacts with the relativistic electrons and is largely transparent to them. The amber region in the inner rectangle is from PEEK of thickness 0.125", except in the circular regions (filter pockets) where the thickness is 0.010" and serves as a substrate for separating the x-ray filters from the imaging plate. The 0.125" PEEK regions is sufficiently transparent to x-rays to allow the reconstruction of the x-ray profile from measurements on these regions. The 0.010" substrate is largely transparent to x-rays and has minimal impact on the residual sensitivity of the Ross filters. (The small attenuation that it produces for x-rays was incorporated into the calculations.) The yellow region indicates the part of the PEEK mask that descends in the empty rectangular region cut out of the aluminum; it has slots machined into it parallel to the aluminum surface which, once the mask is inserted into the rectangular gap in the aluminum layer, provides two degrees of freedom to the x-ray mask allowing the mask and the filters on it to be adjusted in both directions. The amber region in the boundary is a thin layer extending over the Al layer meant to protect the IP from ambient light that could otherwise enter through the gaps around the edges and erase the signal stored in the imaging plate. A thin Al foil (0.001") covering the inner rectangular region was used to prevent ambient light from interacting with the IP through the filter regions.

5.6.2 Design of the Ross Filter Mask

The questions that arise when designing an x-ray filter mask are:

1. What is the optimum filter shape? Candidates were circular and rectangular.
2. What is the optimum filter size? The answer determines the size of the filter cavities machined onto the PEEK mask.
3. For given filter size, what is the optimum separation between the filters on the mask?
4. For given filter size and separation, what is the optimum configuration of the filters on the mask?

These design decisions will determine the quality of the x-ray profile reconstruction and the iso-intensity contours created on it, and the coverage of the x-ray filters by contours (hence the granularity of the spectrum data). From an x-ray spectroscopy standpoint, small, closely packed filters promise the best resolution for the spectrum. With decreasing size, the cost of filters and manufacturing of the PEEK mask cavities increases

(labor cost), handling of the filters becomes more difficult, and processing of the x-ray data becomes more difficult (see **Determination of the Filter Boundaries**). The approach adopted was to select the optimum filter size and separation based on the available budget for the cost and manufacturing time, then optimize the configuration by choosing one which maximize iso-intensity contour crossings and could be acceptably reconstructed. From an x-ray profile reconstruction perspective, the best filter shape is rectangular placed in a regular rectangular array. This is because the arrangement of the filters has horizontal and vertical symmetry and this is the symmetry for which reconstruction using the NNMA algorithm (5.7.1) is most successful. However, circular filters are easier to make (by way of punching them out of thin foils of metal) i.e., are lower in cost, and can be made to lower tolerance; this is also the case with the drilling of circular filter cavities. An investigation showed that a rectangular arrangement of circular filters could be reconstructed with reasonable accuracy. Another investigation to compare the contour coverage showed that filters of either shape, circular or rectangular, provide best contour coverage when arranged in a packed hexagonal (honeycomb) configuration. As a result of these studies a circular filter shape was chosen with diameter $D_{filter} = 4$ mm, horizontal separation $d_{gap} = 1.3$ mm, and arranged in a packed hexagonal configuration, created by offsetting every 2nd row by an amount equal to the diameter of the filter (i.e., 2 mm). The filter mask is shown in Figure 5.20.

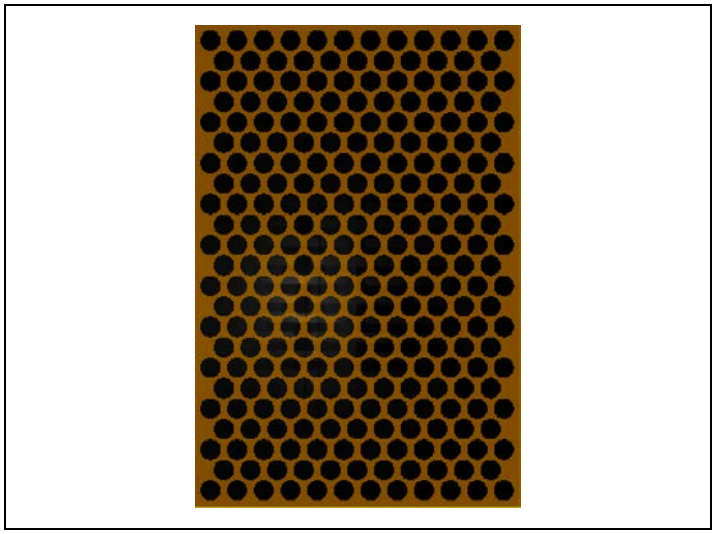

Figure 5.20: 7 cm by 10 cm PEEK x-ray mask with 265 filter cavities

To account for the tolerance of the filter diameters (up to 0.25 mm, with average of 0.15 mm), the filter cavities were machined with a diameter of $D_{Cavity} = 4.3$ mm. A packed hexagonal arrangement with N_{row} rows and N_{col} filters in the odd rows accommodates a total of

$$N_{filters,max} = \frac{N_{row}+1}{2}\times N_{col} + \frac{N_{row}-1}{2}\times(N_{col}-1) = N_{row}N_{col} - \frac{N_{row}-1}{2}$$

filters. The optimum dimensions for the x-ray mask, taking into account the imaging plate area, historical (i.e., LWFA 3.0) x-ray pointing stability, the requirement for the mask to clear the electron signal, and other geometric criteria, was $w_{mask} = \sim 7\ cm$ and $h_{mask} = \sim 10\ cm$. For a packed hexagonal configuration, one can write

$$w_{mask} = N_{col}\times D_{filter} + (N_{col}-1)\times d_{gap}$$

$$h_{mask} = N_{row}\times D_{filter}$$

from which result $N_{col} = \frac{w_{mask}+d_{gap}}{D_{filter}+d_{gap}}$ and $N_{row} = \frac{h_{mask}}{D_{filter}}$. Plugging in above values for w_{mask}, d_{gap}, and D_{filter}, gives the value $N_{col} = Floor(12.73) = 12$ and $N_{row} = Floor(23.26) = 23$. Therefore for filter cavities of diameter 4.3 mm separated by gaps of 1.3 mm, the $7\ cm \times 10\ cm$ mask area is large enough to accommodate a packed hexagonal arrangement with $N_{row} = 23$ and $N_{col} = 12$. Therefore a total of 265 filter cavities were available for the placement of the Ross filters.

Positioning of Filters on the Mask

Two arrangements of Ross x-ray filters were used in the LWFA 4.0 experiment. The first, referred to as *Filter Configuration I*, was used for 2 weeks and assigned the filters using a semi-random placement algorithm which attempted to maximize the odds of filters in the same Ross pair being crossed by an iso-intensity contour by only accepting random assignments that placed sibling filters (belonging to same pair) in adjacent positions on the filter mask. It also took into account the observed variation in the x-ray position during the LWFA 3.0 experiment. The second arrangement of filters, referred to as *Filter Configuration II*, was used during the last week of the experiment (starting with shot 8349) and aimed at optimizing the arrangement of filters in order to match the observed shape and landing position of the x-ray beams up to that point in the experiment. Filters were assigned to the PEEK mask (Figure 5.20) in rounds. In each round, filters in all 7

pairs in Table 5-2 were sequentially assigned to a position (pocket) on the mask. The algorithm for the random assignment of filters on the mask, used in Filter Configuration I, first assigned the filter to a row on the mask by treating the selected row (i.e., the Y coordinate) as the realization of a uniform random variable; within that row, the algorithm assumed the position of the filter (i.e., the X coordinate) is another uniform random variable. There are 10 distinct (in element or thickness) filter types in Table 5-2 and a contour that crossed all 10 filters, would yield data for 7 different energy bins for the spectrum on that contour. However, since a fully random assignment of the filters is not optimal in maximizing the number of filters crossed, the following modifications were made to the random assignment:

- When assigning the first filter in a Ross pair (element A in Table 5-2) to a filter pocket on the PEEK mask, the random filter assignment was rejected (and repeated) if it was adjacent to a filter of same kind. This was meant to minimize the probability of multiple filters of the same type appearing near each other and then on the same contour.
- When assigning the second filter in a Ross pair (element A in Table 5-2) to a filter pocket on the PEEK mask, preference was given to the 6 pockets arranged hexagonally around the first filter in a Ross pair. This was meant to increase the probability that a contour would cross both filters in a Ross pair.
- In Filter Configuration I (Figure 5.21, left), element used in adjacent Ross pairs, e.g., Zr in pairs 2 and 3, were assigned separately for each pair in each round (each round sequentially assigned filters for 7 Ross pairs). As may be seen in Table 5-2, Zr was assigned once as element B of pair 2 (Zn + Zr) and again as element A of pair 3 (Zr + Mo). This had the consequence that those elements were assigned a higher weight for appearing on the mask and resulted in occasional over-representation of the reused filters on the mask but was intended to minimize the odds of two filter pairs dependent on this filter (neighboring energy bins) remaining incomplete as the result of the reused filter not appearing on the contour.

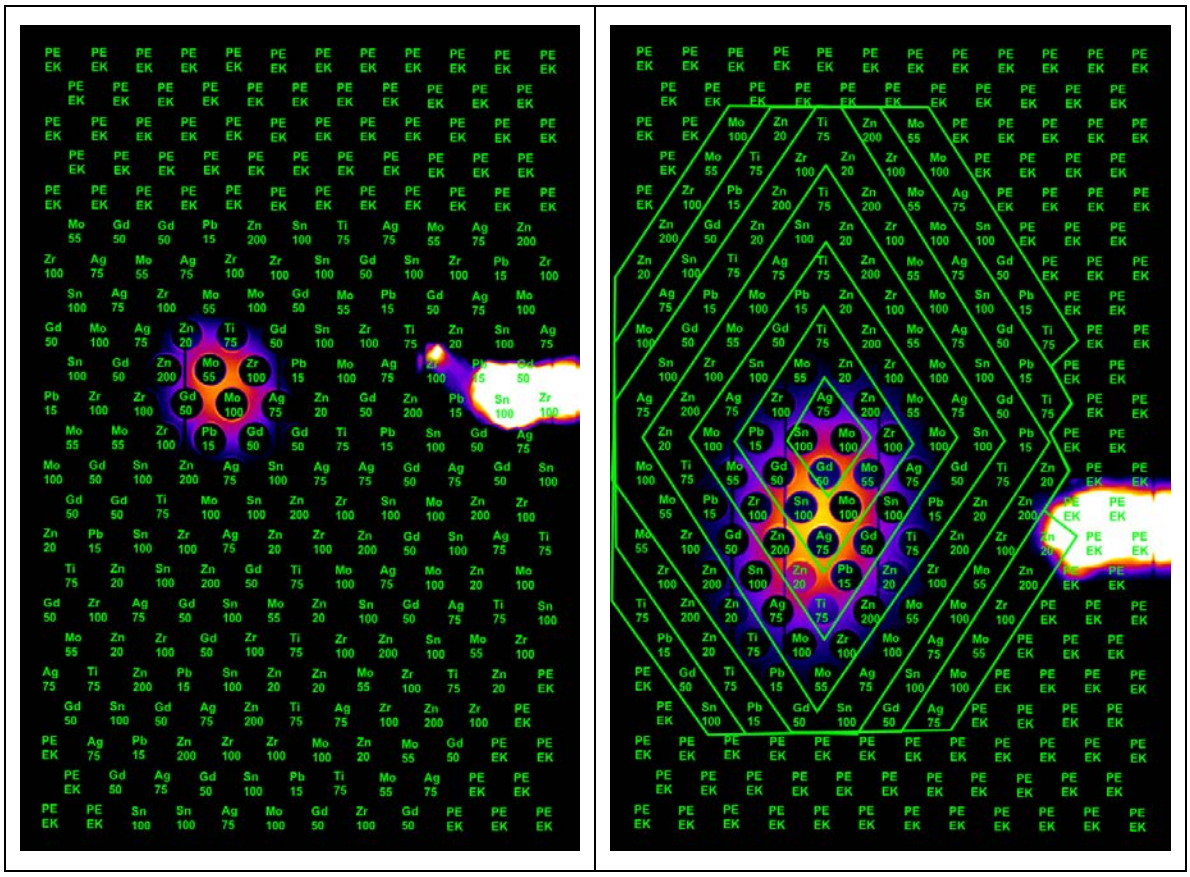

Figure 5.21: The two configurations used to position x-ray filters on the PEEK mask in LWFA 4.0. Left: semi-random filter arrangement (Filter Configuration I, here shown for shot 8292). Right: manual filter arrangement (Filter Configuration II, here shown for shot 8353). Only the pockets inside the diamond region were utilized for filters.

- As the pockets began to fill up, it could happen that no pockets were available for the assignment of element B in the hexagonal region round the A element of a filter pair. In such cases, the sibling pair was assigned to the first available location on the mask starting from the top-left corner and searching row-wise from the left.

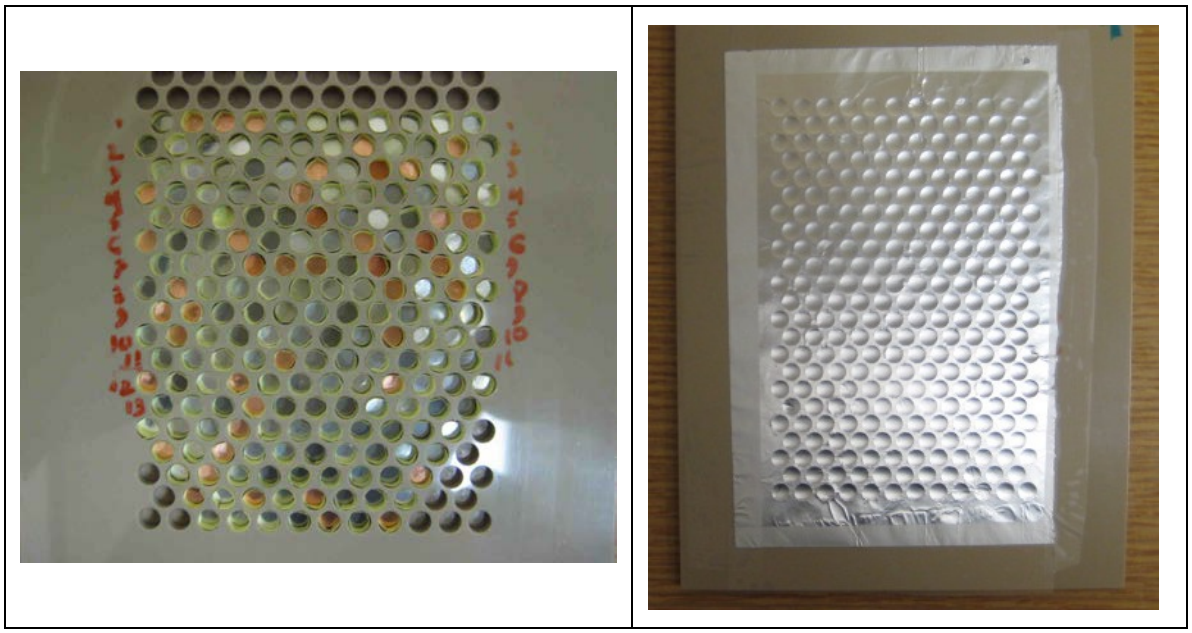

Figure 5.22: Left: x-ray filters arranged on the PEEK mask using Filter Configuration I (only 2 of the 5 unused rows in the top are shown). Right: x-ray filter mask covered with thin Al foil to make it light tight.

In Filter Configuration II (Figure 5.21, right), steps were taken to further optimize the filter arrangement on the mask. In order to reduce the odds of duplicate filters appearing on the same contour, the criterion for the weighting of the elements on the mask was changed such that all elements, instead of all filter pairs, had roughly the same odds of appearing on the mask. The pointing variability of x-ray beam up to that point in the experiment indicated a larger range for the Y coordinate of the x-ray landing position on the mask than in the previous round (LWFA 3.0). This was incorporated into the new filter arrangement; in addition, the regions of the mask where the x-ray beam had not landed (the corner regions, labeled with 'PEEK' in the figures) were excluded. To better accommodate the profile of the betatron x-rays, the random assignment approach was replaced with a manual placement of the 10 distinct filters into the Ross filter array in a clockwise arrangement (indicated by straight lines in the figure). This arrangement took the shape of the x-ray profile into account and yielded somewhat higher number of data points per contour but, as seen in the figure, was still susceptible to the pointing variability of the x-ray beam. Following the assignment of x-ray filters to positions on the PEEK mask, the filters were carefully placed in the assigned position (Figure 5.22) and kept in place with O-rings of material transparent to x-rays (vacuum-compatible paper), then the mask was covered with a thin (0.001") Al foil to make it tight to ambient light.

5.7 Methodology for Processing X-ray Data from GeV LPA

The scaling laws for the betatron radiation from mono-energetic electrons show the variation in the betatron radiation observables with the electron energy [45]:

$$N_{ph} \propto N_e N_\beta K \propto N_e N_\beta \sqrt{\gamma n_e} r_\beta \quad \text{Eq. 5.12}$$

$$\theta_r \propto K/\gamma \propto \sqrt{n_e}\, r_\beta / \sqrt{\gamma} \quad \text{Eq. 5.13}$$

$$\hbar\omega_c \propto \gamma^{1.5} \sqrt{n_e} K \propto \gamma^2 n_e r_\beta \quad \text{Eq. 5.14}$$

These scalings relate the number of photons N_{ph}, x-ray beam divergence θ_r, and x-ray critical energy $\hbar\omega_c$, to the number of electrons (i.e., charge) N_e, number of betatron oscillations N_β, relativistic gamma of the electron γ, plasma density n_e, and the betatron oscillation amplitude r_β. (These scaling are valid for the case where the electron energy does not change, i.e., no acceleration, but may be applied using the electron parameters at dephasing time.) These equations suggest, and it was empirically confirmed during the LPA experiments, that the spectrum of the betatron x-rays incident on a detector pixel changes with the position of the pixel. This is particularly the case for GeV LPAs due to the smaller divergence of the x-ray beam (Eq. 5.13), and the resulting larger variation of the spectrum from pixel to pixel on the detector. Therefore, in order to determine the differential x-ray attenuation for the two attenuators in a differential filter using non-adjacent pixels on the x-ray profile, the intensity of the incident radiation needs to be made commensurate for those pixels. One way of achieving this is by using an x-ray transmittance map created by dividing the measured and reconstructed signals [43]. Since the photo-stimulated luminescence (PSL) at a pixel on the same imaging plate detector is the convolution of the detector's energy-dependent sensitivity to x-rays [39], [44] and the incident x-ray spectrum, the use of a transmittance map to relate the signals at two non-contiguous pixels on the detector implicitly assumes that the spectra at the two pixels have the same shape and only differ by a factor. In fact, the shape of the betatron x-ray spectrum changes with its position on the detector. Another approach is to use a multi-channel x-ray spectrometer [46] consisting of multiple layers of filters sandwiched between imaging plates. By comparing PSL at same pixel position on different IPs (channels), this approach ensures that successive channels are measuring the same incident x-ray spectrum, albeit after passage through the non-sensitive layer of the

previous channels. However, multi-channel x-ray spectrometers using IPs present a number of difficulties. For one, since incident x-rays suffer scattering in the non-sensitive layers of the IP, GEANT4 simulation has to be employed to determine the required correction before the PSL on corresponding pixels on adjacent IP layers may be compared. Such modeling of the scattering requires precise knowledge of the IP material in order to determine the correction to be applied, and the determination of the x-rays scattering in the IP itself requires an a priori knowledge of the x-ray spectrum. Furthermore, the passage of x-rays through the non-sensitive layers of the IP absorbs a large fraction of the incident x-ray photons, a problem further compounded with increasing channel number, i.e., as more IP layers are traversed by the x-rays. This leads to unacceptably low S/N ratio with increasing channel number. In addition, the intensity of betatron x-rays in GeV LPAs is higher due to its scaling with $\sqrt{\gamma}$ and this can lead to saturations of the signal on the first imaging plate layer. Removal of saturation requires repeated scans of the IP and the determination of the extent to which signal has faded due to rescanning (see Appendix C.2), a procedure which introduces a statistical uncertainty into the calculation. In a layered multi-channel spectrometer where there is a one-to-one correspondence between the number of channels and IPs, channels other than the first (directly exposed to incident x-ray radiation) are unlikely to require rescanning (as a result of the signal reduction due to absorption in the non-sensitive parts of the channel one imaging plate) and this can introduce a systematic difference between the saturated first channel and the unsaturated remaining channels in the spectrometer which do not require a rescan. In contrast, using the method presented here, in the absence of detector saturation, the measurements for all spectrometer channels come from a single scan of the same IP. When there is detector saturation, data for all channels originate from the unsaturated scan of the IP, and are subsequently corrected to incorporate fading due to rescanning. In the latter scenario, all measurements are similarly corrected for signal fading due to rescan, lowering the probability of a systematic difference arising among the various channels.

In the sections that follow, the details of a methodology for the processing of single-shot x-ray measurement data from a GeV LPA are presented. This includes the reconstruction

of the x-ray profile from filtered x-ray data and its verification; as a preprocessing step for reconstruction, boundaries of x-ray filters and fiducial shadows are determined and pixels affected by the presence of filters or fiducials are removed. The creation of iso-intensity contours on the reconstructed x-ray profile image, and their use in the sampling of filter data are then discussed. A complication that may arise when the x-ray radiation dose is very high is the saturation of the PMT in the imaging plate scanner. In the presence of saturation, depending on the severity (i.e., whether it is minor and only affects off-filter pixels, or also affects on-filter pixels), reconstruction and/or sampling may have to be done on a subsequent unsaturated scan. When it is only the x-ray profile reconstruction that is performed on a subsequent unsaturated scan, contours that are iso-intensity on the unsaturated scan remain so on any previous scan and may still be used for their sampling. When the sampling of filter data is also performed on a subsequent scan, a saturation factor is calculated and applied to all filter measurements. The calculation of the saturation factor is described in Appendix C.2.

5.7.1 Reconstruction of the Filtered X-ray Beam Profile

The methodology for the spatially resolved spectroscopy of betatron x-rays presented in this dissertation requires the creation of iso-intensity contours on the reconstructed x-ray profile. A reconstruction algorithm was therefore developed and applied to the betatron x-ray beam profile to recover the full x-ray profile (i.e., without filters) on the IP detector. The important criterion for the image reconstruction algorithm was the preservation of thresholded regions. This is because iso-intensity contours correspond to the boundaries of thresholded regions on the reconstructed image. Figure 5.23 shows a typical x-ray image where, in the preprocessing step (a), pixels affected by the presence of filters (and fiducials) have been removed to leave behind only the x-ray signal directly incident on the imaging plate. In (b), the same image is shown following reconstruction, and in (c) the reconstructed image has been thresholded (shown in red) to about 50% of its peak intensity, with the boundary of the thresholded region (in green) designating an iso-intensity contour. Image (d) shows the pre-reconstruction x-ray profile, similarly thresholded as in image (c) and the same iso-intensity contour restored on the image. Because the reconstruction algorithm has preserved the intensity profile, nearly all pixels

inside the contour are thresholded pixels while few pixels outside it are. An adequately reconstructed x-ray image has 2 features:

- Average off-filter pixel value on the contour restored on the data image should be close to the contour's nominal value. This is because the reconstruction algorithm fills the gaps in the input image at the same time that it removes the random noise. If the image noise is white noise, the average off-filter, but on-contour, pixel value on the data image is expected to match the nominal contour value on the reconstructed image.
- On-filter, on-contour pixel values should have dispersion (e.g., standard deviation) smaller than the dispersion of pixel value on-filter as a whole (i.e., on- or off-contour). The reason for this, as will be explained below, is that filter data sampled on iso-intensity contours correspond to the same incident x-ray spectrum for all pixels on the contour.

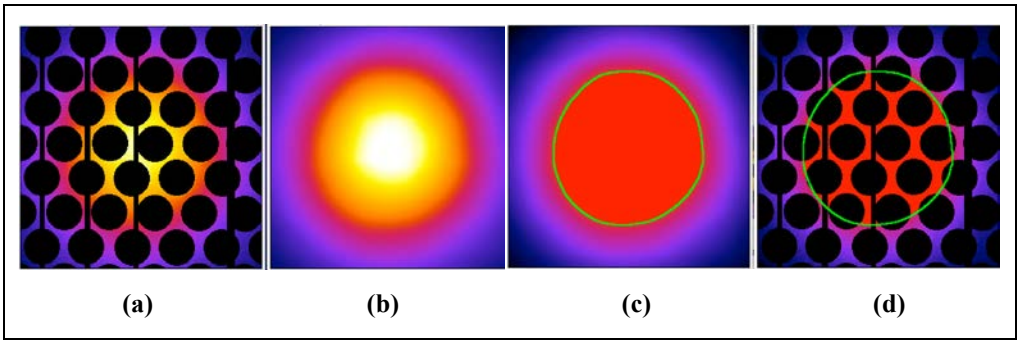

Figure 5.23: (a) Preprocessed x-ray profile used as input to the reconstruction algorithm, (b) reconstructed x-ray profile, (c) iso-intensity contour created on a thresholded reconstructed x-ray profile image, (d) same contour restored on similarly thresholded pre-reconstruction image (right).

The details of the reconstruction algorithm are provided in Appendix B.

5.7.2 The Iso-intensity Ansatz

As discussed, the small average FWHM of the x-ray (< 6 mrad), the relatively large variation in the pointing direction of the radiation cone axis during the experiment (up to 12 mrad), and the relatively low repetition rate of the TPW laser, made the use of x-ray CCDs and crystal spectrometers impractical, hence the decision to use a 7-bin Ross differential filter array arranged in a packed hexagonal configuration (Figure 5.24). A reconstruction algorithm was applied to the betatron x-ray image to recover the full profile (i.e., without filters); this permitted the drawing of iso-intensity contours (Figure

5.25) on the reconstructed image. ImageJ Wand Tool is used to draw iso-intensity contours on the thresholded images. These contours are routed between pixels having values smaller than and greater than the threshold value. The ansatz was adopted that such contours are constant spectrum contours. By sampling the x-ray filter data on contours (Figure 5.26) it was possible to perform single-shot spatially resolved measurements of the betatron radiation spectrum.

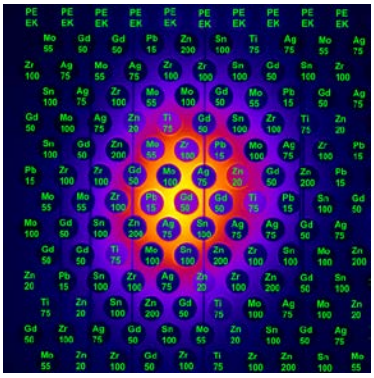

Figure 5.24: Ross filters used to detect the spectrum of betatron x-rays

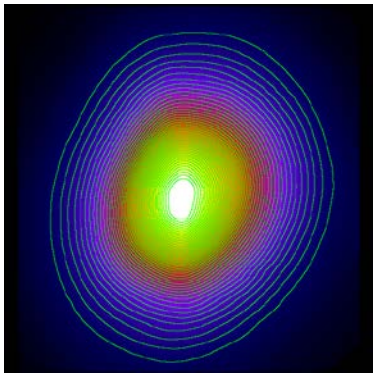

Figure 5.25: Iso-intensity contours produced on the reconstructed x-ray profile

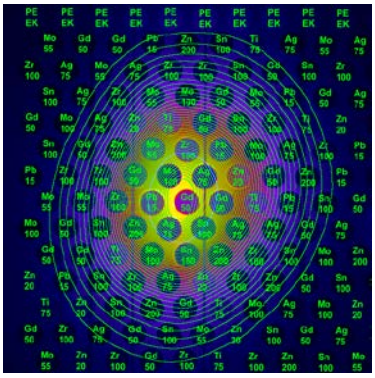

Figure 5.26: Iso-intensity contours overlaid on x-ray image to sample filter data

The reconstructed profile was used for the creation of iso-intensity contours (Figure 5.25); these were then overlaid on the raw (i.e., unreconstructed) image for the sampling of the detector data (Figure 5.26). The density of the iso-intensity contours is one of the factors determining the density of spectral data points used to reconstruct the spectrum N as a function of energy, E, and angles θ and ψ. Each pair of sibling filters crossed by an iso-intensity contour yields one spectral data point $N(E,\theta,\psi)$, where E is the midpoint of the energy bin designated by the K-edges of the filters in the pair; and θ and ψ are determined by the position of the pixels on the contour with respect to the position of the x-ray sources. When there is azimuthal symmetry, i.e., for circular contours, each contour crossing of a Ross pair yields spectral data points for $N(E,\theta)$ and $N(E,-\theta)$ with ψ taking all values in the range 0 to 2π. In the case of eccentric x-ray profiles, the assumption of $N(E,\theta) = N(E,-\theta)$ may still be applied to symmetrize, and therefore double the number of, the data points. In such cases, $\theta = \theta_{avg}$, where averaging is done

over all pixels on the contour. The standard deviation of θ is then used to express the error $\delta\theta$.

A dense set of contours does not guarantee a dense set of spectral data points, since it is the crossing of Ross pairs by contours that determine the spectral density, and this is determined by the position and shape of the x-ray spot on the detector, and the arrangement of filters on the mask; however a dense set of contours provides a larger set of angles for a given energy when the contour happens to intersect a pair of filters, therefore it is a necessary requirement. Contours were chosen to be as dense as possible taking into account the finite pixel resolution of the imaging plate. In practice, for a given shot, the maximum intensity (i.e., smallest) contours was chosen to have 95% of the maximum PSL of the image, and new contours were created around it in 1% decrements in intensity. Constant spectral resolution at different angles was maintained by enforcing regular spacing between the contours; this required the lowering of the contour decrement to 0.5% once the contour level had reached 1/3 of the maximum image PSL. When possible, contour intensity went as low as a few percent of the maximum. The limit to this was determined by the presence of the wakefield-accelerated electron signal on the same imaging plate would lead to the deformation of the iso-intensity contours. Spectral data sampled on deformed regions of iso-intensity contours were considered contaminated by the background electron signal and were excluded from analysis.

Denoting by $R(\hbar\omega)$ the IP response function (sensitivity) for x-rays, and by $S(\hbar\omega,\theta) = dN_\gamma(\hbar\omega,\theta)/d(\hbar\omega)$ the number of photons per unit energy per pixel, the PSL value at a pixel is obtained by evaluating the convolution integral $\int_0^\infty d(\hbar\omega)\, R(\hbar\omega) dN_\gamma/d(\hbar\omega)$. Assuming the same response function for all pixels on the IP detector, it follows from this integral that the most plausible reason for two pixels to have the same PSL is for the incident x-ray to have the same spectrum $\frac{dN_\gamma}{d(\hbar\omega)}$ at both pixels. Therefore the ansatz was adopted that contiguous detector pixels having same PSL are measuring the same x-ray spectrum, i.e., iso-intensity contours represent contours of constant spectrum. If pixels on the iso-intensity contour receive incident photons from the same spectrum, it is expected that measurements on the intersection of a filter and an iso-intensity contour be equal,

with any difference representing the random Poisson noise, the x-ray profile reconstruction error, and possible local variation in filter density. The small variance (< 3%) in the filtered x-ray measurements sampled on iso-intensity contours compared to measurements from the all areas of the same filter (> 7%), further validates the ansatz that iso-intensity contours designate contours of constant spectrum. By sampling the x-ray filter data on such contours (Figure 5.26) it was possible to perform single-shot measurements of the spectrum without the need for a transmittance map or multiple layers of IP. Selecting the dimension of the x-ray filters and their arrangement in order to maximize the number of differential filter pairs crossed by the iso-intensity contours, enhanced the number of spectral data points and made it possible to spatially resolve the x-ray spectrum on the full x-ray profile using a single-shot x-ray measurement.

5.7.3 Sampling of X-ray Data on Iso-intensity Contours

A number of steps are involved in sampling x-ray filters on a given iso-intensity contour. These steps can roughly be divided into 4 main groups:

I.	*Threshold reconstructed image at value corresponding to contour value*
II.	*Create iso-intensity contour on the reconstructed image*
III.	*Restore iso-intensity contour on the sampling image*
IV.	*Sample filters along the iso-intensity contour*

In this section, details of the final step are discussed.

Determination of the Filter Boundaries

In order to automate the sampling of the imaging plate x-ray measurements on iso-intensity contours, it was necessary to accurately determine the boundaries of individual filters on the imaging plate detector. For this purpose, x-ray image pixels were divided into 3 categories (Figure 5.27):

1. *Accepted X-ray Filter Data* pixels: referred to as *accepted*, this is the subset of pixels that could be used as attenuation data (i.e., recorded the x-ray signal after the passage of the x-rays through the full thickness of the filter);

2. *Rejected X-ray Filter Data* pixels: referred to as *rejected*, this is the subset of pixels that were affected by edge effects (e.g., those near the filter boundary where the filter edge is raised by the punching machine and the thickness differs from the spec);
3. *X-ray Profile Data* pixels: referred to as *profile*, this is the subset of pixels that were x-ray profile pixels (i.e., were unaffected by the filters); these pixels are external to those in subsets 1 and 2; they also exclude pixel affected by fiducial shadows.

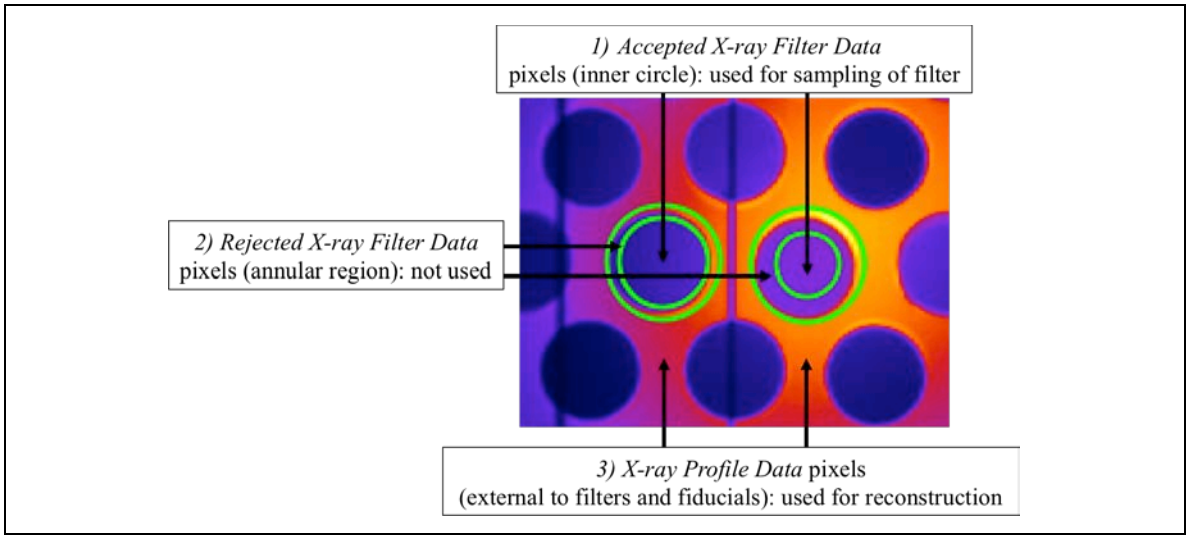

Figure 5.27: Division of x-ray image pixels into accepted, rejected, and profile pixel categories; filter on the left-hand side uses annular region of width 0.5 mm (5 MS IP pixels) to exclude boundary pixels; filter on the right-hand side uses annular region of width 1 mm and is more conservative.

It was necessary to determine the 3 pixel subsets above on every filter and for all shots that yielded x-ray data. This was a formidable task and a strategy, in 3 steps, was developed to tackle it based on dividing the shots that yielded x-ray data into two set based on whether they used Filter Configuration I or Filter Configuration II (see 5.6.2). In each case, a *Reference X-ray Shot* was chosen and the filter boundaries were carefully determined on the reference shot (Step 1). The adjustment of boundaries to work with non-reference shots required less effort. Boundaries on other shots were then determined by globally adjusting those on the corresponding reference shot (Step 2). In this manner, the most time-consuming task, careful determination of filter boundaries, was only done twice, i.e., once for each reference shot in Step 1. In Step 3, armed with boundary coordinate information for all filters in the x-ray image, it was possible to automatically determine the category (see Figure 5.27) to which that pixel belonged.

The chosen Reference X-ray Shots were shots 8320 and 8351 for Filter Configuration I and Filter Configuration II, respectively. These shot were selected based on the quality of the x-ray signal. Steps 1-3 are described are described below; the terminology for the (capitalized) names of images is defined in Appendix C, Table C-1.

Step 1. Filter Boundary Determination for Reference X-ray Shots

I. For each Reference X-ray Shot, open its Unsaturated PSL Image for X-rays, then process each filter by creating a circle of diameter 45 pixels around the filter (using ImageJ macro MakeCircleAroundFilter.ijm) and fine tune its position to completely contain the pixels subset 1 and 2 above;

II. add the circular selection from previous step to the ImageJ ROI Manager, and rename it “filter,row,col”, e.g., “Sn100,12,4”;

III. record the coordinates of the circular selection (using ImageJ macro GetSelectionCoordinates.ijm) and save to a file "boundaries - filter,row,col.txt" e.g., "boundaries - Sn100,12,4.txt";

IV. set the pixels inside the circles to *NaN* by using ImageJ *Process ➢ Math ➢ Macro...* and specifying *v=NaN*;

V. once all filter coordinates have been recorded, save all the selections in the ROI Manager to a file; this (.zip) file is referred to as the *Reference X-ray Shot Filter ROIs* and will be used for all other shots in the same set as the reference shot.

VI. once all filters have been processed, save the image to create the Unsaturated PSL Image for X-rays with Filters Removed for this reference shot.

The steps above were done carefully for individual filters for Reference X-ray Shots 8320 and 8351. Non-reference shots were then processed using the boundary information created for reference shots as follows:

Step 2. Filter Boundary Determination for Non-Reference X-ray Shots

I. for each shot, open its Unsaturated PSL Image for X-rays; determine its Reference X-ray Shot, and open its Reference X-ray Shot Filter ROIs;

II. use *More... ➢ OR (Combine)* functionality of the ROI Manager to combine individual ROIs into a single composite ROI; use arrows to shift the combined ROI until accepted and rejected pixels (categories 1 and 2 in image Figure 5.27)

for each filter are enclosed inside the corresponding ROI; record the horizontal and vertical shift, $(\Delta x, \Delta y)$, in pixels, required to achieve this;

III. update the coordinate of all filter ROIs in the ROI Manager by shifting them by an amount $(\Delta x, \Delta y)$. This has been implemented in the ImageJ macro RoiManagerMoveSelections.ijm. Once run, the updated filter ROIs are written to a (.zip) file referred to as the *X-ray Shot Filter ROIs* for the given shot;

VII. set the pixels inside the circles to *NaN* by using ImageJ *Process ➢ Math ➢ Macro...* and specifying *v=NaN*; save the image to create the Unsaturated PSL Image for X-rays with Filters Removed for this shot;

IV. write the updated boundaries for the filters to files "boundaries - filter,row,col.txt"; this is done by closing the ROI Manager, re-opening the Reference X-ray Shot Filter ROIs, and running the ImageJ macro RoiManagerUpdateBoundaryFiles.ijm.

Step 3. Determination of Pixel Type (Accepted, Rejected, Profile)

The steps described so far, determine the boundaries of all filters for all shots. Armed with this information, it is possible to trace along an iso-intensity contour and know when a particular filter has been crossed. However, as shown in Figure 5.27, not all pixels on a filter are useful as data. In particular, pixels near the boundary suffer from edge effects. The boundaries themselves correspond to the outer circle in the image which surrounds the 4.3 mm diameter cylindrical cavity machined into the PEEK mask for the placement of the 4.0 mm diameter x-ray filters; the boundaries were selected to have the slightly larger diameter of 4.5 mm to both encompass the filter area as well as include any leakage of light from the filter cavity (with a substrate thickness of only 10 mil) into the region external to the cavity. This was necessary because such leakage would affect the Reconstructed X-ray Image and lead to distortion of iso-intensity contours. To use the boundary files to sample of filtered x-ray measurements, it is therefore necessary to determine a margin inside the boundary in the form of an annular region; pixels inside this region would not contribute any data. A conservative margin was determined to be 1 mm, or 10 pixels on the MS IP. Note that this approach is different from the one taken for LWFA 3.0 x-ray data. There, the removal of filter pixels for the purpose of x-ray profile reconstruction was decoupled from the determination of filter boundaries for the purpose

of sampling. In LWFA 4.0, the sheer number of filters (up to 265 for Filter Configuration I) made the creation of separate ROIs for reconstruction and sampling onerous. Therefore the approach was adopted to create 4.5 mm boundaries suitable pixel removal (i.e., reconstruction), and then exclude a 1 mm annular region inside it and use the concentric region of diameter 3.5 mm for sampling. The advantage of this method is that it can be automated. Knowing filter boundary coordinates for all filters for a given shot, it is possible to trace pixels along any iso-intensity contour and programmatically determine at each point along a contour whether the pixel is an Accepted X-ray Filter Data pixel, Rejected X-ray Filter Data pixel, or an X-ray Profile pixel.

As described in 5.7.2, iso-intensity contours drawn by the Wand Tool in ImageJ, are created such that on one side of the contour are pixels having value greater than the threshold value and on the other side of the contour are pixels with value less than the threshold value. An answer to the question, "what is the value of the x-ray signal at a point on the contour", that is consistent with how contours are created, is one of the following:

1. (4-pixel Averaging Method) x-ray signal on a point on the contour is the value obtained by interpolation of the 4 pixels surrounding that point (known as the von Neumann Neighborhood)
2. (2-Pixel Averaging Method) x-ray signal on a point on the contour is the average of two neighboring pixels on either side of the contour

The 4-pixel averaging method (see Figure 5.28), uses the same 4 pixels, shown in gray, to calculate the x-ray signal at contour location (X,Y), independent of the contour direction. This method of signal sampling on a contour, requiring 4 data pixels for each contour pixel, is algorithmically somewhat easier to implement, but more likely to run into problems (i.e., missing data) near fiducial shadows, as well as the boundaries of the sampling region (inner circles in Figure 5.27).

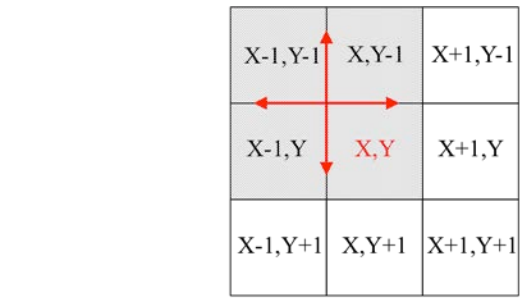

$$Z_{4PA}(X,Y) = 0.25 \times \{ Z(X\text{-}1,Y\text{-}1) + Z(X\text{-}1,Y) + Z(X,Y\text{-}1) + Z(X,Y) \}$$

Figure 5.28: 4-pixel averaging (4PA) method of calculating the x-ray signal Z at point (X,Y) on an iso-intensity contour, consistent with routing of contour between above- and below-threshold pixels. X-ray signal at location (X,Y) does not depend on contour direction.

In contrast, the 2-pixel averaging method, is directly related to how a contour is routed between pixels; therefore the creation of a contour and the sampling on a contour are consistent with one another. In addition, since it requires only 2 data pixels for each contour pixel, it is more likely to yield a valid data point as fewer pixels are required to stay clear of the fiducial shadows or filter boundaries.

To demonstrate the 2-pixel averaging method, in Figure 5.29, the pixel with coordinates (X,Y) is the pixel on the iso-intensity contour for which the x-ray signal is being calculated. Note that the default coordinate system in ImageJ assigns (0,0) to the top left corner of the image. The pixel at this location is pixel (0,0). With 2-pixel averaging, at pixel (X,Y) on the contour, the target pixels to be averaged depend on the position of the next pixel on the contour. There are 4 cases and the target pixels used for 2-pixel averaging, shown in gray, are different in each case. For example, the top-left image shows the contour going from pixel (X,Y) to pixel (X,Y+1), where coordinates refer to the top-left corner of the pixel. Since the contour segment was routed between pixels (X,Y) and (X-1,Y), the x-ray signal Z at pixel (X,Y) is the average of x-ray-signals Z(X,Y) and Z(X-1,Y). Similarly, in the other 3 cases, the x-ray signal is calculated as the average signals adjacent to the contour and shown in gray). Note that in 2 of the cases, x-ray signal at point (X,Y) does not depend on Z(X,Y).

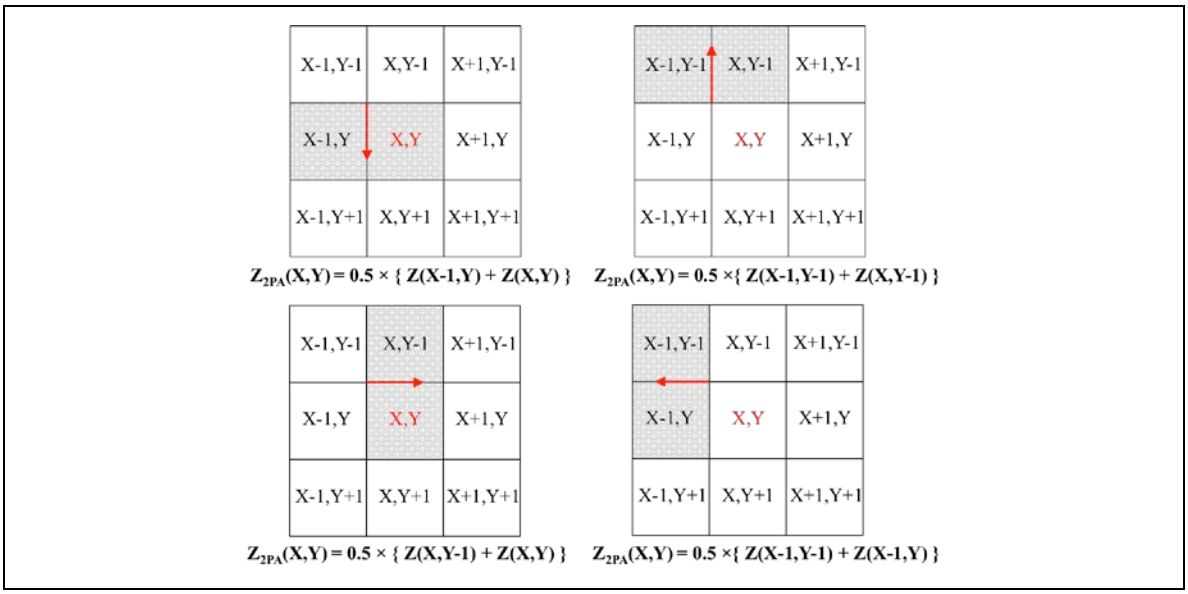

Figure 5.29: 2-pixel averaging (2PA) method of calculating the x-ray signal Z at point (X,Y) on an iso-intensity contour, consistent with routing of contour between above- and below-threshold pixels. X-ray signal at location (X,Y) depends on the direction of contour at (X,Y).

For the x-ray spectra presented in this dissertation, sampling of x-ray data on iso-intensity contours used the 2-pixel averaging method.

In order to combine the 2-pixel averaging method of x-ray data sampling on an iso-intensity contour with the previous categorization of x-ray image pixels into the 3 categories of accepted, rejected, and profile pixel (Figure 5.27), the two target pixels were considered as accepted pixel for a given filter on the Sampling Image only when they were completely inside the 2.5 mm diameter sampling circle concentric with the 4.5 mm boundary circle determined for that filter (see **Determination of the Filter Boundaries**). Partially contained pixels were rejected. Any pixels that were fully or partially within the 1.0 mm wide annular region external to the sampling circle, were rejected. All pixels on the Sampling Image that were neither accepted nor rejected filter data pixels, were categorized as profile pixels. The average value of the profile pixels on a contour was compared to the nominal contour value on the Reconstructed X-ray Image. The average value was typically within 1-2% of the nominal contour value; this was an indication that iso-intensity contours created on a Reconstructed X-ray Image were valid for use on the Sampling Image.

5.7.4 Analysis of the Sampled X-ray Data

Since iso-intensity contours were assumed to be iso-spectral, it followed that points on the spectrum could self-consistently be calculated using x-ray filter measurements only when those measurements were done on the same contour. However, since not all 7 bins in the Ross filter array yield data on most contours, there are fewer than 7 data points available for most contours; this is especially the case for the smaller contours, i.e., those closer to the peak intensity on the detector. Therefore, a representation of the spectrum as a function of the energy alone doesn't work well for most contours, at the same time that it hides the angular dependence of the spectrum, making a comparison of spectra for different shots also difficult. The data is less sparse with respect to changes in the contour size; this is because contours can be drawn tightly as long as they are separated by ~2 pixels (limit set by the resolution of the IP and the read-out system). A 3D representation of the spectrum therefore provides a denser set of data to constrain a smooth surface.

Angular Dependence of X-ray Spectra

In the general case of x-ray profiles not having azimuthal symmetry, each pixel on a contour could be assigned a pair of angles (θ, ψ). The polar angle θ is the angle between the line joining the x-ray source to the position of that pixel on the detector and the line joining the x-ray source perpendicularly to the detector (assumed to be the maximum intensity position on the x-ray profile on the detector and the x-ray center). The azimuthal angle ψ is measured with respect to the horizontal and vertical lines crossing at the x-ray center. For a hypothetical circular contour, the polar angle θ would vary from 0 (forward direction) to a maximum value determined by the size of the detector and the position of the x-ray on the detector. (This changed from shot to shot). The azimuthal angle ψ would change from 0 to 2π. On an iso-intensity contour, θ would remain fixed and ψ would change from 0 to 2π. In fact, iso-intensity contours always have non-zero eccentricity and in some cases are significantly elongated along one axis, which is not necessarily horizontal or vertical on the detector. This means that to replace the contour dependence of the spectrum on the contour value *C*, one would need to add dependence on both θ and ψ:

$$S(E, C) = S(E, \theta, \psi)$$

To determine the pair (θ, ψ) for a contour pixel on an iso-intensity contour, one needs

1. i_{pixel}, j_{pixel}: coordinates of the pixel on the contour
2. i_{XC}, j_{XC}: coordinates of the x-ray center on the detector
3. $d_{source-IP}$: perpendicular distance from the x-ray source to the x-ray center

Using the coordinates of the contour pixel and x-ray center, the distance between the two is simply $d_{pixel-XC} = \sqrt{\left(i_{pixel} - i_{XC}\right)^2 + \left(j_{pixel} - j_{XC}\right)^2}$; (θ, ψ) are calculated as

$$\theta = \tan^{-1} \frac{d_{pixel-XC}}{d_{source-IP}}$$

$$\psi = \sin^{-1} \frac{-(j_{pixel} - j_{XC})}{d_{pixel-XC}}$$

Eq. 5.15

Having calculated the spectrum on an iso-intensity contour, and knowing (i_{pixel}, j_{pixel}) for all pixels on the contour, (θ, ψ) for all pixels on the contour may be computed. For a contour C_0 with N_{C_0} pixels, each point on the spectrum $S(E, C_0)$ is replaced by N_{C_0} points on the spectrum $S(E, \theta_{C_0}, \psi_{C_0})$. Note that all pixel coordinates in these equations refer to the default coordinate system used by ImageJ, where point (0,0) is the top-left corner of the image, hence the negative sign in the formula for ψ.

Spectral Reconstruction

One of the differences between the stacked IP method of x-ray spectroscopy and the method presented in this dissertation is that in the former, the points on the spectrum at higher energies are recovered from the inner layers on the IP stack (i.e., higher channel number) and have therefore larger error bars because scattering from multiple layers of the non-sensitive layers of the IP must be taken into account. In the present method, filters are randomly distributed on the IP and a point on the spectrum at a given energy can be contributed by any contour; the corresponding angle θ, however, will be determined by the size of the contour; larger contours correspond to larger angles. Larger contours are, however, likely to cross more Ross filter pairs, due to their larger perimeters and the random placement of the filters on the mask; therefore the density of spectrum data points along the energy axis tends to increase as the contour size increases. The

maximum possible number of energy data points that a given contour may contribute to the spectrum equals the number of energy bins in the Ross filter, in this case 7. Therefore, a given circular contour corresponding to angle θ may contribute up to 7 points $S(E_i, \theta)$, $i = 1, \cdots, 7$, where E_i is assigned to the midpoints of the energy bin for Ross pair i crossed by contour at angle θ. Due to azimuthal symmetry, there are additional data points $S(E_i, -\theta) = S(E_i, \theta)$; therefore one contour may contribute up to 14 data points to the spectrum. Even though the signal-to-noise ratio decreases with the contour intensity, a larger contour is more likely to produce a larger sample of pixel data and correspondingly smaller standard error of the mean because a large contour may cross a filter of given type, designated by its K-edge energy, at several places on the contour. When this happens, all the pixels are pooled to create a larger sample, which is then used to calculate the average and the standard error. Figure 5.30 shows a typical spatially resolved spectrum for the betatron x-ray radiation from the GeV LPA. This image was obtained after applying interpolation to the spectral data calculated using the relation

$$S_{avg}(E_k \le E \le E_{k+1}) = \left(\frac{dN}{dE}\right)_{avg} [photons/keV/sr] = \frac{\Delta PSL}{C \int_{E_k}^{E_{k+1}} R(E)(T_k(E) - T_{k+1}(E))dE} \quad \textbf{Eq. 5.16}$$

where S_{avg} is the average number of photons per unit energy per pixel for energies in the bin bounded by energies E_k and E_{k+1} in the residual sensitivity function, $R(E)(T_k(E) - T_{k+1}(E))$, of the Ross filter. $R(E)$ is the response function of the detector (imaging plate), $T_k(E)$ and $T_{k+1}(E)$ are the transmission functions for the two filters in the Ross pair having K-edge at energies E_k and E_{k+1}, ΔPSL is the differential reading of the detector (imaging plate) for the filters in that pair, and C is a geometric factor. Since detector data were sampled on iso-intensity contours, the resulting S_{avg} calculated according to Eq. 5.16 is specific to that contour. (Inner contours, representing x-ray radiated in the forward direction, correspond to small radiation cone angle θ.) Conversion between contour level and angle, required to produce Figure 5.30, is straightforward for contours with eccentricity of 0, i.e., circular contours. In practice, many of the x-ray profiles, and their iso-intensity contours, had non-zero eccentricity. In such cases, the

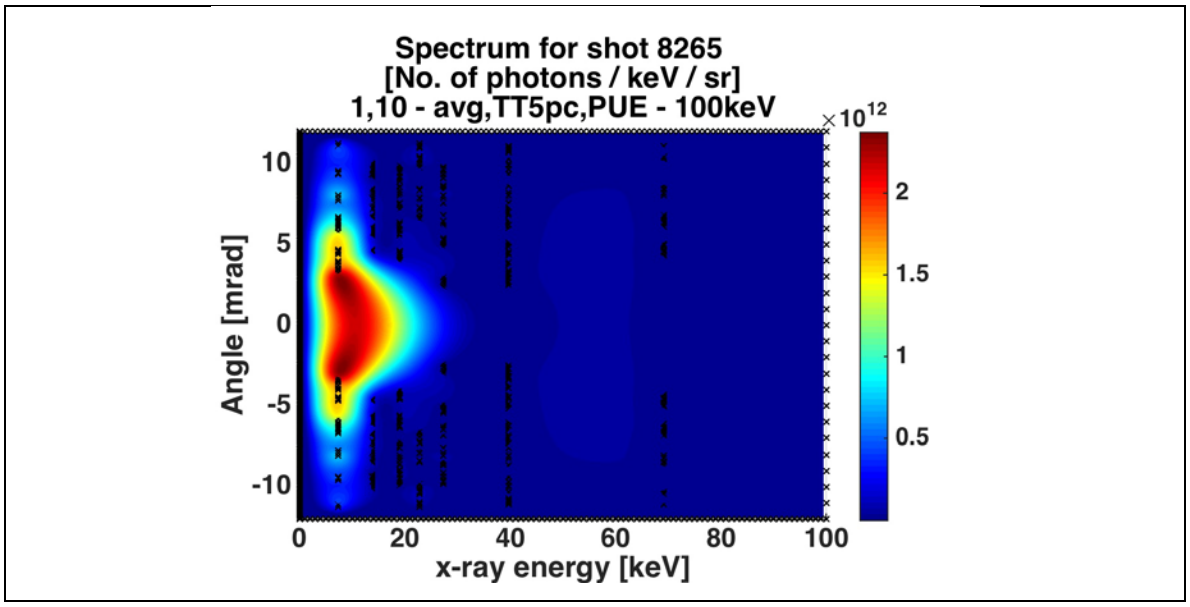

Figure 5.30: Spatially-resolved spectrum for the betatron x-ray radiation from the GeV LPA

spectrum acquires an azimuthal dependence, requiring a 4-D representation of S_{avg} vs. θ, ψ, and E. In the case of circular contours, however, each contour, depending on its angle θ and the position of the x-ray spot on the intersection of all contours with the x-ray data together yield values for $S(E_i, \theta)$ for different values of θ ranging from 0 (for radiation on axis) to a maximum value determined by the position of the x-ray spot on the detector and typically ~10-12 mrad. (Note that the detector spans 10 mrad on either side of the line joining the its center to the gas cell.) Due to the azimuthal symmetry of circular contours, for each spectral data point $S(E_i, \theta)$, there is another data point $S(E_i, -\theta) = S(E_i, \theta)$, effectively doubling the number of data points. For the x-ray results considered for this paper, this yielded between 128 (most sparse) to 411 (least sparse) points on the spectrum $S(E, \theta)$.

To reconstruct the spectrum in 3 dimensions on a 2D regular grid of energy and angle (θ), the spectral data points calculated according to Eq. 4 were interpolated. Several interpolation techniques were considered. Given the number of data points, algorithms such as cubic spline and biharmonic spline interpolation [47], which minimize curvature and produce a surface reproducing all data points, are easily applicable. Biharmonic spline interpolation has the advantage over cubic spline that it is not triangulation-based

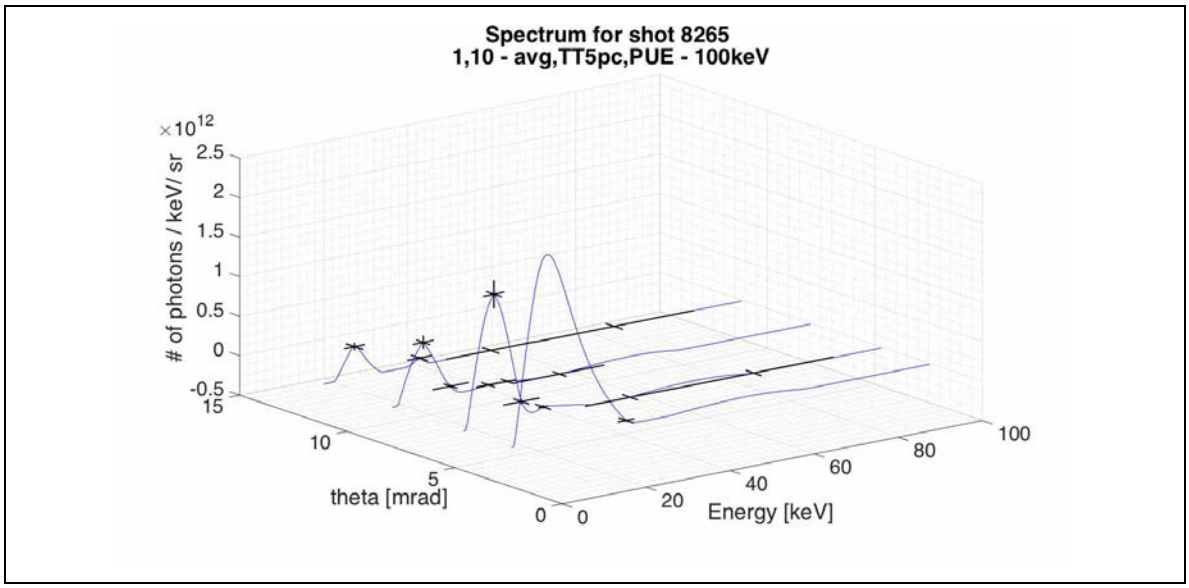

Figure 5.31: Data points, their errors, and corresponding fits, for several contours for each of the spectra in **Figure 5.30**.

[48], hence does not exclude grid points outside the convex hull of the (irregularly spaced) data points. Instead, it is a distance-based method, i.e., it determines a single radially symmetric Green function around every data point. It calculates a linear combination of these basis functions, by formulating and solving a linear system of equations, one for each data point. While this makes biharmonic spline interpolation computationally unsuitable for x-ray profile reconstruction (see Appendix B for discussion), it can readily handle the number of spectral data points (> 100 and < 500). It also tends to bridge over gaps in the data if the gap separates symmetric regions of data. This clearly applies to the x-ray data analyzed in this dissertation, where in the case of iso-intensity contours corresponding to small θ, the contours closest to the axis yield few, if any, data points, and for circular contours a contour crossing a filter yields a data point for θ and $-\theta$. It was decided therefore to reconstruct the spectrum in 3D using biharmonic spline interpolation.

Statistical Analysis of the X-ray Data

The x-ray spectrum has an error that, depending on the x-ray image, contour level, and other factors, is 10-40%; therefore an exact fit to the data, as is done by an interpolant, can be restrictive. To reduce the error, factors contributing to the spectrum error were analyzed. One source of error is from the statistical distribution of pixel values along iso-

intensity contours. As discussed in Appendix F.1, this component scales as $1/\sqrt{n}$, where *n* is the sample size (number of pixels on the intersection of an iso-intensity contour and a filter) and is typically the smallest component of the total error. The other source of error is from the background signal for the x-ray data; the background has a component that is the radiation created whenever there is ablation of the gas cell entrance aperture by the laser; this background is homogeneous on the x-ray filters and cancels whenever pairs of filter measurements are differenced, as is the case for differential or Ross filters. Another source of background signal is the high-energy tip of the magnetically deflected electron signal; this background is not homogeneous, impacts larger contours, and does not necessarily cancel when filter measurements are differenced. This is because the two filters in a pair can be on different regions of a contour, one closer to the electron signal and affected by it, another farther from the electron signal and unaffected. Filter measurements impacted by the high-energy electron signal were identified and excluded from calculations. Another source of error is the imperfect reconstruction of the x-ray profile (possibly due to residual electron background), which leads to small local deformities in the iso-intensity contours. Sources of outliers in the sampled filter data are pixels affected by local deformities in the iso-intensity contours and/or affected by residual background signal. A statistical outlier detection algorithm (Thompson's Tau [49]) was applied to detect possible systematic outliers and exclude them from the data using a 95% confidence interval. This reduced the spectrum error to 10-20% in most cases. To illustrate the impact of the error bars on the interpolation of spectrum data in 3D, Figure 5.31 shows the same spectra as in Figure 5.30 but for selected contours, displaying the data points produced by those contours, their error bars, as well as the portion of the 3D interpolated spectrum passing those data points. In most cases, in particular at energies below 35 keV, the features of the reconstructed spectrum are robust to variations in the data points commensurate with the error bars.

This chapter presented a complete methodology for the spectroscopy of x-rays from GeV LPAs and the analysis of the measurement data. In the next chapter, the results from the 4 rounds of experiments covered by this dissertation will be presented and discussed.

Chapter 6 Experimental Results

6.1 Introduction and Overview

In this chapter, the experimental results from 4 rounds of laser-wakefield acceleration experiments that the author participated in are presented. These took place in the periods of 11/11/2011-12/02/2011 (Round 1), 04/17/2012-05/06/2012 (Round 2), 01/14/2013-02/15/2013 (Round 3), and 04/28/2014-05/30/2014 (Round 4). The insights acquired during each round were applied in the one that followed; these led to enhancements in diagnostics, peak electron energy, and reproducibility. To highlight this progression, the experiments, and the main results, are presented chronologically. In each case, a selection of the measurements for the accelerated electrons and the betatron x-rays, and when available, a discussion of the simulation results, will be presented.

The 4th round of experiments provided the richest set of measurements for the x-ray beam observables (spatially resolved spectrum, divergence, photon number, and critical energy), making it possible to use these, together with the electron beam charge, to compute effective values for parameters that characterize the GeV LPA, i.e., the electron energy, its oscillation amplitude, and the number of oscillations, and then to investigate their mutual consistency. This analysis is shown in the final section of this chapter.

The experiments were conducted using the TPW laser [50] which has a repetition rate of about ~6 shots per day. The ~100 J, 150 fs laser pulse was focused using an f/47 optics onto the entrance aperture of a gas cell filled with helium (initially doped, later undoped) to a density in the range $1–6 \times 10^{17}$ cm^{-3}, and providing a maximum acceleration distance of 10 cm. The laser-wakefield acceleration took place in the highly nonlinear blowout or "bubble" regime [13]–[15], in which the laser-plasma interaction is sufficiently strong to produce full plasma cavitation. The self-injected accelerated electrons emerging from the exit aperture of the gas cell passed through a magnetic spectrometer comprised of a 1.1 T magnet and two racks of tungsten fiducials to permit a deconvolution of electron energy and its launch angle [31]. The laser pulse itself was optically deflected into a beam dump and the magnetically deflected electrons and undeflected x-ray emerging from the gas

cell were detected on a high-sensitivity imaging plate detector 2.7 m downstream from the gas cell.

In the initial two rounds of laser-wakefield experiments covered by this dissertation, diagnostics for the spectroscopy of x-rays were not deployed. Information on betatron x-rays is therefore limited to photon number and FWHM for the x-ray data from those experiments. In the following rounds, spectroscopy of x-rays was performed using differential or Ross filters; these were placed in the path of the x-rays just prior to reaching the imaging plate. The accelerated electrons, having been deflected in the magnetic field, largely cleared these filters. In the 3rd round, x-ray spectroscopy was performed by means of differential filters (discussed in detail elsewhere in this work). To determine the spectrum from filter data, an integral equation is to be solved. The usual approach is to assume that the *residual sensitivity* for each pair of filters (i.e., response of adjacent filters, differenced, and multiplied by detector sensitivity) is narrow (i.e., approximating a delta function) in order to solve the integral. As shown in Figure 5.11 of Chapter 5.4, this assumption is not always accurate. The large FWHM of the residual sensitivity curves therefore determined the error in energy (i.e., horizontal error bars). In addition, the lowest x-ray energy that could be measured was limited by the thickness of the IP protective layer (12 mil Al) which produces attenuation of $> 50\%$ for x-ray with energies $\lesssim 14.5$ keV, before taking into account the attenuation produced by the laser beam deflector. It was found that by calculating the x-ray spectrum using the differential filtering technique, then using it as a the 'guess' spectrum input in spectroscopy using maximum entropy methods [51], better results could be obtained. (This approach was investigated and found to hold great promise for future work, discussed in Chapter 7.) The x-ray filter design did not take x-ray profile reconstruction into account and required considerable effort. The intersection of filters and iso-intensity contours was also not well thought out. In the 4th round, to decrease uncertainty in energy, a switch was made to Ross filters [52] by selecting pairs of adjacent elements from the periodic table (i.e., Z differs by 1), then selected material types and thicknesses to yield residual sensitivities with narrow FWHM and flat if possible, extending to ~100 keV. The 12-mi IP cover was replaced with one using a polymer layer in the x-ray region, to extend the lower range of

spectrum energies to < 10 keV. The configuration of the filters was optimized for x-ray profile reconstruction, and its geometry was optimized to maximize coverage by iso-intensity contours.

6.2 1st Experimental Round ("LWFA 1.5")

The first laser-wakefield experiment the author participated in (Nov. 2011), followed an earlier initial experiment driven by the TPW laser, in Jan. 2011. That first attempt to accelerate electrons in a petawatt laser-driven plasma accelerator was successful is producing self-injected, collimated (8 mrad divergence), 600 pC bunch of electrons with energies up to 350 MeV in a plasma of density $n_e = 10^{17}$ cm^{-3}, which was an order of magnitude lower than in previous self-injected laser-plasma accelerators [53]. However, the experiment consisted of 20 shots of which only 1 produced electrons. The relatively poor results were attributed to the existence of multiple hot spots in the far field of the laser profile, and to the longer than optimal (i.e., ~150 fs) pulse durations. Radiochromic film and ICT had been used for electron diagnostics, and there was some disparity between their charge measurements, possibly attributable to EMP affecting the ICT measurements. The next experiment [54], conducted from 11/11/2011 to 12/02/2011, followed the introduction of adaptive optics, in the form of the deformable mirror, into the TPW laser system; this led to significantly improved laser profile. In addition, we began the doping of the helium gas with nitrogen in order to induce ionization-induced injection. To improve diagnostic sensitivity, the RCF was replaced with high sensitivity (MS) imaging plates. An EJ-260 (green) plastic scintillator, imaged using a Basler scA640-70fm (mono) CCD, was used as a real-time diagnostic for the presence of high-energy electrons. The experiment produced self-injected, dark current free quasi-monoenergetic ($\Delta E \approx 0.1$ GeV) electrons accelerated to > 1 GeV (1.25 GeV max). Mismatched propagation, where the laser intensity remains high enough for ionization injection only during the initial portion of its propagation through the plasma, is believed to have led to localized injection. The electron beam was collimated down to 0.25 mrad FWHM divergence. This was an order of magnitude lower than the 2.3 mrad previously reported for 0.5 GeV electron beam [10]. The pointing stability was less than 2 mrad. The experiment produced a typical charge of 10 pC per shot, and minimal betatron radiation.

Simulation of Laser-Plasma Interaction

In order to improve the results obtained in the initial laser-wakefield experiment, it was decided to introduce ionization-induced injection. Simulations using laser pulse parameters from the previous experiment showed that, for a plasma of density $n_e = 5 \times 10^{17}$ cm^{-3}, relativistic self-focusing would occur leading to the on-axis the peak intensity to exceed the level required for ionization-induced injection to take place. The condition for the trapping of electrons from ionization-induced injection to occur, $\Delta\Psi \lesssim -1$ [55], where Ψ is the normalized on-axis wake potential, would also be satisfied (Figure 6.1). Figure 6.2 shows the simulation results using the laser parameters from a representative shot in the initial experiment (shot 1943). At a plasma density $n_e = 5 \times 10^{17}$ cm^{-3}, a laser pulse of peak power ~0.16 PW (31.9 J/197 fs) (exceeding the critical power 0.038 PW required at this density, see Eq. 2.8) would relativistically self

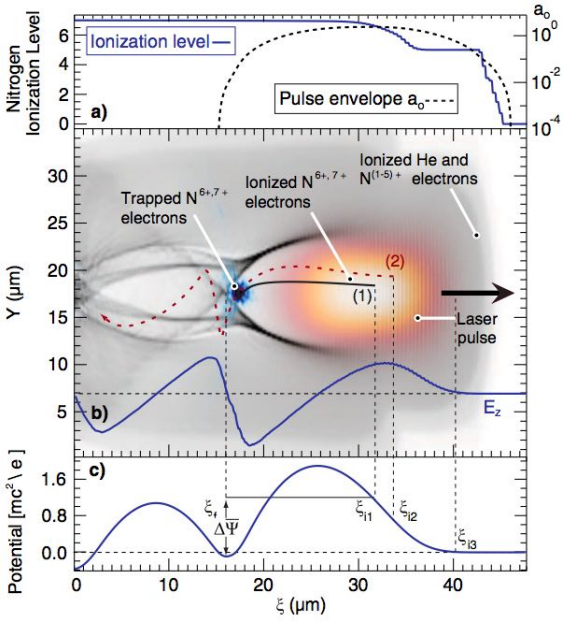

Figure 6.1: Condition for the trapping of ionization-induced injected electron, $\Delta\Psi \lesssim$ -1, where Ψ is the normalized on-axis wake potential [55].

focus within 1 cm of propagation into the plasma, and acquire a greater than ten-fold increase in the on-axis intensity to 2×10^{19} W/cm^{-2}, large enough to ionize the inner-

shell electrons of the impurity atoms (nitrogen). Since this intensity would only be maintained for < 0.5 cm, electron injection would be localized, a requirement for the

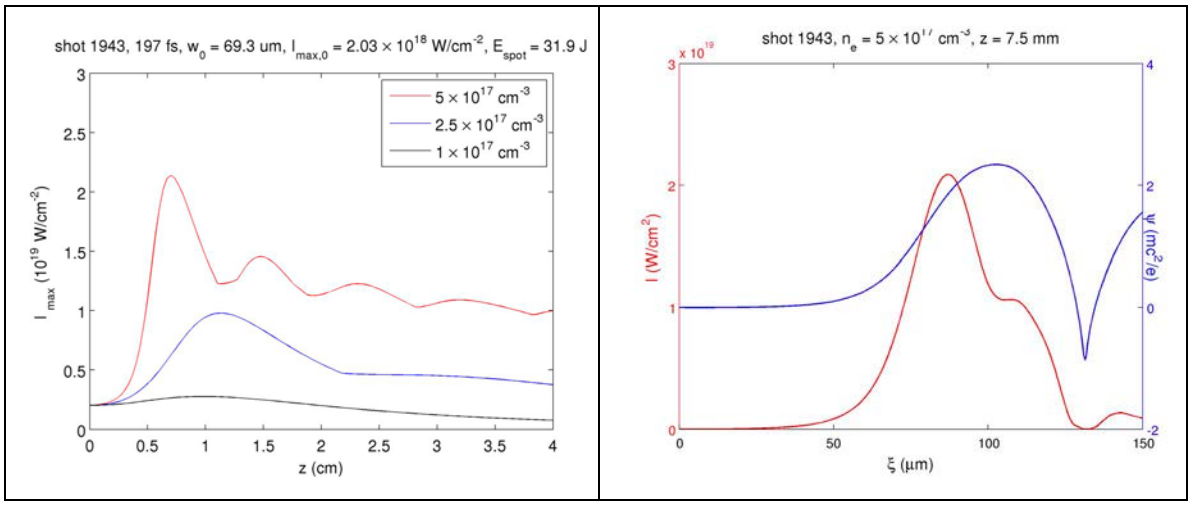

Figure 6.2: Simulation showed that for plasma density $n_e = 5 \times 10^{17}$ cm^{-3}, relativistic self-focusing would create the conditions required for the ionization-induced injection of electrons (left), and for the trapping of these electrons (right), to occur. [Image courtesy of Austin Yi]

production of quasi-monoenergetic electrons. The change in the normalized on-axis wake potential would be $\Delta\Psi \approx -3$, sufficient for trapping of the electrons. The pulse would also remain undepleted more than 5 cm into the plasma (Figure 6.3). Note that the dephasing length at $n_e = 5 \times 10^{17}$ cm^{-3} is ~95 cm (see Table 2-1).

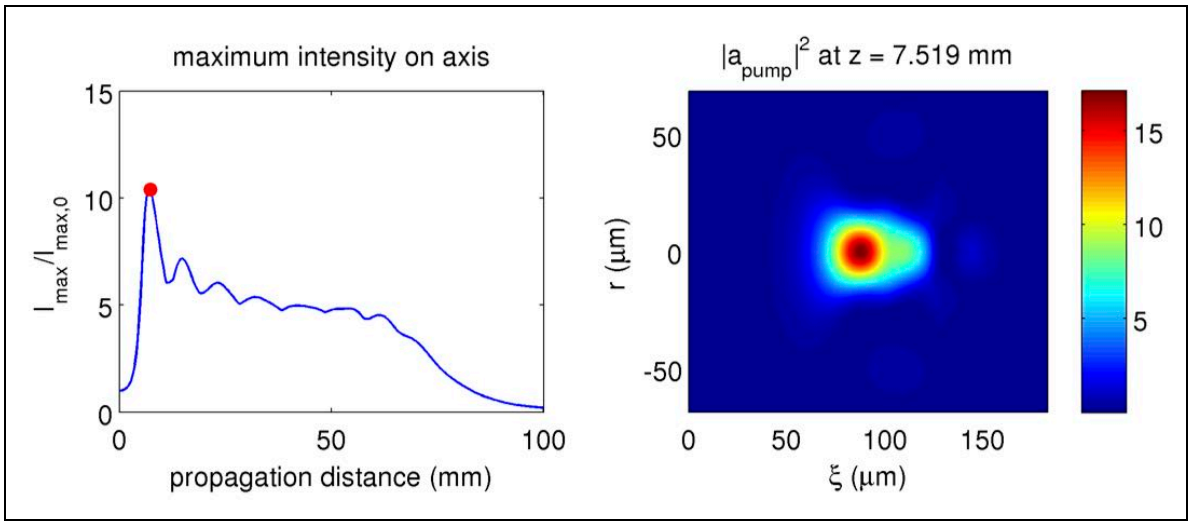

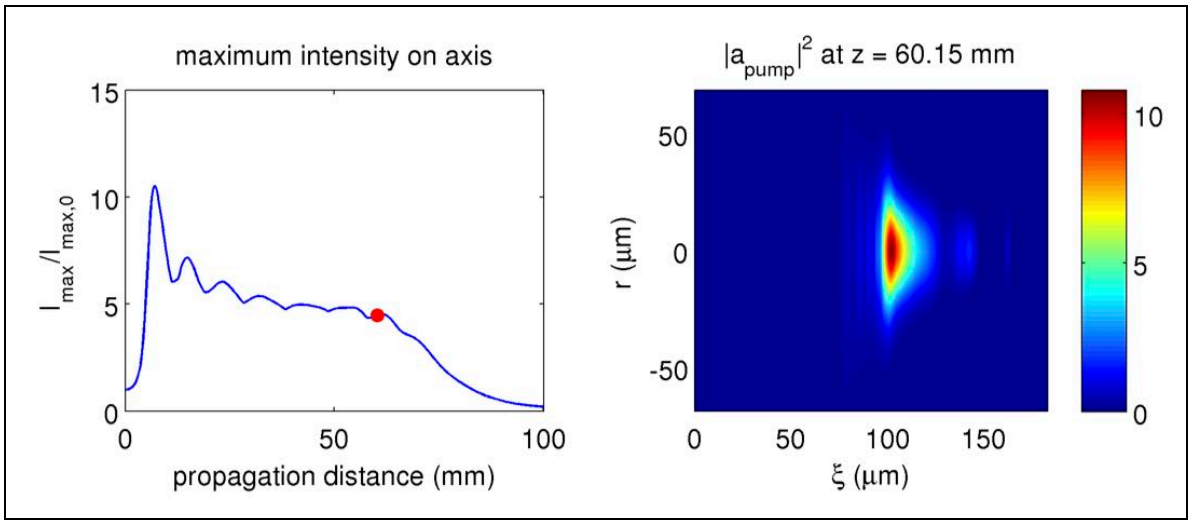

Figure 6.3: Simulation showing that the laser pulse in **Figure 6.2** would remain undepleted more than 5 cm into a plasma of density $n_e = 5 \times 10^{17}$ cm^{-3}. [Image courtesy of Austin Yi]

Simulations indicated that the pulse duration would be an important parameter. Figure 6.4 shows that for a longer laser pulse (360 fs) having peak power of 0.042 PW (barely exceeding the critical power for self-focusing), relativistic self-focusing would not be sufficient for the peak (on-axis) intensity to reach the 2×10^{19} W/cm^{-2} threshold required for the ionization-induced injection.

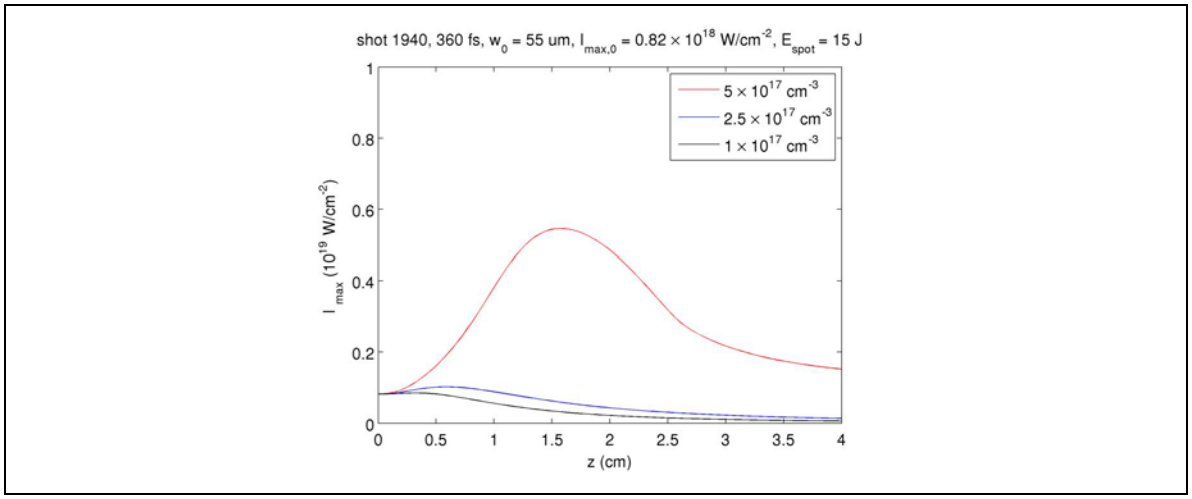

Figure 6.4: Simulation showing that relativistic self-focusing is not sufficient for pulse of duration 360 fs (peak power 0.042 PW) to achieve the ionization-induced injection threshold for plasma densities as high as $n_e = 5 \times 10^{17}$ cm^{-3}. [Image courtesy of Austin Yi]

Experimental Setup

The setup used in the LWFA 1.5 experiment is shown in Figure 6.5. The electron diagnostics consisted of an ICT in the interaction chamber; a 10 cm × 10 cm high-

sensitivity imaging plate (MS IP) in the small diagnostic chamber (closer to the interaction chamber), for the detection of low-energy electrons (100-200 MeV); a 40 cm × 20 cm high-sensitivity imaging plate in the larger diagnostic chamber for the detection of electrons with energies exceeding 300-350 MeV (see also Figure 4.3); and an EJ-260 plastic scintillator external to the large interaction chamber as a real-time diagnostic for

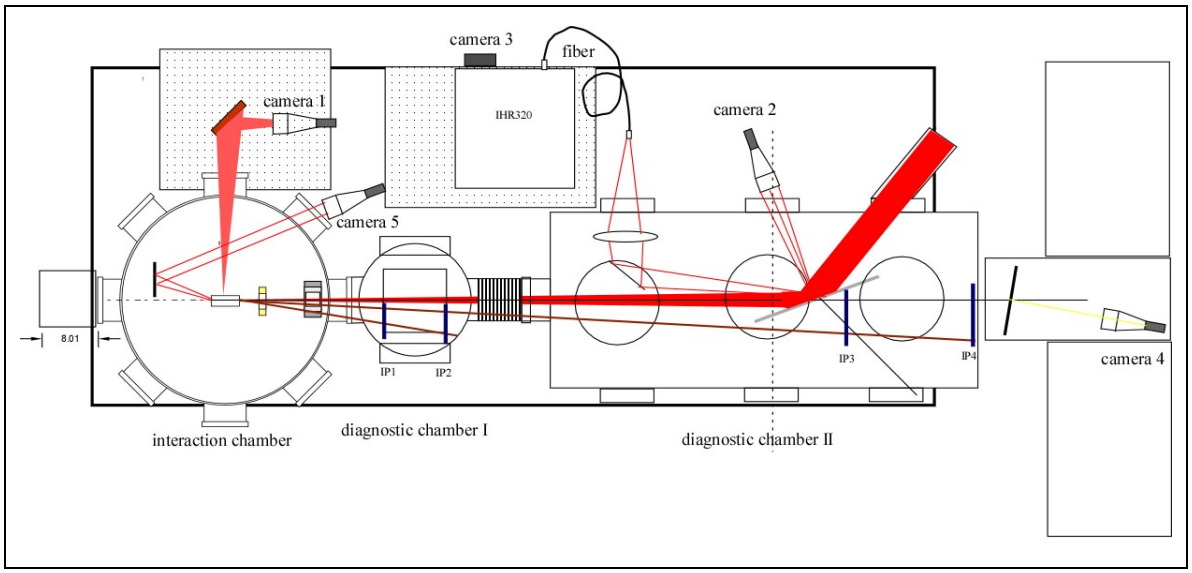

Figure 6.5: The experimental setup for the LWFA 1.5 experiment.

the presence of high-energy electrons. Initially there was an IP placed external to the interaction chamber to allow fast determination of the presence of electrons (i.e., in less time than it would take to break the vacuum and remove the IP inside the chambers), however the successful detection of high-energy electrons by the EJ-260 plastic scintillator largely made this IP redundant. The magnetic spectrometer consisted of the magnet and tungsten fiducials of diameter 1/16" positioned in the path of the magnetically deflected electrons. Initially a magnet of field strength 0.175 T was deployed with the direction of the field providing electron deflection in the vertical plane; this, however, proved to be too weak to provide sufficient deflection for the energetic electrons that were produced and was replaced by a 1.1 T magnet (field strength refers to the center of the magnet) providing deflection in the horizontal plane. One shortcoming of the setup (corrected for the following experiments) was the positioning of the beam deflector inside the diagnostic chamber (Figure 6.6). The titanium frame of the deflector

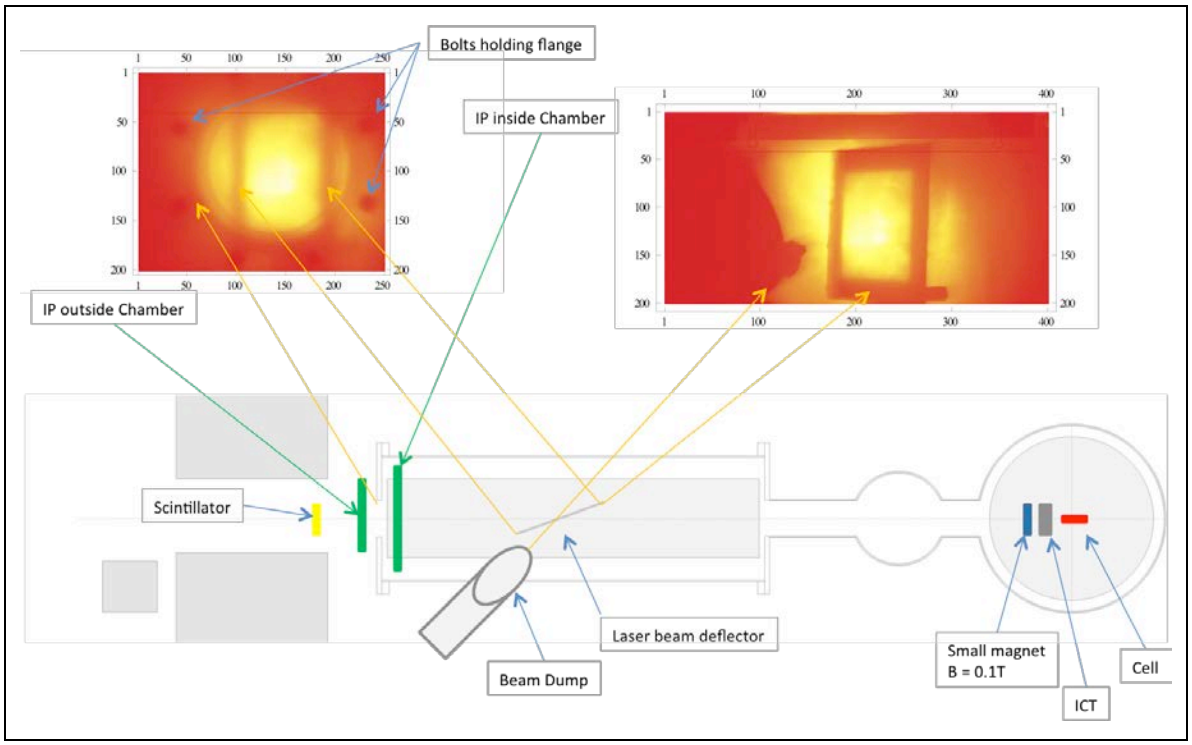

Figure 6.6: View of the inside of the large diagnostic chamber as it appeared on the imaging plates [Image courtesy of Rafal Zgadzaj].

was in the path of the high-energy tip of the electrons deflected in the magnetic spectrometer. This led to the scattering of the most energetic electrons. Figure 6.7, top, shows the impact of scattering of these electrons by the deflector frame for shot 3033 as detected by the imaging plate; the impact of the ~1 mm diameter fiducial (shadow in the middle of the electron streak), as well as the scattering produced by the titanium frame (visible in the center), can be seen in the image. The scattering led to an increase in the electron divergence at high energies between ~0.8 GeV to ~1.1 GeV. In order to correct for this effect, the magnetic spectrometer was modeled using GEANT4 [56]. The simulation incorporated the characteristics of the magnetic field (position, dimensions, and the strength of the magnet), the dimensions of the large diagnostic chamber, the position and angle of the deflector, as well as its material and thickness. It was possible, in a procedure involving multiple iterative simulations, to determine the energy spectrum (Figure 6.8) and launch angles of the accelerated electrons, which would give rise to the scattering effect actually observed. The bottom image in Figure 6.7 shows the simulated scattering using the derived electron energy spectrum; the similarity of the measured and simulated electron signals indicated the correctness of the derived electron energy

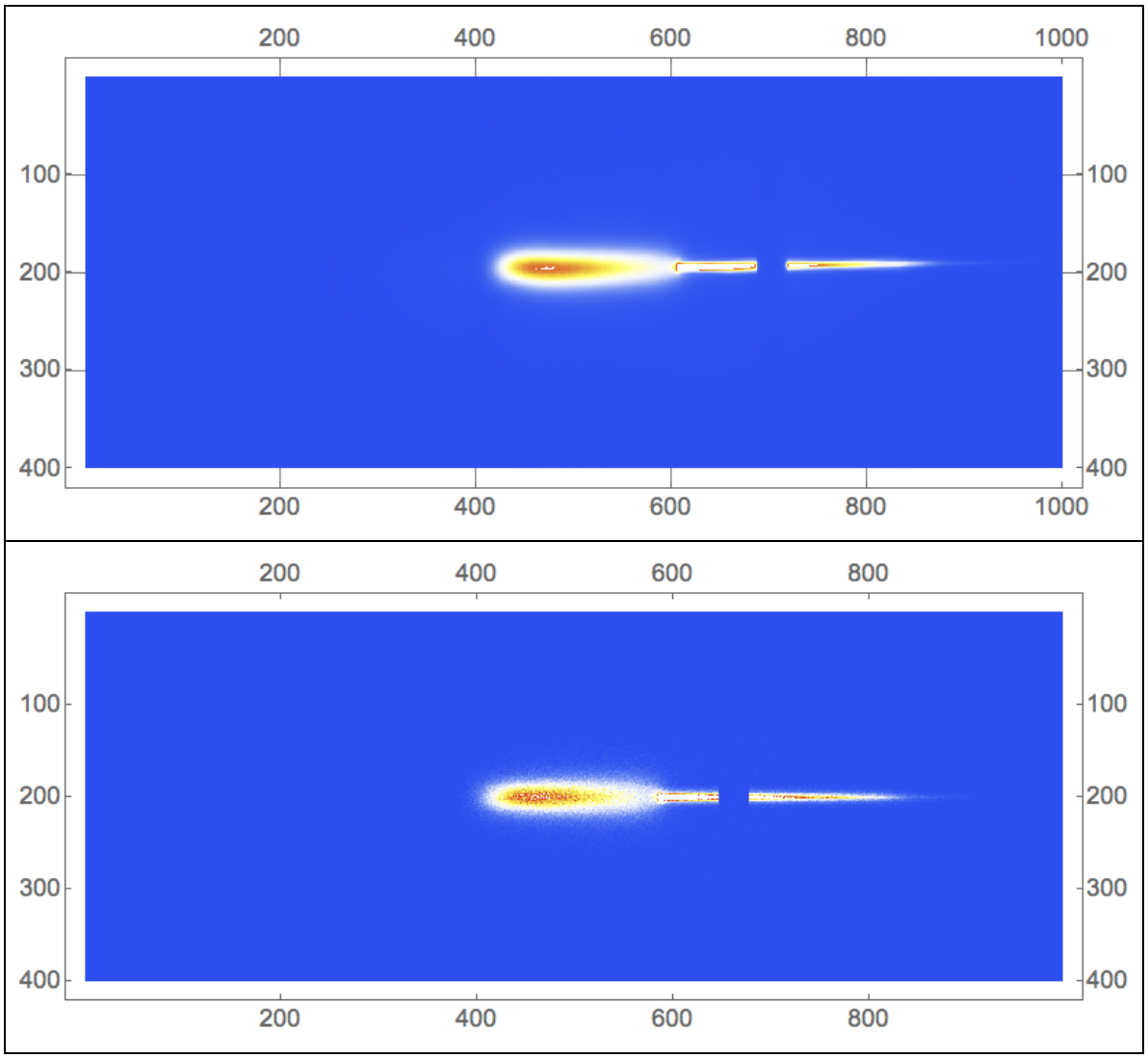

Figure 6.7: Reproduction of the electron signal on the imaging plate using GEANT4 simulation, used to remove the scattering effect (top: measured, bottom: simulated)

spectrum. It was also possible to correct for the scattering of the electrons in the titanium frame and determine the electron divergence for energies > 0.8 GeV. It was possible to reproduce the measured electron deflection (i.e., in a magnetic spectrometer where the magnetic field extends outside the magnet boundaries) using a flattop effective magnetic field of 1.4819 T. This effective magnetic field was henceforth used in all formulas for the deflection of the wakefield-accelerated electrons in the magnetic spectrometer (Chapter 4).

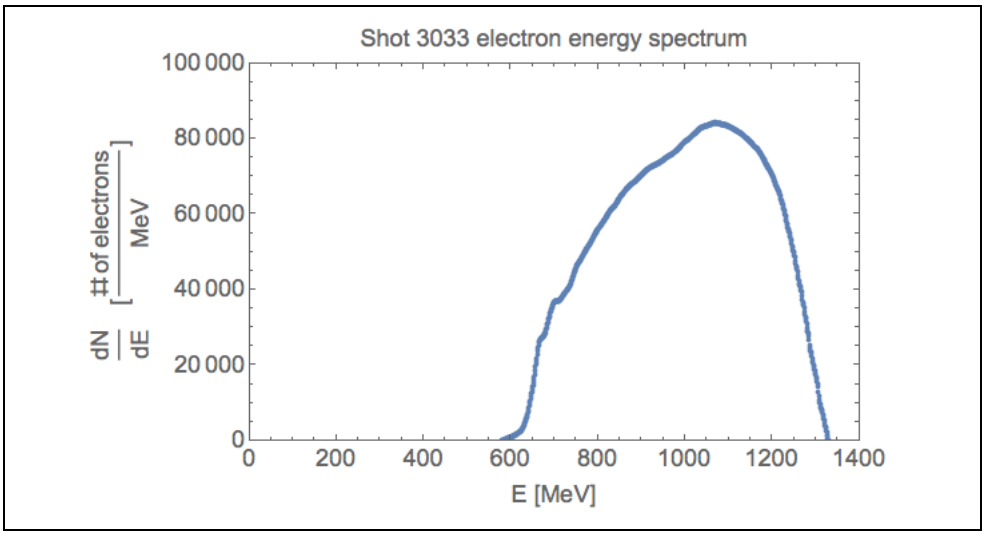

Figure 6.8: Electron spectrum for shot 3033 from the LWFA 1.5 experiment (see also **Figure 6.7**) [Image courtesy of Rafal Zgadzaj]

Diagnostic Measurements for Selected Shots

The laser pulse parameters for shot in this round are displayed in Table 6-1. The production of wakefield-accelerated electrons is the outcome of the nonlinear interaction between the laser pulse and the plasma, and is dependent on factors including laser pulse power, duration, profile, as well as plasma density and doping. Pulses with durations ranging from 134 fs to 176 fs, power in the ranging from ~0.8 to ~1.1 PW, yielded electron bunches with charge ranging from tens of pC to hundreds of pC for plasma density ranging from $\lesssim 4 \times 10^{17}$ cm^{-3} to $\gtrsim 6 \times 10^{17}$ cm^{-3}.

Shot #	Pulse Energy (J)	pulse Duration (fs)	Peak Power (TW)	Peak Intensity (10E18/cm2)	w0 (μm)
2931	149.00	134	1111.9	3.1	40.0
2942	140.30	141	995.0	2.5	42.0
2944	143.72	140	1026.6	2.6	36.0
				3.2	38.0
2946	138.00	138	1000.0	2.1	42.0
2948	150.00	135	1111.1	2.4	43.0
2951	139.00	139	1000.0	N/A	N/A
2953	133.00	146	911.0	N/A	N/A
2963	132.00	164	804.9	2.2	46.0
2966	116.00	170	682.4	1.0	74.0
2970					
2969	141.00	166	849.4	2.3	48.0
2976	154.00	220	700.0	1.0	45.0
				0.9	70.0
2993	156.00	197	791.9	1.9	45.0
2996	135.00	171	789.5	2.5	43.0
3011	139.00	174	798.9	3.8	34.0
3022	122.00	192	635.4	2.6	30.0
				2.7	30.0
3024	121.00	147	823.1	2.9	50.0
3033	130.00	153	849.7	3.9	30.0
3035	116.00	170	682.4	4.0	31.0
3037	140.00	168	833.3	2.9	48.0
3041	140.00	205	682.9	2.6	48.0
3043	132.00	161	819.9	3.2	38.0
				3.0	60.0
3046	128.00	163	785.3	2.2	40.0
				1.9	45.0
3048	139.00	176	789.8	2.4	65.0
				2.5	37.0
3051	123.00	236	521.2	1.6	47.0
3053	123.00	182	675.8	4.7	28.0

Table 6-1: Laser parameters for shots from the LWFA 1.5 experiment

The plastic scintillator diagnostics in this round of experiments yielded measurements for the presence of electrons and confirmed the feasibility of using this detector as a real-time diagnostic for the presence of electrons (Figure 6.9). The imaging plate measurements (Figure 6.10) were successfully used to measure the charge of the electron bunch, as well

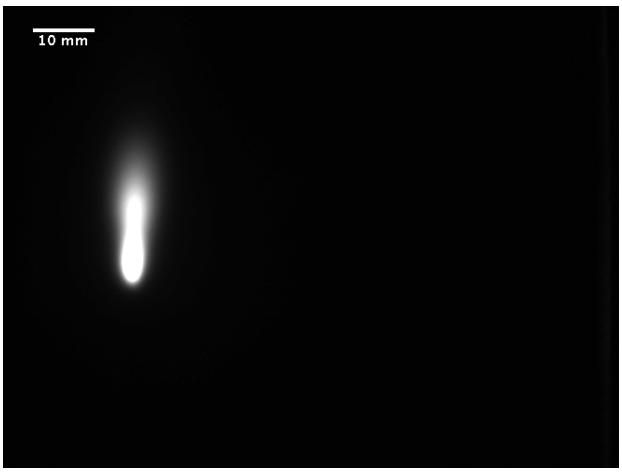

Figure 6.9: The plastic scintillator (EJ-260) image for shot 2931, where a magnet of 0.175 T was used to produce a vertical deflection of accelerated electrons.

Shot	n_e [10^{17} cm^{-3}]	N_2 Doping [%]	Charge > 300 MeV [pc]
2944	5.6	5	26
2946	6.4	5	> 51
2948	4.7	5	> 63
2951	3.7	5	> 51
2953	6	5	75
2970	5.3	5	0.21
3024	4.88	5	> 175
3033	6.2	5	> 11
3048	6	5	> 375

Table 6-2: Plasma density, doping, and charge for selected LWFA 1.5 shots.

as its energy spectrum (Figure 6.12). The IP measurements were, however, beset by saturation of the measured signal. As has been discussed (3.2), this is due to the saturation of the PMT inside the imaging plate read-out system (scanner). A methodology, based on repeated rescanning of the imaging plates with saturated signal (discussed in C.2), was later developed to address this issue and implemented in the experimental rounds that followed. The charge measurements from this experimental round are therefore lower bounds, because the measured PSL from saturated pixels of the IP is not representative of the true PSL. Table 6-2 shows the total charge measured on the

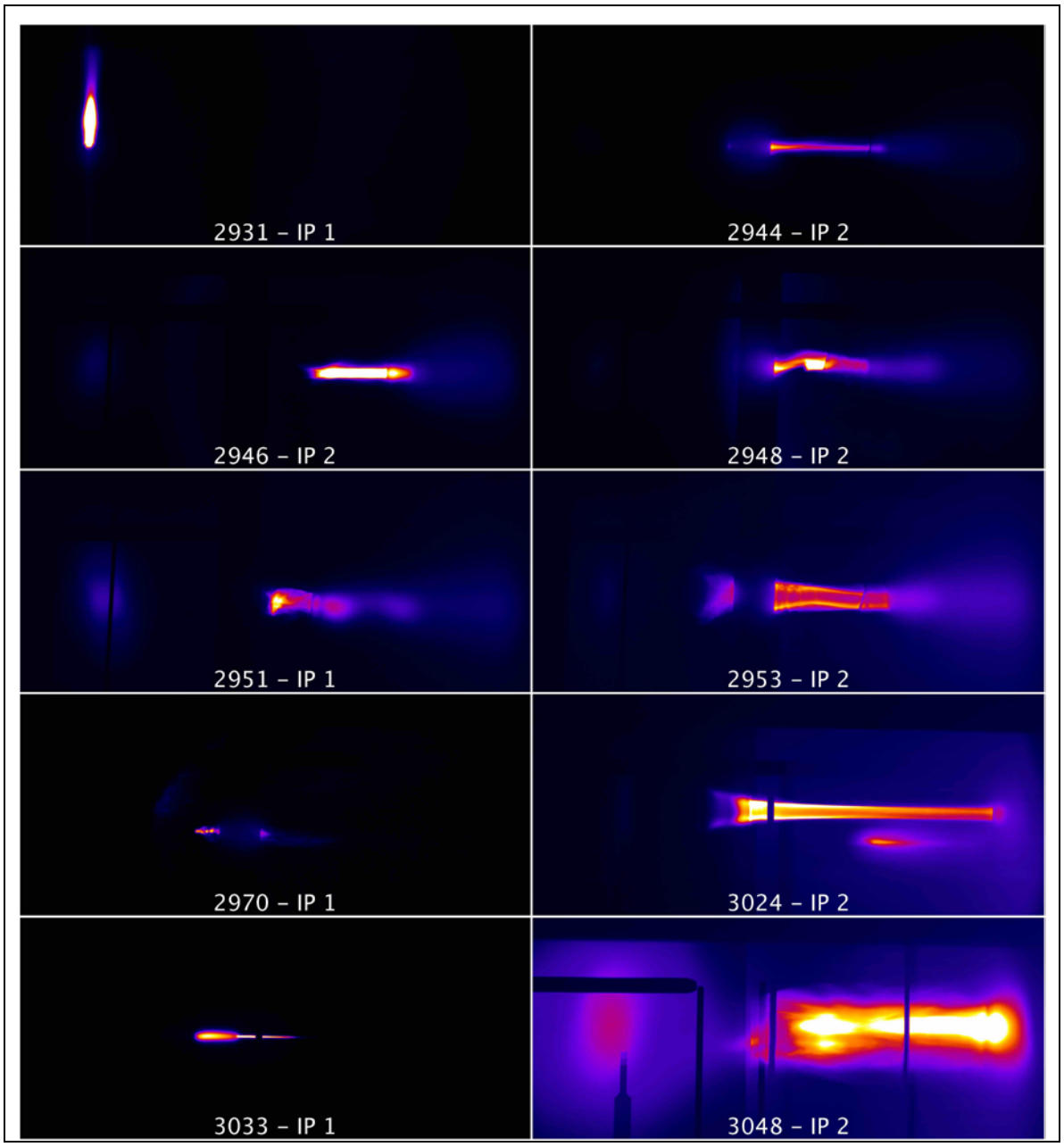

Figure 6.10: Selected measurements of magnetically deflected electrons recorded for the LWFA 1.5 experiment.

large IP (i.e., having energies > 300 MeV) for selected shots from the LWFA 1.5 experiment.

The streaks created on the large IP by the electrons that were magnetically deflected in the horizontal plane using a 1.1 T magnet (Table 6-2), as well as for one shot (2931) that was vertically deflected using a weaker 0.175 T magnet, are shown in Figure 6.10. Each

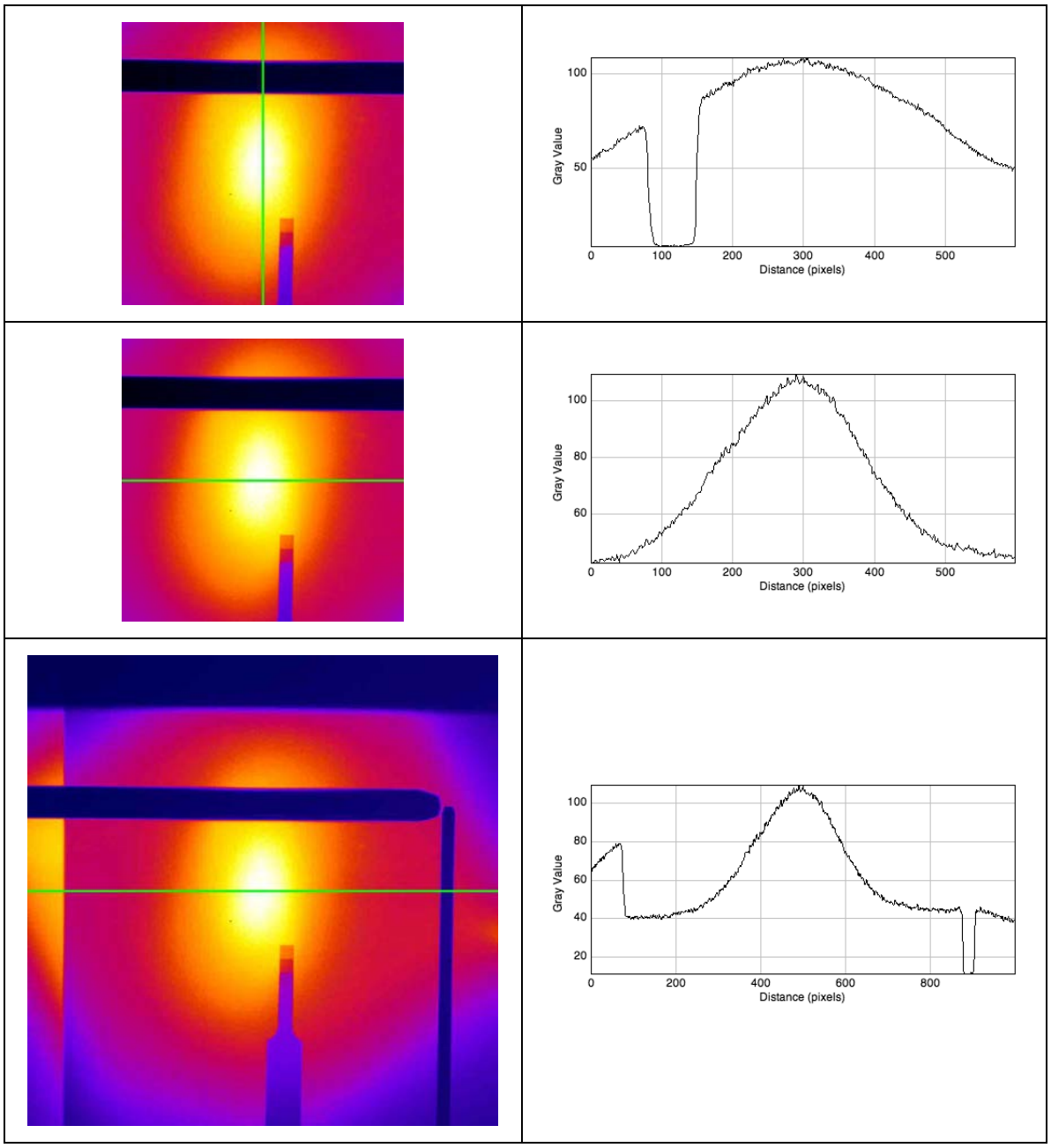

Figure 6.11: Betatron X-ray profile measured for shot 3048 (round 1). X-ray profile plots indicating divergence is the vertical (top row) and horizontal directions (middle row). Horizontal profile plot showing the impact of the beam deflector on the betatron x-ray profile (bottom).

image displays a 2300 × 1000 pixel region of the 4000 × 2000 pixel MS IP; the selection rectangle is vertically symmetrically positioned with respect to the IP center pixel; horizontally it is wide enough to include the betatron radiation. In all cases except the first (for shot 2931 where a weak magnet of strength 0.175 T was used to deflect the

electrons vertically), the electron deflection was in a magnetic spectrometer with magnetic field strength of 1.1 T at the center of the 5 centimeters magnet (1.4819 T effective flat top). In all but a few cases, the electron signal was partially saturated; in such cases, it was only possible to determine the lower bound of the charge, as shown in Table 6-2. Betatron radiation was observed for several of the shots, and in one case (shot 3048), the intensity of the vertically elongated x-ray was strong enough for spectrum measurement using x-ray filters had filters been deployed. However, the aluminum laser beam deflector used in this round was relatively thick (0.0307") and the drop in PSL for the x-ray intensity as it enters the deflector region on the detector gives an indication of an x-ray spectrum. (Absent measurements to enable an accurate deconvolution of the x-ray spectrum and the detector response, any spectral estimate remains qualitative.) The presence of the deflector also hampered the measurement of x-ray divergence (FWHM), as the x-ray profile is partially covered by the deflector. Figure 6.11 shows 600-pixel vertical (top row) and horizontal (middle row) lineouts of the x-ray profile passing through the pixel where the x-ray intensity peaks. FWHM of the x-ray profile, following attenuation by the deflector, is ~15 mrad (~400 pixels on the MS IP) in the horizontal direction, and ~22 mrad (~600 pixels) in the vertical direction. (Note that the polarization of the TPW laser is also vertical.) The bottom row of the image shows a longer (1000 pixel) horizontal profile plot through the peak of the x-ray intensity. On the left-hand side there is a 50% drop in intensity (from 80 PSL to 40 PSL) as the lineout crosses into the beam deflector region. The deflector of thickness 0.0307" (0.78 mm) had been positioned at an angle offset by 23.53 degrees with respect to the plane perpendicular to the diagnostic chamber axis (also the laser propagation direction); this gives an effective path of 1.95 mm (0.78/sin(23.53)) for the x-ray beam through the Al deflector. For a monochromatic x-ray beam, and a flat detector response to x-rays, a 50% attenuation through 1.95 mm of aluminum would correspond to x-ray photons with 28 keV energy. The betatron radiation spectrum is in fact broadband, and the detector response to x-rays is a function of energy, peaking at ~15-20 keV (Figure 5.2). However this results suggests that the x-ray spectrum is dominated by photons with energies $\gtrsim$ 20 keV. The electron energy spectrum is shown in Figure 6.12. (There is a one-to-one correspondence between panels in this images and those in Figure 6.10, with the exception of the first

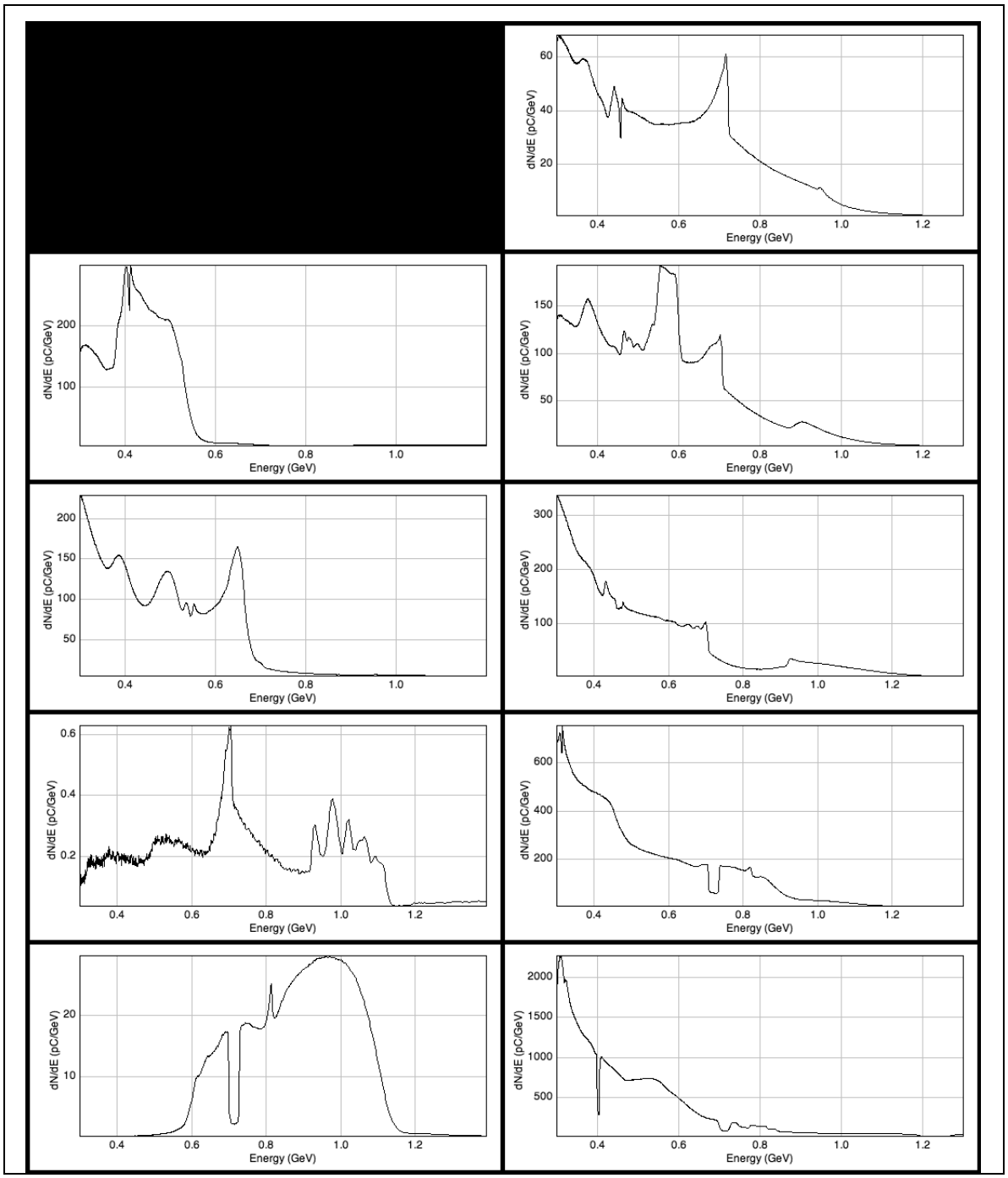

Figure 6.12: Selected electron spectrum measurements for shots in **Figure 6.10** where a 1.1 T magnet was used (excludes shot 2931).

shot.) The energy spectrum was impacted both by the presence of saturation, as well as by the objects in the path of the electron bunch on its way to the detector. One of these objects, the fiducials, produced narrow shadows on the IP images, and resulted in sharp dips in the electron spectrum, however did not materially affect the determination of the

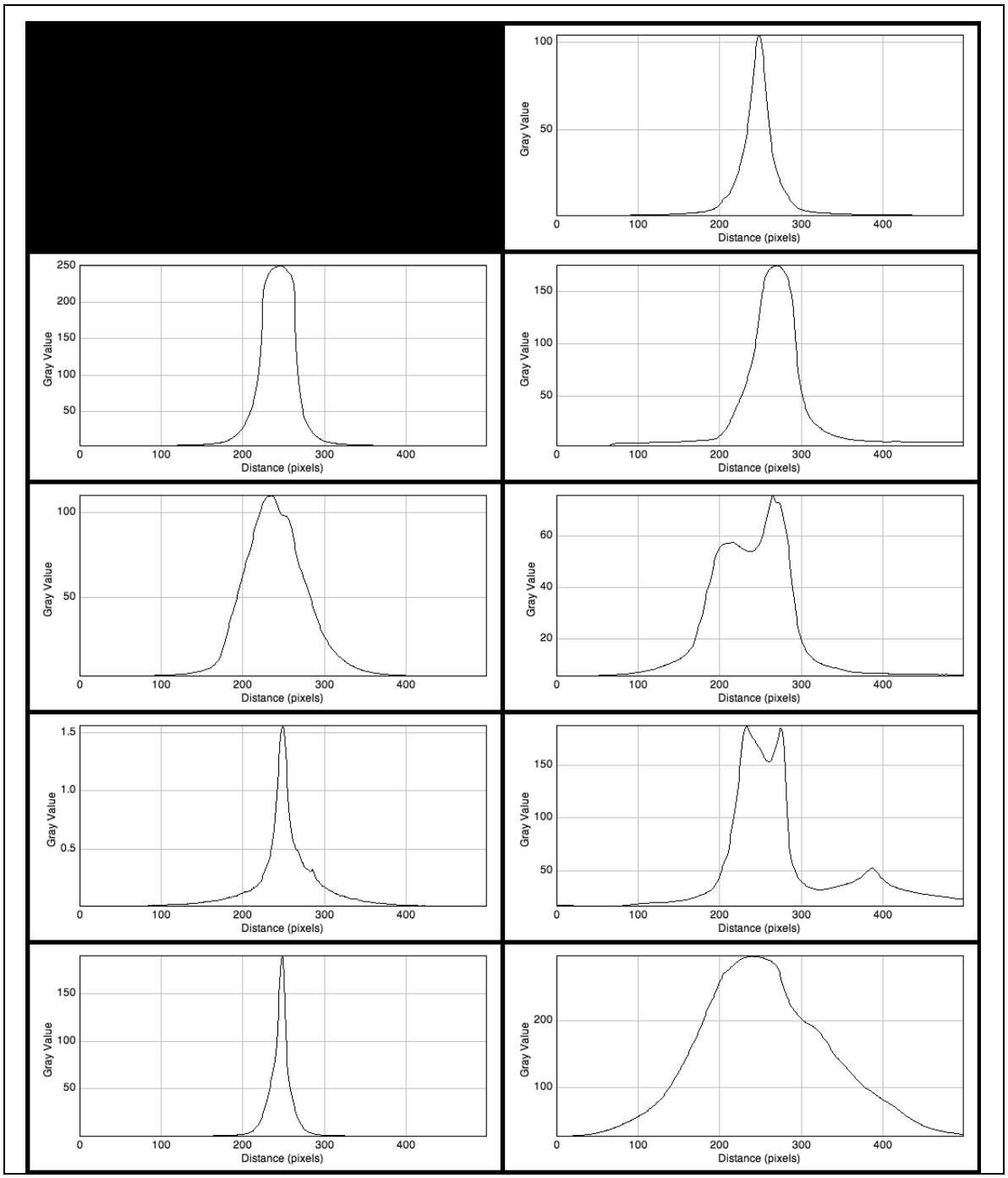

Figure 6.13: Selected electron divergence measurements for shots in **Figure 6.10** where a 1.1 T magnet was used (excludes shot 2931).

electron spectrum. The larger object, the titanium frame of the laser beam deflector, adversely affected the calculation of the energy spectrum in the range 0.8-1.1 GeV. (This was corrected using GEANT4 simulation for shot 3033.) The divergence of the electron streaks, averaged over their lengths, is shown in Figure 6.13. (There is a one-to-one

correspondence between panels in this image and those in Figure 6.10, with the exception of the first shot.) The divergence measurements were performed on the electron streak with scattering effect included, therefore they overestimate the actual electron divergence. Nonetheless, the measured electron divergence is as low as 0.5 mrad in the vertical direction.

6.3 2nd Experimental Round ("LWFA 2.0")

The next round of laser-wakefield experiments at the TPW laser took place between 04/17/2012 and 05/06/2012, with the goal of enhancing the maximum electron energy. In this experiment, wakefield acceleration of electrons from both ionization-induced injection and self-injection was achieved. Initially, the helium gas was doped, as in the previous round, to produce ionization-induced injection of electrons; however, with the lowering of the nitrogen doping, there was evidence suggesting that injection was taking place in the absence of doping, therefore a switch was made to pure helium. Beginning with this experiment, the relatively thick laser beam deflector (0.0307" aluminum, 23.53° offset from perpendicular) from the previous round was replaced with a much thinner deflector (0.001" aluminum, similar offset); this significantly lowered the attenuation of the betatron x-rays by the deflector. The position and angle of the laser beam deflector with respect to the diagnostic chamber axis was modified such that, unlike in the previous round, both electrons and betatron x-rays would clear the deflector frame; this corrective measure allowed a more accurate measurement of the electron energy spectrum and divergence, without the need to take into account the scattering of electrons by the deflector frame (Figure 6.7). There were several improvements to the diagnostics for the electrons and x-rays; among these were the introduction of a more stable and accurate frame for the large imaging plate, the introduction of high resolution (SR) IP (Figure 6.14), improved electron spectrometry using tungsten fiducial arrays optimized by GEANT4 simulation, and the introduction of the combined Lanex-scintillator detector, using an EJ-200 plastic scintillator together with a sheet of Kodak Lanex Regular phosphor, as a real-time diagnostic for the presence of high-energy electrons, as well as a redundant diagnostic for the high-energy electron charge. (The EJ-200 was chosen instead of EJ-212 for its stronger response to ionizing particles, i.e., electrons). A color CCD was used for the separation of the scintillator blue light and the Lanex green light. (This is described in Appendix E.) The experiment was successful in accelerating electrons to > 2 GeV at plasma densities as low as $n_e \sim 3 \times 10^{17} \mathrm{cm}^{-3}$. In this round of experiments, unlike in the previous one, laser pulse propagation took place in the mode-matched regime, producing continuous injection and resulting in poly-energetic electrons. The electron beam had ~0.5-mrad divergence and produced high charge at the nC level.

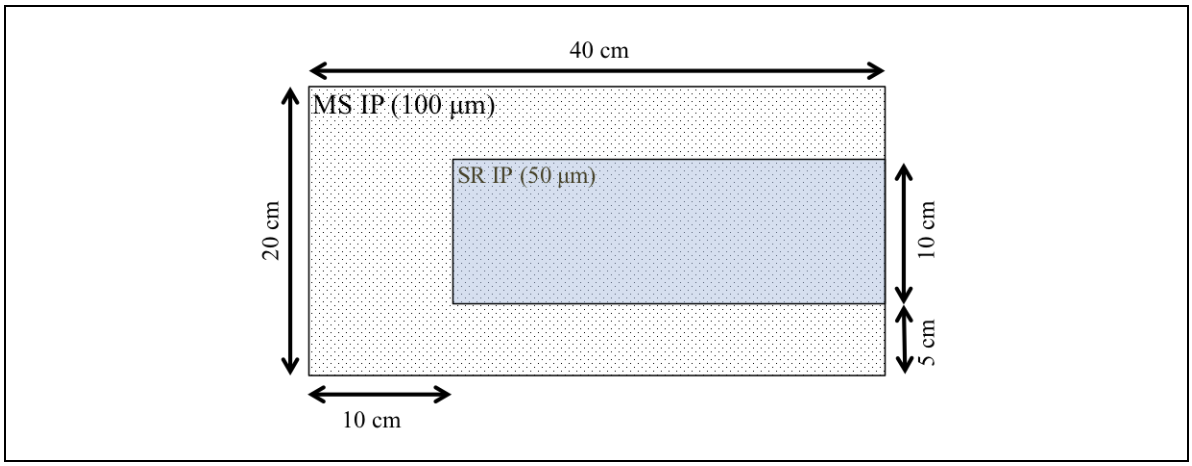

Figure 6.14: Configuration of the imaging plate detectors used for high-energy electron and betatron x-ray diagnostics in the LWFA 2.0 experiment.

Similar results were obtained for pure helium and helium doped with nitrogen. Strong betatron radiation was also observed; however, x-ray filters had not been deployed. A schematic of the experimental setup, showing the various dimensions, is shown in Figure 6.15. F1 and F2 indicate racks of 0.005" diameter tungsten fiducials (3.4) introduced for the precise measurement of the electron energy spectrum by triangulation of the scattering shadows for the electrons on the imaging plate back to the corresponding

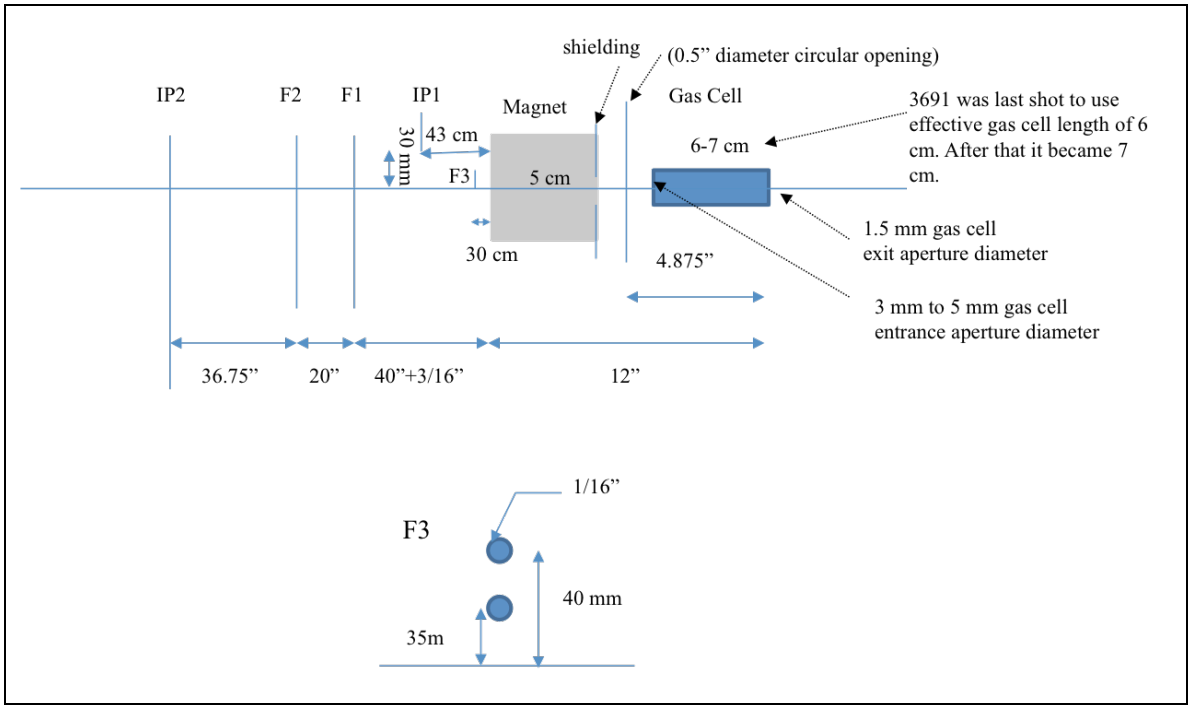

Figure 6.15: Dimensions of the experimental setup in the LWFA 2.0 experiment

fiducials, then back to the x-ray source position inside the gas cell; the latter position is itself determined by triangulation of the scattering shadows for the betatron x-rays on the detector back to the corresponding fiducials and finding the place of intersection inside the gas cell. Together the F1 and F2 fiducials made possible a deconvolution of the electron energy and its (small but non-zero) launch angle). IP1 and IP2 indicate the imaging plate detectors used for the detection of high- and low-energy electrons, respectively. (See also Figure 4.4.)

Diagnostic Measurements for Selected Shots

In this round, the idea of imaging the combined luminescence from the Lanex and scintillator diagnostics using a single color CCD was implemented. The combined diagnostic provided real-time indication for the existence of high-energy electron charge ($\gtrsim$ 1 GeV). In addition, the recovery of the Bayer pattern from the CCD output, the reconstruction of the R, G, and B components, recovery of commensurate Lanex and scintillator images from the RGB data, and the calculation of the electron charge using the Lanex image were successfully carried out. (All details are provided in Appendix E.) Detailed analysis of the color CCD measurements for the Lanex and scintillator diagnostic took place following the experiment and revealed saturation of the CCD pixels for many of the shots which produced the high-energy electrons that would be detectable by this diagnostic. This impacted the calculation of the recovered Lanex image and the resulting charge and indicated the necessity for using ND filters. Nonetheless, measurements from this round enabled the methodology for the separation of the luminescence from the two detectors to be fully worked out. Necessary steps were taken to prevent saturation in the next round of experiments (0).

The measurements from representative shots from this experimental round are shown in Table 6-3. Electron streaks and their energy spectra, as well as the betatron x-ray profiles, for the same shots, are shown in Figure 6.16. Scattering of electrons with energies exceeding 1 GeV from tungsten fiducials of different diameters was simulated in GEANT4 in order to determine the optimum fiducial diameter to create shadows on the detector that were as narrow as possible (to provide energy resolution) while remaining

Shot	E_{peak} [GeV]	Energy Spread of Peak FWHM [%]	Angular Divergence at Peak FWHM [mrad]	Charge in Peak [pC]	Charge below Peak [pC]	Plasma Density n_e [10^{17} cm^{-3}]	E_{TPW} [J]	t_{TPW} [fs]
a (3655)	1.8^{+20}_{-10}	25	0.7	53	600	5.7	100	162
b (3713)	1.9^{+25}_{-10}	13	0.9	35	280	4.8	123	179
c (3750)	1.65^{+15}_{-10}	9	0.8	30	327	3.4	120	149
d (3752)	$1.3^{+0.07}_{-0.05}$	11	0.5	12	83	2.1	129	158
e (3736)	$0.95^{+0.07}_{-0.05}$	12	0.4	10	50	1.7	103	157

Table 6-3: Measurements from representative shots from the LWFA 2.0 experiment

visible. This led to the replacement of tungsten fiducials of diameter 1/16" with new ones having diameter 0.005" which enhanced the resolution of the electron spectrometer to 5% at 2 GeV [32] and enabled the measurement of the peak electron energy to an unprecedented accuracy. In this experiment, for the first time, electrons were accelerated to energies > 2 GeV with peak charge energy reaching 1.9^{+25}_{-10} GeV. Self-injected electrons were also accelerated to ~1 GeV at densities as low as 1.7×10^{17} cm^{-3}. In this round, high sensitivity (MS) IPs were used together with high resolution (SR) IPs in the configuration shown in Figure 6.14. This enabled a comparison of the charge detected on each. As shown in Table 6-4, the two detectors detect electron charge that are in close agreement. In one case, for shot 3713, the charge detected on the two detectors differed. Upon closer scrutiny, this was found to have been caused by the presence of a very small, but sharply saturated, region of a few pixels on the more sensitive (MS) IP. Fortunately, the presence of the lower sensitivity (SR) IP made it possible to replace this measurement with an accurate measurement not affected by pixel saturation. As shown in Figure 6.17, the use of SR IP made the electron spectrum more peaked at ~2 GeV. This figure also

Shot no.	high E tail		peak (FWHM)		low E tail		Total	
	MS	SR	MS	SR	MS	SR	MS	SR
3655	6	5	55	56	134	134	195	195
3713	7	13	37	61	190	325	234	399
3736	1	1	10	11	39	41	50	53
3750	16	15	32	32	222	215	270	262
3752	1	1	13	12	62	56	76	69

Table 6-4: Measurements of charge for various regions of the electron spectrum, performed on two different detectors.

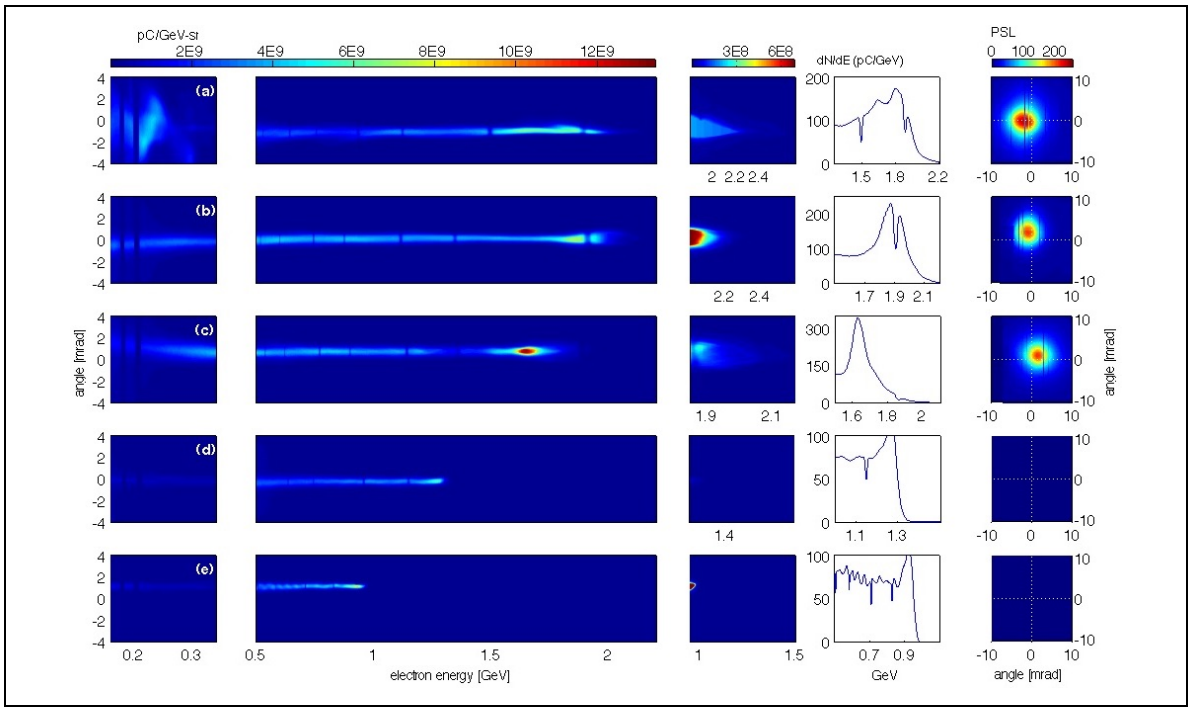

Figure 6.16: Representative electron spectra and x-ray profiles from the 2nd experimental round (from top: shots 3655, 3713, 3750, 3752, 3736)

shows the high-energy tails of the electron streaks using higher relative intensity, to highlight that the tail of the electron streak went as high as 2.3 GeV. Betatron x-rays were detected for shots in panels (a) and (b). There are 2 or more fiducial shadows visible in the x-ray profiles; in each case, these were used to determine the source of x-rays inside the gas cell. Figure 6.18 shows a diagram of the gas cell and the positions of the x-ray source for a sample of 22 shots in this round that produced electron energies > 1 GeV, determined using triangulation of the x-ray fiducial shadows. Highlighted in red and yellow are the x-ray source positions (to within ±10 mm accuracy) corresponding to shots in panels (a) and (b) of Figure 6.17. The source positions are found to be in the last 2.5 centimeters of the 7 cm gas cell, suggesting that x-ray radiation took place in the final 3rd of the plasma length. Also seen in Figure 6.17, are electron spectra identifying, using labels, the shadows created on the detector by the presence of 0.005" tungsten fiducials placed in the path of the electrons; for example, following the triangulation of the shadow labeled as 1-4 in Figure 6.17 (a) to fiducial 1-4 that created it, then to the x-ray source position inside the gas cell, the energy of the scattered electrons corresponding to that fiducial shadow was determined to be 2.00 GeV. (See 3.4 for more details.) This is the energy of the electrons that would have arrived at that position on the detector had they

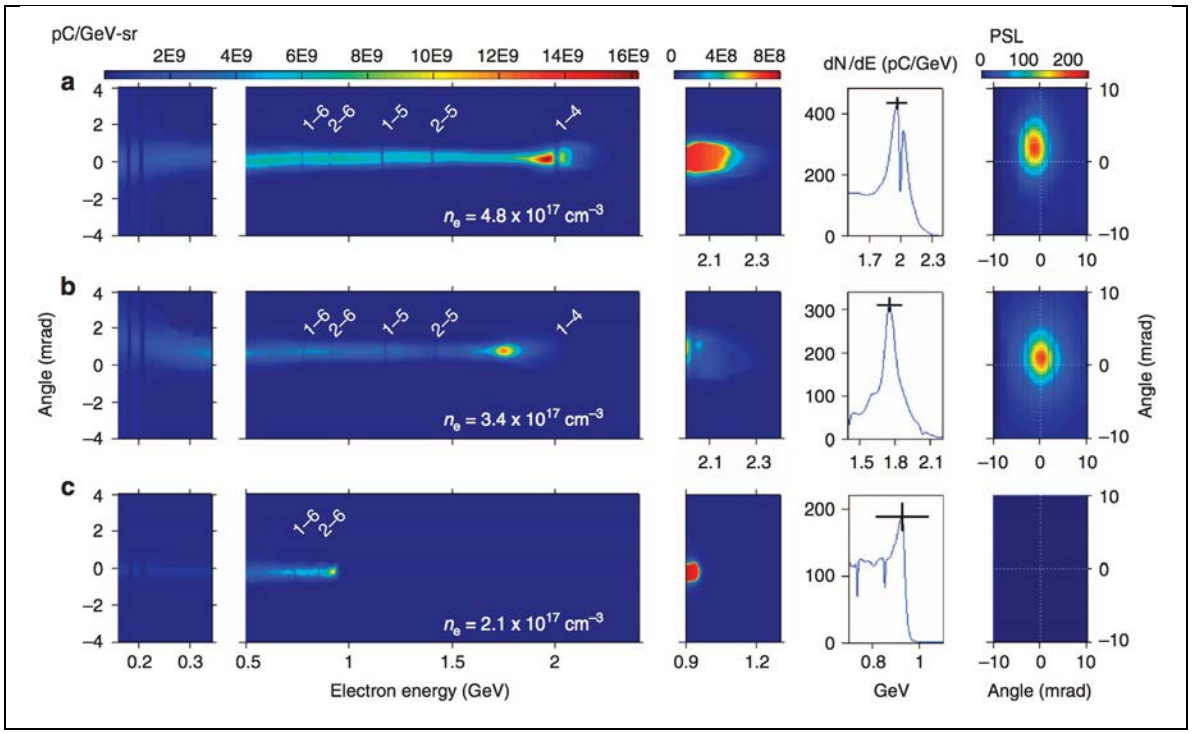

Figure 6.17: Electron spectra and betatron x-ray profiles for 3 of the shots in **Figure 6.16**, where the electron spectrum for shot (3713) saturated on the high-sensitivity detector has been replaced using measurements from the high-resolution detector.

not been scattered by the fiducials in their path. The full set of fiducial shadow positions and their corresponding energies was then fit using formulas in Table 4-1 to determine the free parameter x_∞; then those formulas were used to determine the electron energies corresponding to locations on the detector outside the fiducial region. Figure 6.17 also provides plots of dN/dE, the electron charge distribution as a function of energy, where the horizontal error bars represent the 5% resolution of the magnetic spectrometer at 2 GeV within 2 standard of deviations. This is the uncertainty in the electron energy calibration using fiducial shadows and results from the combined uncertainty in fiducial wire positions (±25 mm transversely, ±2 mm longitudinally), fiducial shadow positions (±1/2 MS IP pixel, or ±50 mm), electron source position (determined by X-ray triangulation) relative to magnet and detector (±75 mm transversely, ±1 cm longitudinally) and the magnetic field (±1%).

Simulation of Laser-Plasma Interaction

Following the experiment, simulations were performed to reproduce the key experimental results obtained in this round. These were: 1) the narrow peak in the charge distribution at

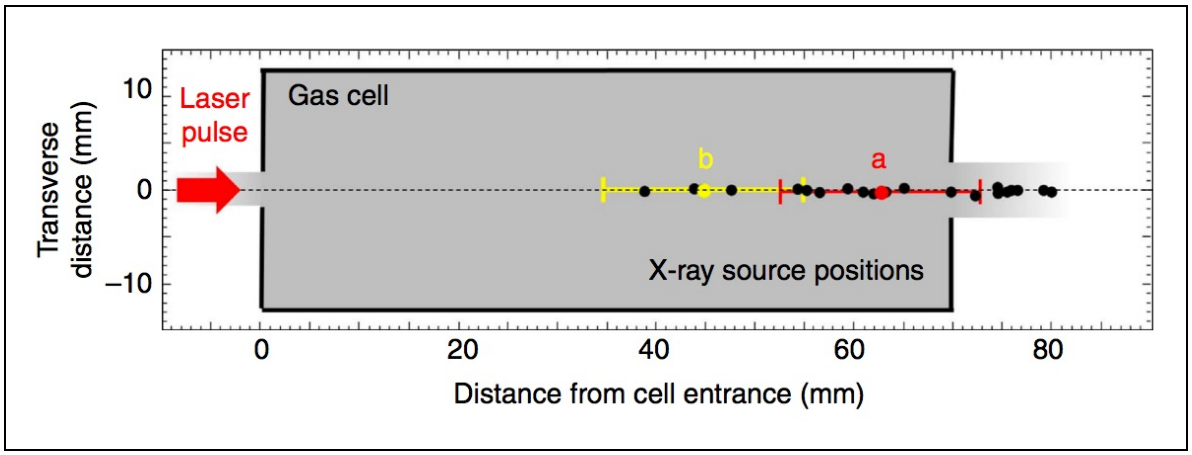

Figure 6.18: Position of the x-ray source (proxy for the electron source) determined using triangulation for shots in panels (a) and (b) of **Figure 6.17**.

2 GeV, 2) the small (sub-mrad) electron divergence, 3) the location of the x-ray source in the last 3rd of the gas cell length, and 4) the low energy electron tail (see Figure 6.16 and Table 6-4). Since the phase profile of the driving laser pulse was not accurately known, and performing a 3D particle-in-cell (PIC) simulation with phase as a free parameter was not feasible (due to the long computational time required to propagate the pulse for the length of the gas cell, i.e., 7 cm), the approach was taken to represent the pulse as a Gaussian or super-Gaussian, i.e., having cylindrical symmetry, with a flat phase front, and use WAKE for the simulation. The driving laser pulse for shot (a) of Figure 6.17 was modeled by a 100-J, 160-fs Gaussian with beam waist parameter of w_0= 275 μm. (This is compatible with the typical spatial profile of the actual laser pulse, seen in Figure 6.19 (a), inset.) This pulse self-focused to intensity 7×10^{19} W cm^{-2} following ~4 cm propagation into the plasma and formed a bubble which, however, evolved too slowly to trigger injection. (Rapid bubble profile evolution facilitates injection [17], [18].) However, a 3rd order super-Gaussian, with same energy and duration, resulted in faster axial intensity evolution and more rapid bubble evolution, and successfully triggered injection. This is shown in Figure 6.19 (a), where after more than 5 cm of propagation, the super-Gaussian pulse undergoes two rapid self-focus/defocus cycles near the cell exit. A first electron bunch that is injected during, and as the result of, the first self-focus at ~5.8 cm, is accelerated to ~2 GeV in the remaining ~1.2 cm of plasma, shown in Figure 6.19 (b). This is in good agreement with the 2 GeV peak observed in Figure 6.17 (a). The driving laser pulse then refocuses near the gas cell exit, triggering a second injection that

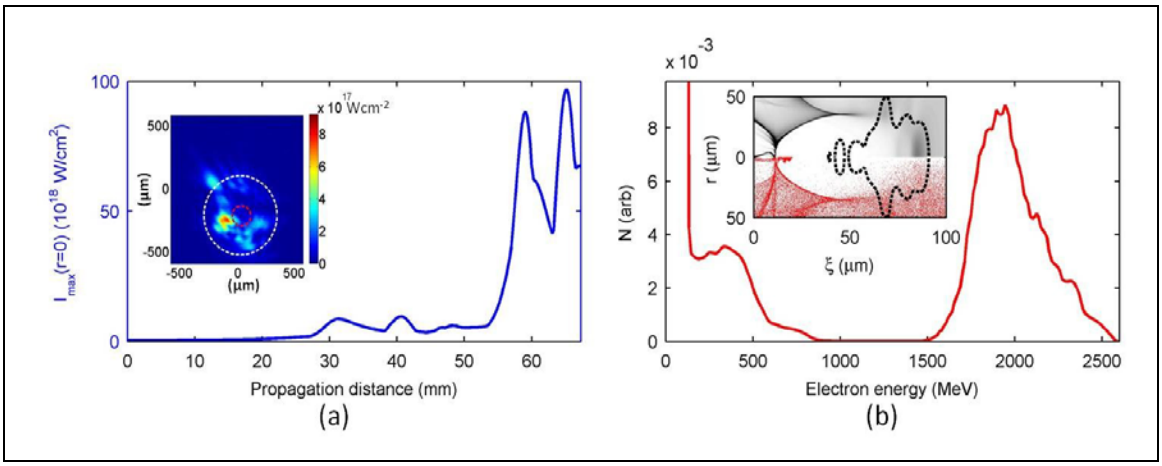

Figure 6.19: Simulations showing the relativistic self-focusing of the laser pulse in plasma [Image courtesy of Austin Yi]

produces the low-energy electron tail that was also observed. This scenario also captures the key observation that betatron X-rays (and thus accelerated electrons) originated near the gas cell exit (Figure 6.18). Figure 6.19, inset, shows the test electrons (candidates for injection) in red, and the ambient plasma electrons in black; ξ denotes the longitudinal distance along the bubble axis. It may be seen that according to this simulation, self-injected electrons were confined within ~2 mm of the axis of the ~30 mm radius bubble, consistent with the observed sub-mrad beam divergence. The inset also shows, as a black dashed curve, the iso-intensity contour of the self-focused laser pulse at the threshold of K-shell ionization of nitrogen; given the spatial distribution of this contour, ionization of nitrogen impurities would have produced a much broader injected profile and a more divergent beam, had doped gas been utilized instead if the pure helium actually used. Such divergent beams were previously reported in experiments relying on the ionization-induced injection of electrons as the mechanism for injecting electrons into the accelerating structure [5]. The WAKE simulations do not capture the quantitative 3D evolution of laser pulse and plasma bubble, but they qualitatively capture injection and acceleration physics, and explain the main experimental observations noted at the beginning of this section.

6.4 3rd Experimental Round ("LWFA 3.0")

This round of experiments ran from 01/14/2013 to 02/15/2013 and used both pure helium and helium doped with 1% nitrogen (Table H-3). To detect the spectrum of the betatron x-ray radiation, copper and aluminum filters of several thicknesses were introduced into the diagnostic chamber in close vicinity to the high-sensitivity (MS) IP. Although the 0.001" thick aluminum deflector, introduced in the previous round, provides more than 50% transmission for x-rays with energy exceeding 6.5 keV, the x-ray transmission in this round was limited by the 0.012" thick aluminum layer used to protect the IP detectors. The effective thickness of the deflector (positioned at an oblique angle to the chamber axis), combined with that of the IP protective layer, would create > 50% attenuation for x-rays with energies $\lesssim$ 16 keV and more than 90% attenuation for x-rays with energies $\lesssim$ 10 keV. Nonetheless, for the first time in these experiments it was possible to perform x-ray spectroscopy betatron radiation produced by accelerated electrons. Acceleration of electrons to $\gtrsim$ 2 GeV energies, which already been achieved in the previous experimental round, was repeated in this round for a larger subset of the shots (Figure 6.21 and Figure 6.22). The various dimensions for the experimental setup are shown in Figure 6.20. To make the measurements by the high-sensitivity (MS) and high-resolution (SR) imaging plates easier to compare, the 30 cm × 10 cm (6000 × 2000 pixel) SR IP used in the previous round (Figure 6.14) was replaced by a 40 cm × 20 cm (8000 × 4000 pixel) SR IP, in order that both of the IPs would have the same dimensions. These IPs were positioned on top of one another (Figure 4.5), such that the electron and x-ray beams would first be detected by the MS IP, then traverse it, and be detected on the SR IP. This arrangement was chosen in order to designate the more sensitive MS IP as the primary detector for the betatron x-rays. The energetic electrons would be undergo minor attenuation propagation through the ferrite layer of the MS IP to reach the SR IP, therefore either detector could be used to detect electrons and the optimum detector would depend on the electron charge. For low-charge shots, the high-sensitivity MS IP would be the appropriate detector; high-charge shots, on the other hand, could lead to saturated scanner read-outs for the MS IP, making the higher-resolution SR IP the better

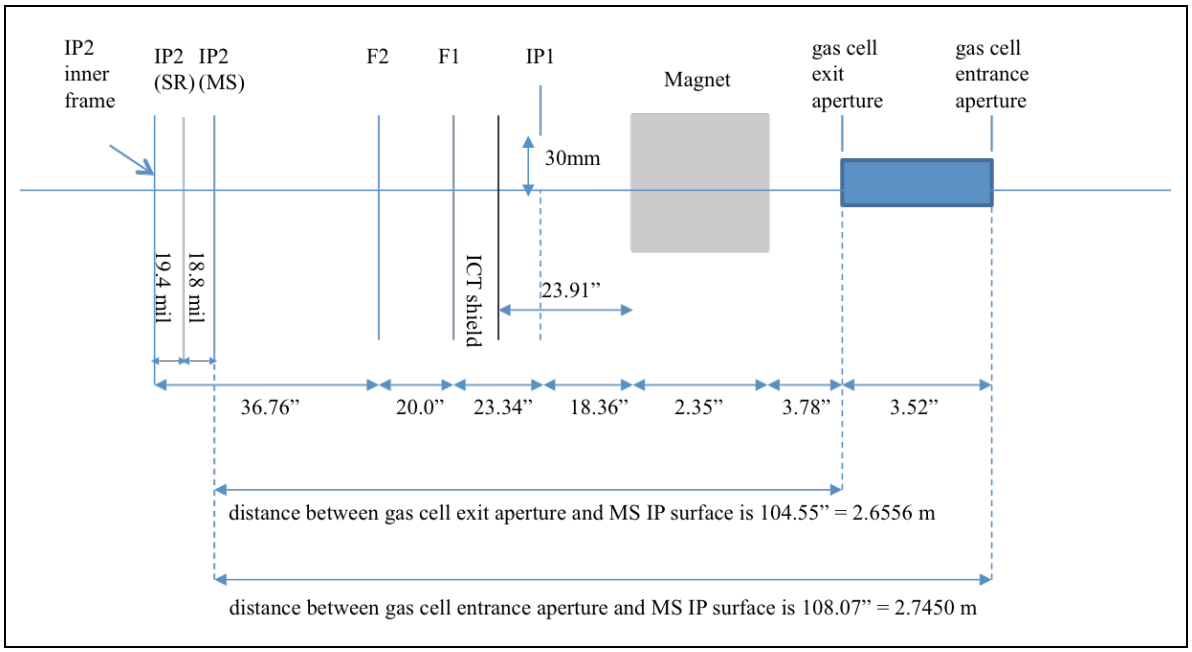

Figure 6.20: Dimensions of the experimental setup in the LWFA 3.0 experiment

detector. The issues encountered during this round were the uncertainty regarding the position of the TPW laser far field (addressed for the next round), and the need to keep peak intensity of the laser pulses relatively low in order to accommodate damage in the M4 mirror of the TPW laser.

Qualitative Presentation of the Diagnostic Measurements

Approximate electron spectrum measurements for the shots from the LWFA 3.0 experiment are shown in Figure 6.21 and Figure 6.22. In several cases, the high-energy electron spectrum reached or exceeded 2 GeV. The charge $\gtrsim$ 300 MeV (measured on the large IP, i.e., farthest from the source) was typically > 100 pC; the total charge approached nC levels in several cases and, for shot 5671, exceeded 3 nC. Of more interest, from a diagnostic point of view, were the betatron x-ray measurements that were done for the first time during these experiments using aluminum and copper filters. A large number of shots in this round produced betatron radiation. Some of the diagnostic details for the electrons and x-rays from shots that produced betatron radiation are provided in Table 6-5. The table shows the number of scans required to remove saturation from IP detectors (as a qualitative indication of the detected electron charge) and the approximate maximum energy (high-energy tail) achieved. The visibility of the

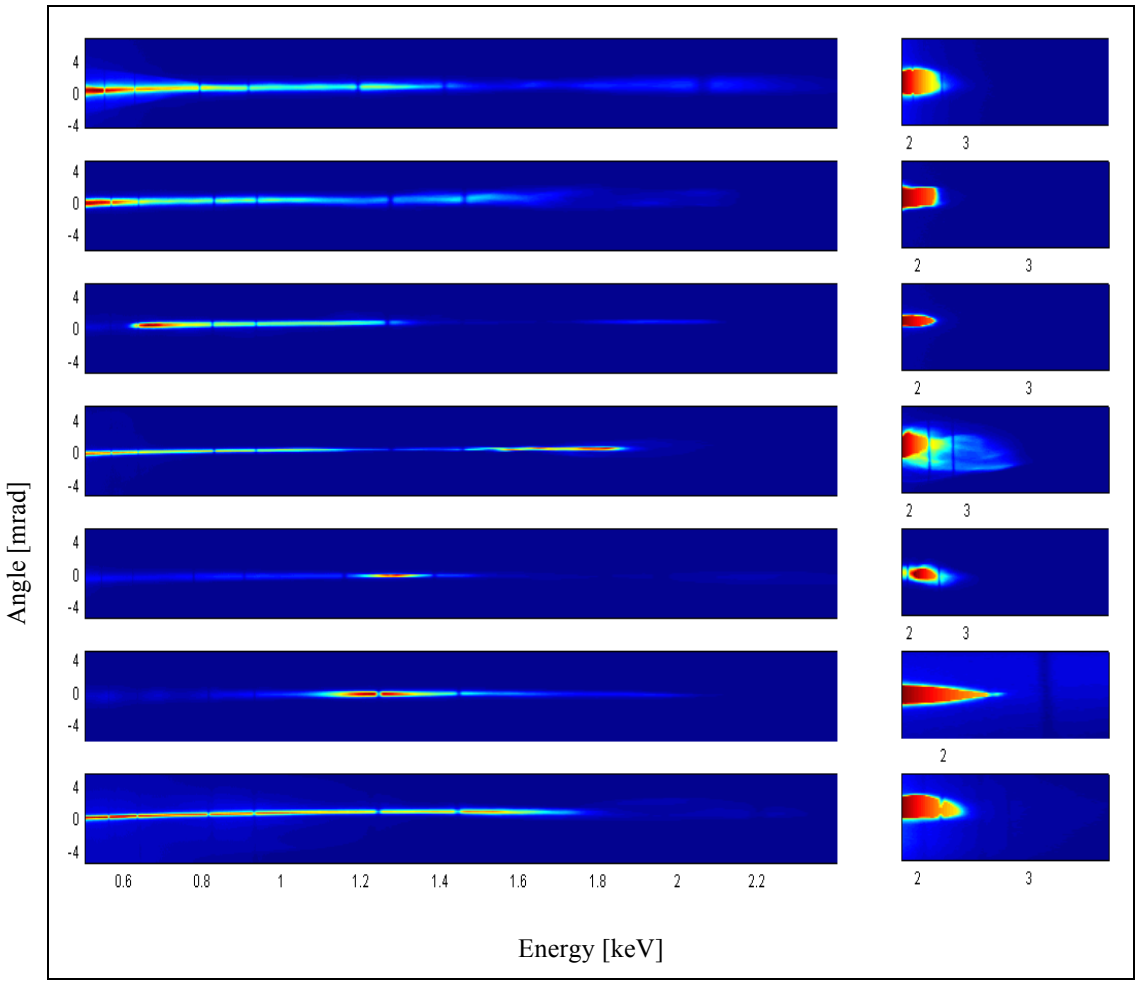

Figure 6.21: Approximate electron spectra for LWFA 3.0 shots producing the most energetic electrons (5483, 5860, 5862, 5769, 5478, 5514, 5518)

x-ray varied from very high to very weak; this is an indication of the detector PSL levels varying from high or saturated to very weak. This was indicative of the signal to noise level of the x-ray measurements and had consequences for x-ray spectroscopy. The variation in the X, Y coordinates of the center of the x-ray profile (as indicated by location of the pixel with peak PSL) are indicative of the pointing stability of the x-ray beam. The poor pointing stability of the x-ray radiation was one of the diagnostic challenges in these experiments. Histograms of the X and Y coordinates of the x-ray center are shown in Figure 6.23. The X coordinate had a shot-to-shot range of 20 mm (200 pixels on the MS IP) while the Y coordinate had a range of 25 mm (250 pixels on the MS IP). The shot-to-shot movement of the landing position of the x-ray spot on the detector meant that the transverse position of the x-ray filters in the path of the x-rays would determine the type of measurements that would be taken for each shot. A gallery

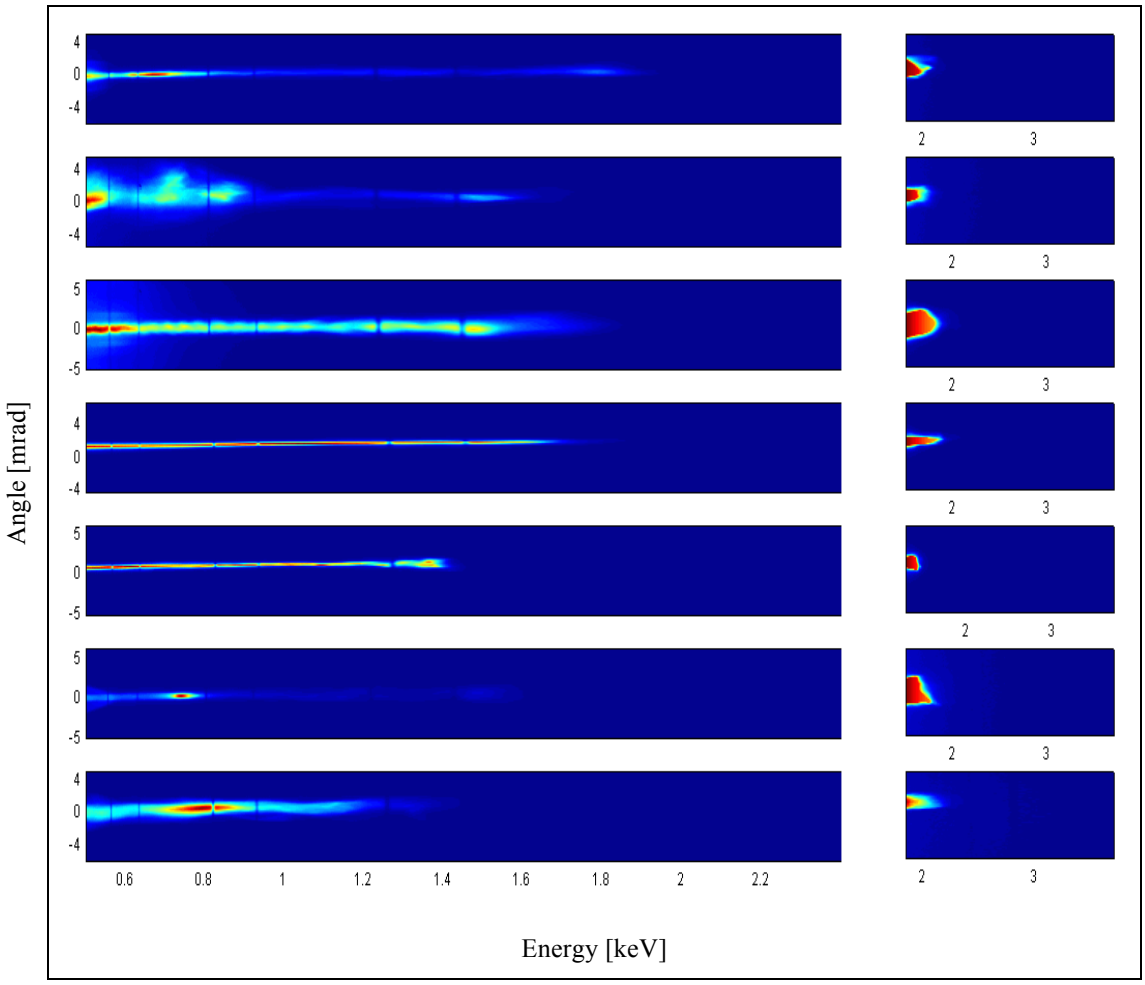

Figure 6.22: Approximate electron spectra for LWFA 3.0 shots producing the most energetic electrons (5559, 5824, 5485, 5839, 5831, 5481, 5804)

of the images of the betatron x-rays, corresponding to rows in Table 6-5 (in chronological order from left to right and top to bottom) is displayed in Figure 6.24. These images show the full x-ray profile, and the shadow that is visible on the profile (in all but the first image) is the result of attenuation that resulted from using filters to determine the spectrum. Initially a differential x-ray filter mask made from copper (denoted as filter Type I in Table 6-5), providing filters with nominal thickness of 0.5 mm, 1 mm, and 2 mm, were used to measure the x-ray spectrum (the first two rows in Figure 6.24). When it became clear that the x-ray energy was not always high enough for measurement by copper filters (attenuation was too high), a new type of differential filter mask (denoted as filter mask Type II in Table 6-5) was made in aluminum and copper versions and providing filters with thickness 0.25 mm, 0.5 mm, 1 mm, and 2 mm (the remaining rows in Figure 6.24). It was known from prior studies that the complete energy

#	Date	Shot	IP Scans		Electron		Betatron X-ray				
			MS	SR	Has Streak?	E_{max} [GeV]	Visibility	X,Y [pixel]	X-ray Filter Mask		
									Type	Material	Combination
1	01/15/13	5478	1	6	Y	2	good, skewed	1931,975	none	NA	NA
2	01/15/13	5481	5	2	Y	1.8	good	2025,1027	I	Cu	NA
3	01/15/13	5483	2	1	Y	2	good	1958,897	I	Cu	NA
4	01/15/13	5485	2	1	Y	2	medium	2039,1025	I	Cu	NA
5	01/18/13	5514	3	5	Y	2.2	saturated	2049,1006	I	Cu	NA
6	01/18/13	5516	2	1	Y	1.8	weak	1948,1046	I	Cu	NA
7	01/18/13	5518	3	2	Y	2.3	medium	2040,1006	I	Cu	NA
8	01/24/13	5559	3	3	Y	1.4	good	1930,860	II	Al	NA
9	01/28/13	5573	2	1	Y	1.2	very weak	2015,880	II	Al	NA
10	02/01/13	5671	2	1	N	0.8	saturated	1961,997	II	Al, Cu	1
11	02/01/13	5673	2	3	Y	1.2	weak, skewed	1998,908	II	Al, Cu	1
12	02/07/13	5714	6	1	Y	1.2	very weak	2047,868	II	Al, Cu	1
13	02/07/13	5722	4	2	Y	1.5	very weak	2054,917	II	Al, Cu	1
14	02/08/13	5751	2	1	Y	1.1	very weak	1968,918	II	Al, Cu	1
15	02/11/13	5762	4	1	Y	0.9	weak	1948,840	II	Al, Cu	1
16	02/11/13	5769	12	3	Y	2.5	medium, skewed	1964,828	II	Al, Cu	1
17	02/12/13	5785	13	2	Y	1	weak	1945,864	II	Al, Cu	2
18	02/12/13	5791	3	1	Y	1.1	very weak	1991,794	II	Al, Cu	2
19	02/13/13	5804	7	6	Y	1.6	saturated	1948,907	II	Al, Cu	2
20	02/13/13	5812	5	1	Y	1.8	weak, skewed	2001,859	II	Al, Cu	2
21	02/13/13	5824	16	1	Y	1.3	saturated	1929,887	II	Al, Cu	2
22	02/14/13	5831	12	2	Y	1.2	weak	1924,885	II	Al, Cu	3
23	02/14/13	5839	6	2	Y	1.1	weak	1853,853	II	Al, Cu	3
24	02/15/13	5860	16	1	Y	1.9	medium, skewed	2004,828	II	Al, Cu	3
25	02/15/13	5862	17	2	Y	1.5	saturated	1938,881	II	Al, Cu	3
26	02/15/13	5866	16	1	Y	1.4	weak	1955,872	II	Al, Cu	3

Table 6-5: Summary of selected diagnostic information for LWFA 3.0 shots that produced betatron radiation.

range of the conventional x-ray spectrum could be covered using only Al and Cu filters of different thicknesses as absorbers [37] and the reasonable assumption was made that these two materials together would yield sufficient measurements for the deconvolution of the betatron x-ray spectra and the detector (IP + filter mask) response functions. It was also assumed, initially, that measurements from different shots, and different locations on different masks, could be combined to determine the x-ray spectrum. This assumption would require that the spectrum not change significantly from shot to shot, and between different regions of the x-ray profile for the same shot. It soon became clear that measurements taken from different shots, i.e., using the Cu mask measurements from one shot and combining them with Al mask measurements from another, gave inconsistent spectral data points, even after correction for the peak intensity of the two shots. To

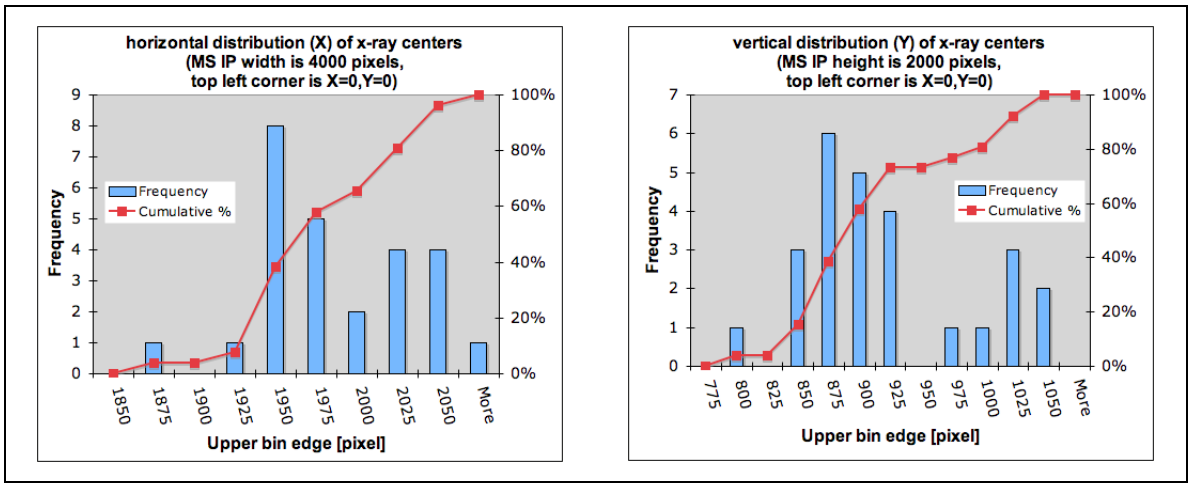

Figure 6.23: Histograms of the coordinates of the x-ray peak intensity pixel on the detector in the 3rd experimental round. The X coordinate had a 20 mm range (200 pixels on the MS IP) [left]. The Y coordinate had a 25 mm range (250 pixels on the MS IP) [right].

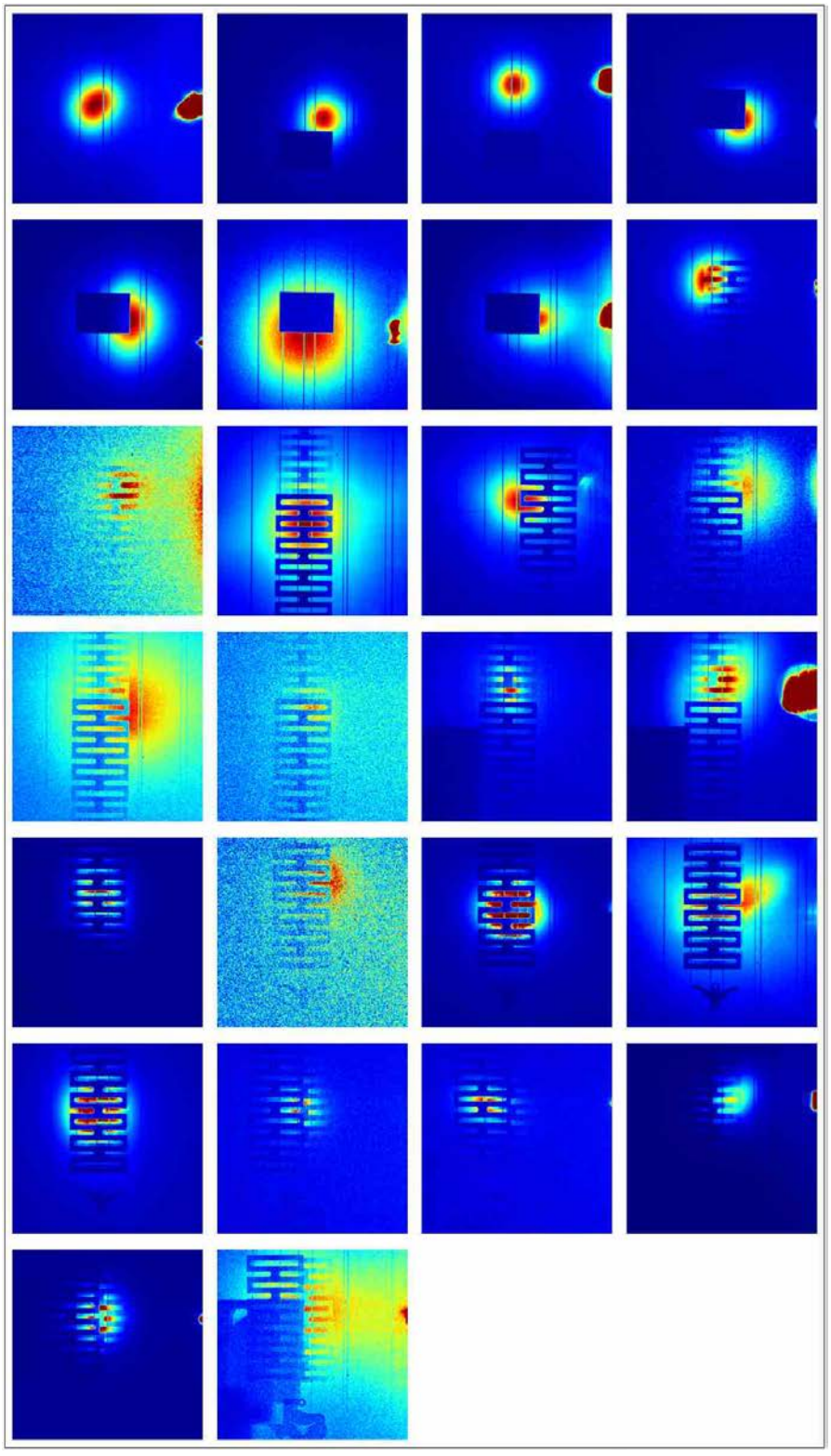

Figure 6.24: Betatron radiation measurements from the LWFA 3.0 experiment: the intensity of the x-ray radiation and its coverage by the filters varied from shot to shot.

address this, the Al and Cu masks were used together in each shot. Several filter combinations (denoted 1, 2, and 3 in Table 6-5) were tried. In combination 1, the two masks were placed vertically side by side, Al on top of the Cu. Then in order to increase the number of spectral data points, the Al and Cu masks were overlaid in two ways. In combination 2, the Al and Cu masks have an offset of half a step, covering a smaller region of the x-ray profile; in combination 3, the masks have an offset equal to half the mask width, covering a relatively larger region of the x-ray profile. Combination 1 (3rd and 4th rows in Figure 6.24) provides adequate coverage of the x-ray profile in vertical direction and accommodates the vertical pointing variation of the x-ray beam. Combination 2 (5th row in Figure 6.24) provides a larger set of unique filter measurements by combining Al and Cu of various thickness; this comes at the prices of worse coverage making it prone to miss region of the x-ray profile. The final configuration chosen, combination 3, provides better horizontal coverage of the x-ray profile as well as a larger set of unique filter measurements than combination 1.

Quantitative Presentation of the Diagnostic Measurements

Attempts to determine the betatron x-ray spectrum started by combining the measurements using filter mask Type I (copper) from one shot with those of the filter mask Type II (aluminum version). These are shown in Figure 6.25, where the Cu (left) and Al (right) masks are shown, for shots 5514 and 5559, respectively. Following a normalization of the measurements from the two shots to make the peak intensity measurements commensurate, deconvolution of the measurements produced the spectrum data points shown in the bottom panel of the figure. It may be seen that the data points obtained for high-energy part of the spectrum (blue) using the Cu mask in shot 5514, when combined with data point for the low-energy part of the spectrum (red) using the Al mask in shot 5559, do not allow a smooth curve to be traced through the data points given the error bars. This indicated that the x-ray spectra for the two shots were different enough to prevent a combination of their differential measurements. There were also indications that even for the same shot, the spectrum changed from one region to another. Attempts to normalize all regions of the x-ray profile to its peak value had mixed success; this is because for a GeV accelerator, where the x-ray beam divergence is relatively

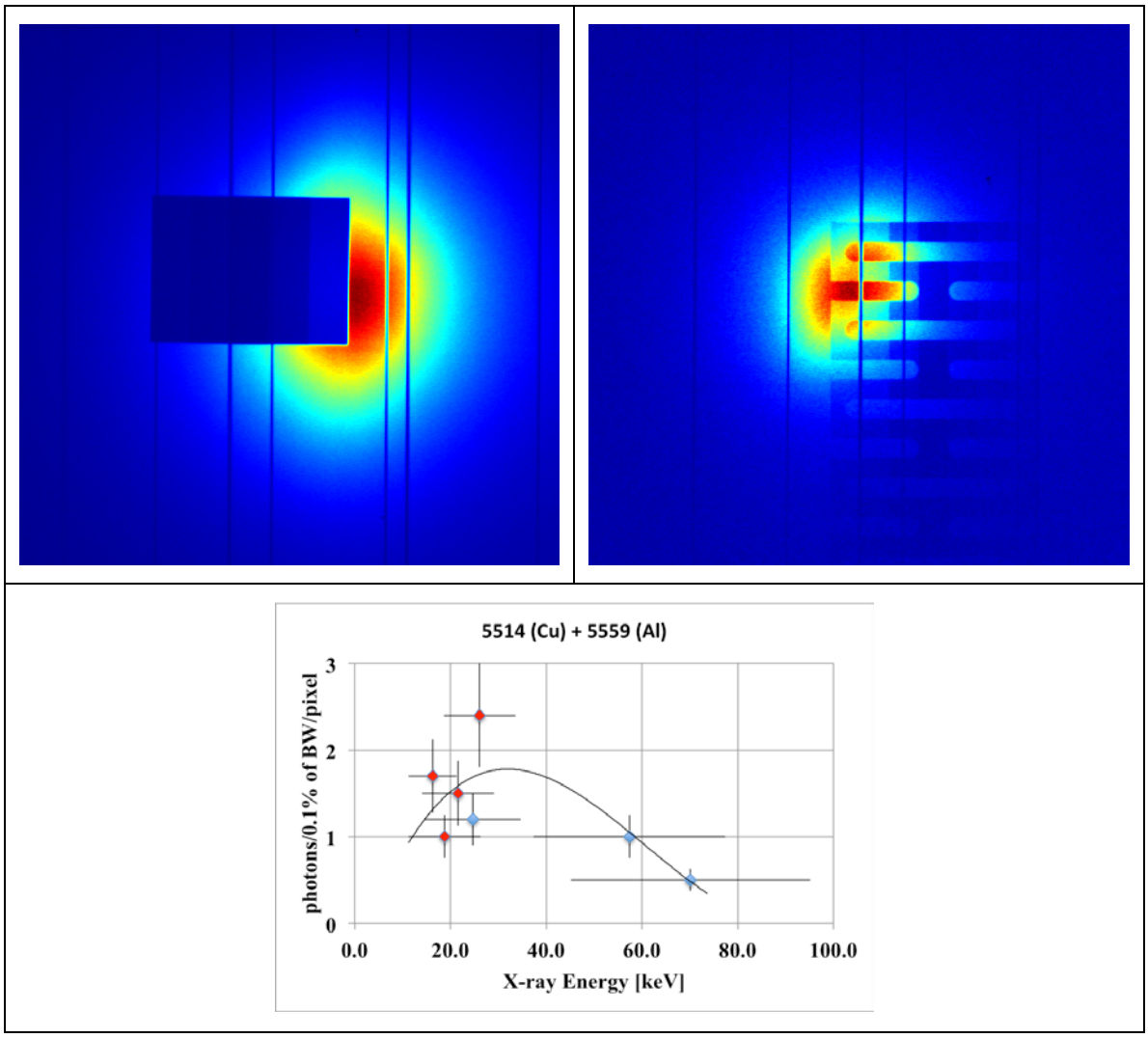

Figure 6.25: Top left: Cu mask Type I used to measure the high-energy region of the x-ray spectrum for shot 5514; top right: Al mask Type II used to measure the low-energy region of the x-ray spectrum for shot 5559. Bottom: betatron spectrum obtained by combining the differential measurements from one shot with those from another.

smaller (Eq. 6.4), the spectrum change, both in its scale as well as its normalized shape, can be significant for different regions of filter masks; the difference in shape may not be addressed by a normalization of the detector measurements, because the detector response function itself is a function of energy, therefore the measurement at each pixel depends both on the shape of the spectrum incident at that pixel and the shape of the response function (i.e., is a convolution integral). To ensure the possibility that measurements for a differential filter pair both referred to the same incident spectrum, filters were sampled on iso-intensity contours. Under the assumption that the incident

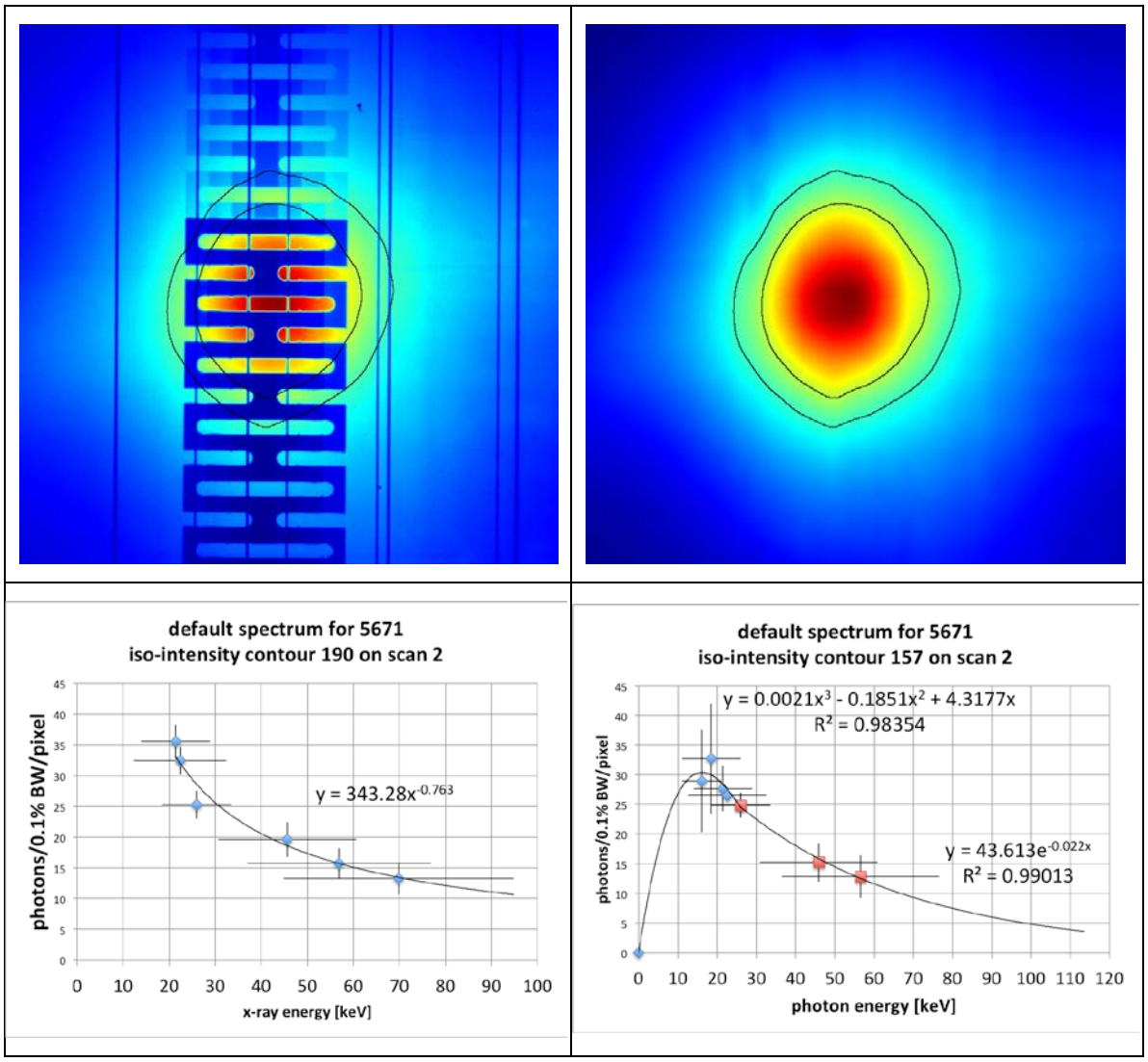

Figure 6.26: Top left: Al (top) and Cu (bottom) masks of Type II used to measure the spectrum for shot 5671; top right: reconstructed x-ray profile and iso-intensity contours for PSL 190 (inner) and PSL 157 (outer). Bottom left: betatron spectrum measured on iso-intensity contour PSL 190; bottom right: betatron spectrum measured on iso-intensity contour PSL 157.

spectrum remained the same on such contours, sampling the filters on contours would ensure that the measurements for a differential pair represented the same spectrum and could be differenced. Figure 6.26, on top left, shows the detector measurement for shot 5671 (using filter mask Type II and combination 1 of the Al and Cu filters.) After a reconstruction of the x-ray profile (5.7.1), iso-intensity contours are drawn on the x-ray profile (top right). These contours are then used to sample the filter masks (top left). The measurements on contour PSL 190, following deconvolution, produce 6 spectrum data points (bottom, left). The measurements on the larger contour, PSL 157, produce 7 spectrum data points (bottom, right). Unlike contour PSL 157, contour PSL 190 does not

cross the mask along filters that would provide the differential measurements required to reveal the spectrum below 20 keV. Although the issue of different iso-intensity contours measuring different parts of the x-ray spectrum can be somewhat mitigated by a careful design of the filter mask, the poor pointing stability of the x-ray beam makes this a feature of differential x-ray spectroscopy performed on iso-intensity contours.

Lanex-Scintillator Detector Measurements

In this round, the Lanex and scintillator combined diagnostic was re-deployed; however, an ND filter of 0.6 was placed in front of the CCD objective lens to prevent saturation of the color CCD pixels. The resulting reduction, of nearly a factor of 4, in the intensity of the luminescence incident on the CCD pixels was successful in preventing CCD saturation in all but a few cases, making it possible to use the CCD measurements quantitatively (e.g., to calculate charge) as well as qualitatively (to detect the presence of high energy electrons). The noise-to-signal ratio of the calculated charge was as low as 10% and as high as 50%, due to background present in the reconstructed images for the CCD channels. This background primarily affected the red, and to smaller degree the blue, channel. An outlier removal algorithm was then applied to them; this process removed speckles, and other outlier pixels. Following that, the background signal (including CCD dark noise, and possible bremsstrahlung background) was subtracted from the images using a rolling ball background removal algorithm. Figure 6.27 the montage of Lanex-scintillator detector measurement for a sample of shots that produced electrons with high enough energy to be detected. On each row, the left image is the RGB image created by combining the reconstructed CCD channel output image; it roughly corresponds to the image observed on the color CCD immediately following the system shot. The image in the middle is the luminescence due to the interaction between energetic electrons and the Kodak Lanex Regular and is recovered from combining the reconstructed R, G, and B CCD channel images in amounts determined by the overlap of the Lanex emission spectrum and the color CCD Relative Response curves (for details see Appendix E). Similarly, the image on the right is the luminescence from the plastic scintillator. In addition to providing a real-time diagnostic for the presence of high-energy electron charge, the recovered Lanex images enabled the calculation of the high-

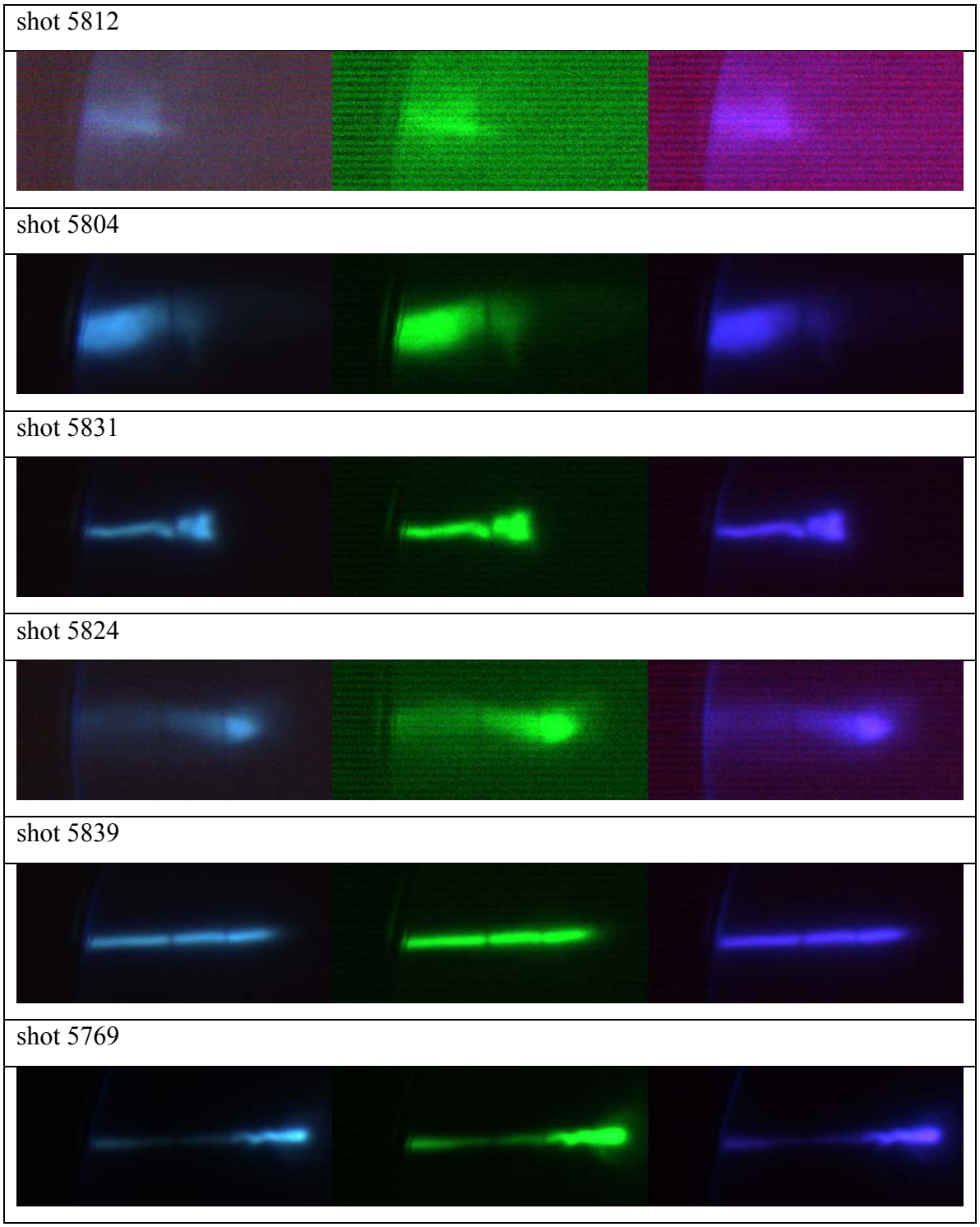

Figure 6.27: Montage of Lanex-scintillator diagnostic results for several LWFA 3.0 shots producing high-energy electrons. Original (raw) CCD image (left), computed Lanex component of the image (middle), computed scintillator component of the image (right)

energy charge. Measurements from shots not affected by saturation, and having the lowest background level, were chosen for this purpose (shots 5831 and 5839). The

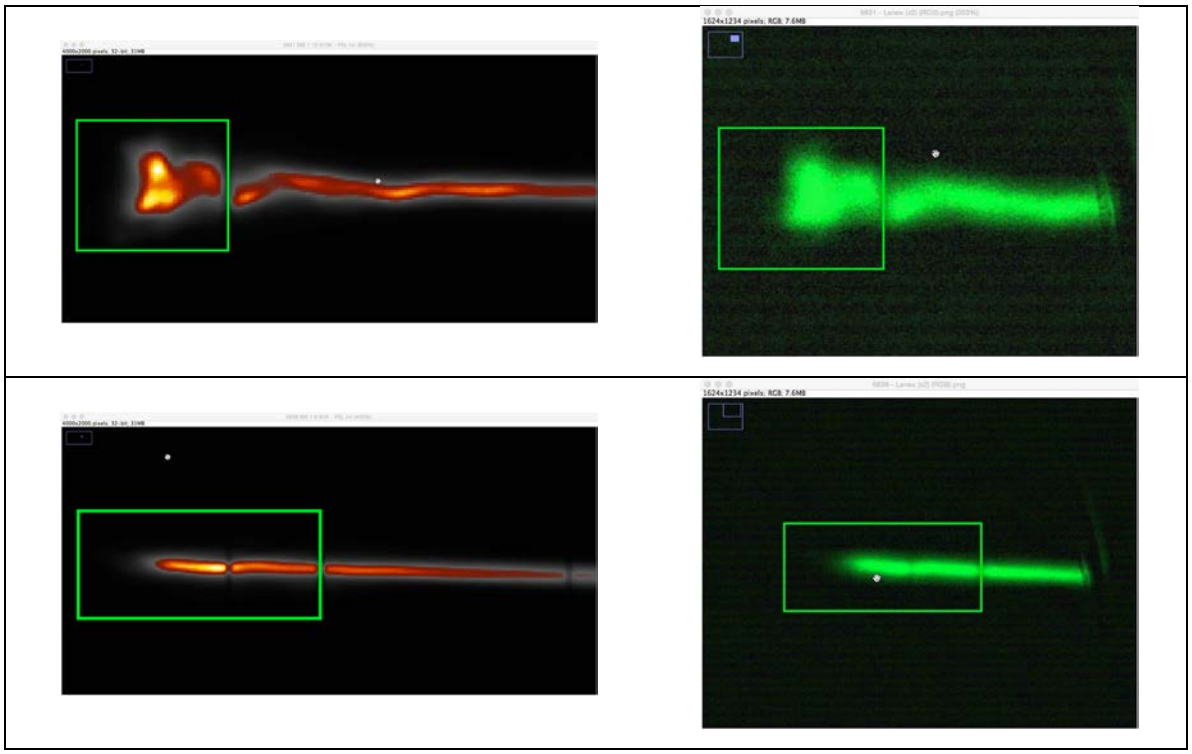

Figure 6.28: Charge from commensurate regions (rectangular selections) of the measurements by the MS IP (left) and Lanex (right) detectors were compared to determine the relative to absolute conversion factor of the color CCD Relative Response curves (**Figure E-5**). Top: shot 5831; bottom: shot 5839.

preliminary step of the calibration of the color CCD Relative Response curve, via the comparison of the commensurate regions of the high-energy electron signal on the Lanex and MS IP detectors (Figure 6.28), produced a relative to absolute conversion factor of $C_{calib} = 0.63 \pm 0.05$ (Appendix E). This step was necessary because only the relative, but not the absolute, quantum efficiency of the Sony ICX274AQ sensor, used in the scA1600-14fc color CCD, was publicly available. This is shown in Figure E-5.) Using this conversion factor, the Lanex-scintillator diagnostic may henceforth be used as an independent method to determine the high-energy electron charge. Unlike the imaging plate, which requires scanning (usually more than once when charge is high and there is scanner PMT saturation), the recovered Lanex signal may immediately be used to calculate the electron charge without the need for breaking the vacuum, removing the IP, and scanning it. This makes it possible to calculate accelerated electron charge in real time.

6.5 4th Experimental Round ("LWFA 4.0")

This experiment ran from 05/05/2014 to 05/30/2014. It benefitted from the optimization of the midfield profile of the laser pulse, and improvements in the diagnostics for a more accurate determination of the laser far field. It was noted that, at times, enhanced charge and photon number resulted when two hot spots were present in the far field of the laser profile. This was attributed to the "double bubble" mechanism [57] and successful attempts were thereafter made to replicate this by using the deformable mirror adaptive optics to dial in two hot spots in the far field of the laser profile. The spectroscopy of the betatron radiation was significantly enhanced by the replacement of Al and Cu differential filters with an array of 7-metal Ross K-edge filters. The design of the x-ray filter mask took into account the accuracy and ease of the reconstruction for the x-ray profile, by using a regular array of circular filter arranged in a packed hexagonal geometry. The geometry of the filters on the mask was optimized to maximize the crossing of filters by contours. The regularity of the geometry increased the data analysis speed and made is possible to process more x-ray data than in the previous experiment (see Figure 5.12 and 5.6) . It also made it possible to spatially resolve the x-ray spectrum. A new imaging plate frame was created for the purpose of housing the new x-ray mask that contained the filters. By removing the protective 0.012" aluminum IP cover used in all previous experiments in the region exposed to the x-ray radiation and instead housing the x-ray filters between a protective layer of 0.001" aluminum foil and 0.010" PEEK polymer substrate (held in place by O-rings made from material transparent to x-rays), it was possible to detect x-rays with energies down to ~7 keV, an increase of 9 keV in the spectral range over the previous experiment. There was a large increase in the amount of charge detected. This led to saturation in the electron signal, and even the x-ray signal, on the MS IP detector on nearly every shot that produced electrons. This required numerous scans of the imaging plates to remove saturation from the signal according to the methodology described in C.2. Charge with energy below 300 MeV, previously detected on small IPs closer to the gas cell, was therefore not detected due to the limited time available between the laser shots for the scanning of IP data. In this experiment, for the first time, an attempt was made to determine the betatron radiation source size using the phase contrast imaging of copper wires of several thicknesses exposed to the x-ray

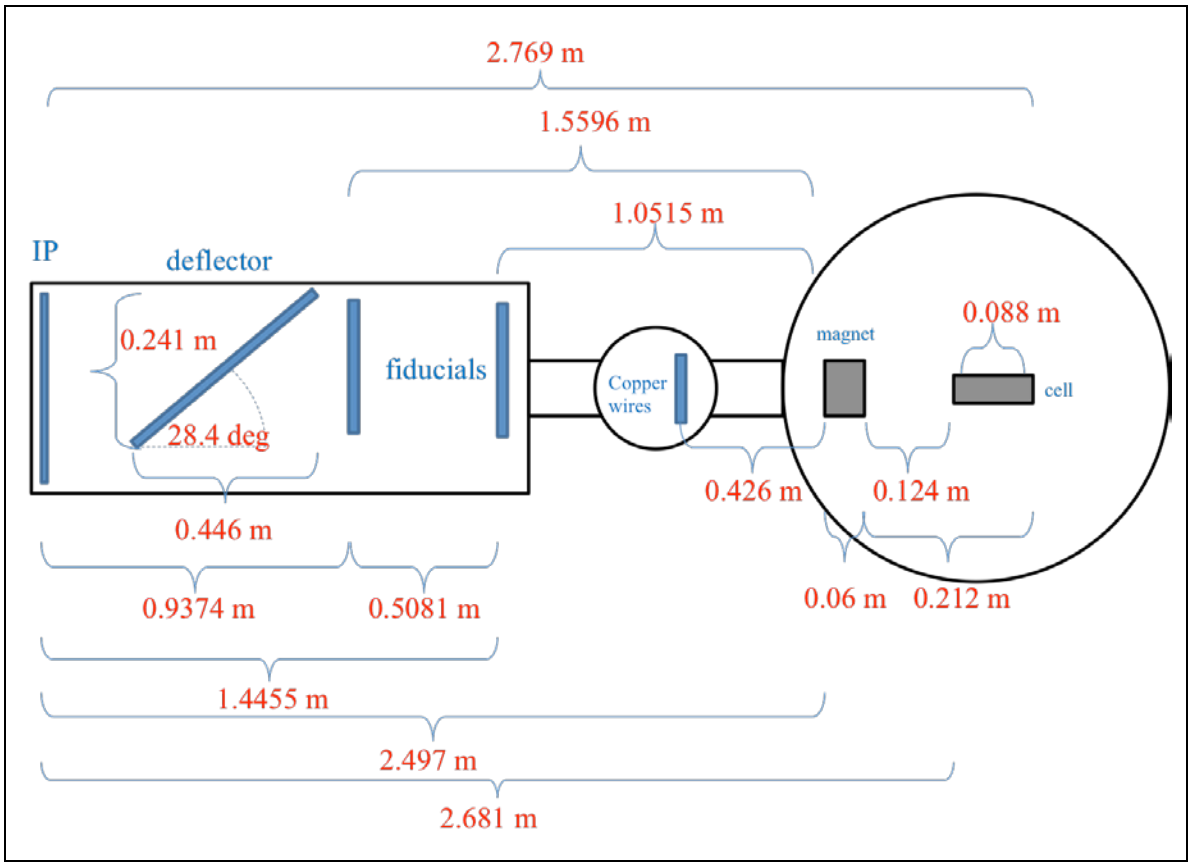

Figure 6.29: Dimensions of the experimental setup in the LWFA 4.0 experiment [Image courtesy of Rafal Zgadzaj].

radiation and the analysis of phase contrast data. The major achievements of this experiment were the stability of energetic electron production (90% of the shots produced energetic electrons), the spatially resolved measurement of the spectrum of the betatron radiation, and enhanced charge (~ 2nC) and photon production (exceeding 10^{10} photons) using the "double bubble" mechanism. Figure 6.29 shows the various dimensions used in the experimental setup in this round. Due to a shift in the relative positioning of the imaging plate detector and gas cell, the average position of the x-ray center pixels on the 4000 × 2000 pixel MS IP changed from (in pixels) X = 1976 ± 49, Y = 909 ± 71, in the previous round to X = 1862 ± 34, Y = 938 ± 68. The more than 1-cm systematic shift in the X coordinate of the x-ray profile center had the consequence that the betatron radiation largely cleared the tungsten fiducial wires closest to the chamber axis and used for locating the x-ray source position via triangulation of the fiducial shadows on the x-ray profile. The x-ray source position can be used for a deconvolution of the electron energy from its launch angle using the scattering shadows created by the fiducials in the

streak produced by the magnetically deflected electrons on the detector (3.4). To compensate for the shift in the x-ray profile center, the fiducial racks were both moved 0.5" towards the chamber axis. In what follows, important experimental results from this experimental round are presented.

Overview of the Diagnostic Measurements

The majority shots in this experimental round (~90%) produced high-energy electrons, and almost all of these were accompanied by intense betatron radiation. Figure 6.30 is a gallery of selected betatron x-ray measurements from this round. The x-ray profiles have been reconstructed to remove the shadows due to the presence of filters and fiducial wires. In all cases the images are centered such that the center of the 550 × 550 pixel image (100-μm pixel size) coincides with the geometric center of the x-ray profile (G.1). The x-ray measurements reveal a large variation in the x-ray divergence. The FWHM of the x-ray profiles in Figure 6.30 was determined using the standard method of applying the factor $2\sqrt{2 \ln 2} \sim 2.3548$ to the standard deviation of a Gaussian fit to the line-out drawn across the center of the x-ray profile and along the major axis. The FWHM ranged from 4.3 mrad to 11.0 mrad, averaging at 6.4 mrad with a standard deviation of 1.4 mrad. In addition to the varying divergence, the shape of the x-ray profile also changed from shot to shot, with elongation of the x-ray profile observed parallel to the direction of the driving laser polarization (vertical), perpendicular to the direction of the polarization, and rotated with respect to the direction of the polarization. The pointing variability of the x-ray beam posed a challenge to its diagnostics. Figure 6.31 displays the histograms of the X and Y coordinates of the geometric center of the x-ray profile on the detector; the average and standard deviation of the coordinates were (in 100-μm pixels) X = 1862 ± 34, Y = 938 ± 68. To appreciate the impact of this variation, note that when expressed in radians, the X coordinate of the x-ray center had a range of 6.6 mrad and the Y coordinate had a range of 12.8 mrad; this exceeds the average FWHM of the x-ray profile itself, i.e., 6.4 ± 1.4 mrad. The pointing variability of the x-ray beam was greatly mitigated by the use of a new design (see 5.5.1) for the x-ray filter array. Also note that the vertical variability of the x-ray beam was larger in this round compared to the

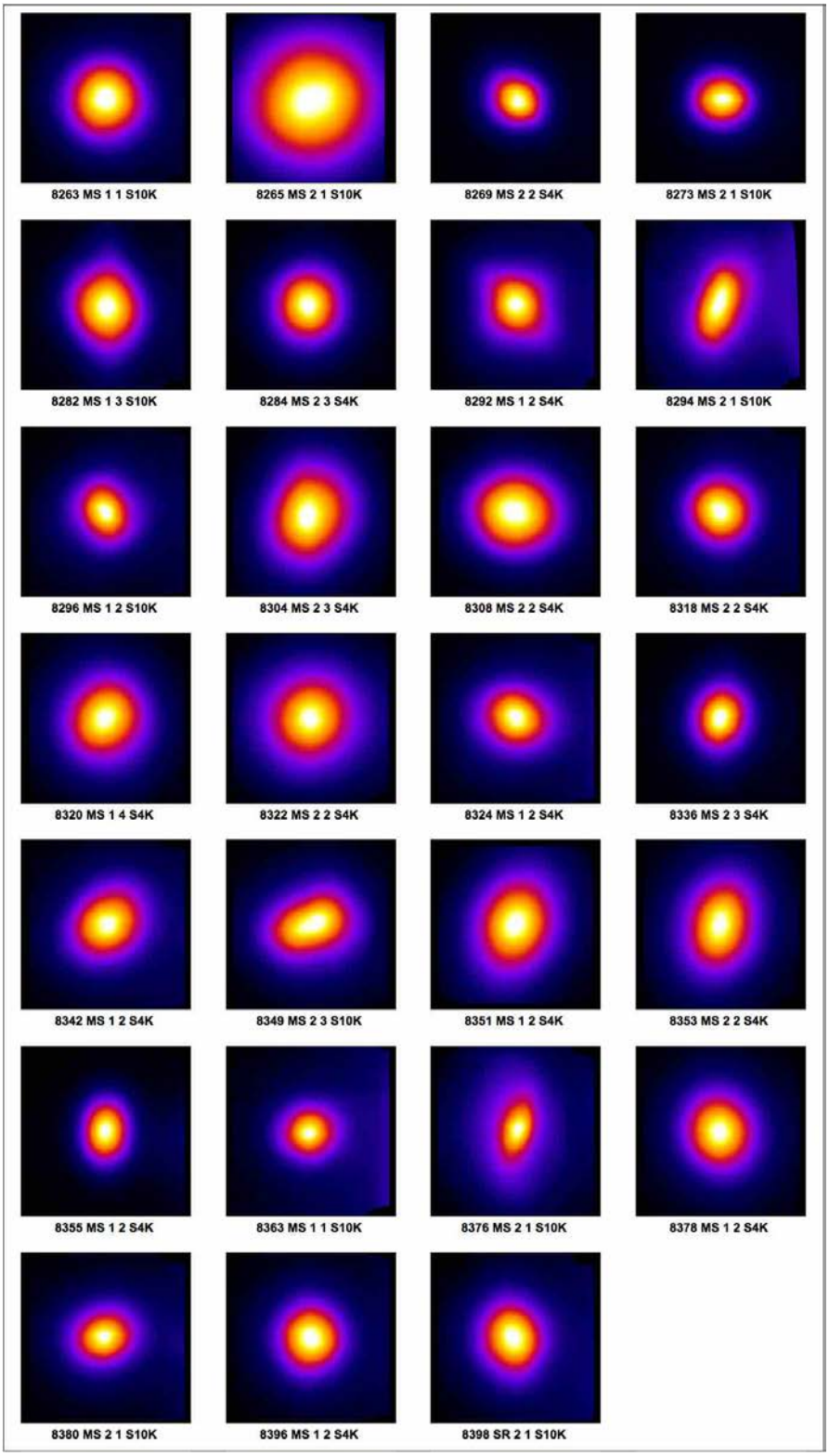

Figure 6.30: Reconstructed betatron radiation measurements from the LWFA 4.0 experiment showing the shot-to-shot variation in the shape of the x-ray beam.

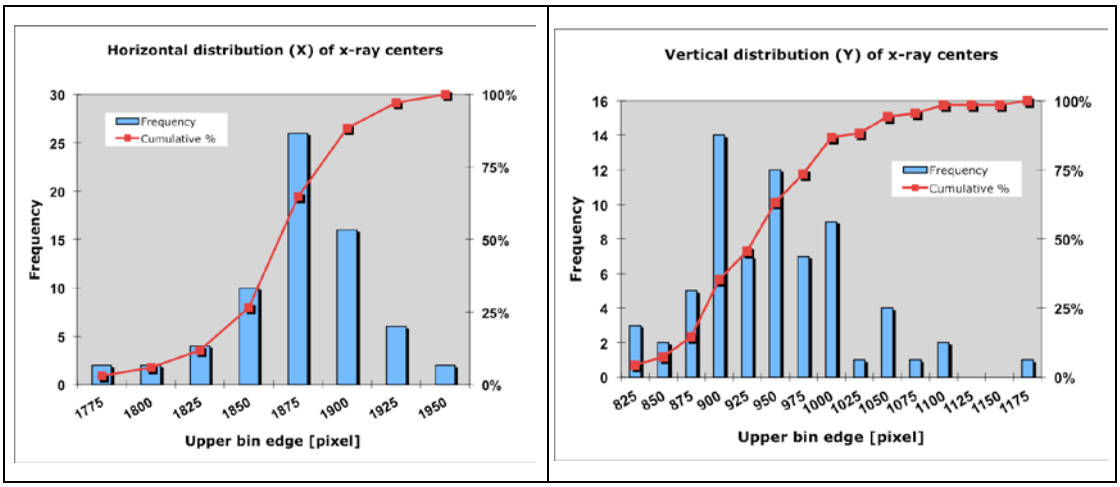

Figure 6.31: Histograms of the coordinates of the x-ray peak intensity pixel on the detector in the 4th experimental round. The X coordinate had an 18 mm range (180 pixels on the MS IP) [left]. The Y coordinate had a 35 mm range (350 pixels on the MS IP) [right].

previous round (the range for Y increased from 25 mm to 35 mm), making the new design even more important in the x-ray measurements.

One of the goals of laser-wakefield experiments driven by the TPW laser has been to improve the reproducibility of the results by determining the link between experimental parameters and various observables. Given the nonlinear interaction between the laser and plasma, there is the small region of the parameter space (determined by the plasma density, laser pulse duration, spot size, and power) that is favorable to the production of energetic electrons. It was determined in the early rounds of the experiment that, given the typical parameters of the TPW laser pulse, plasma densities $\gtrsim 1 \times 10^{17}$ cm^{-3} and $\leq 6 \times 10^{17}$ cm^{-3} were favorable to the production of an electron beam with significant (> 100 pC charge). This corresponds to plasma periods ranging from 352 fs to 144 fs (Eq. 2.3). It was also found early on that a pulse duration $\gtrsim$ 130 fs and $\leq$ 170 fs was favorable to producing resonant interaction between the laser pulse and the plasma. The success of the 1st round of experiments covered by this dissertation (LWFA 1.5) is also attributed to improvements in the laser pulse far field accomplished by the introduction of deformable mirror adaptive optics. During the 3rd round of experiments (LWFA 3.0) the importance of the midfield of the laser pulse was recognized. Note that the focusing and alignment of the TPW laser pulse at the gas cell entrance is done with the low-energy OPA laser beam.

Thermal effects that accompany the high-energy (system) shot can cause the actual far-field position to differ from that determined for the OPA pulse. In addition, due to the non-Gaussian nature of the TPW laser pulse profile, the midfield laser profile can be materially different from the profile at the far field. The measurement and optimization of the midfield laser profile, using adaptive optics, was therefore recognized as important and carried out in the 4th round of experiments (LWFA 4.0). This is believed to have led to the production of energetic electron beams with significant charge for a large percentage (~90%) of the shots. A gallery of selected imaging plate measurements from the MS IP detector (100 μm pixel size) is shown in several figures (Figure 6.33 to Figure 6.37). In each case, the total measured charge (i.e., > 300 MeV) is displayed on the image. These images represent a 1700 × 400 pixel region of the first scan of the imaging plate and, in all cases, are vertically centered to coincide with the Y coordinate of the geometric center of the betatron x-ray; therefore the changing vertical position of the electron streak on the images from shot to shot is indicative of the different vertical offset between the electron bunch and the betatron radiation it produced. At a distance of 272.5 cm from the center of the gas cell, the 4-cm (400 MS IP pixels) height of each image panel represents a divergence of $\lesssim$ 15 mrad. In all cases, the first IP scan displays significant amount of pixel saturation due to the very high charge that was obtained in this round over the full range of the electron energy spectrum. Although these measurements are not suitable for the calculation of the electron charge and its energy spectrum due to this saturation of the detector measurements, they are suitable for the measurement of the full extent of the electron divergence and reveal features that are harder to discern in the unsaturated scans of the imaging plate. In particular, in a number of cases, the divergence of the electrons varied significantly with energy. In other cases, more than one electron bunch was produced; after deflection in the magnetic spectrometer, this appeared as more than one streak on the detector. These features are expected to correlate with the laser parameters as will be discussed below. Figure 6.38 to Figure 6.40 show the magnetically deflected electron bunches detected on the unsaturated scan of the imaging plate. These images represent a 1700 × 200 pixel region of the last scan of the imaging plate (the height of each image represents ~7.3 mrad); as in the previous images, they are vertically centered to coincide with the Y coordinate of the

geometric center of the betatron x-ray, therefore the changing vertical position of the electron streak on the images from shot to shot is indicative of the different vertical offset between the electron bunch and the betatron radiation it produced. These measurements can be used to calculate the electron bunch charge and energy spectrum, when combined with the electron saturation factor calculated according to the methodology described in C.2. In addition, these images reveal the fine features of the electron streak, including peaks in the charge distribution, and the shadows created by the tungsten fiducials that were in the path of the electron in the magnetic spectrometer. These fiducial shadows may be used to calculate the electron energy spectrum to high accuracy (5% resolution at 2 GeV), as described in 3.4. The vertical green lines in all images indicate, from right to left, electron energies ~1 GeV, ~1.5 GeV, ~2 GeV, ~2.5 GeV, and ~3 GeV, respectively. The high-energy tail of the electrons is evident in the saturated images (Figure 6.33 to Figure 6.37). The majority of the electron bunches approach or exceed ~1.5 GeV in energy; in a number of cases they exceed ~2 GeV and even approach or exceed ~2.5 GeV; in one case, for shot 8269, the high-energy tail of the electron streak exceeds 3 GeV.

This experimental round also produced many measurements of the betatron x-ray beams suitable for spectroscopy. Initially an attempt was made to calculate the x-ray spectrum on selected contours. The contour-specific x-ray spectra for two shots (8351 and 8378), in per unit energy (PUE, Eq. 5.5) and per unit bandwidth (PUBW, Eq. 5.9) representations, are shown in Figure 6.32. In the case of shot 8351, the spectrum corresponds to contour PSL 88; for shot 8378, the spectrum corresponds to contour PSL 55. In both cases, the 2nd scan of the MS IP detector was used for contour creation (scan 1 exhibited saturation), then saturation factors were calculated (C.2) and used to determine effective scan 1 detector measurements. The iso-intensity contour in each case was selected to provide the maximum number of Ross filter pair crossings. Out of a maximum of 7 possible pairs (corresponding to 7 points on the spectrum), in one case the contour yields 6 data points (8351) and in the other it yield 5 data points (8378). Neither contour yields a data point for the lowest energy bin of the Ross filter array (pair 1 in Table 5-2) which would correspond to a point on the spectrum at ~7.3 keV. As a result,

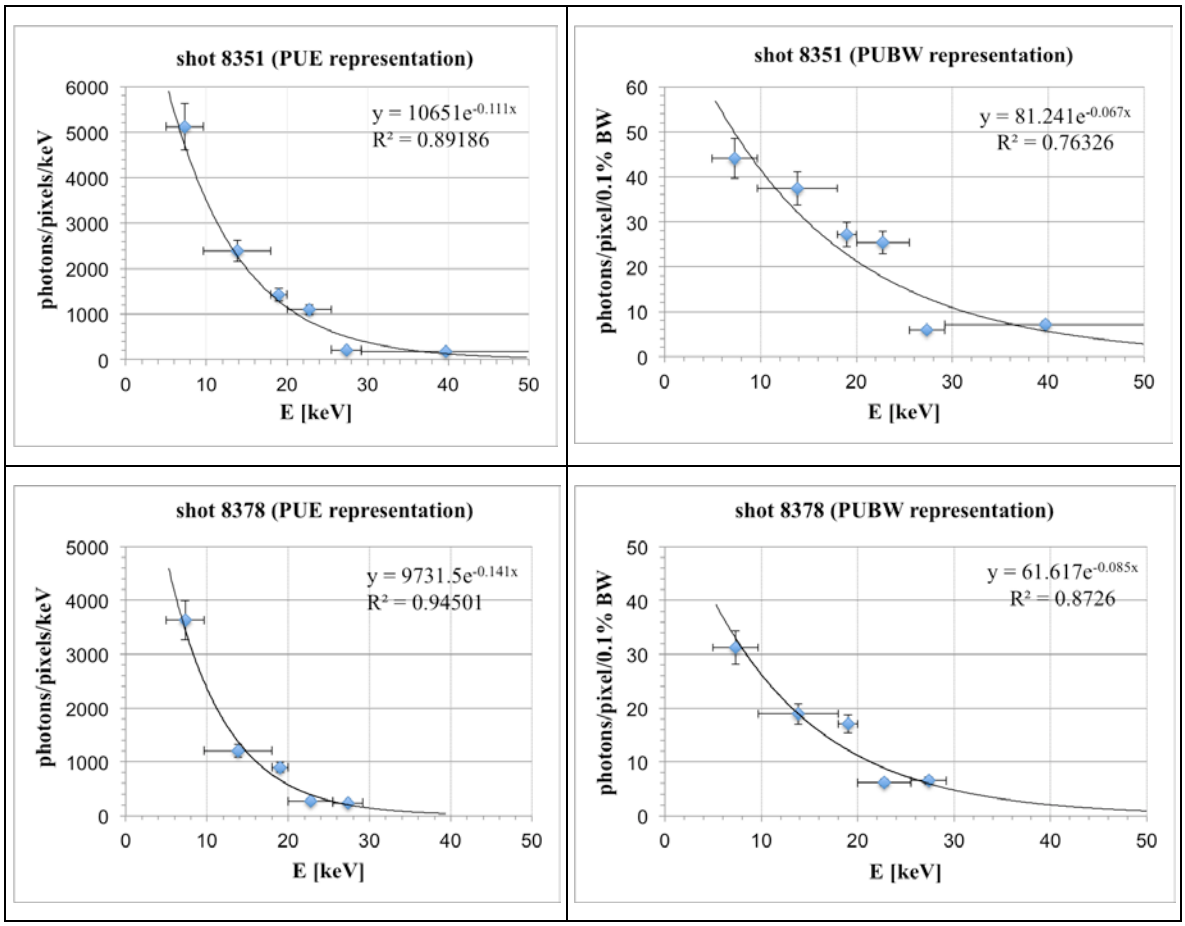

Figure 6.32: Contour-specific x-ray spectra, in PUE and PUBW representations, for 2 shots (8351 contour 88 PSL and 8378 contour 55 PSL) from the 4th experimental round.

the peak of the contour-specific spectrum is not unambiguously determined in either case. Other iso-intensity contours that would reveal the peak of the spectrum had fewer crossings in the high-energy side of the spectrum. Evidently, except in the cases where the iso-intensity contour crosses all 10 distinct filters required to complete the 7 different Ross pairs, contour-specific spectra are beset by the presence of gaps. For this reason, the contour-specific representation of the x-ray spectrum was abandoned in favor of a spatially resolved representation, where points on the spectrum from many contours were combined to reproduce the x-ray spectrum in 3 dimensions. This approach has the advantage that it can be used to fit a surface to points on the spectrum in 3 dimension, where the independent variables are the x-ray photon energy and the contour level (or the angle theta defined in Eq. 5.15). In most regions of the spectrum, the presence of gaps along one dimension (e.g., energy) of the spectrum is largely compensated by the presence of sufficient data in that neighborhood along the other dimension (angle), and

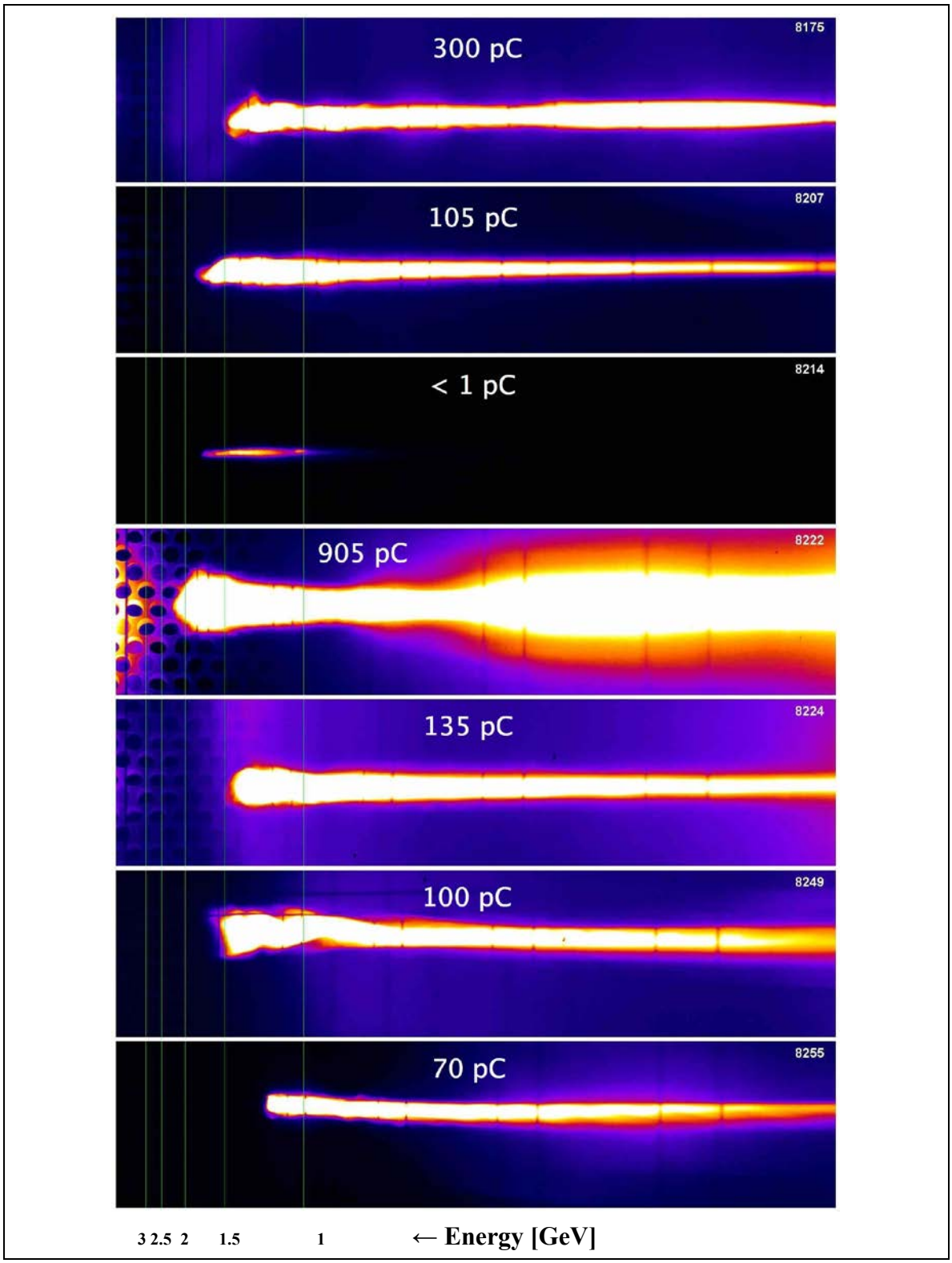

Figure 6.33: First (saturated) scan of the imaging plate detector for shots 8175, 8207, 8214, 8222, 8224, 8249, 8255, showing charge accelerated to ≳ 300 MeV. In each case, the image height is ≲15 mrad.

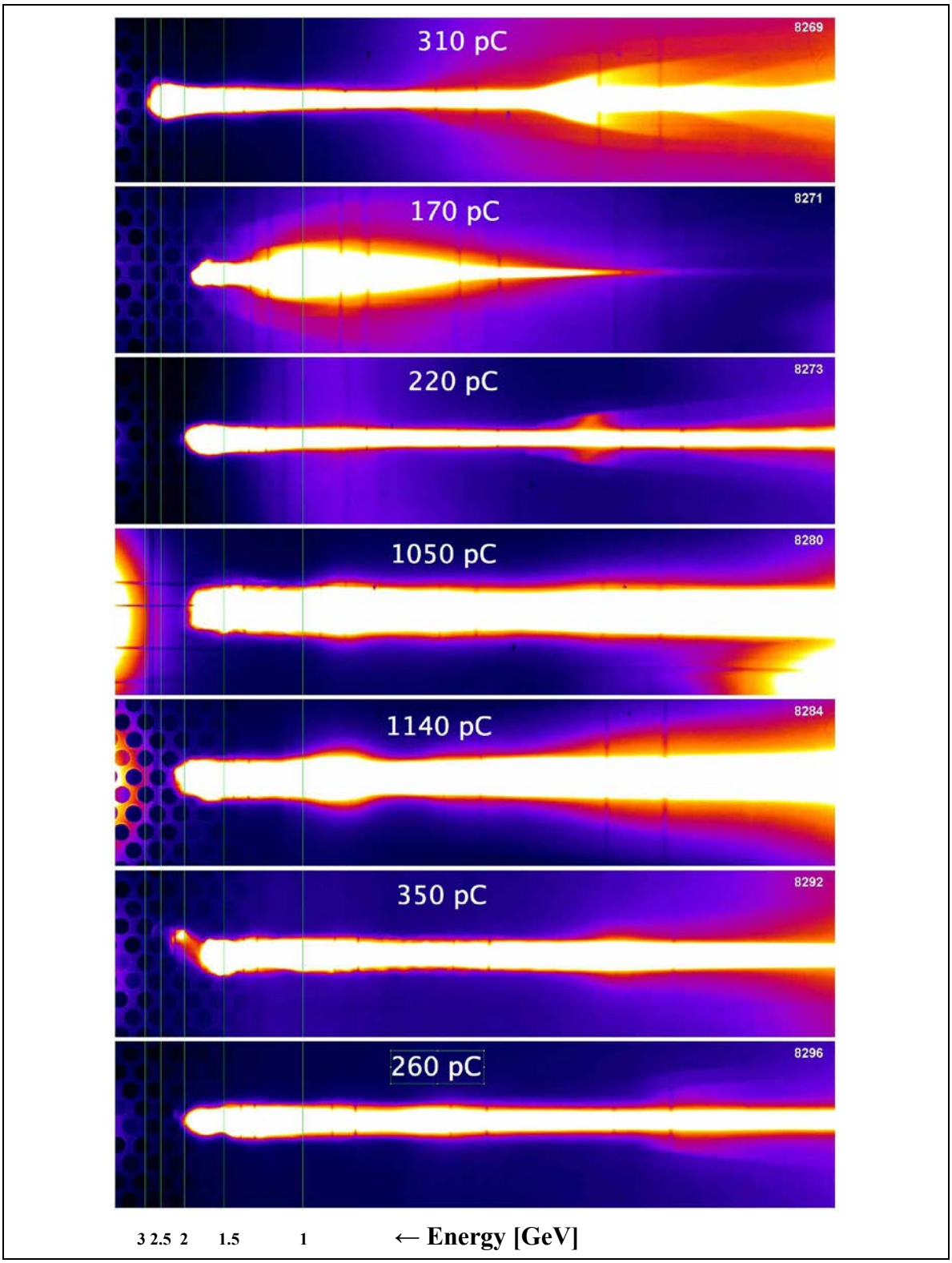

Figure 6.34: First (saturated) scan of the imaging plate detector for shots 8269, 8271, 8273, 8280, 8284, 8292, 8296, showing charge accelerated to ≳ 300 MeV. In each case, the image height is ≲15 mrad.

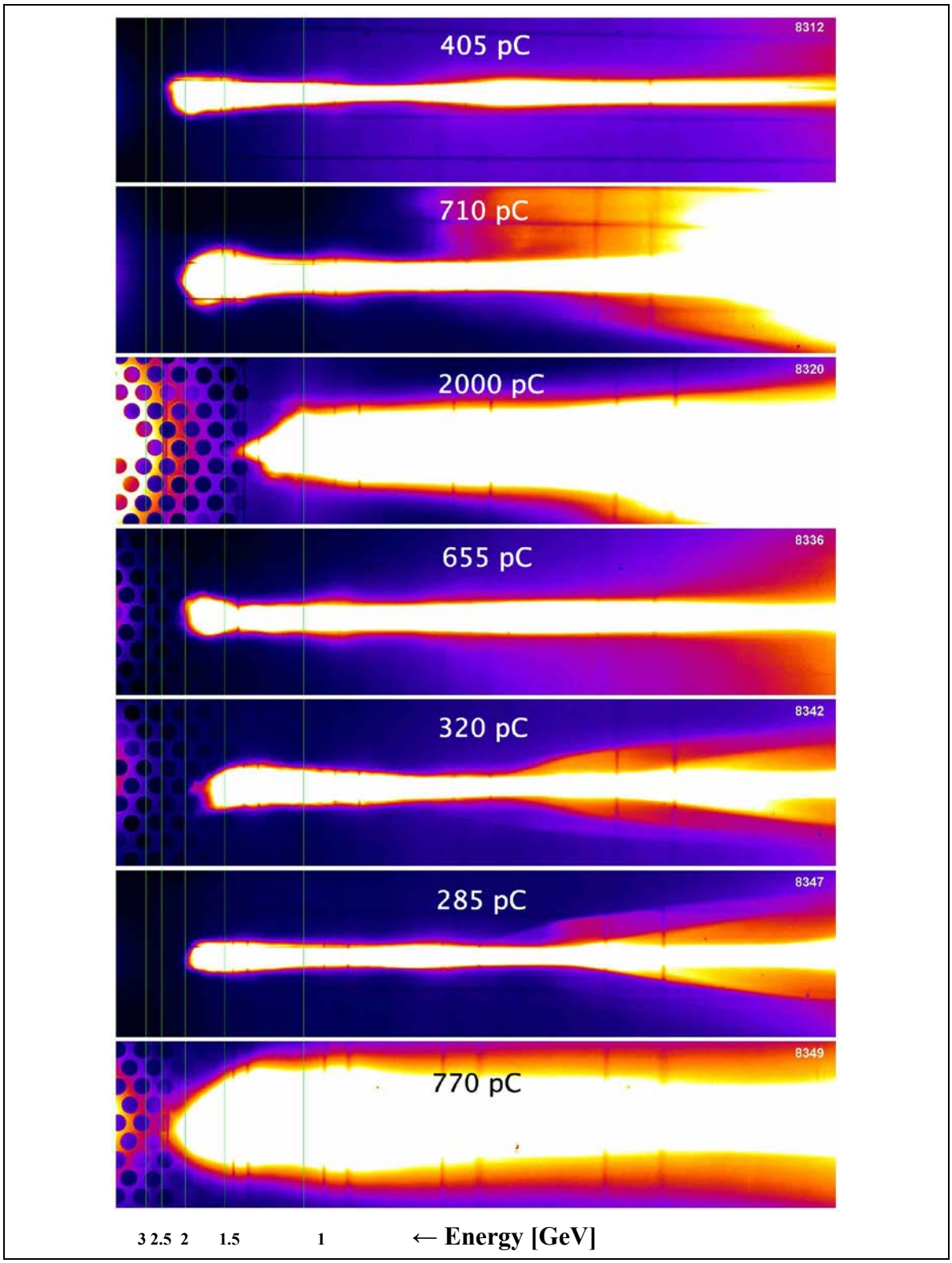

Figure 6.35: First (saturated) scan of the imaging plate detector for shots 8312, 8316, 8320, 8336, 8342, 8347, 8349, showing charge accelerated to ≳ 300 MeV. In each case, the image height is ≲15 mrad.

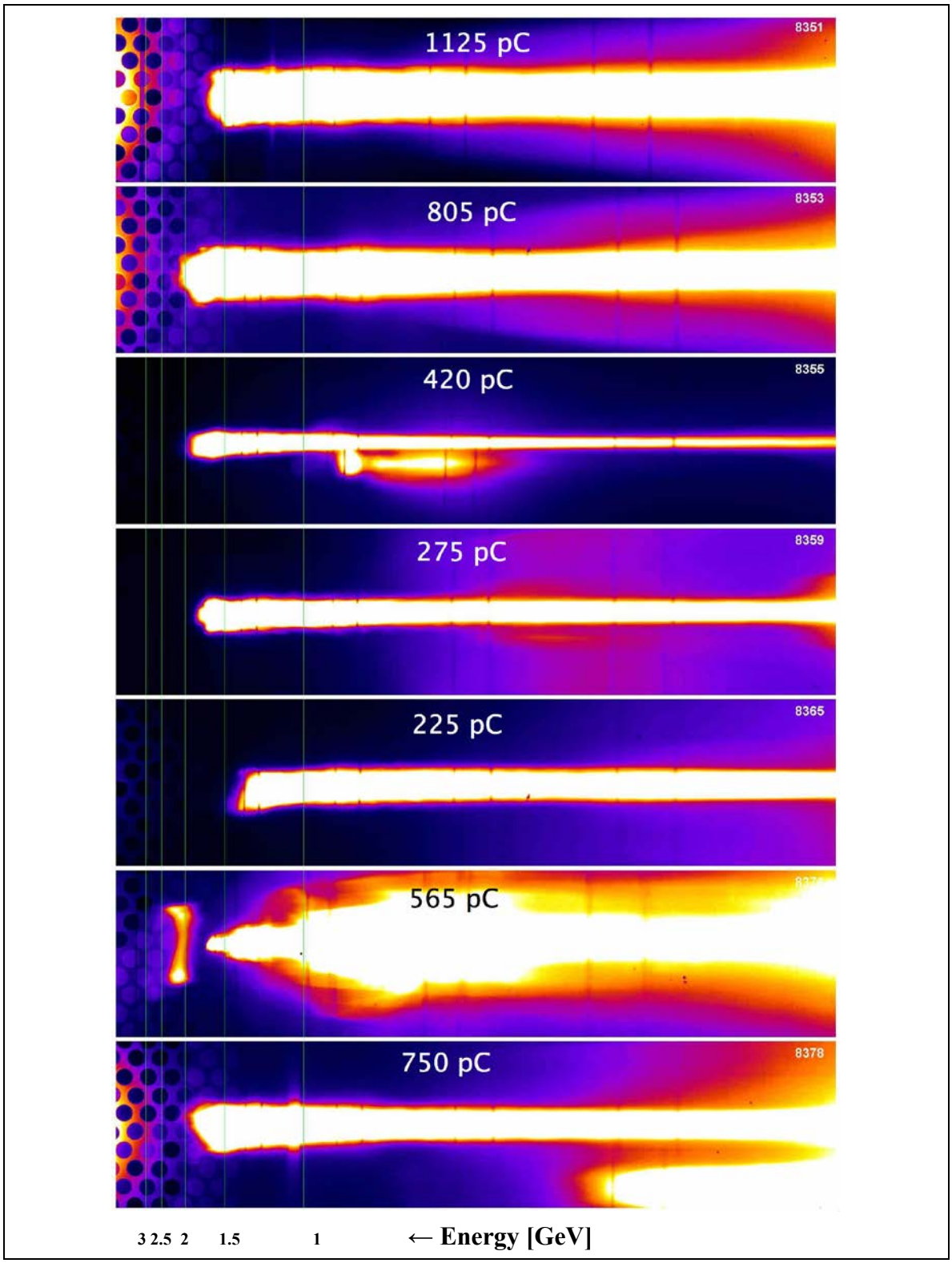

Figure 6.36: First (saturated) scan of the imaging plate detector for shots 8351, 8353, 8355, 8359, 8365, 8376, 8378, showing charge accelerated to ≳ 300 MeV. In each case, the image height is ≲15 mrad.

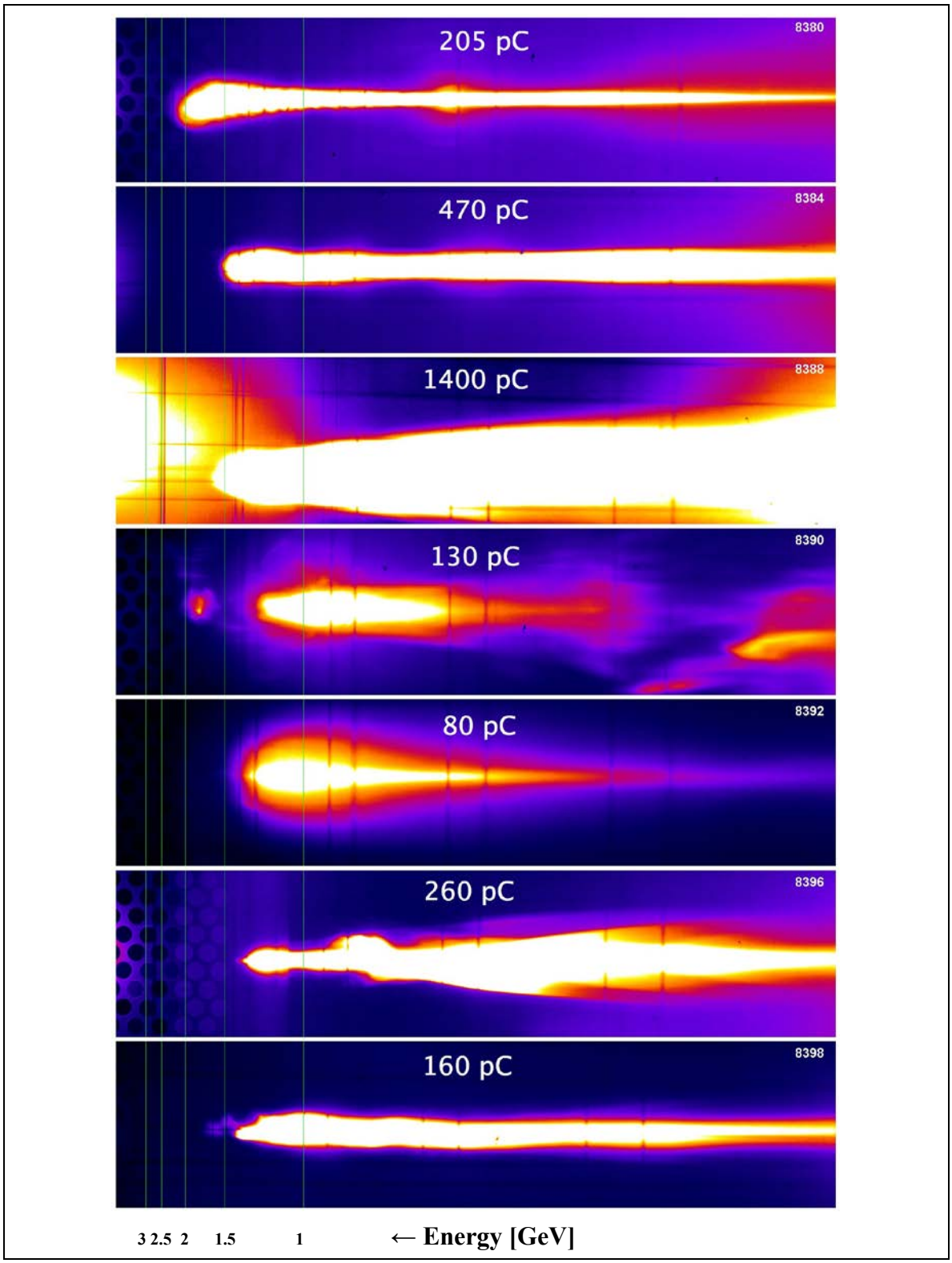

Figure 6.37: First (saturated) scan of the imaging plate detector for shots 8380, 8384, 8388, 8390, 8392, 8396, 8398, showing charge accelerated to ≳ 300 MeV. In each case, the image height is ≲15 mrad.

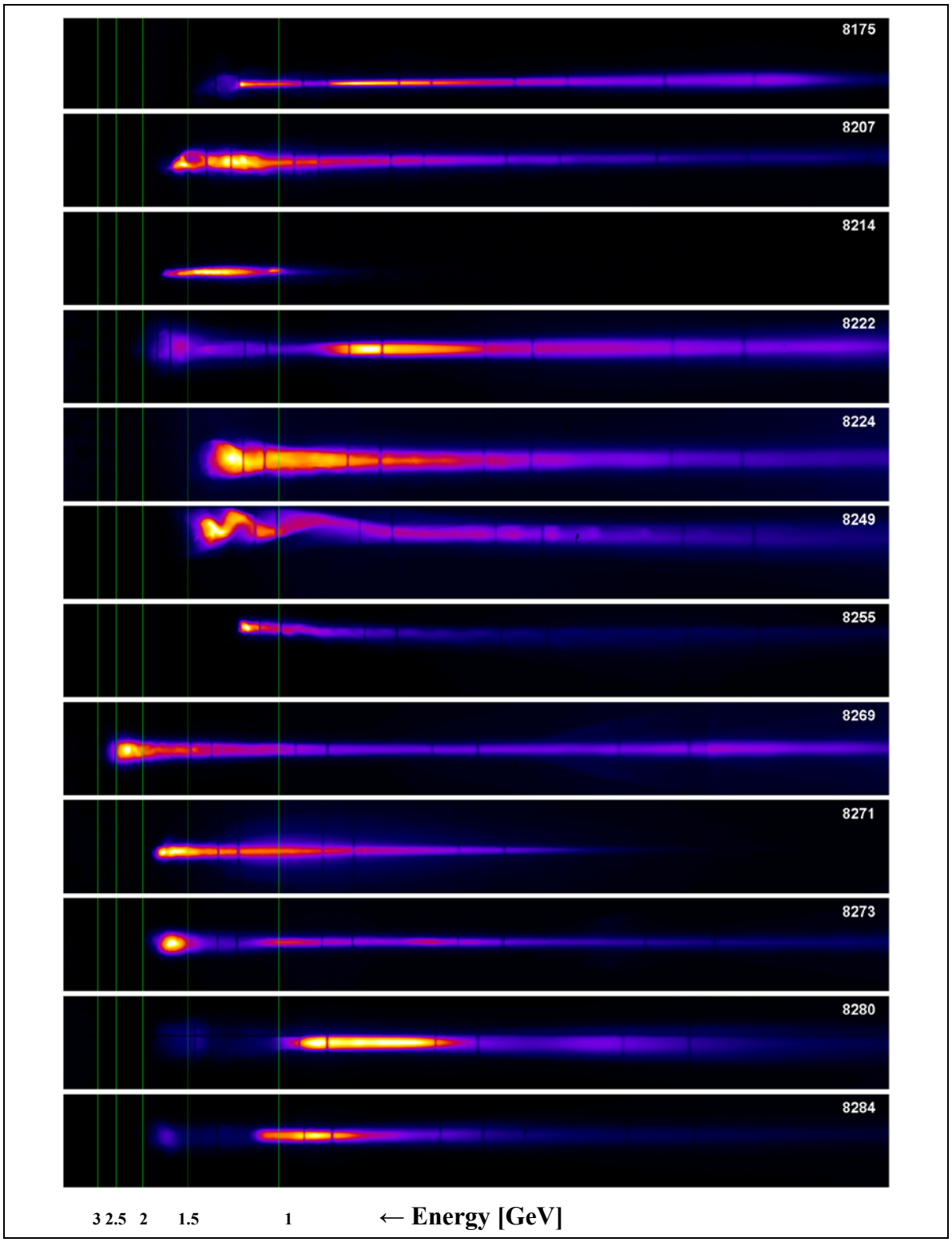

Figure 6.38: Last (unsaturated) scan of the imaging plate detector for shots 8175, 8207, 8214, 8222, 8224, 8249, 8255, 8269, 8271, 8273, 8280, 8284, showing charge accelerated to $\gtrsim$ 300 MeV. In each case, the image height is ~7.3 mrad.

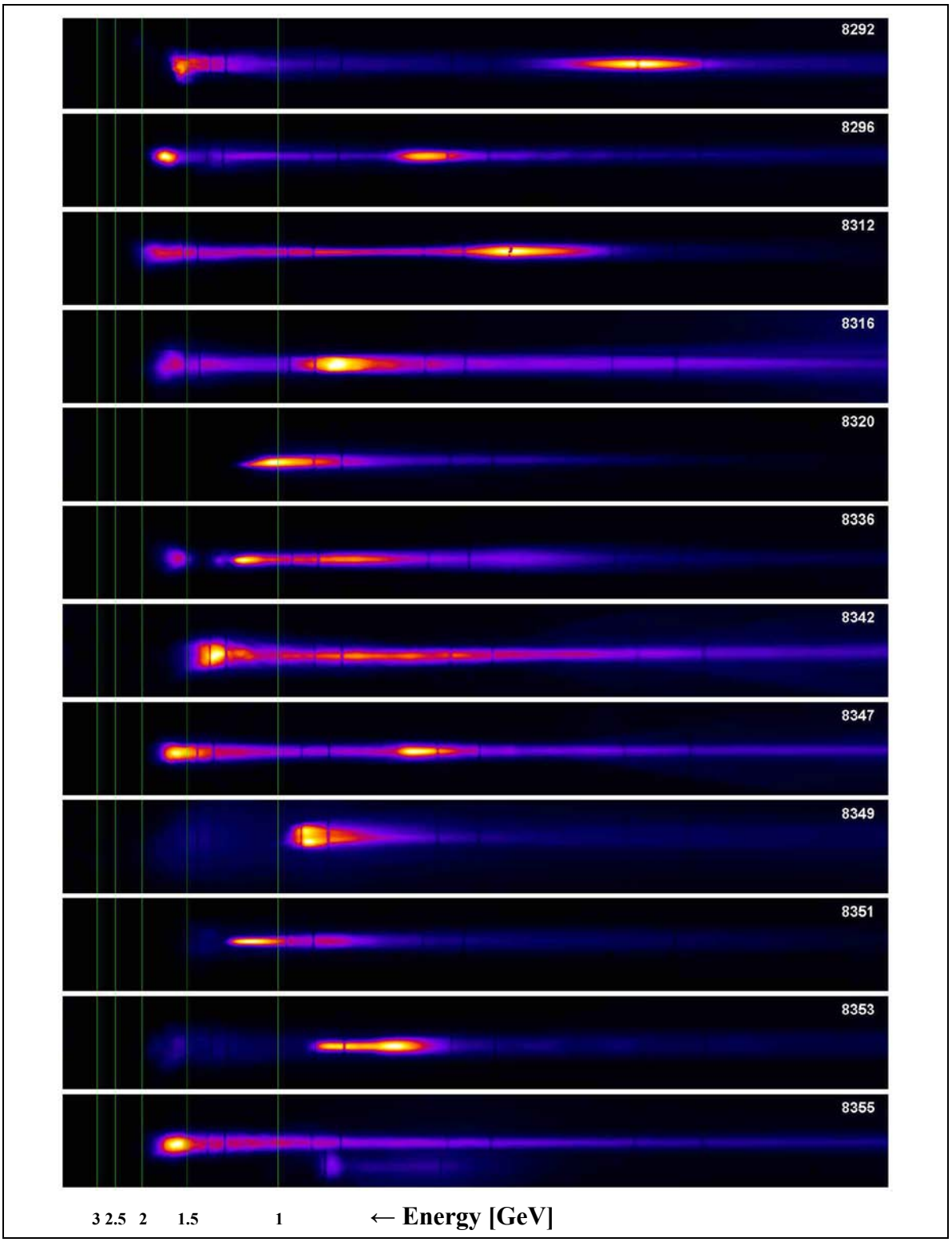

Figure 6.39: Last (unsaturated) scan of the imaging plate detector for the shots 8292, 8296, 8312, 8316, 8320, 8336, 8342, 8347, 8349, 8351, 8353, 8355, showing charge accelerated to ≳ 300 MeV. In each case, the image height is ~7.3 mrad.

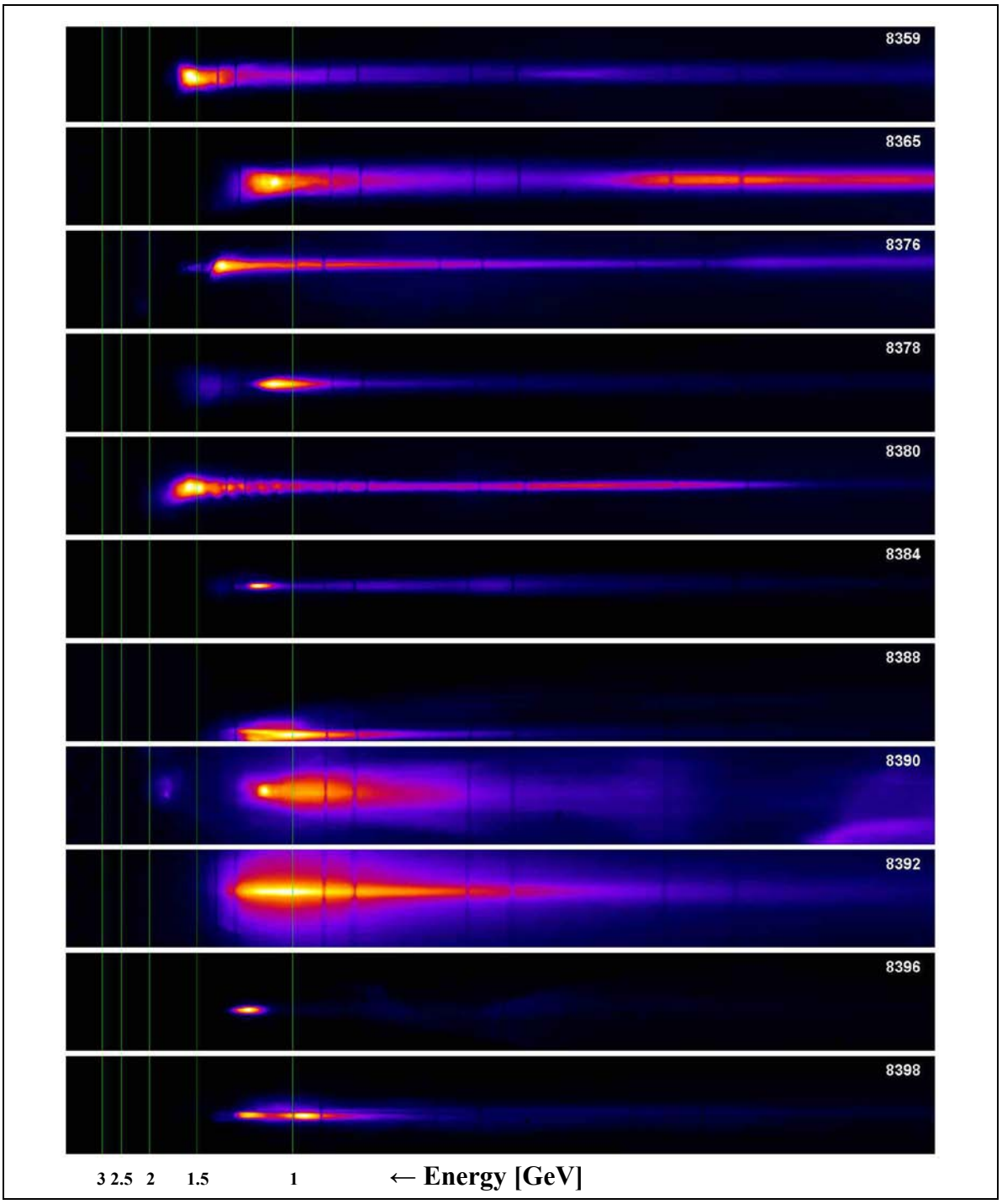

Figure 6.40: Last (unsaturated) scan of the imaging plate detector for the shots 8359, 8365, 8376, 8378, 8380, 8384, 8388, 8390, 8392, 8396, 8398, showing charge accelerated to $\gtrsim$ 300 MeV. In each case, the image height is ~7.3 mrad.

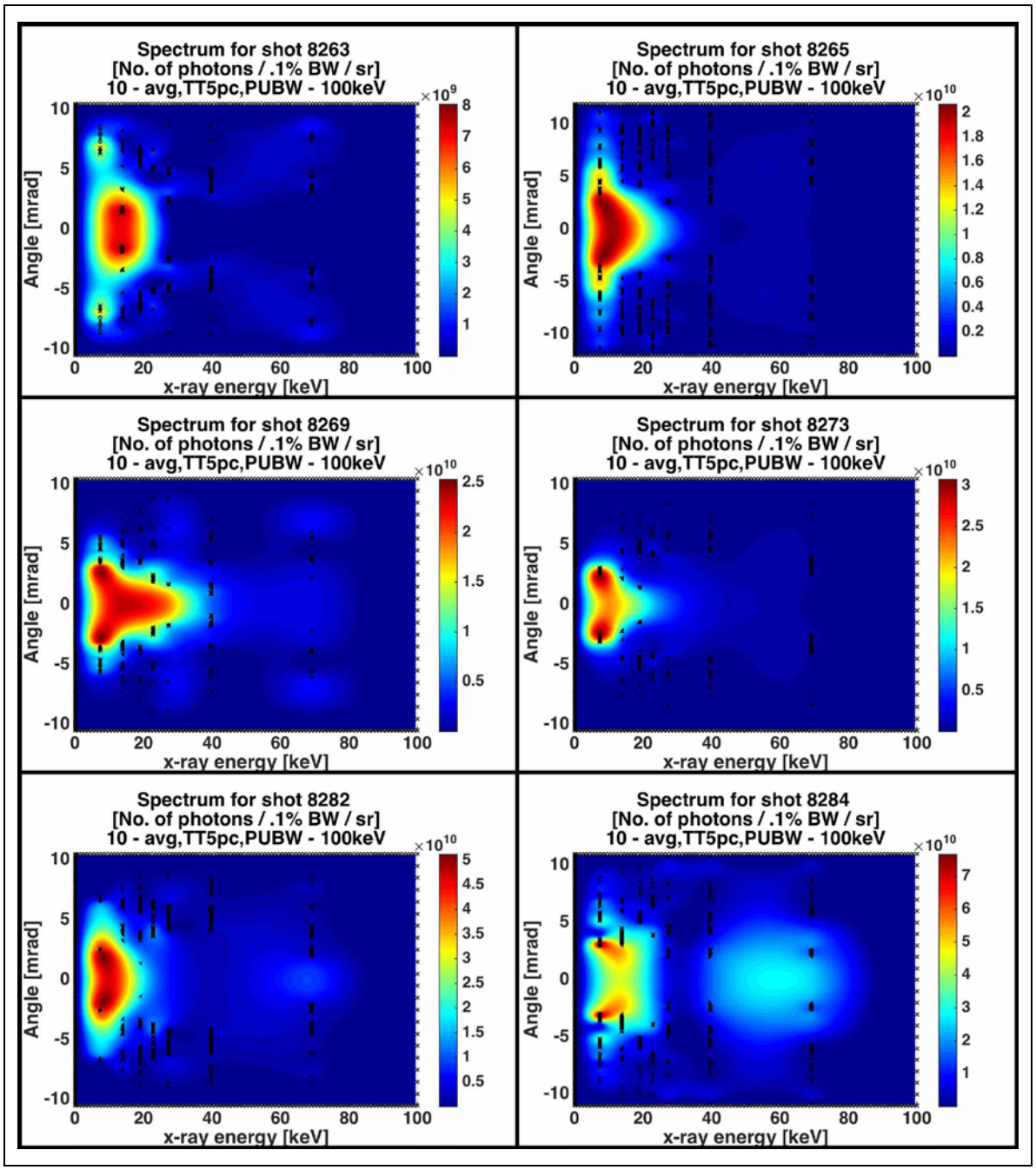

Figure 6.41: Spatially-resolved spectra for shots 8263, 8265, 8269, 8273, 8282, 8284.

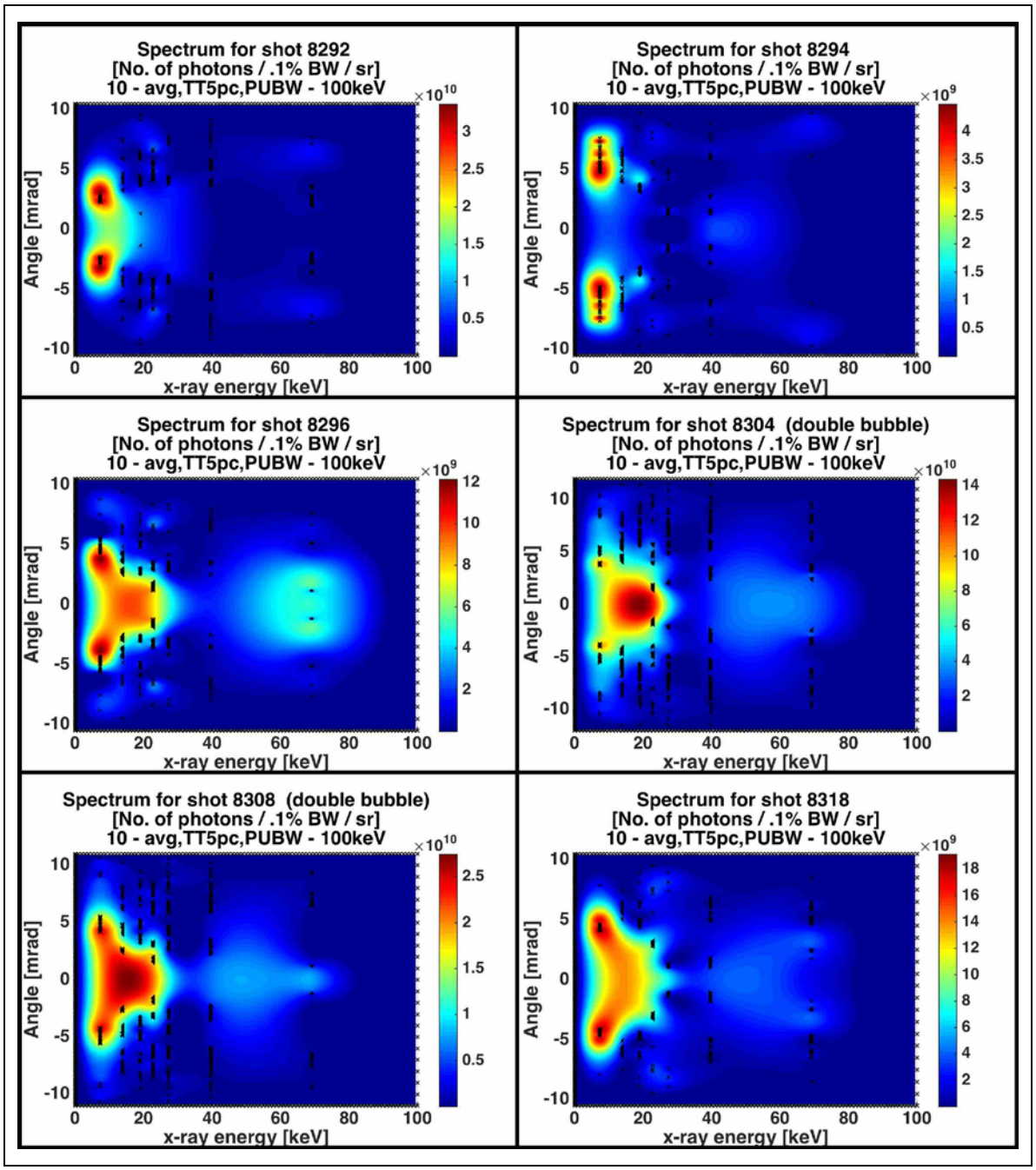

Figure 6.42: Spatially-resolved spectra for shots 8292, 8294, 8296, 8304, 8308, 8318.

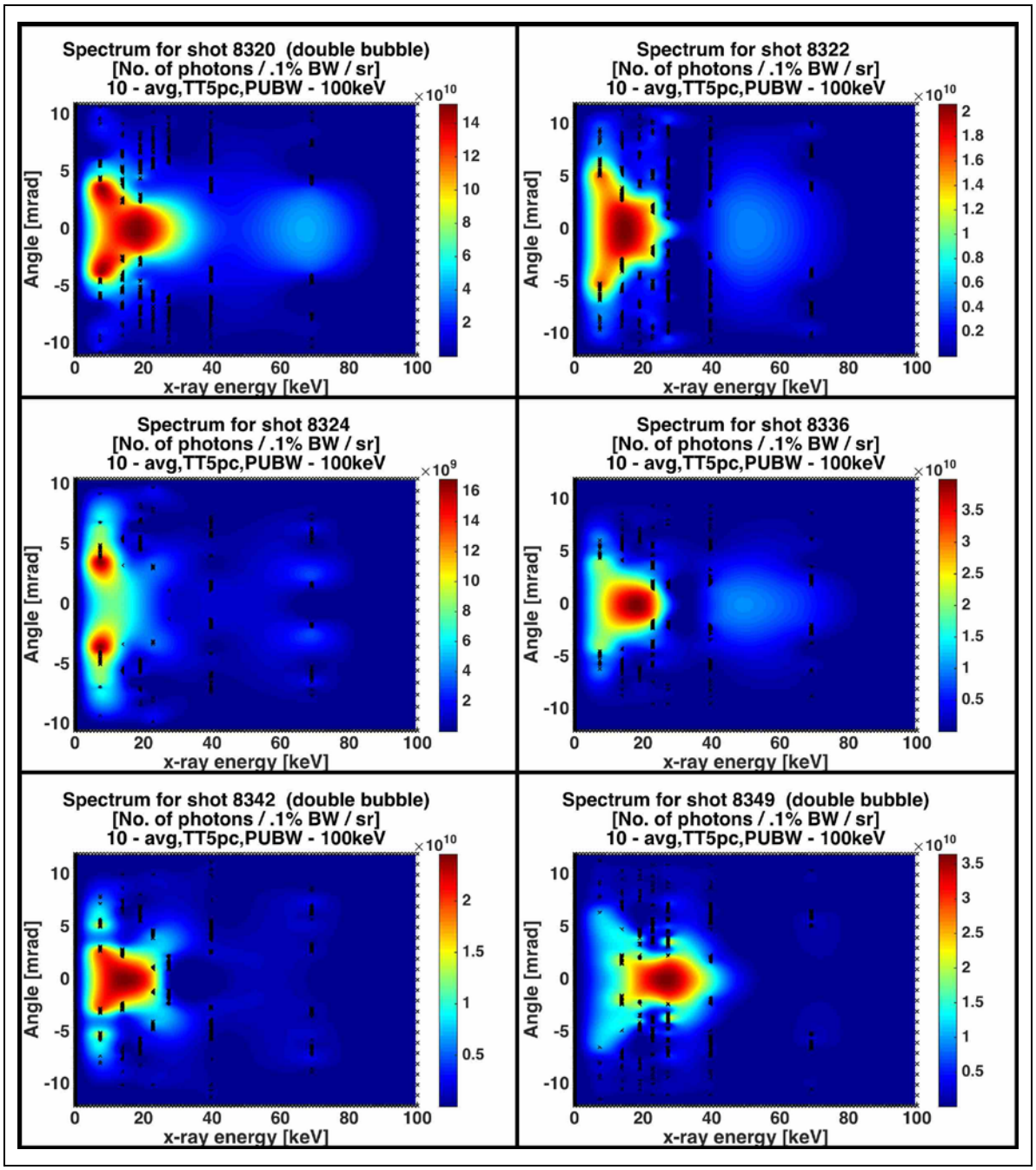

Figure 6.43: Spatially-resolved spectra for shots 8320, 8322, 8324, 8336, 8342, 8349.

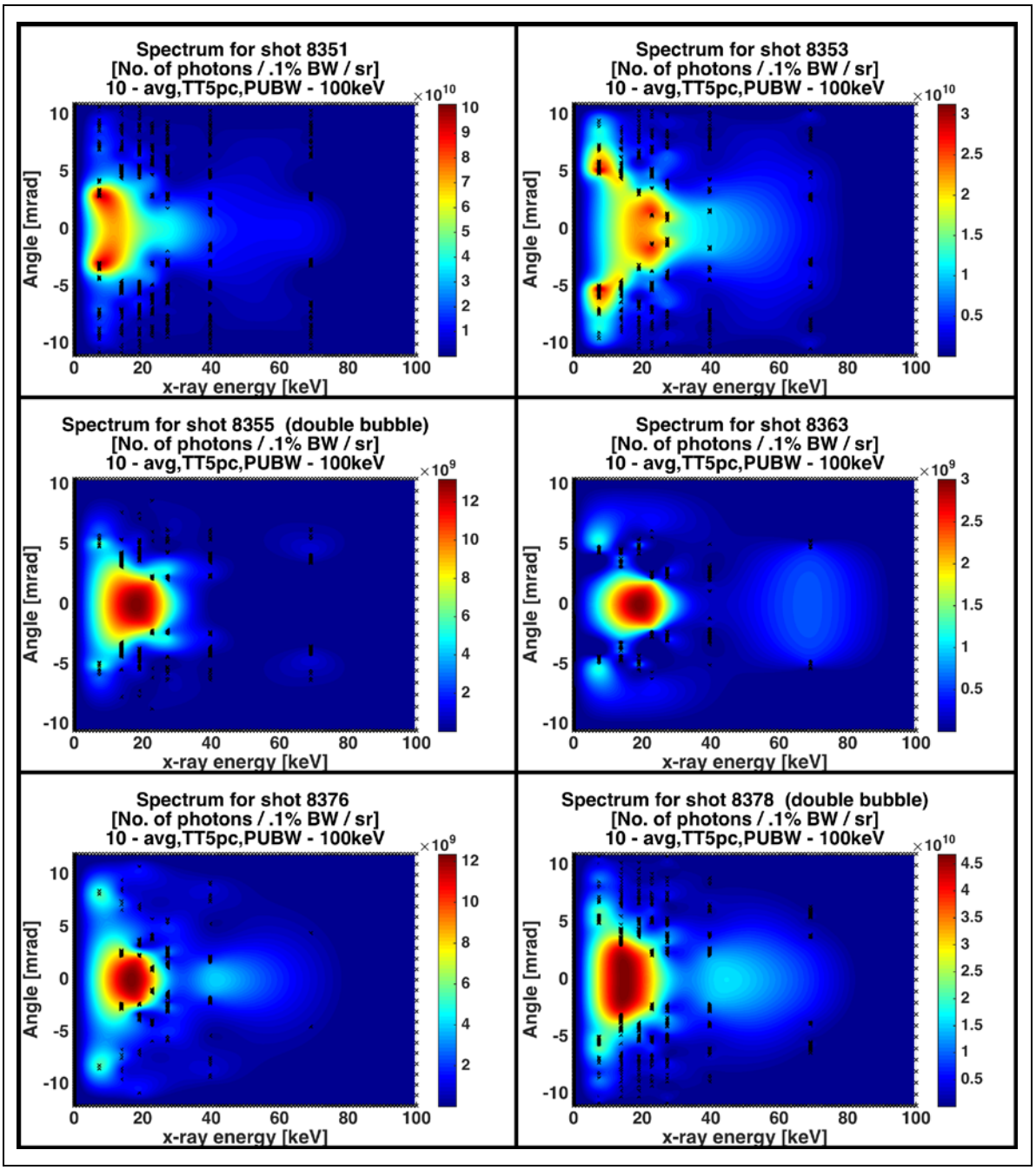

Figure 6.44: Spatially-resolved spectra for shots 8351, 8353, 8355, 8363, 8376, 8378.

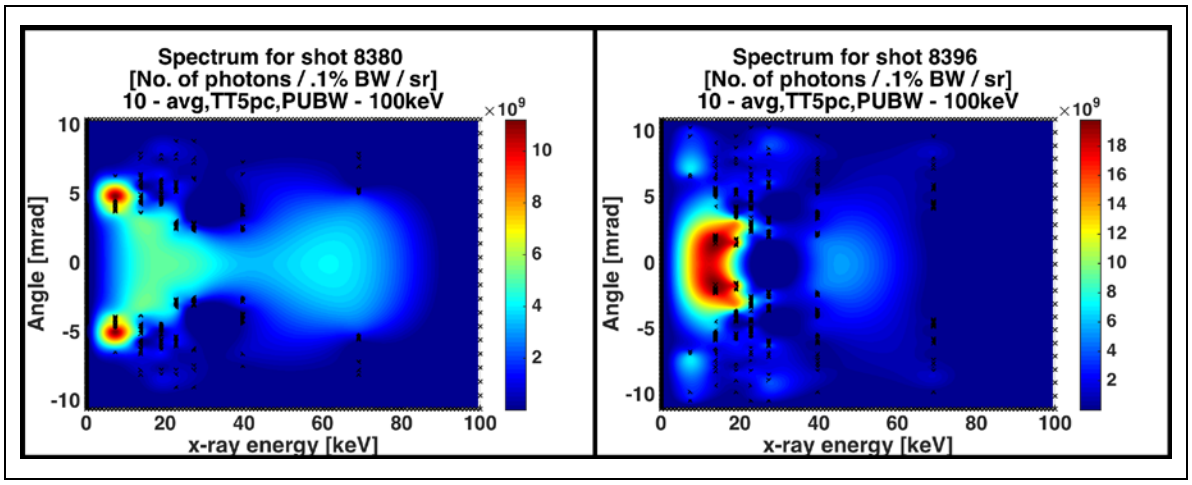

Figure 6.45: Spatially-resolved spectra for shots 8380, 8396.

this would act as a constraint during the fitting process. Since the K-edge filter mask was deployed for a large selection of the shots in this round, and the redesign of the x-ray spectrometer was done with the automation of the various steps (described in 5.7.3: Sampling of X-ray Data on Iso-intensity Contours) in mind, it was possible to calculate the spatially resolved spectra for a large sample of shots. These are shown in Figure 6.41 to Figure 6.45. The x-ray spectra change, in both shape and scale, from shot to shot.

Detailed Presentation of Parameter and Diagnostic Results for Selected Shots

Experimental parameters and diagnostic results for a sample of 7 shots from this experimental round is presented in this section. This sample was chosen to highlight important results, such as highest electron energy, charge, and photon number, as well as give an indication of how the interplay of the various factors, such as the plasma density and laser parameters, can produce different outcomes.

1. Shot 8269 (Yielded high-energy electrons)

Laser parameters and selected diagnostic measurements for shot 8269 are shown in Table 6-6. The high-energy tail of the electron spectrum for this shot exceeded 2.5 GeV.

Shot 8269	
Plasma Density	4.72×10^{17} cm^{-3}
TPW Laser Pulse Energy	136 J
TPW Laser Pulse Duration	141 fs
TPW Laser Pulse Power	961 TW
TPW Laser Pulse Fluence	5.37×10^{5} J cm^{-2}
TPW Laser Pulse Intensity	3.80×10^{18} W cm^{-2}
a_0	1.75
Fractional Energy Enclosed within Circle of 80 μm Radius	0.379
Radius of Circle with 50% of Mode Energy	104.3 μm
Max Electron Energy	> 2.5 GeV
Electron Charge > 300 MeV	~300 pC
Electron Charge > 1 GeV	~100 pC
X-ray Critical Energy	(18.2 ± 3.0) keV
X-ray FWHM	4.7 mrad
No. of X-ray Photons (double integral of spectra in Figure 6.51*)*	$(2.7 \pm 0.4) \times 10^{9}$

Table 6-6: Parameters and diagnostics for high-energy shot 8269.

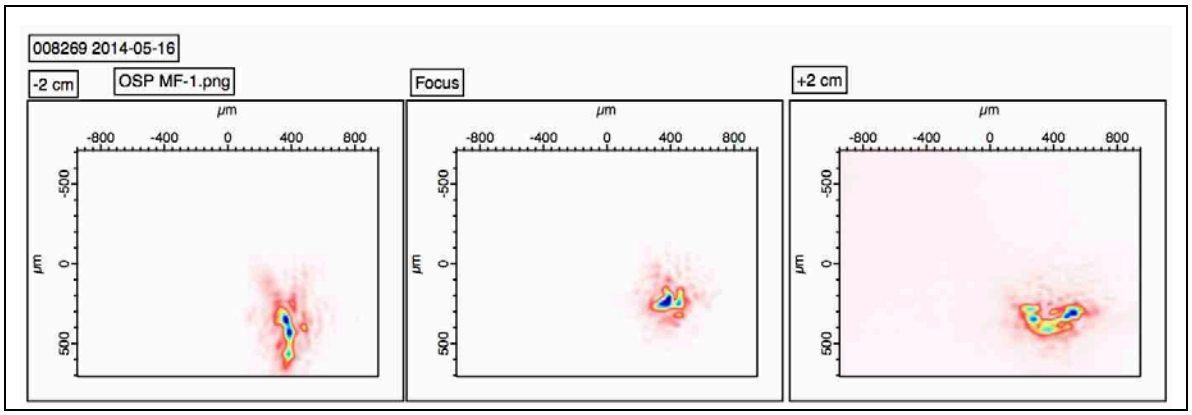

Figure 6.46: Laser profiles for high-energy shot 8269 at far field - 2 cm (left), far field (middle), and far field + 2 cm (right).

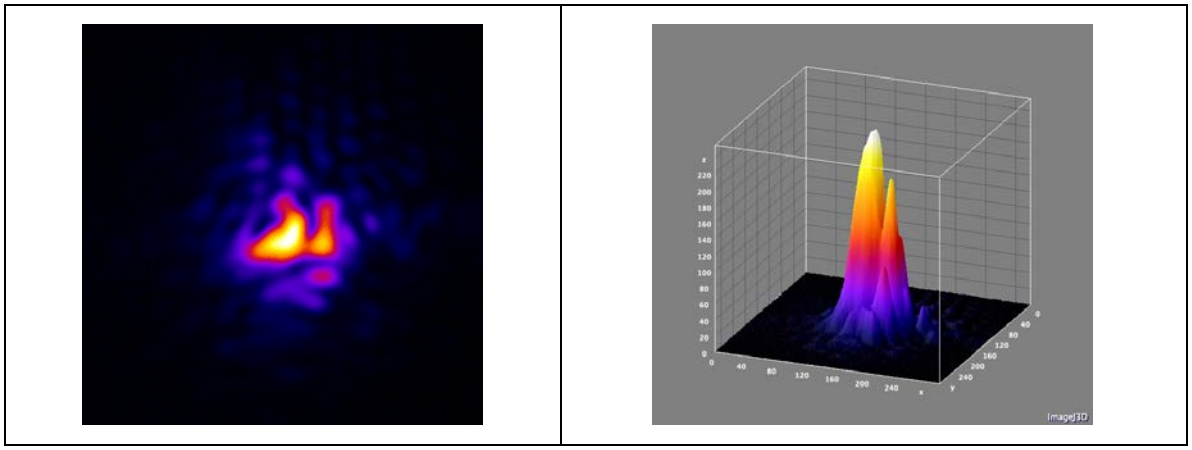

Figure 6.47: 2D and 3D representations of the far field laser profile for high-energy shot 8269.

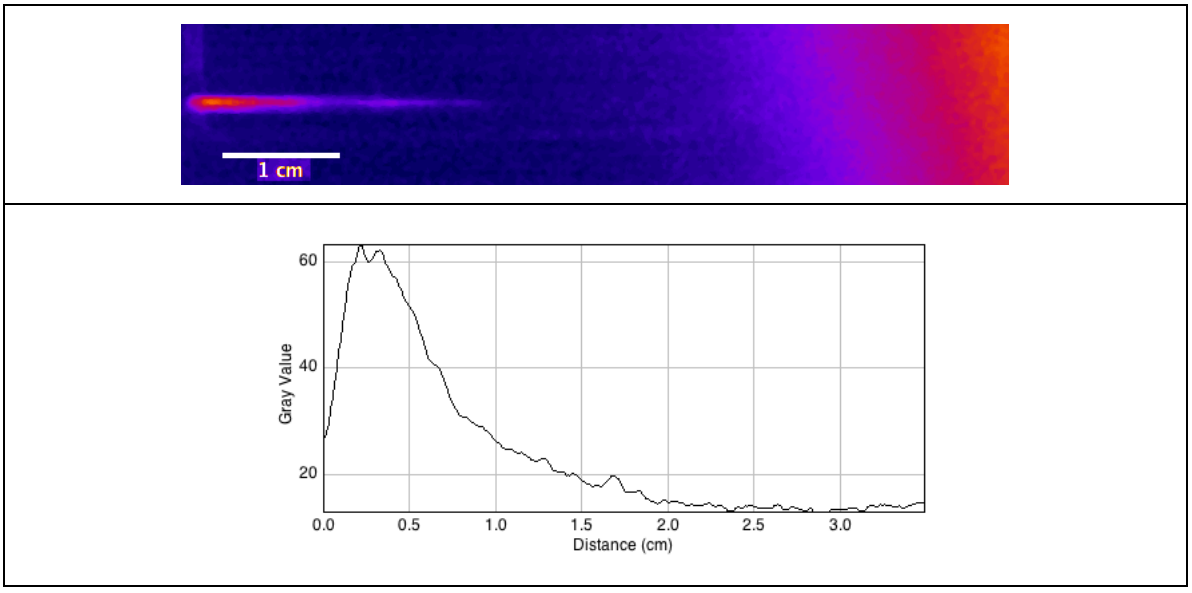

Figure 6.48: Gas cell side scatter for high-energy shot 8269.

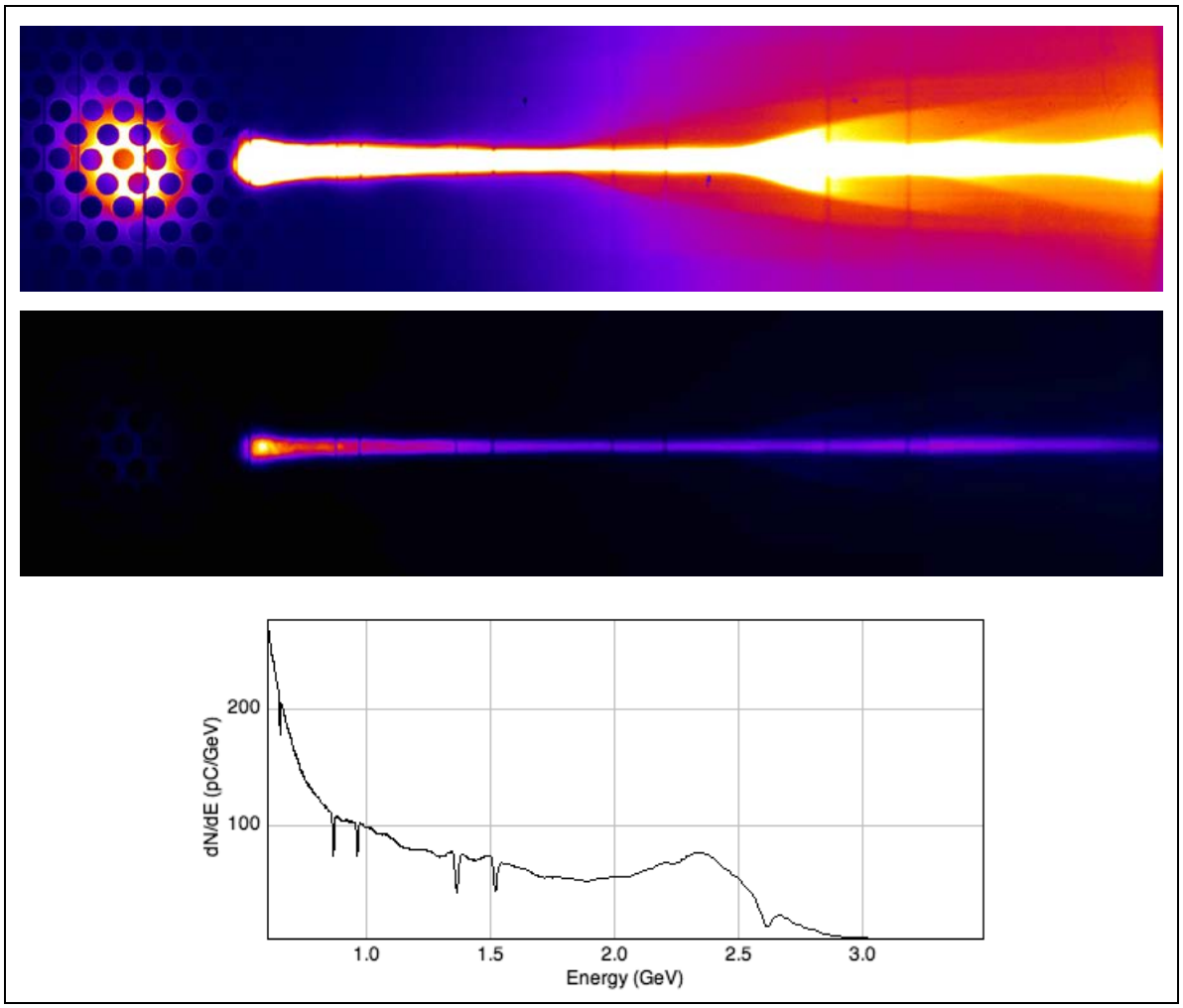

Figure 6.49: Betatron x-rays and magnetically deflected electrons for high-energy shot 8269 detected on the saturated (top) and unsaturated (middle) imaging plate scans; electron energy spectrum (bottom).

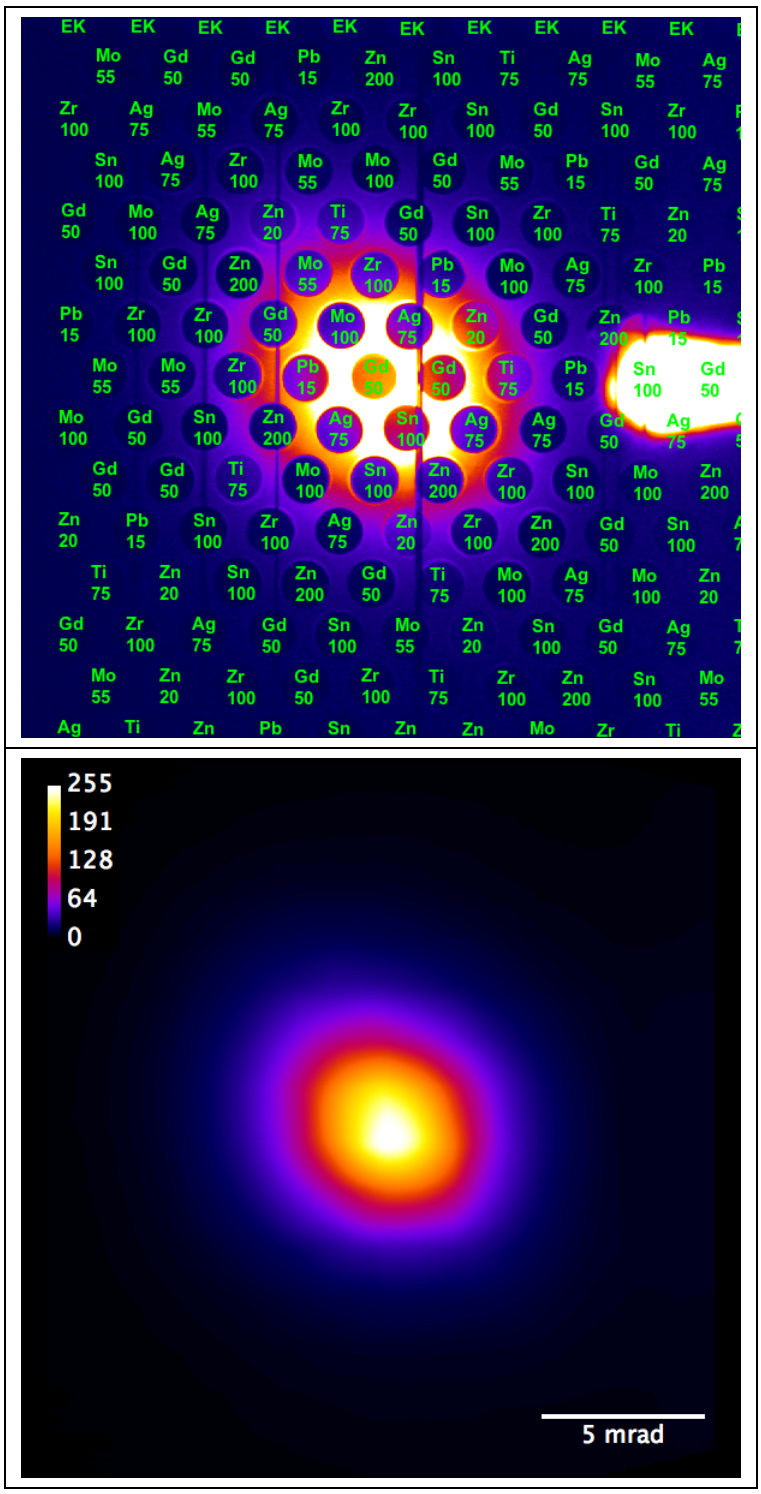

Figure 6.50: Top: betatron x-ray profile, and the K-edge filters used for its spectroscopy, for the high-energy shot 8269. Bottom: the reconstructed x-ray profile.

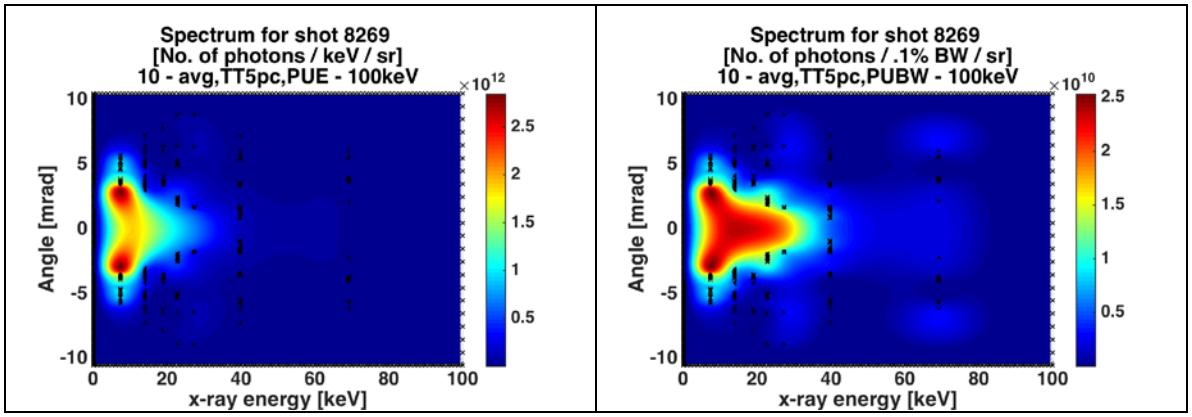

Figure 6.51: Spatially resolved spectrum for high-energy shot 8269, in per unit energy (left) and per unit bandwidth (right) representations.

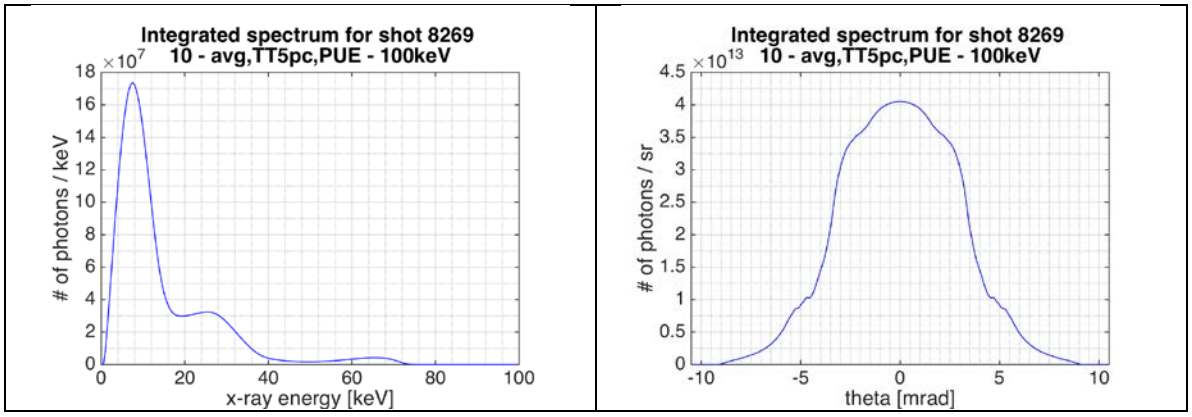

Figure 6.52: Integrated spectrum for high-energy shot 8269. Left: Spatially integrated spectrum; right: energy-integrated spectrum.

2. Shot 8380 (Yielded high-energy electrons)

Laser parameters and selected diagnostic measurements for shot 8380 are shown in Table 6-7. The high-energy tail of the electron spectrum for this shot exceeded 2.0 GeV.

Shot 8380	
Plasma Density	3.95×10^{17} cm^{-3}
TPW Laser Pulse Energy	128.9 J
TPW Laser Pulse Duration	133 fs
TPW Laser Pulse Power	962 TW
TPW Laser Pulse Fluence	6.11×10^{5} J cm^{-2}
TPW Laser Pulse Intensity	4.56×10^{18} W cm^{-2}
a_0	1.92
Fractional Energy Enclosed within Circle of 80 μm Radius	0.412
Radius of Circle with 50% of Mode Energy	98.0 μm
Max Electron Energy	> 2.0 GeV
Electron Charge > 300 MeV	~207 pC
Electron Charge > 1 GeV	~70 pC
X-ray Critical Energy	(29.4 ± 1.4) keV
X-ray FWHM	5.0 mrad
No. of X-ray Photons (double integral of spectra in Figure 6.58*)*	$(1.4 \pm 0.2) \times 10^{9}$

Table 6-7: Parameters and diagnostics for high-energy shot 8380.

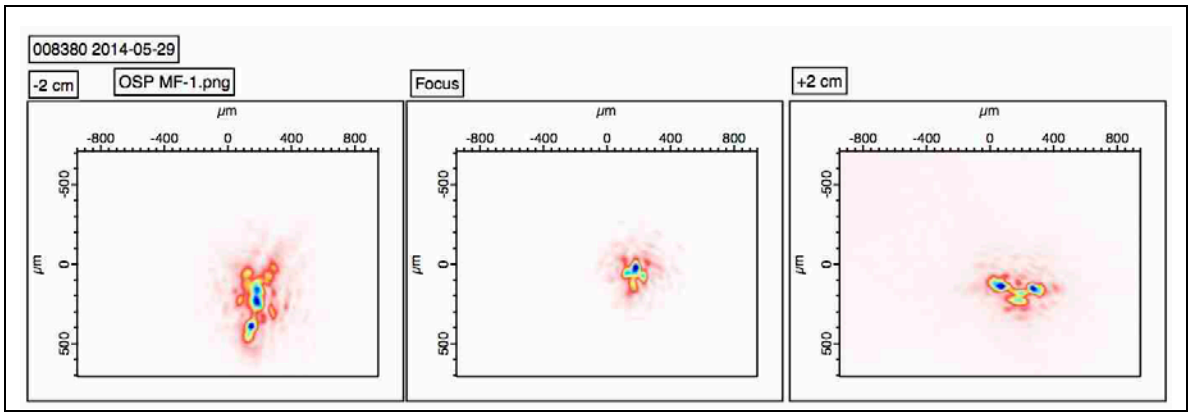

Figure 6.53: Laser profiles for high-energy shot 8380 at far field - 2 cm (left), far field (middle), and far field + 2 cm (right).

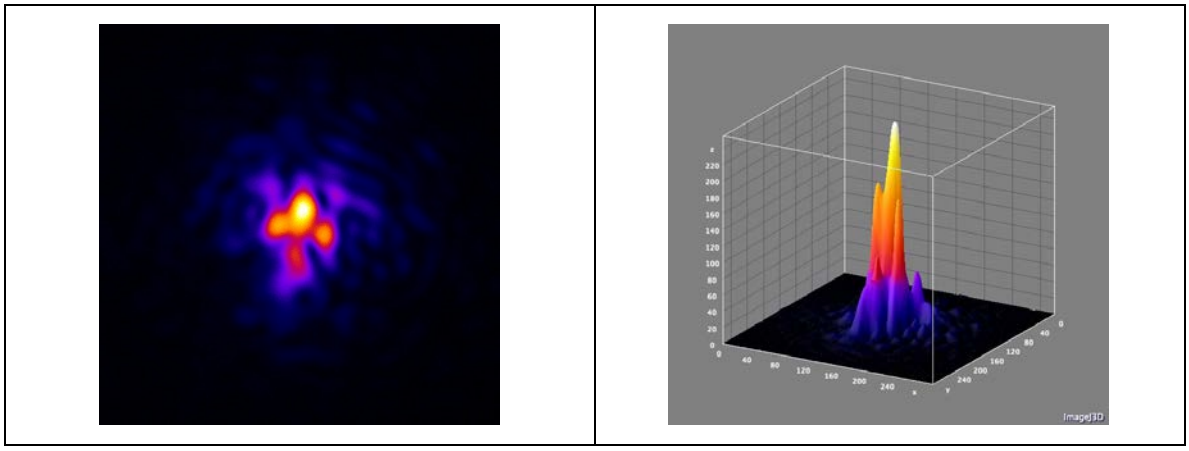

Figure 6.54: 2D and 3D representations of the far field laser profile for high-energy shot 8380.

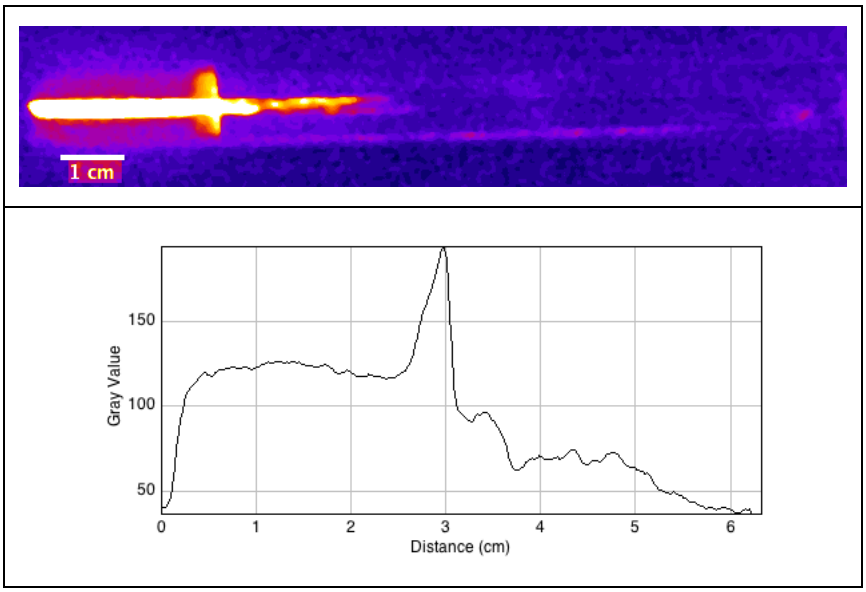

Figure 6.55: Gas cell side scatter for high-energy shot 8380.

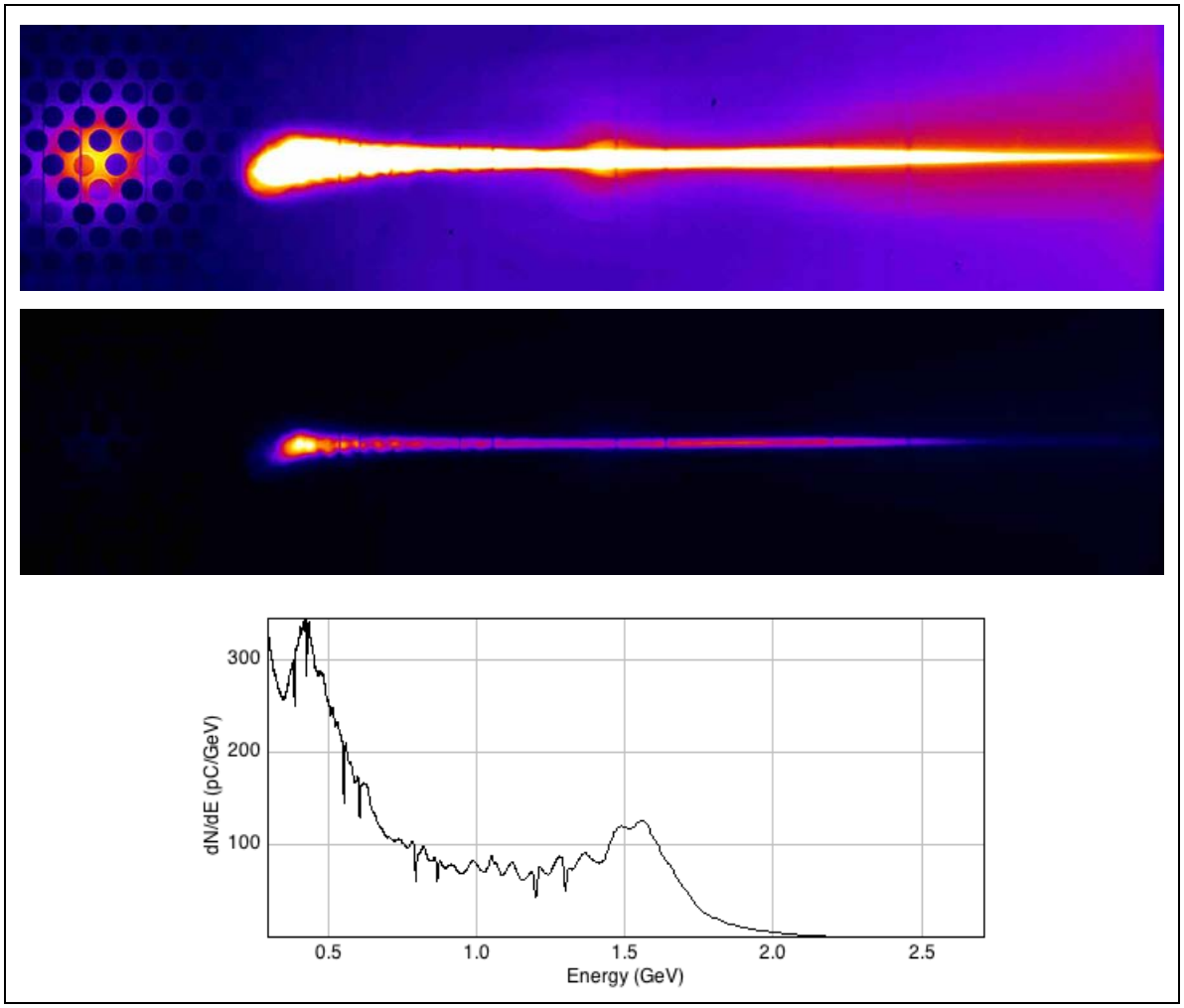

Figure 6.56: Betatron x-rays and magnetically deflected electrons for high-energy shot 8380 detected on the saturated (top) and unsaturated (middle) imaging plate scans; electron energy spectrum (bottom).

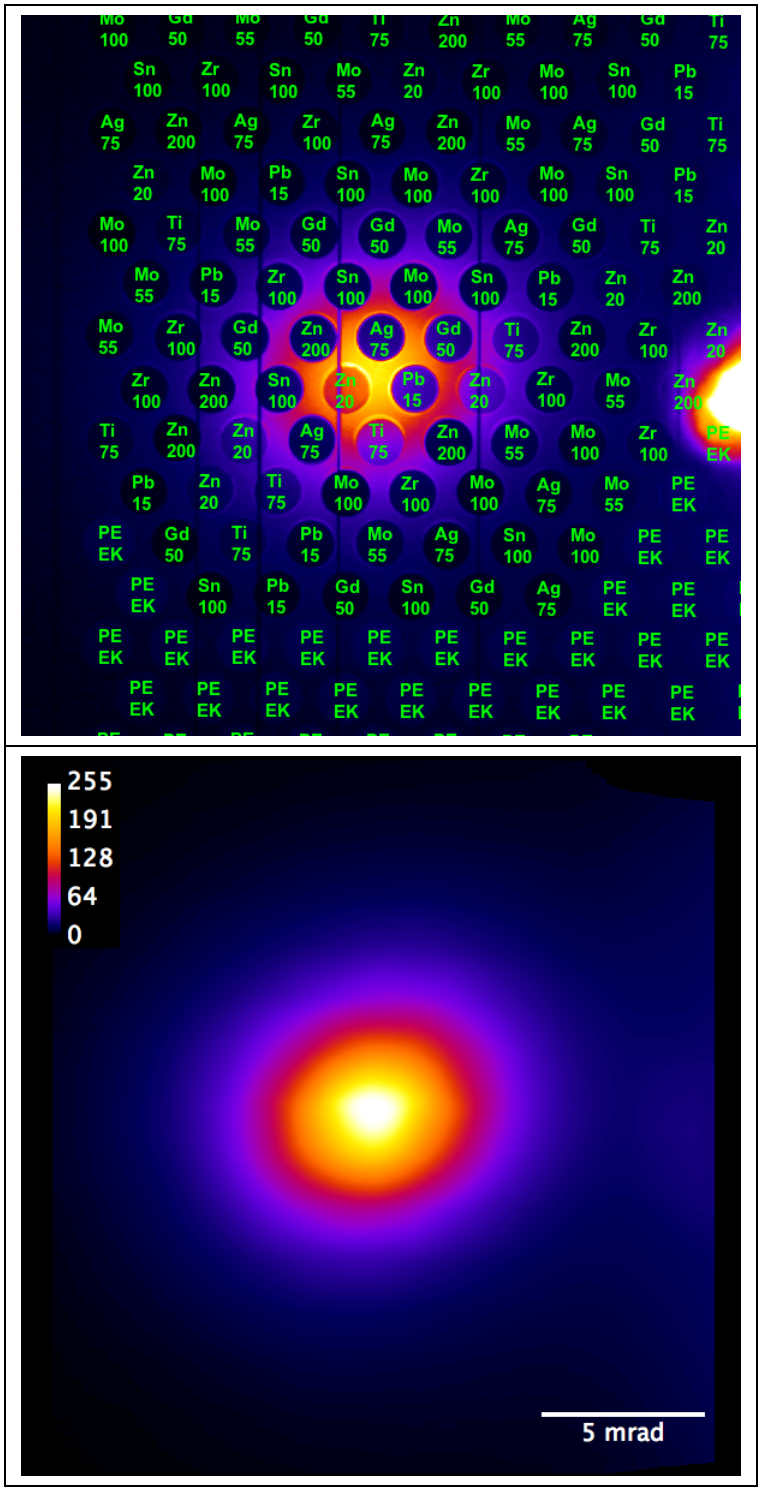

Figure 6.57: Top: betatron x-ray profile, and the K-edge filters used for its spectroscopy, for the high-energy shot 8380. Bottom: the reconstructed x-ray profile.

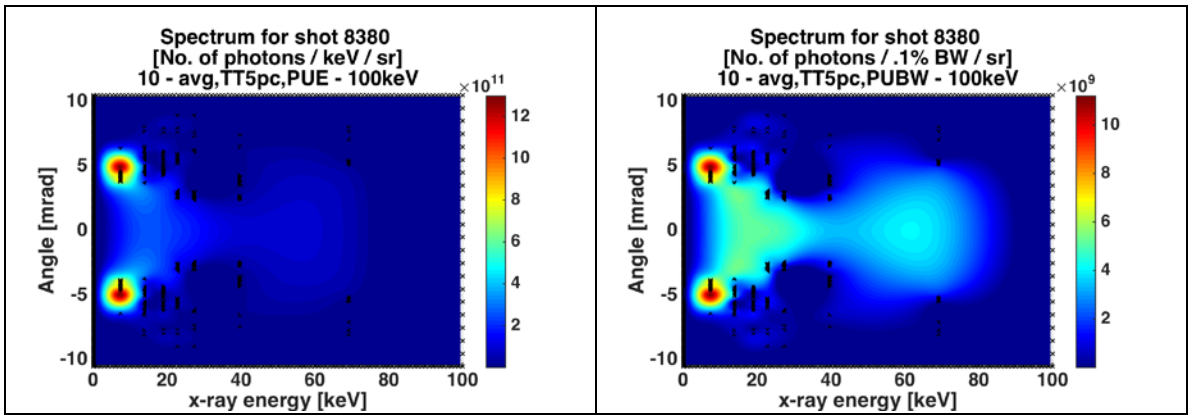

Figure 6.58: Spatially resolved spectrum for high-energy shot 8380, in per unit energy (left) and per unit bandwidth (right) representations.

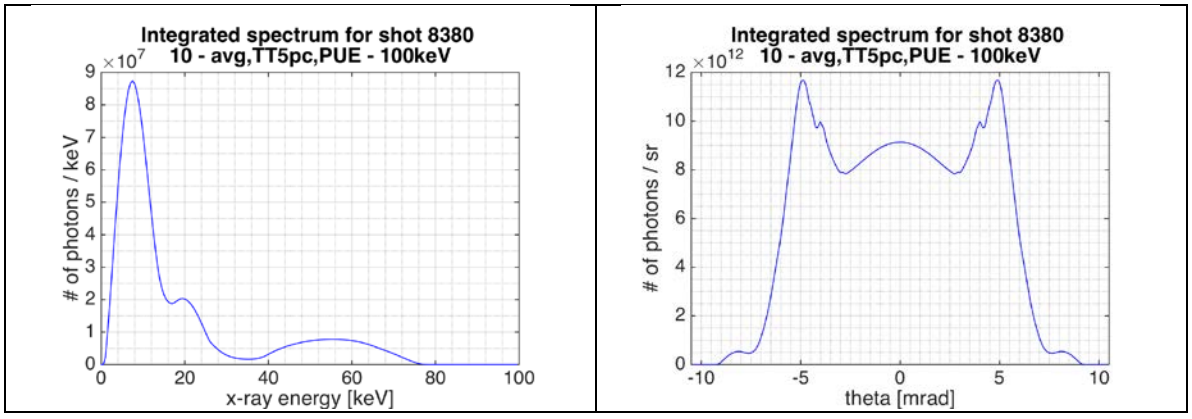

Figure 6.59: Integrated spectrum for high-energy shot 8380. Left: Spatially integrated spectrum; right: energy-integrated spectrum.

3. Shot 8263 (Yielded sub-GeV electrons)

Laser parameters and selected diagnostic measurements for shot 8263 are shown in Table 6-8. The high-energy tail of the electron spectrum for this shot remained under 0.8 GeV.

Shot 8263	
Plasma Density	5.05×10^{17} cm^{-3}
TPW Laser Pulse Energy	138 J
TPW Laser Pulse Duration	142 fs
TPW Laser Pulse Power	966 TW
TPW Laser Pulse Fluence	4.31×10^{5} J cm^{-2}
TPW Laser Pulse Intensity	3.02×10^{18} W cm^{-2}
a_0	1.56
Fractional Energy Enclosed within Circle of 80 μm Radius	0.24
Radius of Circle with 50% of Mode Energy	144.46 μm
Max Electron Energy	> 0.6 GeV
Electron Charge > 300 MeV	~130 pC
Electron Charge > 1 GeV	0 pC
X-ray Critical Energy	(25.6 ± 1.0) keV
X-ray FWHM	6.6 mrad
No. of X-ray Photons (double integral of spectra in Figure 6.66*)*	$(1.2 \pm 0.2) \times 10^{9}$

Table 6-8: Parameters and diagnostics for low-energy shot 8263.

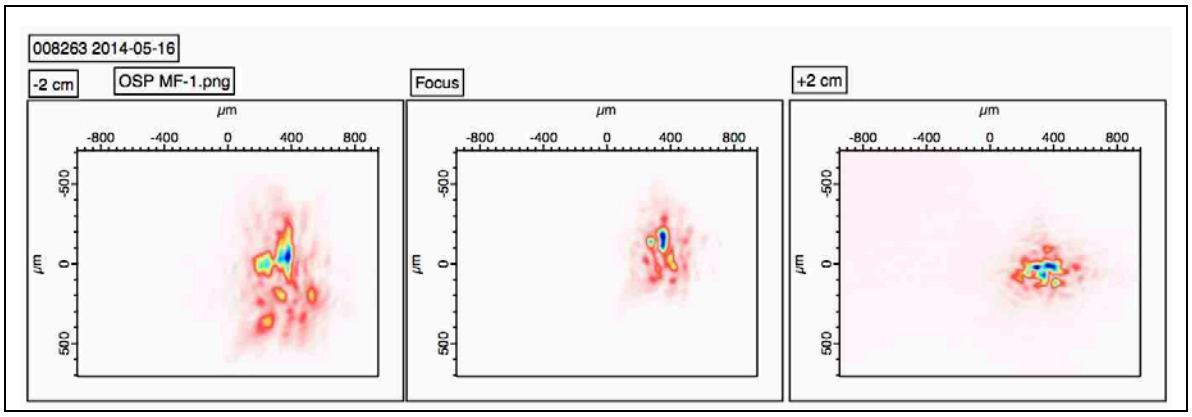

Figure 6.60: Laser profiles for low-energy shot 8263 at far field - 2 cm (left), far field (middle), and far field + 2 cm (right).

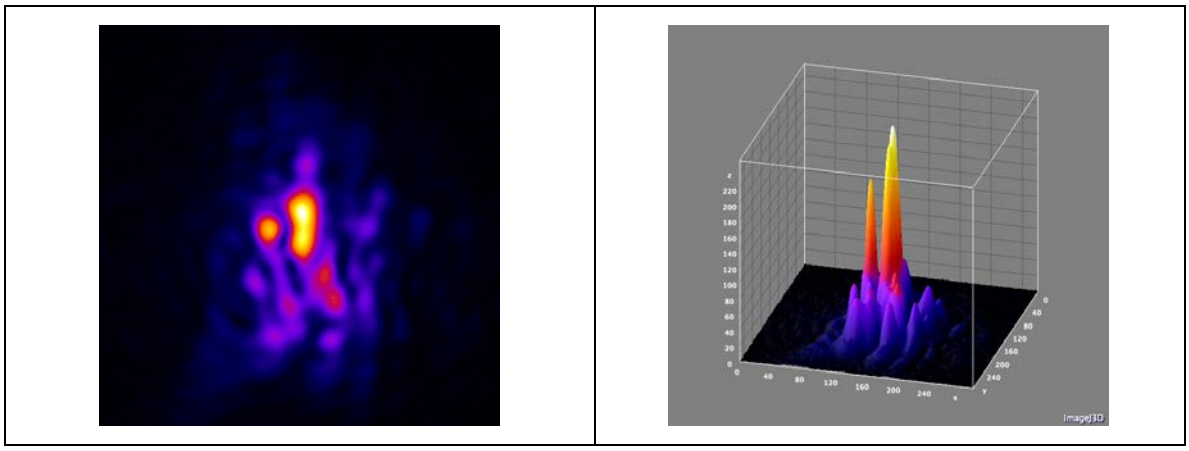

Figure 6.61: 2D and 3D representations of the far field laser profile for low-energy shot 8263.

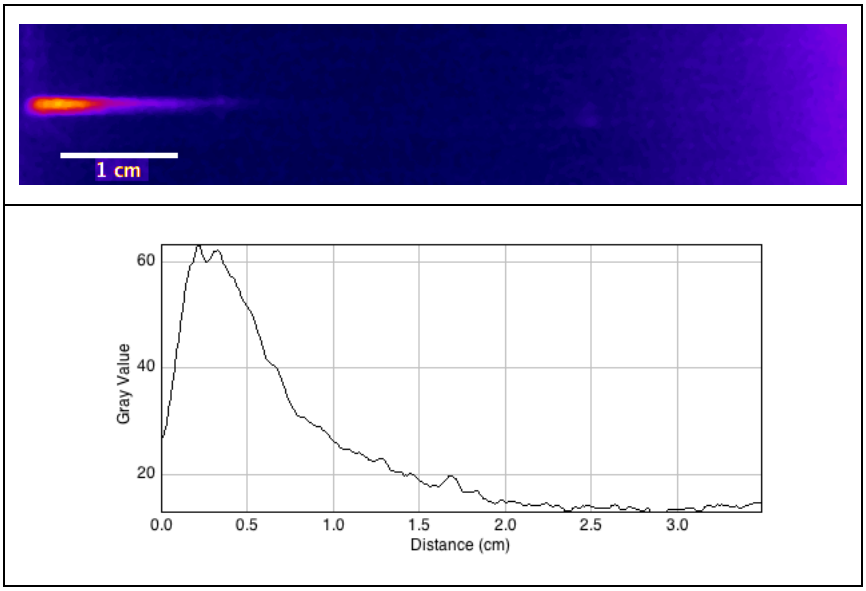

Figure 6.62: Gas cell side scatter for low-energy shot 8263.

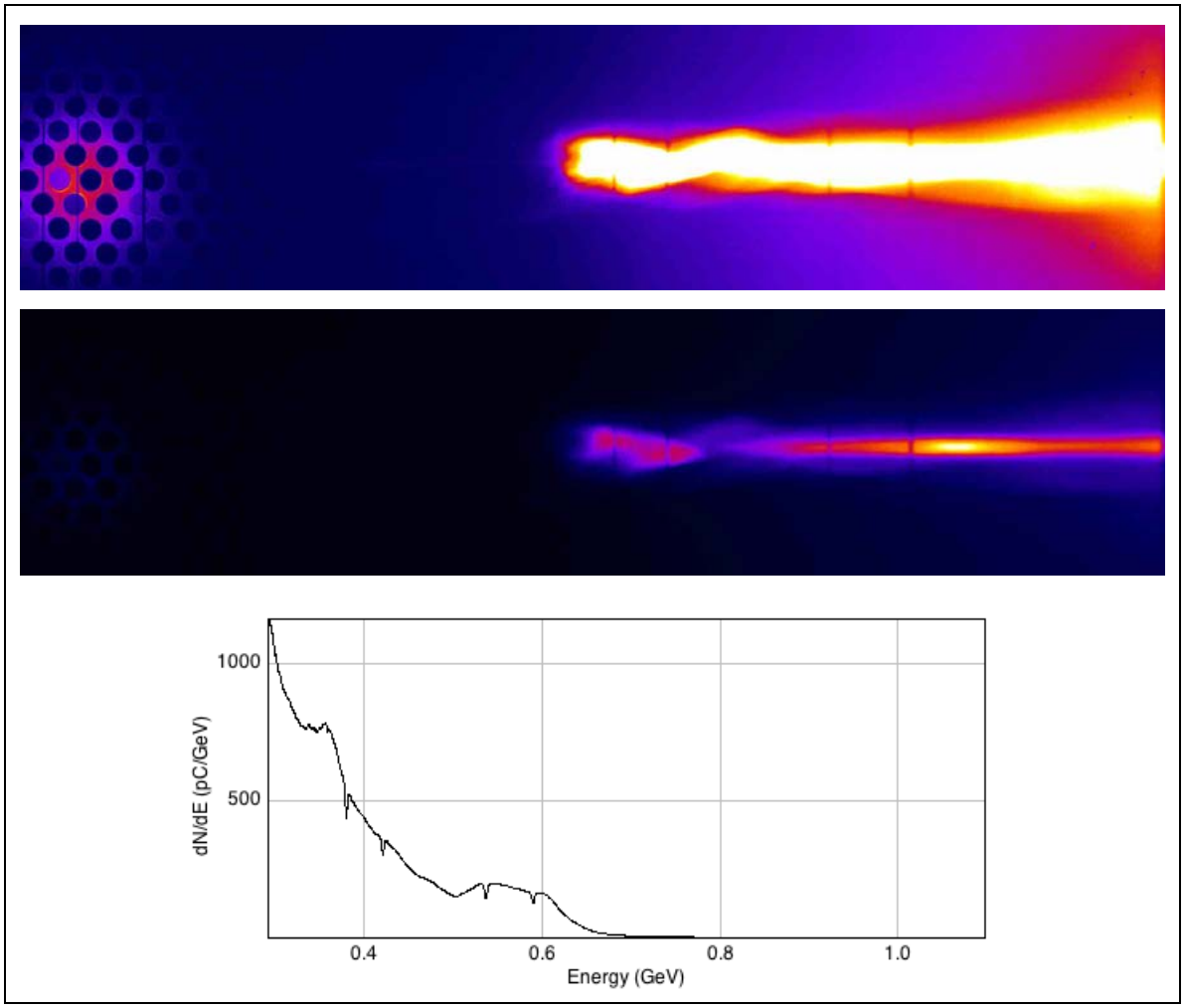

Figure 6.63: Betatron x-rays and magnetically deflected electrons for low-energy shot 8263 detected on the saturated (top) and unsaturated (middle) imaging plate scans; electron energy spectrum (bottom).

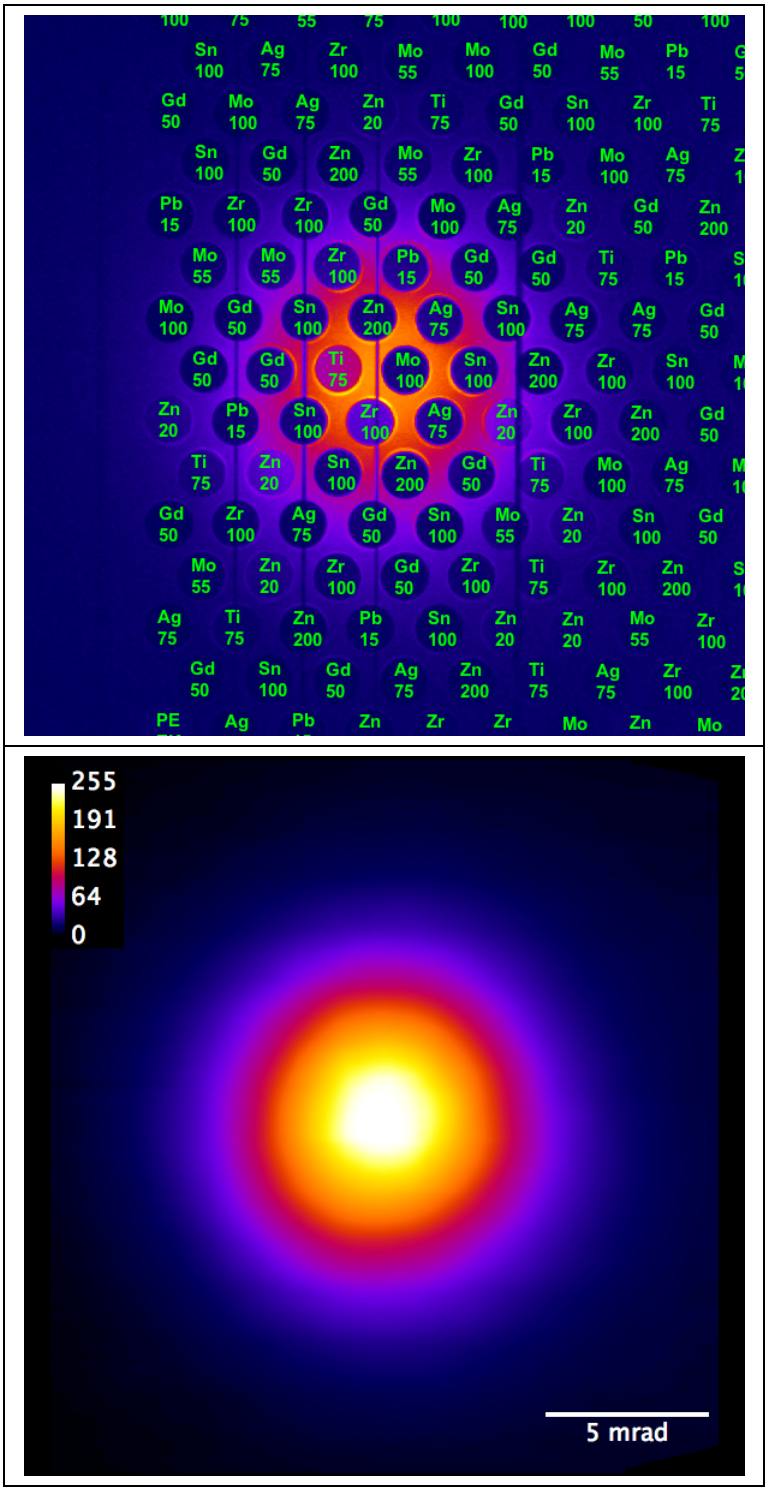

Figure 6.64: Top: betatron x-ray profile, and the K-edge filters used for its spectroscopy, for the low-energy shot 8263. Bottom: the reconstructed x-ray profile.

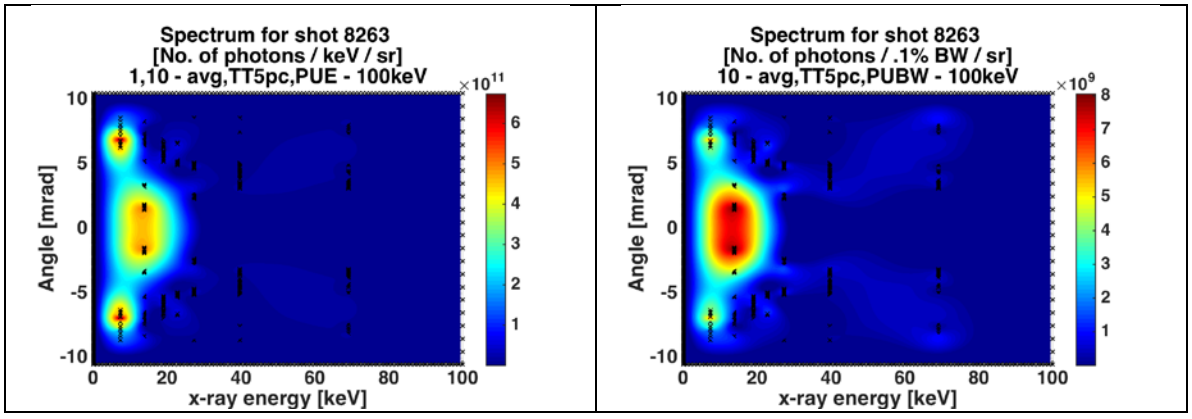

Figure 6.65: Spatially resolved spectrum for low-energy shot 8263, in per unit energy (left) and per unit bandwidth (right) representations.

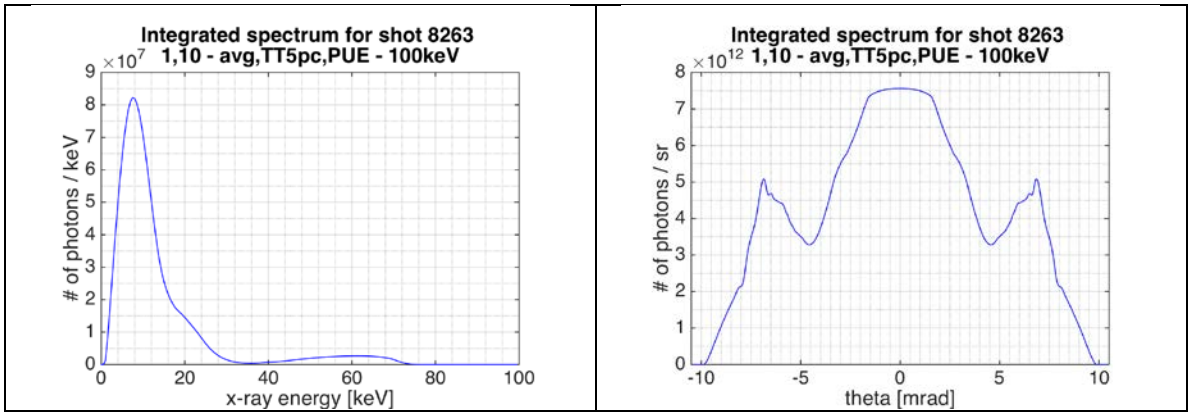

Figure 6.66: Integrated spectrum for low-energy shot 8263. Left: Spatially integrated spectrum; right: energy-integrated spectrum.

4. Shot 8320 ("Double Bubble")

Laser parameters and selected diagnostic measurements for shot 8320 are shown in Table 6-9. The laser far-field profile for this shot had two distinct and separated hot spots and this is believed to have led to the production of about average charge and photon number.

Shot 8320	
Plasma Density	4.28×10^{17} cm^{-3}
TPW Laser Pulse Energy	126 J
TPW Laser Pulse Duration	134 fs
TPW Laser Pulse Power	938 TW
TPW Laser Pulse Fluence	5.854×10^{5} J cm^{-2}
TPW Laser Pulse Intensity	4.36×10^{18} W cm^{-2}
a_0	1.88
Fractional Energy Enclosed within Circle of 80 μm Radius	0.350
Radius of Circle with 50% of Mode Energy	100.35 μm
Max Electron Energy	> 1.2 GeV
Electron Charge > 300 MeV	~2 nC
Electron Charge > 1 GeV	~340 pC
X-ray Critical Energy	(20.2 ± 4.8) keV
X-ray FWHM	7.0 mrad
No. of X-ray Photons (double integral of spectra in Figure 6.72*)*	$(2.4 \pm 0.3) \times 10^{10}$

Table 6-9: Parameters and diagnostics for double-bubble shot 8320.

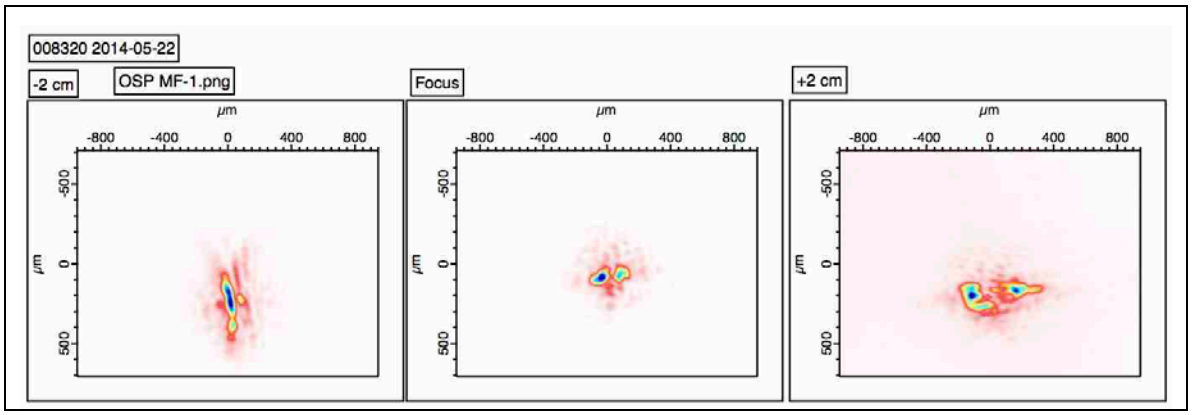

Figure 6.67: Laser profiles for double-bubble shot 8320 at far field - 2 cm (left), far field (middle), and far field + 2 cm (right).

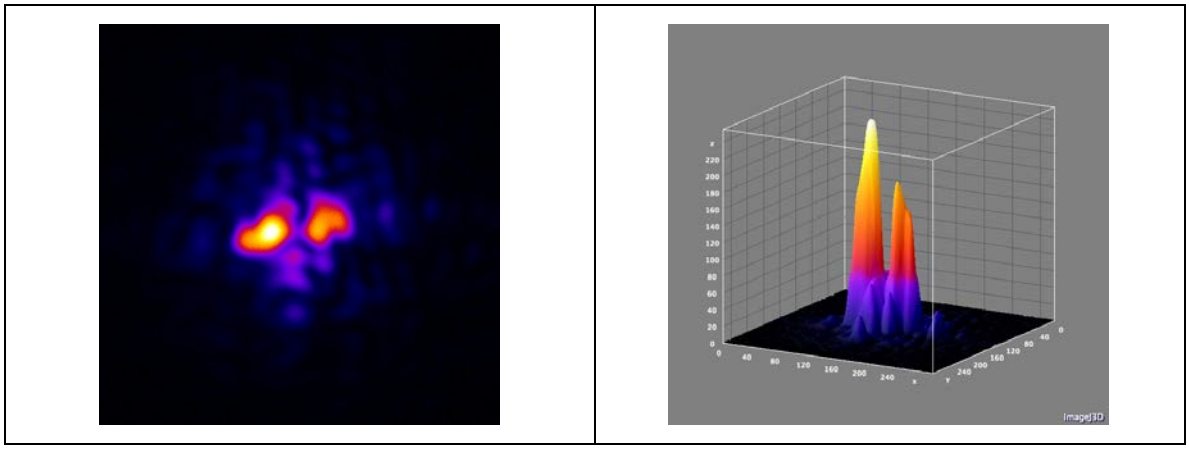

Figure 6.68: 2D and 3D representations of the far field laser profile for double-bubble shot 8320.

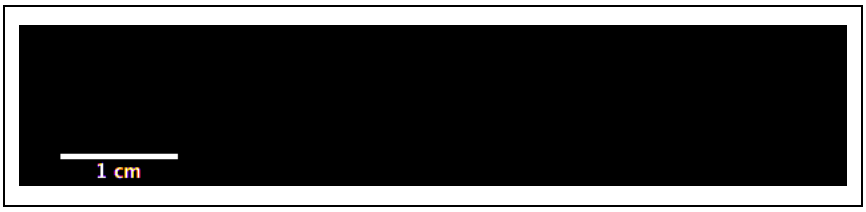

Figure 6.69: Gas cell side scatter for double-bubble shot 8320 (CCD failure).

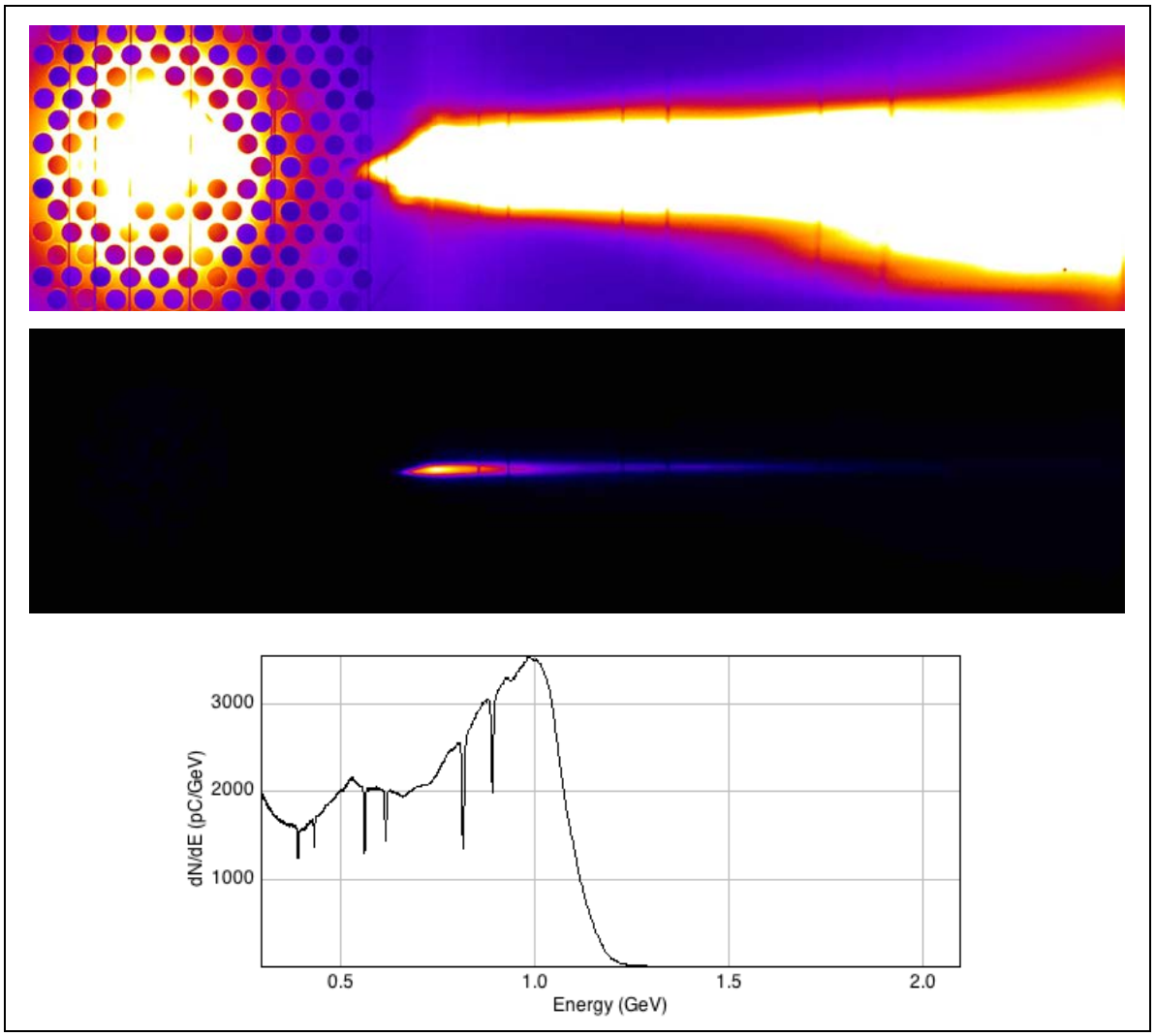

Figure 6.70: Betatron x-rays and magnetically deflected electrons for double-bubble shot 8320 detected on the saturated (top) and unsaturated (middle) imaging plate scans; electron energy spectrum (bottom).

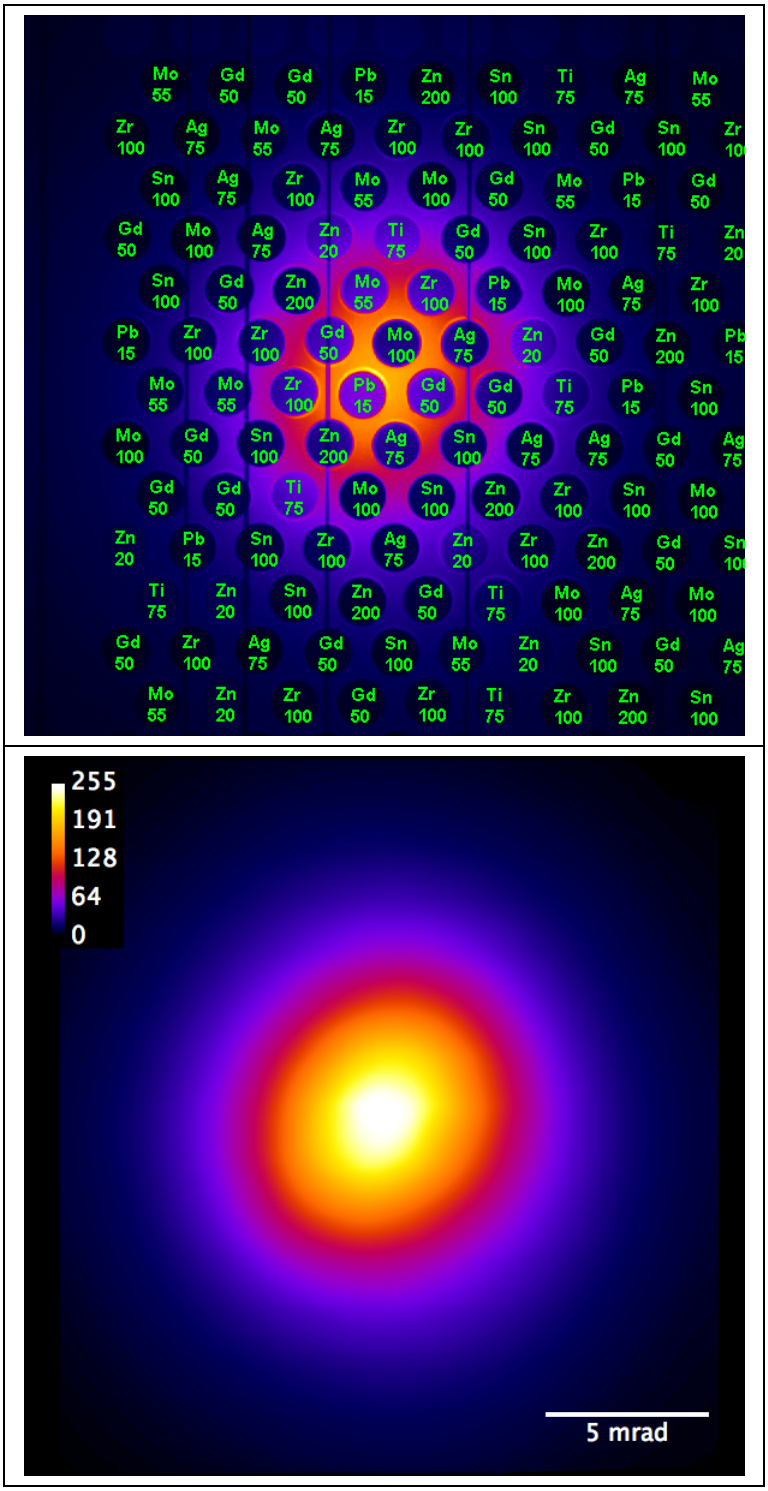

Figure 6.71: Top: betatron x-ray profile, and the K-edge filters used for its spectroscopy, for the double-bubble shot 8320. Bottom: the reconstructed x-ray profile.

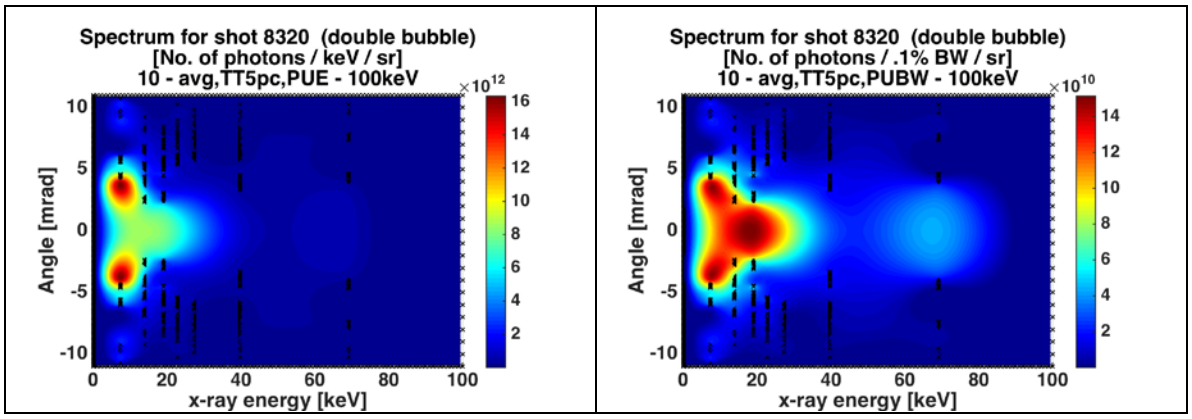

Figure 6.72: Spatially resolved spectrum for double-bubble shot 8320, in per unit energy (left) and per unit bandwidth (right) representations.

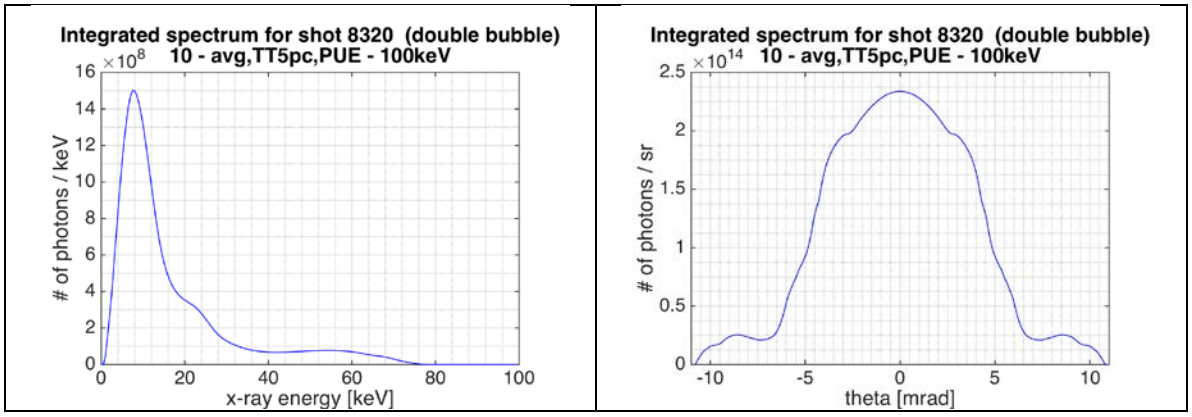

Figure 6.73: Integrated spectrum for double-bubble shot 8320. Left: Spatially integrated spectrum; right: energy-integrated spectrum.

5. Shot 8304 ("Double Bubble")

Laser parameters and selected diagnostic measurements for shot 8304 are shown in Table 6-10. The laser far-field profile for this shot had two distinct and separated hot spots and this is believed to have led to the production of about average charge and photon number.

Shot 8304	
Plasma Density	4.47×10^{17} cm^{-3}
TPW Laser Pulse Energy	133.1 J
TPW Laser Pulse Duration	134 fs
TPW Laser Pulse Power	990 TW
TPW Laser Pulse Fluence	5.412×10^{5} J cm^{-2}
TPW Laser Pulse Intensity	4.02×10^{18} W cm^{-2}
a_0	1.80
Fractional Energy Enclosed within Circle of 80 μm Radius	0.265
Radius of Circle with 50% of Mode Energy	130.98 μm
Max Electron Energy	> 1.5 GeV
Electron Charge > 300 MeV	~1.9 nC
Electron Charge > 1 GeV	~117 pC
X-ray Critical Energy	(26.7 ± 3.1) keV
X-ray FWHM	7.7 mrad
No. of X-ray Photons (double integral of spectra in Figure 6.79*)*	$(2.7 \pm 0.3) \times 10^{10}$

Table 6-10: Parameters and diagnostics for double-bubble shot 8304.

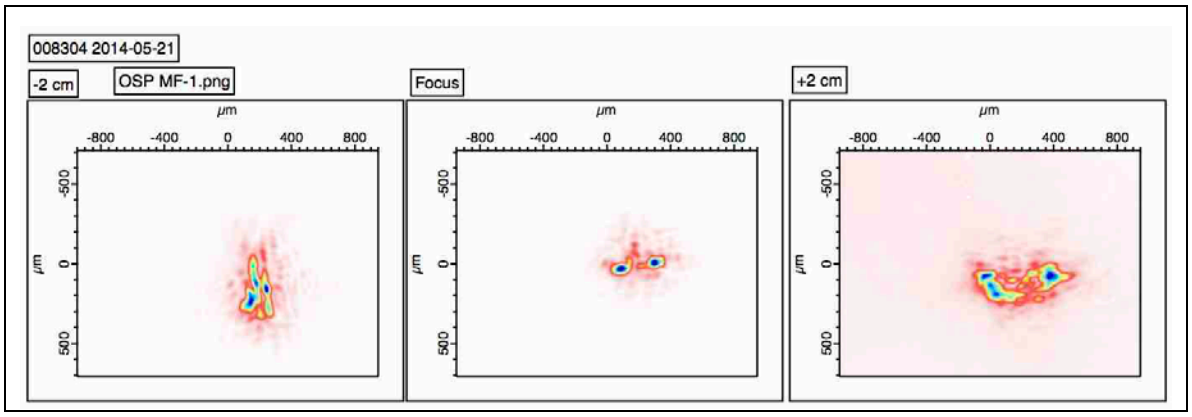

Figure 6.74: Laser profiles for double-bubble shot 8304 at far field - 2 cm (left), far field (middle), and far field + 2 cm (right).

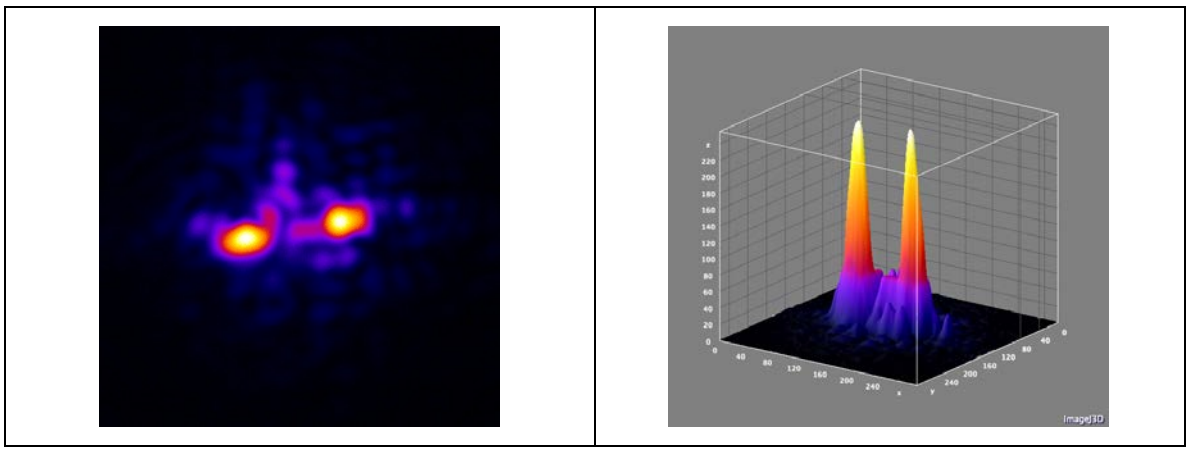

Figure 6.75: 2D and 3D representations of the far field laser profile for double-bubble shot 8304.

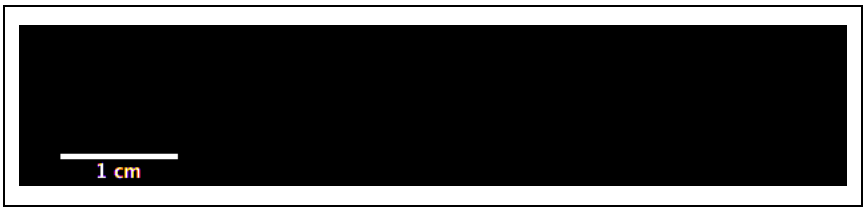

Figure 6.76: Gas cell side scatter for double-bubble shot 8304 (CCD failure)

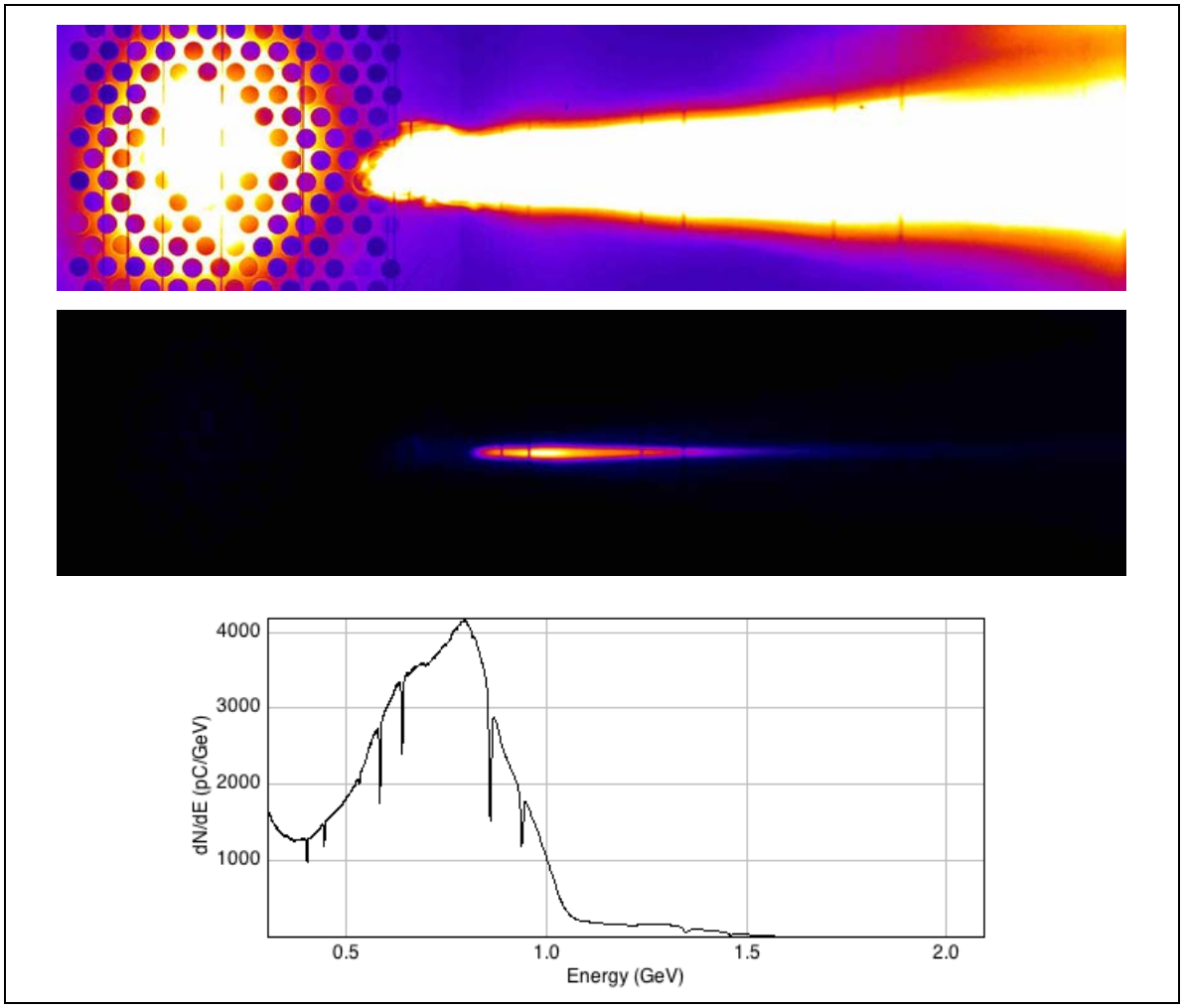

Figure 6.77: Betatron x-rays and magnetically deflected electrons for double-bubble shot 8304 detected on the saturated (top) and unsaturated (middle) imaging plate scans; electron energy spectrum (bottom).

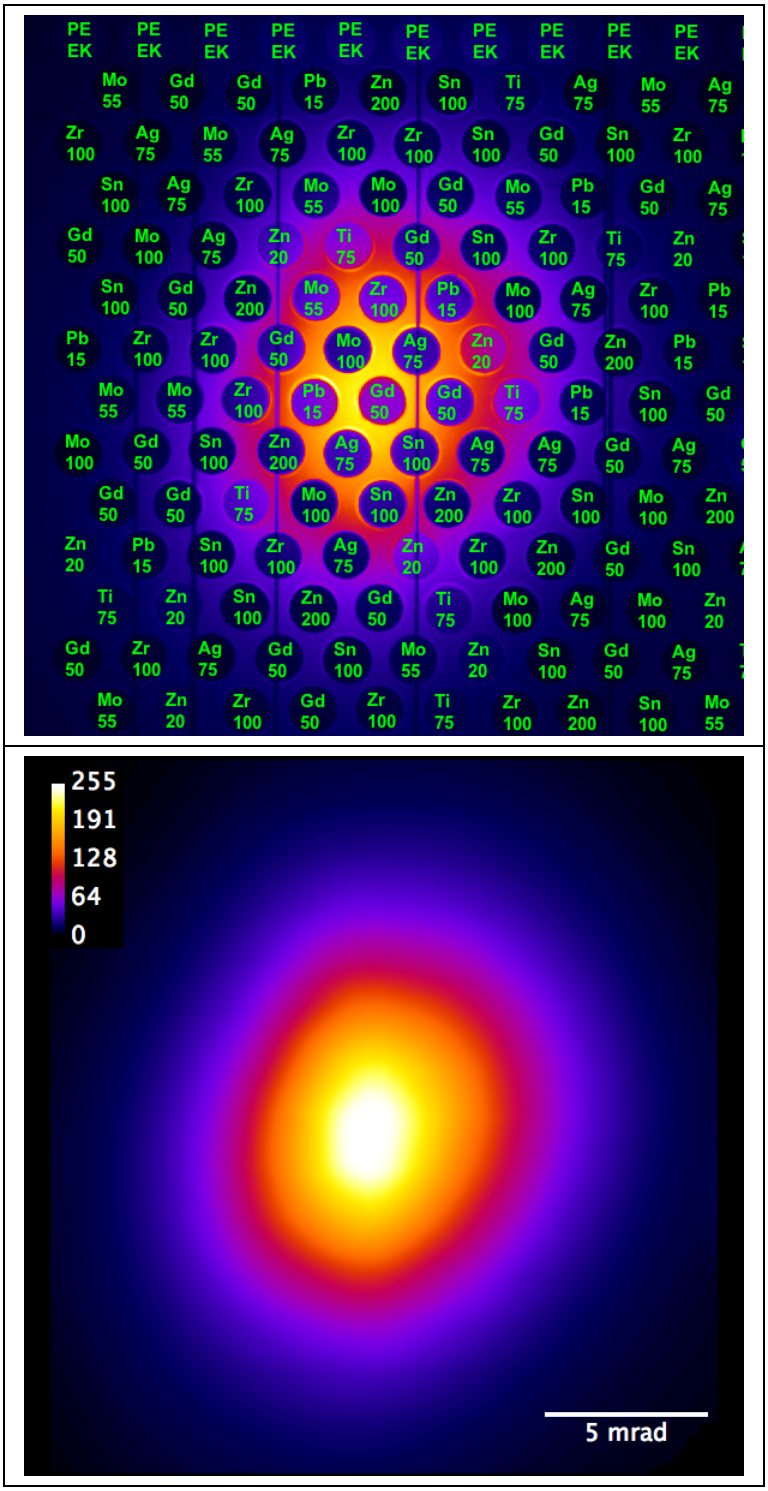

Figure 6.78: Top: betatron x-ray profile, and the K-edge filters used for its spectroscopy, for the double-bubble shot 8304. Bottom: the reconstructed x-ray profile.

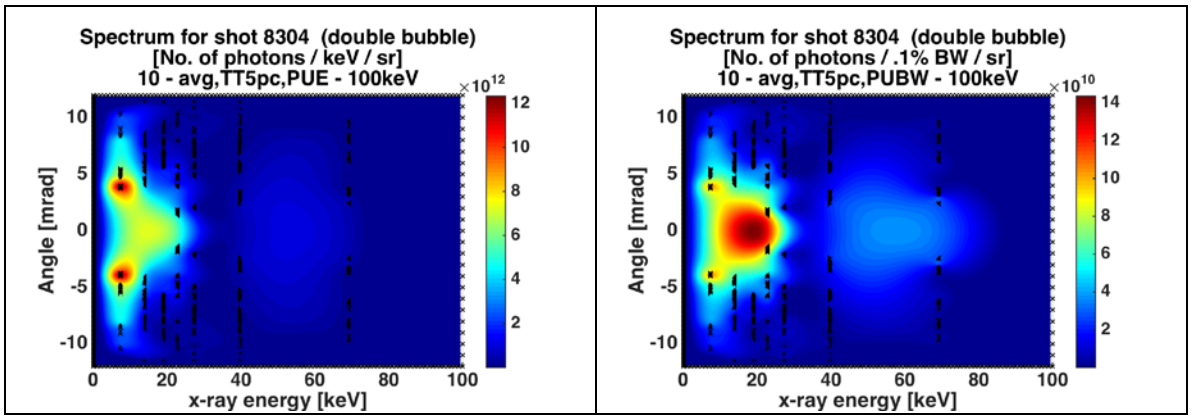

Figure 6.79: Spatially resolved spectrum for double-bubble shot 8304, in per unit energy (left) and per unit bandwidth (right) representations.

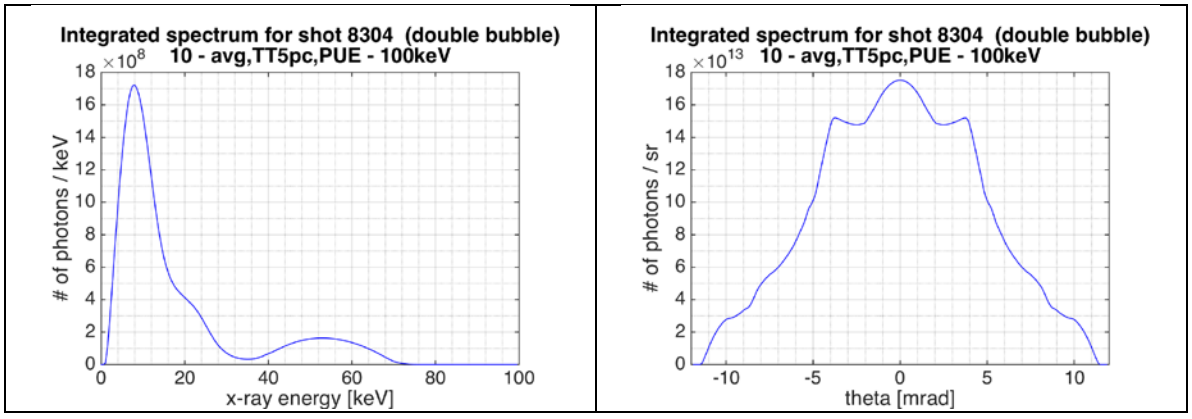

Figure 6.80: Integrated spectrum for double-bubble shot 8304. Left: Spatially integrated spectrum; right: energy-integrated spectrum.

6. Shot 8388 ("Double Bubble")

Laser parameters and selected diagnostic measurements for shot 8388 are shown in Table 6-11. The laser far-field profile for this shot had two distinct and separated hot spots and this is believed to have led to the production of about average charge and photon number.

Shot 8388	
Plasma Density	5.62×10^{17} cm^{-3}
TPW Laser Pulse Energy	122.6 J
TPW Laser Pulse Duration	141 fs
TPW Laser Pulse Power	867 TW
TPW Laser Pulse Fluence	5.394×10^{5} J cm^{-2}
TPW Laser Pulse Intensity	3.82×10^{18} W cm^{-2}
a_0	1.76
Fractional Energy Enclosed within Circle of 80 μm Radius	0.345
Radius of Circle with 50% of Mode Energy	105.35 μm
Max Electron Energy	> 1.5 GeV
Electron Charge > 300 MeV	~2.57 nC
Electron Charge > 1 GeV	~0.98 nC
X-ray Critical Energy	NA
X-ray FWHM	7.8 mrad
No. of X-ray Photons (total PSL divided by max. IP sensitivity)	$> 1.3 \times 10^{10}$

Table 6-11: Parameters and diagnostics for double-bubble shot 8388.

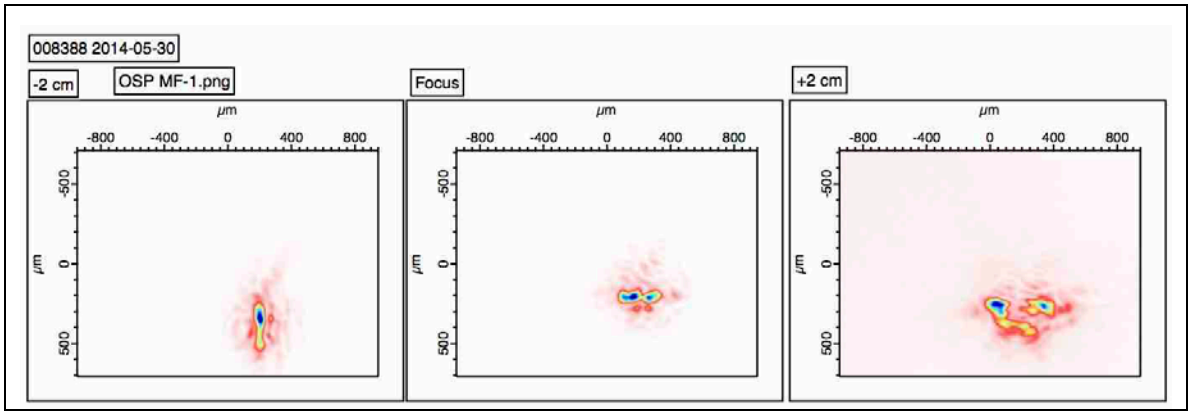

Figure 6.81: Laser profiles for double-bubble shot 8388 at far field - 2 cm (left), far field (middle), and far field + 2 cm (right).

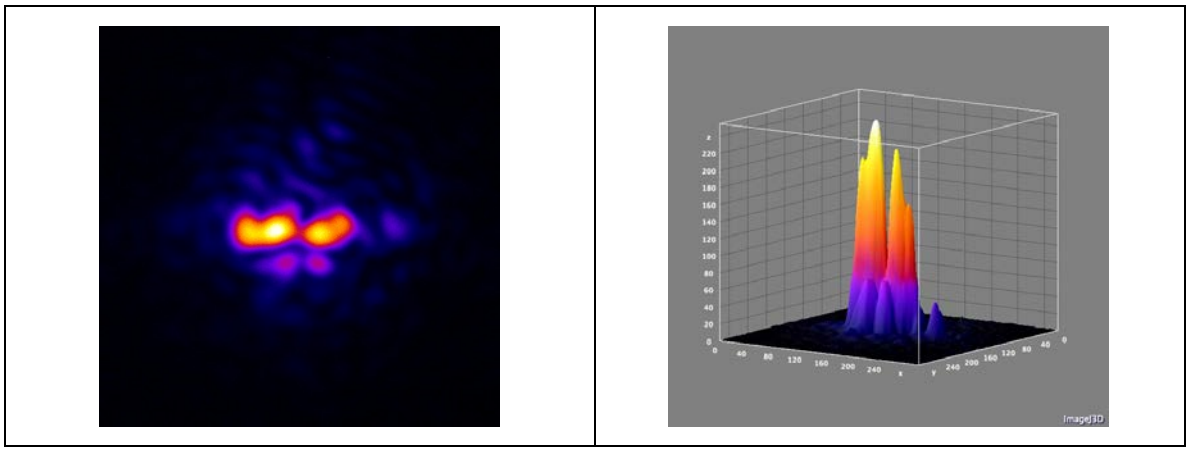

Figure 6.82: 2D and 3D representations of the far field laser profile for double-bubble shot 8388.

Figure 6.83: Gas cell side scatter for double-bubble shot 8388 (CCD failure)

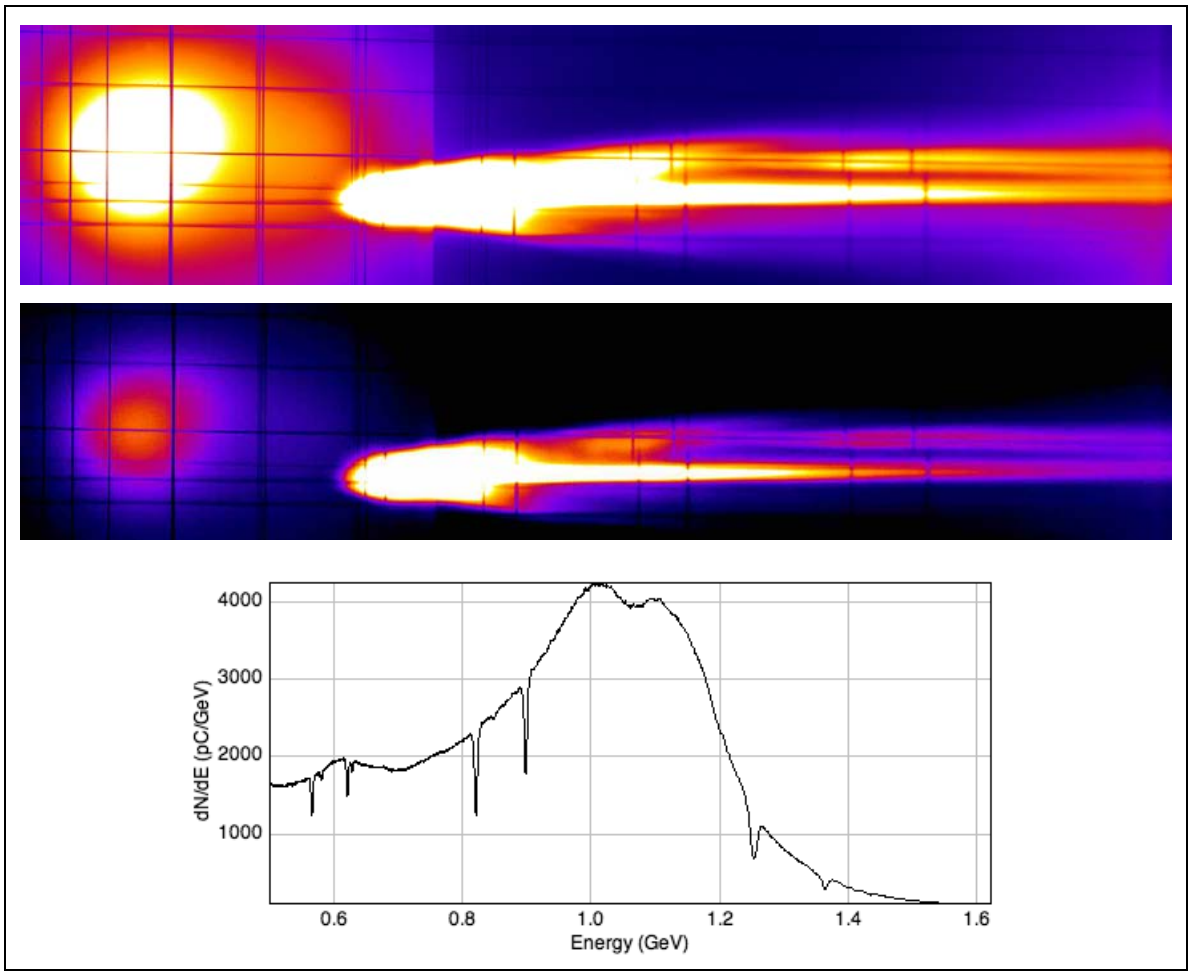

Figure 6.84: Betatron x-rays and magnetically deflected electrons for double-bubble shot 8388 detected on the saturated (top) and unsaturated (middle) imaging plate scans; electron energy spectrum (bottom).

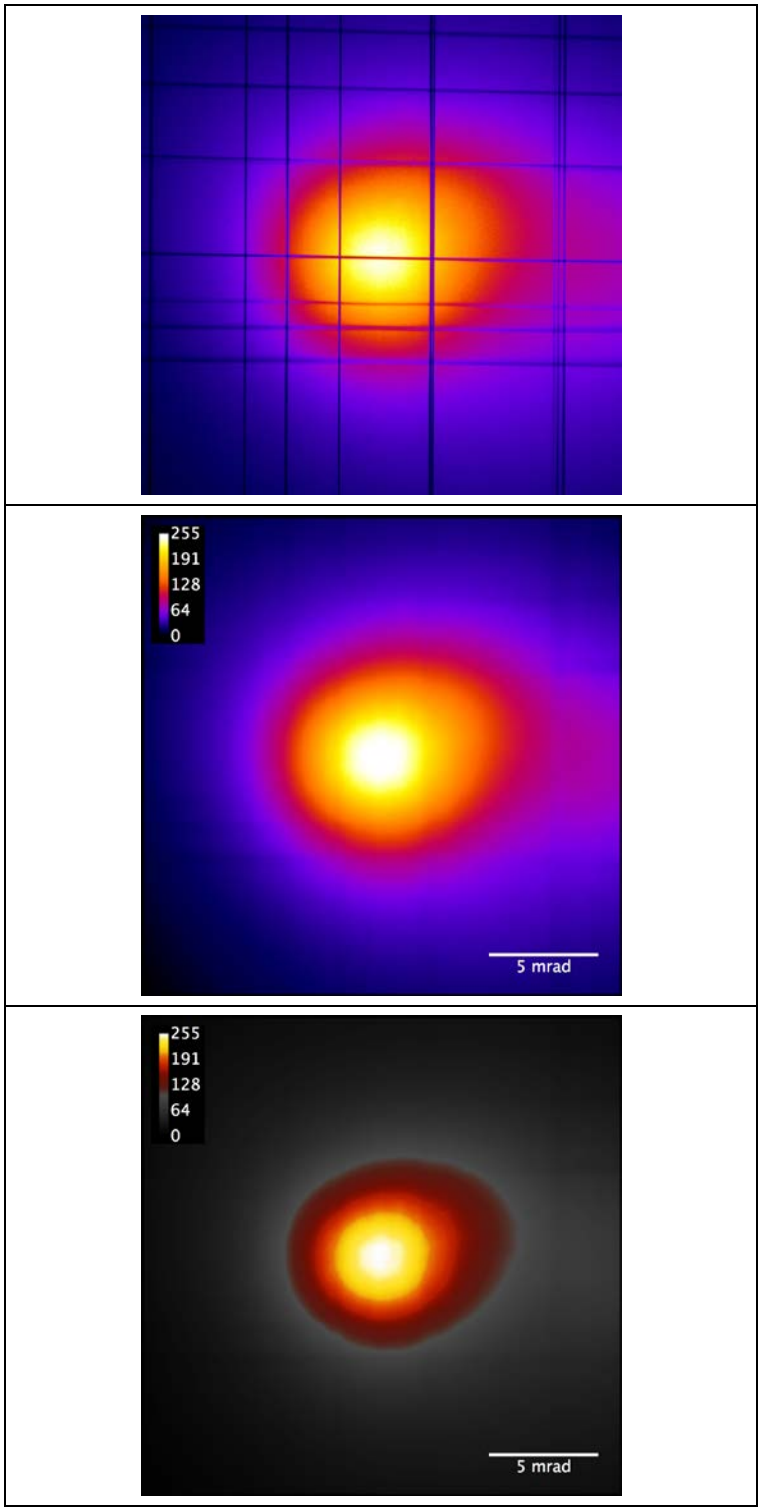

Figure 6.85: Top: betatron x-ray profile, showing shadows from tungsten fiducial wires (vertical), and copper wires (horizontal), for the double-bubble shot 8388. Bottom: the reconstructed x-ray profiles.

7. Shot 8294 (Varying electron divergence)

Laser parameters and selected diagnostic measurements for shot 8294 are shown in Table 6-9. The electron divergence, and launch angle, varied significantly with energy.

Shot 8294	
Plasma Density	4.23×10^{17} cm^{-3}
TPW Laser Pulse Energy	126 J
TPW Laser Pulse Duration	185 fs
TPW Laser Pulse Power	528 TW
TPW Laser Pulse Fluence	3.23×10^{5} J cm^{-2}
TPW Laser Pulse Intensity	1.35×10^{18} W cm^{-2}
a_0	1.04
Fractional Energy Enclosed within Circle of 80 μm Radius	0.212
Radius of Circle with 50% of Mode Energy	172.62 μm
Max Electron Energy	> 1.7 GeV
Electron Charge > 300 MeV	~290 pC
Electron Charge > 1 GeV	~66 pC
X-ray Critical Energy	(18.4 ± 1.4) keV
X-ray FWHM	7.6 mrad
No. of X-ray Photons (double integral of spectra in Figure 6.91*)*	$(9.3 \pm 1.4) \times 10^{8}$

Table 6-12: Parameters and diagnostics for shot 8294 (shot with varying divergence).

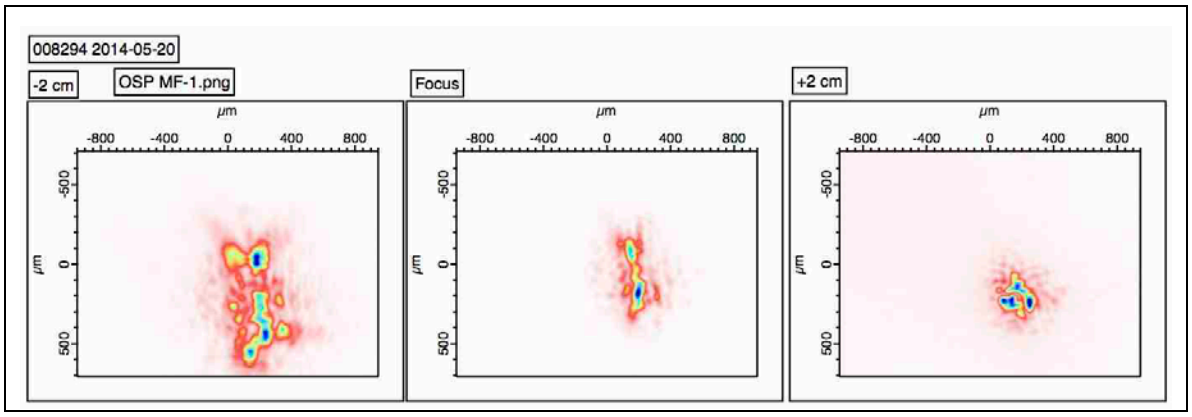

Figure 6.86: Laser profiles for shot 8294 (shot with varying divergence) at far field - 2 cm (left), far field (middle), and far field + 2 cm (right).

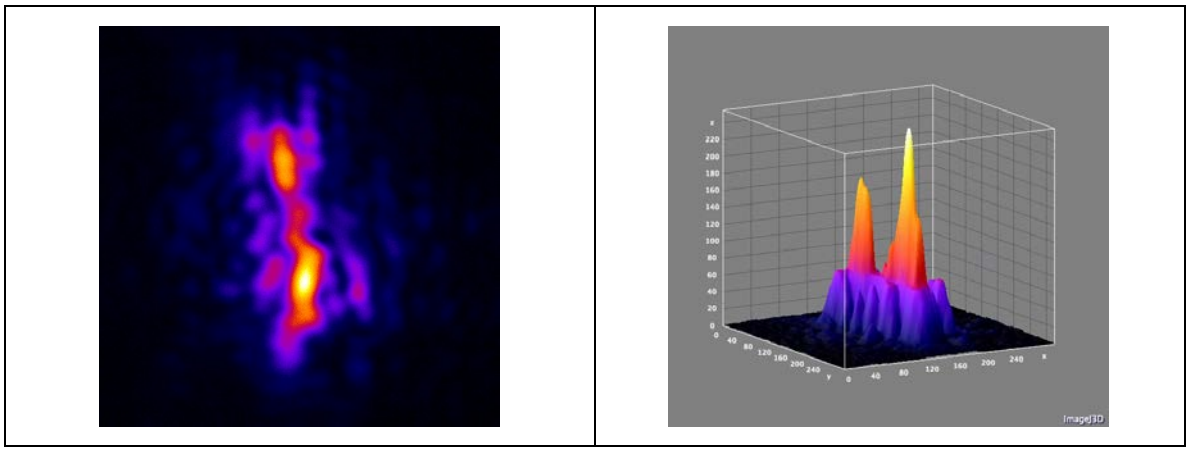

Figure 6.87: 2D and 3D representations of the far field laser profile for shot 8294 (shot with varying divergence).

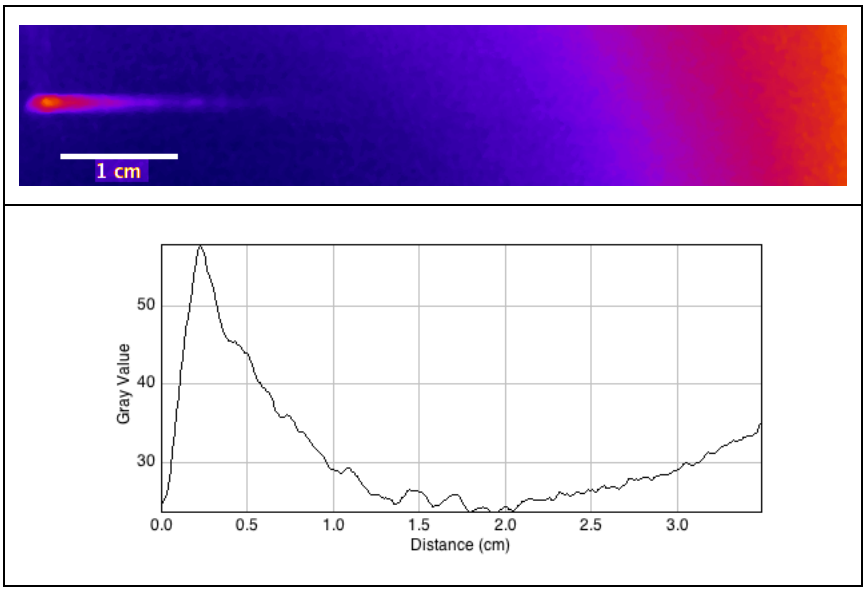

Figure 6.88: Gas cell side scatter for shot 8294 (shot with varying divergence).

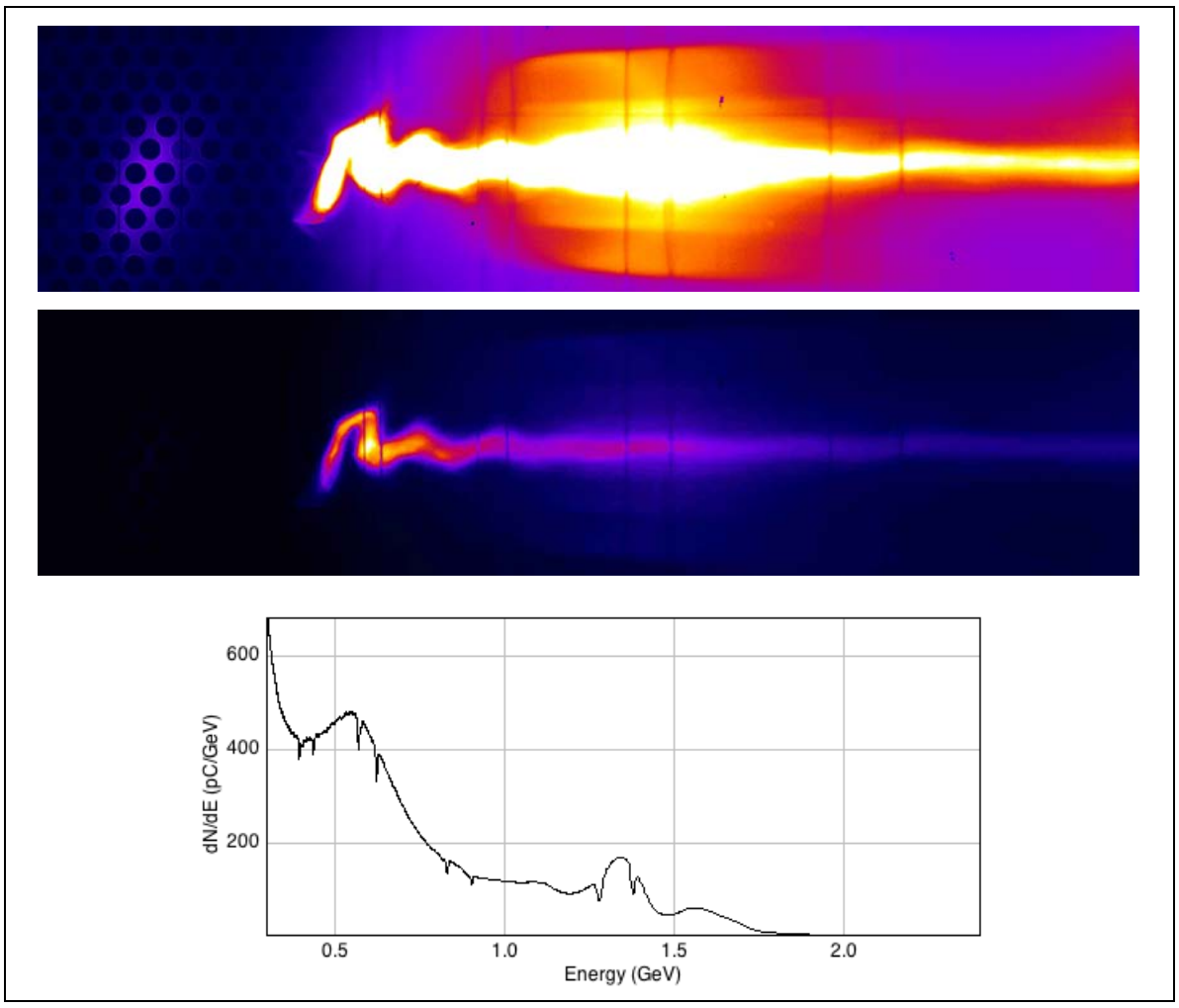

Figure 6.89: Betatron x-rays and magnetically deflected electrons for shot 8294 (with varying divergence) detected on the saturated (top) and unsaturated (middle) imaging plate scans; electron energy spectrum (bottom).

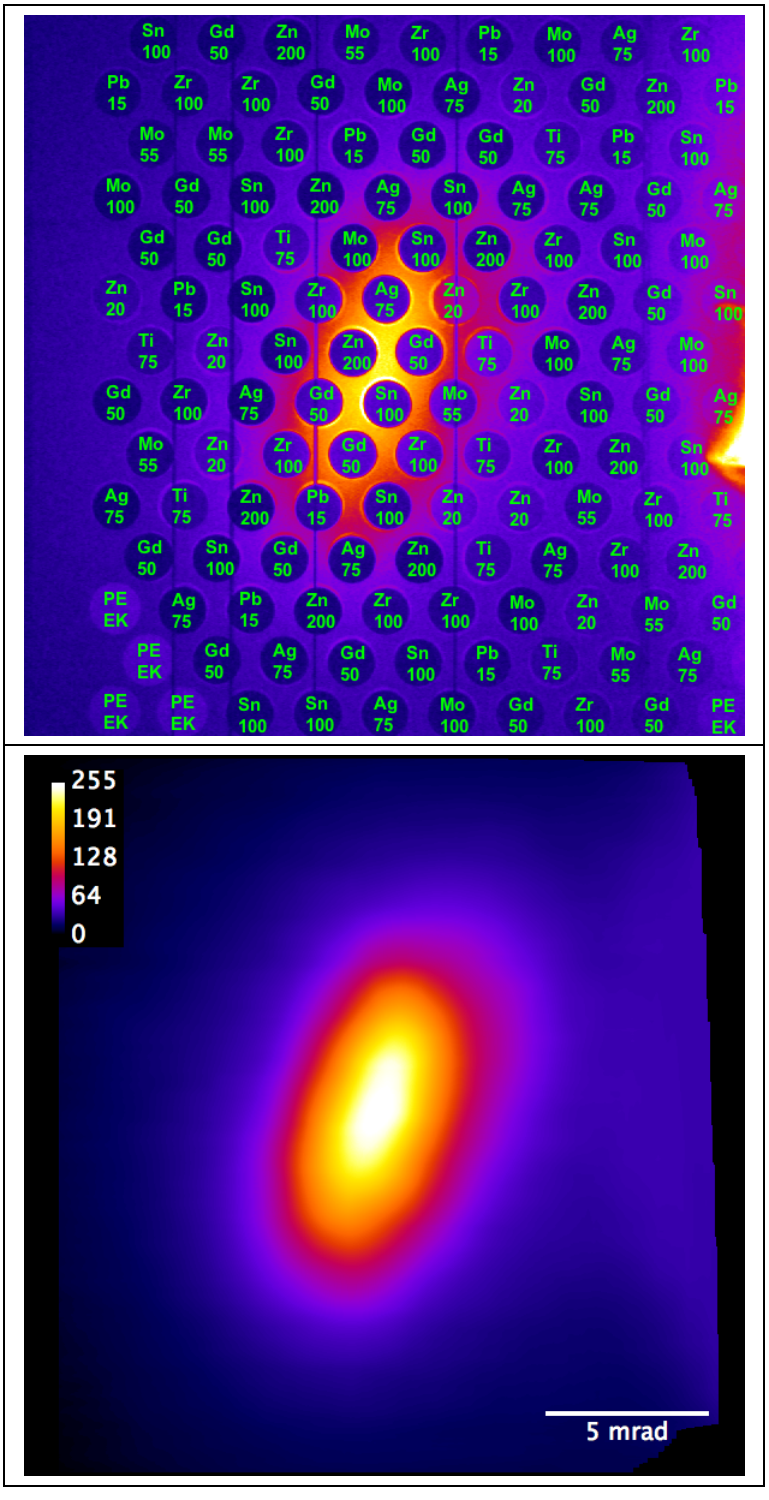

Figure 6.90: Top: betatron x-ray profile, and the K-edge filters used for its spectroscopy, for shot 8294 (shot with varying divergence). Bottom: the

reconstructed x-ray profile.

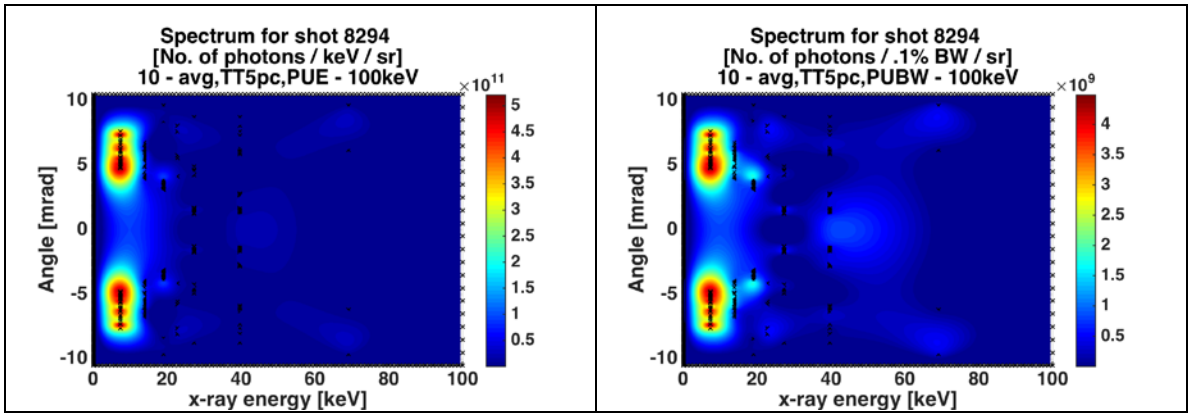

Figure 6.91: Spatially resolved spectrum for shot 8294 (shot with varying divergence), in per unit energy (left) and per unit bandwidth (right) representations.

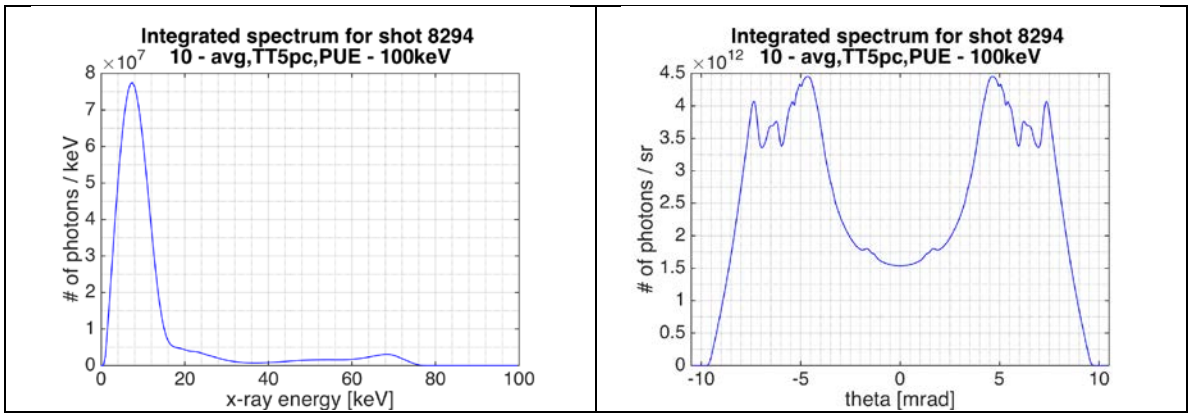

Figure 6.92: Integrated spectrum for shot 8294 (shot with varying divergence). Left: Spatially integrated spectrum; right: energy-integrated spectrum.

6.6 Theoretical Discussion of the X-ray Results

It can be shown [12], starting from the Liénard-Wiechert potential, that for an electron that is at position $\boldsymbol{r}(t)$ at time t, with velocity $\boldsymbol{\beta}$, the energy radiated per unit frequency, per unit solid angle, in direction indicated by the unit vector $\boldsymbol{n}$, is

$$\frac{d^2I}{d\omega\, d\Omega} = \frac{e^2}{16\pi^3\varepsilon_0 c} \times \left| \int_{-\infty}^{\infty} \frac{\boldsymbol{n} \times \left[(\boldsymbol{n}-\boldsymbol{\beta})\times\dot{\boldsymbol{\beta}}\right]}{(1-\boldsymbol{\beta}.\boldsymbol{n})^2} e^{i\omega(t-\boldsymbol{n}\cdot\boldsymbol{r}(t)/c)} \right|^2 \qquad \textbf{Eq. 6.1}$$

where boldface letters indicate 3-vectors, and $\dot{\boldsymbol{\beta}} = d\boldsymbol{\beta}/dt$. From Eq. 6.1 it can immediately be seen that for energy to be radiated by an electron, $\dot{\boldsymbol{\beta}} \neq 0$, i.e., it needs to be accelerated. Also the denominator vanishes when $\boldsymbol{\beta}.\boldsymbol{n} = \beta\cos\theta = 1$, where θ is the angle between the direction of electron motion and direction of observation; therefore the radiation is maximum for relativistic electrons ($\beta = 1$) and in the direction of their motion ($\theta = 0$). When a relativistically intense laser pulse interacts with underdense plasma, it produces a cavitation in its wake, and when there is complete blowout of electrons, a bubble forms in the plasma. The space charge produces electrostatic forces in the bubble parallel and transverse to the direction of propagation of the laser pulse. An electron injected into the bubble accelerates under the longitudinal forces in the relativistically moving bubble. Depending on the direction of its momentum as it was injected into the bubble, the electron will also have an initial transverse momentum; however the transverse forces in the bubble act as restoring forces on the electron causing it to oscillate at the same time that it accelerates longitudinally. For an electron moving longitudinally, the same force transverse to $\boldsymbol{\beta}$ is more effective (by a factor of γ^2) in producing acceleration, $d\boldsymbol{\beta}/dt$, than forces parallel to $\boldsymbol{\beta}$ [45]. It follows that the transverse restoring force inside the plasma bubble, producing what is known as the betatron motion, is the primary source of radiation by the electron. Since the plasma bubble moves at the group velocity of the laser pulse, electron oscillation takes place in a relativistically boosted frame; this produces an upshift in the frequency of radiated photons to the x-ray region of the electromagnetic spectrum. The spectrum of the betatron radiation is parameterized by the strength parameter K, which is equal to the ratio of the radiation divergence half angle and the approximate radiation cone angle, Ψ and $\Delta\vartheta$, respectively, in Figure 6.93 [45]. Since the latter angle is equal to $1/\gamma$, where γ is

relativistic gamma of the electron , one has $K = \Psi/\Delta\vartheta = \gamma\,\Psi$. As shown in the figure, small values of K

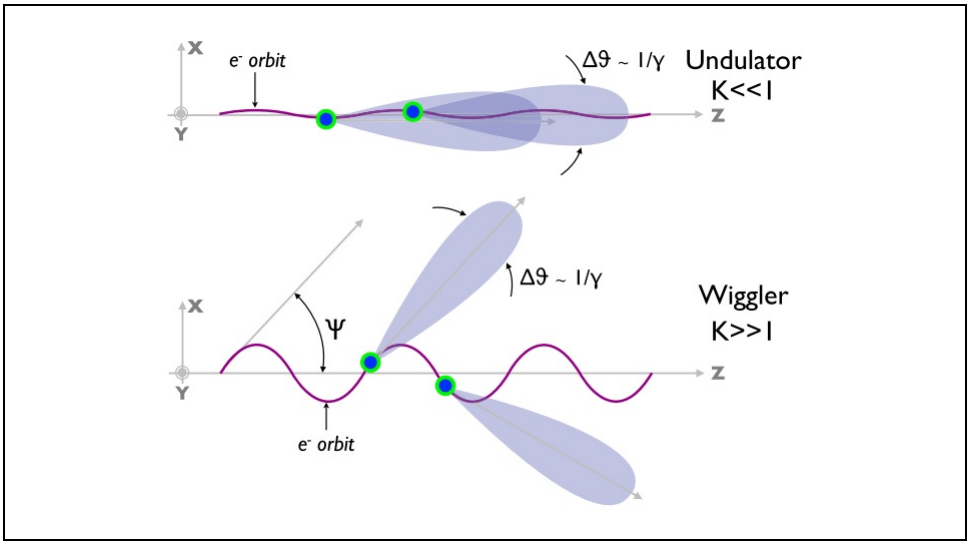

Figure 6.93: The two limiting regimes for the betatron oscillation [Image from Corde et. al [45]]

indicate that the radiation is largely in the forward direction with the variation in the direction of the radiation cone axis smaller than the radiation cone angle itself; large values of K, on the other hand, are indicative of larger oscillation amplitudes, causing the direction of the radiation cone to change at different points on the electron trajectory. The betatron radiation spectrum is synchrotron-like, but decays more slowly than the synchrotron radiation spectrum at frequencies higher than the critical frequency, $\omega_c = \frac{3}{2}\gamma^3\frac{c}{\rho}$ [12], where ρ is the radius of curvature of the electron at a given point on its trajectory and in the lab frame. The two limiting cases of betatron motion, corresponding to $K \ll 1$ and $K \gg 1$, are denoted as the *undulator* and *wiggler* regimes, respectively. In the undulator regime, the radiation is at a fundamental frequency, which, however, changes with the direction of observation. In the wiggler regime, the radiated spectrum contains the fundamental frequency, as well as its harmonics, up to the critical frequency (itself changing with the direction of observation), after which the spectrum decays exponentially. In the asymptotic wiggler limit ($K \gg 1$), Eq. 6.1 reduces to Eq. 6.2 [35]

$$\frac{d^2I}{d\omega\, d\Omega} \approx N_\beta \frac{6\,e^2}{\pi^2 c}\frac{\gamma^2\zeta^2}{1+\gamma^2\theta^2}\times\left[\frac{\gamma^2\theta^2}{1+\gamma^2\theta^2}K_{1/3}^2(\zeta)\;\boldsymbol{u}_\pi^2 + K_{2/3}^2(\zeta)\,\boldsymbol{u}_\sigma^2\right] \qquad \textbf{Eq. 6.2}$$

where N_β is the number of betatron oscillations, $\zeta = \frac{\omega}{\omega_c}(1+\gamma^2\theta^2)^{3/2}$, and $K_{1/3}$ and $K_{2/3}$ are modified Bessel functions. The terms in this expression, explicitly identified by the unit vectors $\boldsymbol{u}_\pi$ and $\boldsymbol{u}_\sigma$, are the contributions from radiation polarized in the plane of electron trajectory and perpendicular to it, respectively. It follows from this formula that the on-axis spectrum (i.e., for $\Psi = 0$ in the figure) peaks for $\zeta = 1/2$; this corresponds to $\omega_c = 2 \times \omega_{peak}$. Therefore, the on-axis critical energy may be determined by doubling the energy at which the spatially resolved betatron spectrum peaks on the axis. The critical energy is reduced with increasing angle of observation with respect to the direction of longitudinal motion of the electron.

The distinguishing features of the radiation from electrons accelerated to > 1 GeV energies may be understood by referring to the scaling laws obtained in the wiggler limit for the betatron radiation [58]:

$$N_\gamma \propto N_e N_\beta K \propto N_e N_\beta \sqrt{\gamma n_e} r_\beta \qquad \textbf{Eq. 6.3}$$

$$\theta_r \propto K/\gamma \propto \sqrt{n_e}\, r_\beta / \sqrt{\gamma} \qquad \textbf{Eq. 6.4}$$

$$\hbar\omega_c \propto \gamma^{1.5}\sqrt{n_e} K \propto \gamma^2 n_e r_\beta \qquad \textbf{Eq. 6.5}$$

These scalings relate the number of photons N_γ, x-ray beam divergence half angle θ_r (Ψ in Figure 6.93), and x-ray critical energy $\hbar\omega_c$, to the electron charge N_e, relativistic gamma of the electron γ, and the plasma density n_e. Figure 6.94 shows an estimate for the total photon number as a function of charge (using 25% and 10% error bars for the photon number and charge, respectively, on each side of the data point) for a large subset of shots in the 4th experimental round. This estimate for the photon number was in each case obtained by dividing the total PSL on the reconstructed x-ray profile image by the average imaging plate detector sensitivity to x-rays between 10 and 30 keV, using the response curves in Figure 5.14. (In the case of MS IPs, this is 5.52 mPSL/photon; for the SR IP it is 1.75 mPSL/photon.) The conservative total photon number averaged at 2.1 × 10^9 photons and was as high as 1.3 × 10^{10} photons. This compares favorably with the average total photon number of 10^8 generated in sub-GeV accelerators [40]. According to Eq. 6.3, the increased photon number may be attributed to the larger electron energy γ (> 2000 vs. ~200) and charge N_e (~1 nC vs. ~10 pC), which together more than compensate

for the lower plasma density n_e used in the GeV accelerator (~5 × 10^{17} cm^{-3} vs. ~1 × 10^{19} cm^{-3}). The total number of x-ray photons detected followed an increasing trend with

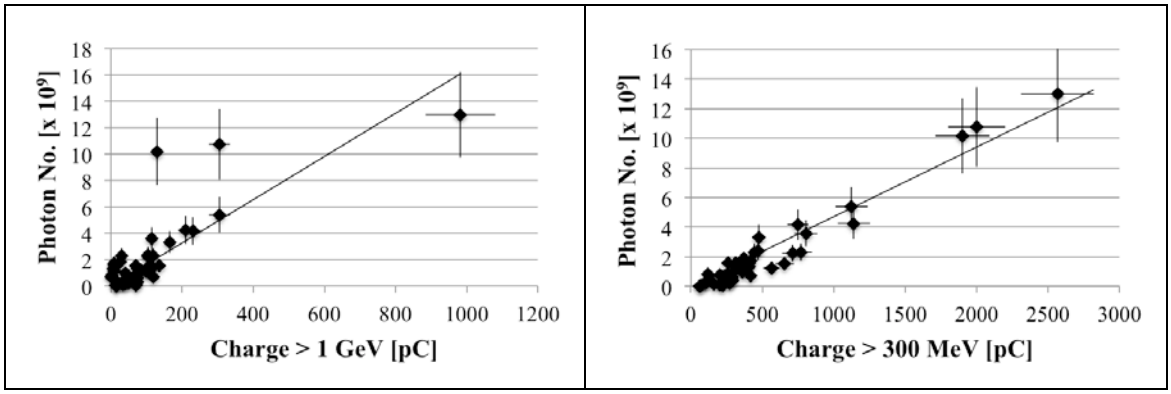

Figure 6.94: Variation of the photon number with charge above 1 GeV (left) and charge above 300 MeV (right), in the GeV LPA

respect to charge above 1 GeV (Figure 6.94, left), with the scatter about the linear trend attributable to the variation in peak electron energy for different shots. However, the linear trend is even stronger when the number of photons is plotted against charge above 300 MeV (Figure 6.94, right). (As discussed elsewhere, charge < 300 MeV was not measured in the 4th experimental round as the result of the time constraint posed by the repeated IP scanning that was necessary due to the high charge produced during this round.) A more careful analysis, discussed later in this chapter, showed that it was necessary to include charge > 300 GeV in order for a consistent parameter space for the betatron oscillations, given the various observables, to emerge. We also observed evidence of enhanced photon flux when two hot spots were dialed into the TPW laser pulse using adaptive optics. This had been suggested by simulation [57] and several of the shots with highest photons numbers in these experiments belonged to this category. The outliers in Figure 6.94 (right) corresponds to this type of 'double bubble' shot, where two hot spots in the driving laser's far-field profile (see, e.g., Figure 6.82), separated by a distance of ~3/4 of the spot size for an individual hot spot, merged inside the plasma and produced enhanced charge and photon number (see Figure 6.84). For the same sample of shots, an x-ray beam FWHM divergence averaging (5.9 ± 1.5) mrad, and as low as ~4 mrad, was observed (Figure 6.95), a factor of 3-5 smaller than the ~13-20 mrad divergence reported for sub-GeV accelerators ([34], [41]) and in agreement with the scaling in Eq. 6.4.

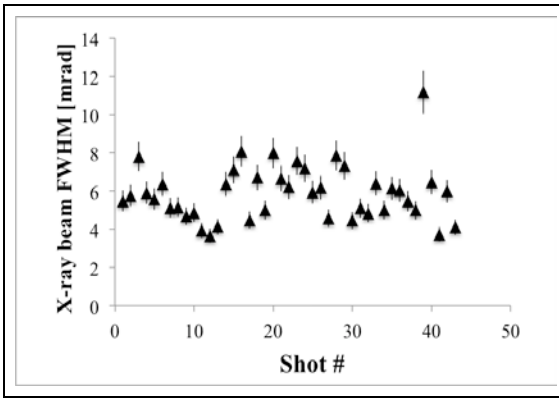

Figure 6.95: FWHM divergence of x-ray beam in GeV LPA

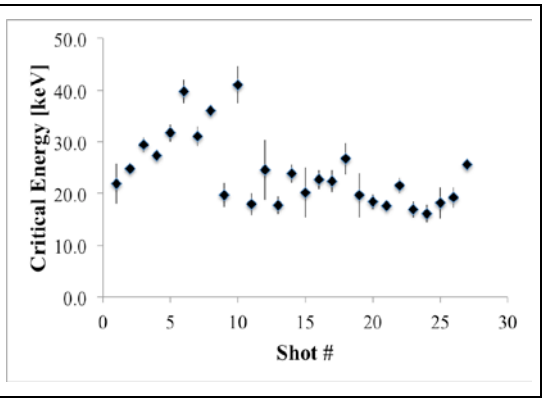

Figure 6.96: Critical energy of the x-ray beams in the GeV LPA

The spatially-resolved spectra of the x-rays from the GeV LPA was calculated for a smaller sample of 26 shots for which x-ray filters had been deployed for spectroscopy of the x-ray beam and the MS IP was used as detector (see Figure 6.41 to Figure 6.45). These showed the x-ray energy at which the spectrum peaks shifting to larger energies with decreasing angle of observation, consistent with what would be expected for synchrotron-type radiation [59]. The critical energy $\hbar\omega_c$ shifts to energies $\gtrsim$ 20 keV (Figure 6.96) from < 10 keV typical for sub-GeV LPAs [60]. (The calculation of error bars is described below.) In several cases the critical energy exceeded or approached 40 keV. The shift to larger energies follows from the scaling in Eq. 6.5 but is smaller than what would be expected given the γ^2-dependence. This may be attributed to the counterbalancing effect of the lower plasma density n_e in the GeV accelerator.

Eq. 6.6 gives the strength parameter K in terms of the plasma density, n_e, and the betatron oscillation amplitude, r_β. As previously noted, when $K \ll 1$, the radiation is monochromatic; when $K \gg 1$, the spectrum resembles that from the synchrotron radiation, having harmonics up to the critical frequency ω_c, after which it drops exponentially. The scaling laws previously given in Eq. 6.3-Eq. 6.5 for the number of photons, N_γ, beam divergence half angle, θ_r, and the critical energy, $\hbar\omega_c$, as well as for the betatron period (wavelength), λ_β, are repeated below, but now in equation form, in terms of the strength parameter [58]:

$$K = 1.33\times10^{-10}\gamma^{0.5}n_e^{0.5}[cm^{-3}]r_\beta[\mu m] \quad \textbf{Eq. 6.6}$$

$$N_\gamma = 5.6\times10^{-3}N_eN_\beta K = 1.33\times5.6\times10^{-13}N_eN_\beta\gamma^{0.5}n_e^{0.5}[cm^{-3}]r_\beta[\mu m] \quad \textbf{Eq. 6.7}$$

$$\theta_r[mrad] = K/\gamma = 1.33\times10^{-10}n_e^{0.5}[cm^{-3}]r_\beta[\mu m]/\sqrt{\gamma} \quad \textbf{Eq. 6.8}$$

$$\hbar\omega_c[eV] = \hbar\frac{3}{2}K\gamma^2\omega_\beta = \left(\hbar\frac{3}{2}K\gamma^2\right)\frac{\omega_p}{\sqrt{2\gamma}} = 3.94\times10^{-11}\gamma^{1.5}n_e^{0.5}[cm^{-3}]K$$

$$= 5.24\times10^{-21}\gamma^2 n_e[cm^{-3}]r_\beta[\mu m] \quad \textbf{Eq. 6.9}$$

$$\lambda_\beta[\mu m] = 2\pi\gamma r_\beta[\mu m]/K \quad \textbf{Eq. 6.10}$$

In addition, the relation between the observable peak on-axis x-ray energy, $\hbar\omega_{peak}$, and the critical energy, $\hbar\omega_c$, is given in Eq. 6.11 [35]:

$$\hbar\omega_{peak}[eV] = 0.5 \times \hbar\omega_c[eV] \quad \textbf{Eq. 6.11}$$

Together, these relations provide a complete set of betatron radiation parameters, *K*, γ, r_β, N_β, λ_β, and $\hbar\omega_c$ for monoenergetic electrons, in terms of the observables N_e, N_γ, θ_r, and $\hbar\omega_{peak}$ and the experimental parameter n_e (plasma density). These equations may be applied to the observables from the final experimental round, to verify the internal consistency of the measurements, as well as determine effective values for the unknown parameters *K*, γ, r_β, N_β, λ_β, and $\hbar\omega_c$ in the case of betatron x-rays produced by non-monoenergetic electron bunch of charge $N_e e$. These effective parameters obtained by applying Eq. 6.6-Eq. 6.11 to experimental observables will be denoted K_{eff}, γ_{eff}, $r_{\beta,eff}$, $N_{\beta,eff}$, $\lambda_{\beta,eff}$, and $\hbar\omega_{c,eff}$. As a first step, note that from the spatially resolved spectra determined for the spectra in the 4th experimental run, it is possible to numerically determine $\hbar\omega_{peak}$, the energy at which the on-axis spectrum peaks. This was done for a set of 26 shots, then $\hbar\omega_{c,eff}$ calculated according to Eq. 6.11. The next step is to write Eq. 6.7-Eq. 6.9 in terms of the effective parameters γ_{eff}, $r_{\beta,eff}$, and $N_{\beta,eff}$ and experimental observables N_e, N_γ, θ_r, and $\hbar\omega_c$:

$$N_\gamma = A \times N_e\, N_{\beta,eff}\, \gamma_{eff}^{0.5}\, r_{\beta,eff}[\mu m] \quad \textbf{Eq. 6.12}$$

$$\theta_r[mrad] = B \times r_{\beta,eff}[\mu m]/\gamma_{eff}^{0.5} \quad \textbf{Eq. 6.13}$$

$$\hbar\omega_c[eV] = C \times \gamma_{eff}^2\, r_{\beta,eff}[\mu m] \quad \textbf{Eq. 6.14}$$

where *A*, *B,* and *C* are constants dependent on the plasma density n_e:

$$A = 5.6\times1.33\times10^{-13}\sqrt{n_e[cm^{-3}]}$$
$$B = 1.33\times10^{-10}\sqrt{n_e[cm^{-3}]} \quad \textbf{Eq. 6.15}$$
$$C = 5.24\times10^{-21}n_e[cm^{-3}]$$

Solving Eq. 6.12-Eq. 6.14 for γ_{eff}, $r_{\beta,eff}$, and $N_{\beta,eff}$ in the terms of the observables $\hbar\omega_c$, θ_r, N_γ, and N_e, and the constants *A*, *B,* and *C* (Eq. 6.15), yields the relations in Eq. 6.16 to Eq. 6.18 for the effective betatron oscillation parameters:

$$\gamma_{eff} = \left(\frac{B}{C}\times\frac{\hbar\omega_c}{\theta_r}\right)^{2/5} \quad \textbf{Eq. 6.16}$$

$$r_{\beta,eff} = \frac{\theta_r}{B}\left(\frac{B}{C}\times\frac{\hbar\omega_c}{\theta_r}\right)^{1/5} \quad \textbf{Eq. 6.17}$$

$$N_{\beta,eff} = \frac{B}{A}\frac{N_\gamma}{N_e\theta_r}\left(\frac{B}{C}\times\frac{\hbar\omega_c}{\theta_r}\right)^{-2/5} \quad \textbf{Eq. 6.18}$$

Using the values observed for the critical energy ($\hbar\omega_c$), divergence (θ_r), number of x-ray photons (N_γ), and the number of electrons (N_e, calculated as the detected electron charge, in Coulombs, divided by the charge of one electron, 1.602×10^{-19} C), the effective oscillation parameters have been calculated (Figure 6.97). The uncertainty in these parameters due to uncertainty in the number of photons, δN_γ, uncertainty in the critical energy, $\delta(\hbar\omega_c)$, and the uncertainty in the divergence half angle, $\delta\theta_r$, are

$$\delta\gamma_{eff} = \gamma_{eff}\sqrt{\left(\frac{2}{5}\frac{\delta(\hbar\omega_c)}{\hbar\omega_c}\right)^2 + \left(\frac{2}{5}\frac{\delta\theta_r}{\theta_r}\right)^2} \quad \textbf{Eq. 6.19}$$

$$\delta r_{\beta,eff} = r_{\beta,eff}\sqrt{\left(\frac{1}{5}\frac{\delta(\hbar\omega_c)}{\hbar\omega_c}\right)^2 + \left(\frac{4}{5}\frac{\delta\theta_r}{\theta_r}\right)^2} \quad \textbf{Eq. 6.20}$$

$$\delta N_{\beta,eff} = N_{\beta,eff}\sqrt{\left(\frac{\delta N_e}{N_e}\right)^2 + \left(\frac{\delta N_\gamma}{N_\gamma}\right)^2 + \left(\frac{2}{5}\frac{\delta(\hbar\omega_c)}{\hbar\omega_c}\right)^2 + \left(\frac{3}{5}\frac{\delta\theta_r}{\theta_r}\right)^2} \quad \textbf{Eq. 6.21}$$

The uncertainty in the critical energy, $\delta(\hbar\omega_c)$, is the result of the uncertainty in the determination of the energy $\hbar\omega_{peak}$ at which the on-axis spectrum peaks. The spectrum

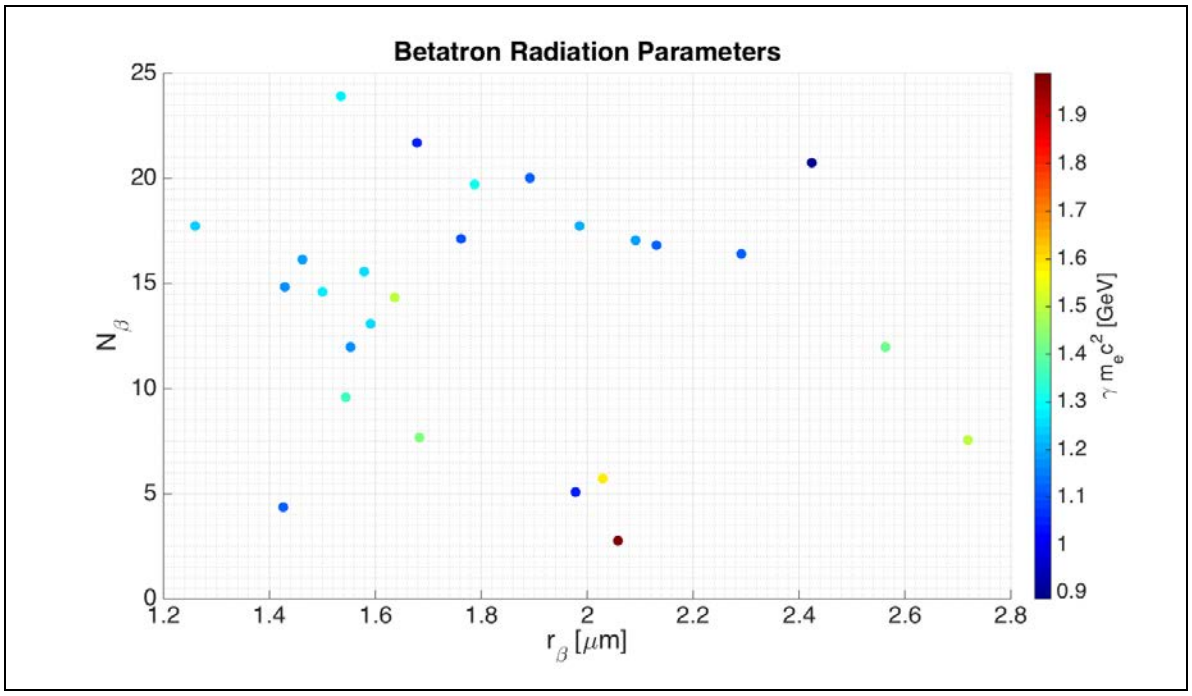

Figure 6.97: 3D plot of the effective betatron radiation parameters (relativistic gamma, betatron oscillation amplitude, and number of betatron oscillations)

data, in the per unit energy representation, were fit using two different fitting algorithms, biharmonic spline interpolation (5.7.4) and gridfit. The former method attempts to bridge over the on-axis gaps in the data (from small iso-intensity contours), whereas the latter does not. The difference in the on-axis peak energy from the two methods was used as an indication of the error in the peak energy. (The difference is as low as ~1% and as high as ~24%, depending on the x-ray spectrum, averaging at ~10%.) The critical energy was then calculated as twice the on-axis peak energy [35]. To calculate the x-ray beam divergence, a Gaussian fit was done to a line-out of the intensity along the major axis of the x-ray beam profile. Then the standard deviation of the Gaussian was multiplied by the factor $2\sqrt{2\ln 2}$ for the conversion of Gaussian standard deviation to Gaussian FWHM. The beam divergence, θ_r (denoted by Ψ in Figure 6.93), equals half of the Gaussian FWHM divided by the distance between the x-ray source and the detector (2.725 m for LWFA 4.0, using the middle of the gas cell as the position of the x-ray source; see Figure 6.29). The error in the beam divergence, $\delta\theta_r$, is the uncertainty in determining the FWHM as the result of the eccentricity that exists in the x-ray profile. The standard deviation of theta (θ is defined in 5.7.4) as a ratio of the average theta for all pixels on a representative iso-intensity contour (in all cases the one having intensity equal to 50% of

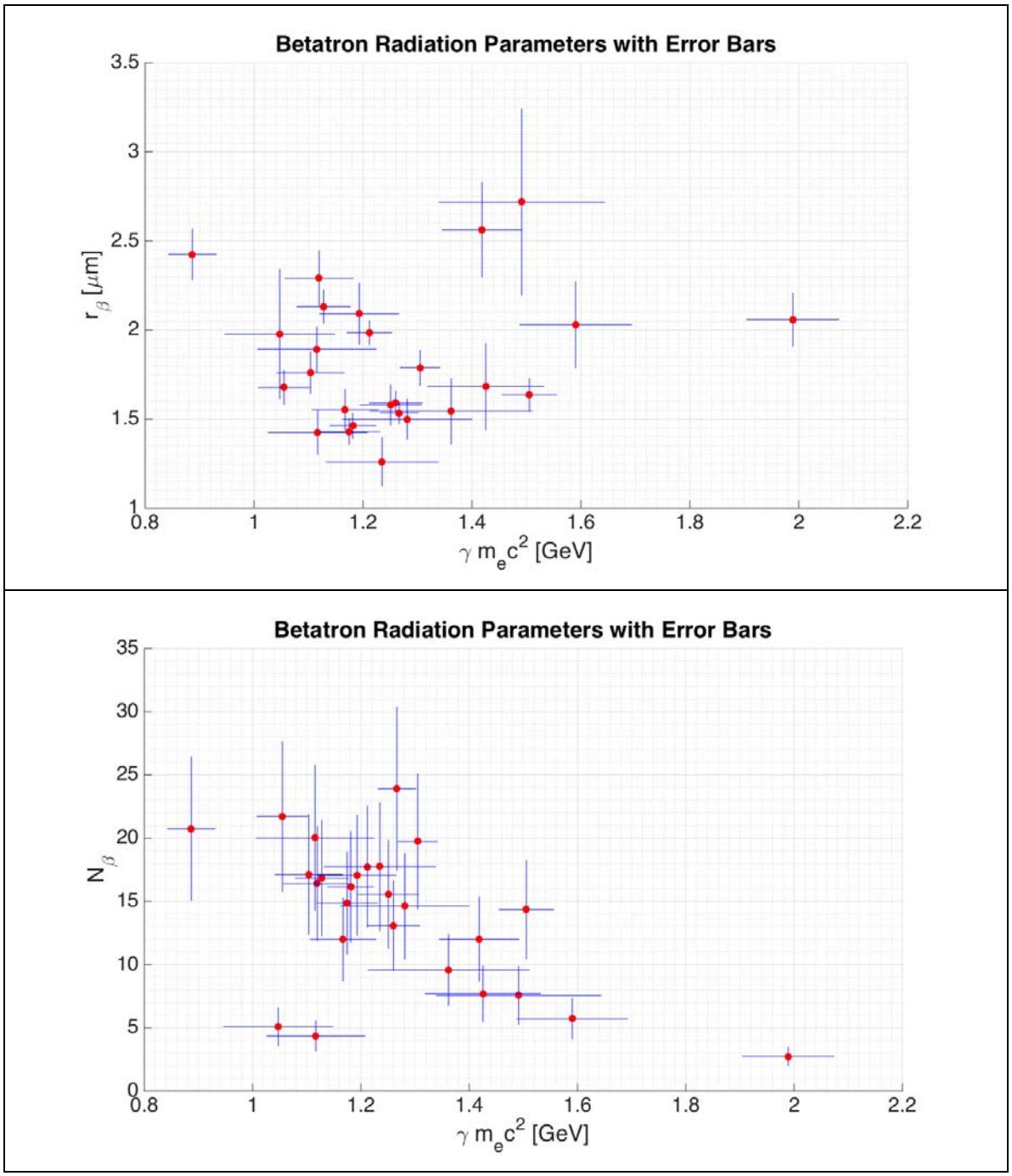

Figure 6.98: 2D plots of the effective betatron radiation parameters (relativistic gamma, betatron oscillation amplitude, and number of betatron oscillations) with error bars

the peak intensity on the reconstructed x-ray profile image), was selected a suitable proxy for $\delta\theta_r/\theta_r$. (Note that for a circular x-ray beam profile, the standard deviation of theta vanishes, as does $\delta\theta_r$.) To calculate the number of photons, N_γ, the spatially resolved spectrum obtained from a biharmonic spline interpolation of the spectrum data was

integrated over both energy and angle. The interpolation was applied to spectrum data in both the PUE (per unit energy) and the PUBW (per unit bandwidth) representations of the spectrum. The latter highlights the high-energy portion of the x-ray spectrum and, almost always, produces a larger value for the total photon number. (The difference is as low as ~2% and as high as ~18%, depending on the x-ray profile. The average difference was ~13%.) The average integrated photon number, using the two representations of the spectrum data, was used for N_γ; half of their difference was used as δN_γ. In cases where the spatially resolved spectrum was based on the interpolation of an insufficient number of data points near the axis (small observation angle), a more conservative calculation of N_γ was used where the total PSL of the reconstructed x-ray profile was divided by the mean imaging plate sensitivity in the region 10-30 keV. (For the MS IP this is ~5.5 mPSL per photon.) In such cases, δN_γ = 25% was used. This approach provides a lower bound to the photon count because, as described in Appendix B, the peak region of the x-ray profile is flattened by the reconstruction algorithm. Figure 6.97 shows plots of the betatron radiation parameters γ_{eff}, $r_{\beta,eff}$, and $N_{\beta,eff}$. Figure 6.98 shows the uncertainties $\delta\gamma_{eff}$, $\delta r_{\beta,eff}$, and $\delta N_{\beta,eff}$. The effective electron energy, γ_{eff}, calculated according to Eq. 6.16, ranged from 1735 to 3893 (0.89-1.99 GeV) and averaged 2471 (1.26 GeV). The effective betatron oscillation amplitude, $r_{\beta,eff}$, calculated according to Eq. 6.17, ranged from 1.3 μm to 2.7 μm with an average of 1.8 μm. The effective number of betatron oscillations, $N_{\beta,eff}$, calculated according to Eq. 6.18, ranged from 2.7 to 23.9, with an average of 14.2 oscillations. The effective betatron period (wavelength), $\lambda_{\beta,eff}$, was between 1.3 and 4.8 mm, with an average of 3.1 mm. The product $\lambda_{\beta,eff} \times N_{\beta,eff}$, a measure of the distance the electron propagated inside the plasma before exiting the gas cell, ranged from 4.2 mm to 69.4 cm with an average of 44.0 mm; this is about half the total length of the gas cell (10 cm). It is important to note that γ_{eff}, $r_{\beta,eff}$, and $N_{\beta,eff}$ are sensitive to the method used to determine θ_r. As seen in Figure 6.30, x-ray profiles are often elongated and horizontal or vertical line-outs do not necessarily coincide with either the major or minor axis of the elongated profile. The method used here calculated the FWHM of the x-ray by drawing a line-out through the geometric center of the x-ray profile and along its major axis. A calculation of the FWHM based on horizontal or

vertical line-outs would yield different, often smaller, results for θ_r and larger values for the number of betatron oscillations, $N_{\beta,eff}$. It was previously noted in relation to Figure 6.94 that the number of photons correlated better with the total measured charge (> 300 MeV) than with total charge with energies > 1 GeV. This was also confirmed when both charges were used to calculate $N_{\beta,eff}$. Using the lower charge value (i.e., > 1 GeV), the number of betatron oscillations was on average ~537 cycles which is incompatible with the length of the gas cell used. The strength parameter *K* was between 5.7 and 11.4 with an average of 7.7, indicating that the betatron radiation was in the wiggler regime, as was previously confirmed from the spectroscopy of the betatron x-rays. Whereas in the undulator regime, the x-ray spectrum is monochromatic for fixed observation angle (Ψ in the Figure 6.93), in the wiggler regime, the spectrum is broadband. This was experimentally observed (Figure 6.41).

Chapter 7 Concluding Remarks and Suggestions for Future Work

During the course of the petawatt laser-driven LPA experiments discussed in this dissertation, electrons were accelerated to a peak energy of 2 GeV (Figure 6.17) and a tail energy approaching 3 GeV was also achieved (Figure 6.49). The peak energy electrons were generated more consistently and in larger numbers than in any other laser-plasma accelerator, with more than 100 picocoulombs (typical, and up to ~1 nC) accelerated above 1 GeV, and the maximum total accelerated charge approaching or exceeding two nanocoulombs (Table 6-9, Table 6-10, Table 6-11). The photon number for the x-rays generated by these electrons routinely exceeded the 10^9 level; in a number of cases more than 10^{10} photons were detected (e.g., Table 6-11, Figure 6.94), a level that is 2 orders of magnitude higher than in other laser-plasma accelerators. Using the methodology developed for the spatially resolved spectroscopy of these photons, it was possible for the first time to determine the spectrum of the betatron x-ray radiation over the full range of the x-ray profile, and calculate effective parameters for the GeV accelerator that linked the electron and photon observables (6.6).

For each of the 4 rounds of laser-wakefield experiments discussed in this dissertation, the insights acquired from the preceding round were incorporated into the design of the diagnostics for the next round, and the development of a consistent methodology for the analysis of acquired data. Following the initial run, imaging plates were selected as the preferred detector for both electrons and x-rays because of their high sensitivity, dynamic range, and immunity to EMP. However, during the first round (LWFA 1.5) it became evident that due to the high electron charge, and the lower dynamic range of the PMT used in the IP scanner, the imaging plate measurements exhibited saturation which rendered charge measurements inaccurate. To tackle this issue, a methodology was developed to reconstruct an unsaturated version of the imaging plate data from the saturated version (C.2: Reconstruction of Saturated Imaging Plate Data). This technique became all the more important as the total charge in the electron bunch and the total

number of x-ray photons increased in the rounds that followed. This increase was in response to improvements to the driving laser far-field (round 2) and mid-field (round 4) profile. The thickness, and the positioning, of the laser beam deflector used in the first round adversely impacted the diagnostics of the betatron x-rays (Figure 6.11). In the rounds that followed, the deflector with effective thickness of 1.95 mm was replaced with a thinner version having effective thickness ~64 μm; this allowed a more accurate detection of the x-ray signal. It was determined during the 3rd experimental round that in order to obtain sufficient number of spectral data points to reconstruct the x-ray spectrum, the residual sensitivity functions (Eq. 5.4, Eq. 5.8) would need to be sufficiently numerous and well separated along the energy axis (Figure 5.6 vs. Figure 5.11) to enable the reconstruction of the x-ray spectrum from the measurements of the transmitted signal following attenuation by the x-ray filters (Eq. 5.5, Eq. 5.9). This indicated the use of different materials and thicknesses. However, using rectangular filter masks (Figure 5.9) and arranging them side by side or overlaid (Figure 5.10), made the task of betatron x-ray profile reconstruction, and the subsequent x-ray spectroscopy, challenging and slow (Figure 5.12). In addition, in such geometries, the pointing variability of the x-ray beam (Figure 6.23, Figure 6.31) made it difficult to control the overlap (Figure 5.7) between the x-ray beam and the filters (i.e., the detectors); this was hard to mitigate given the low repetition rate of the driving laser. The analysis of x-ray measurements from the 3rd round (Figure 6.25) also indicated that the change in the x-ray spectrum, from shot to shot and on different regions of the x-ray profile, was large enough that only single-shot measurements, taken on the same iso-intensity contours, could be used to reconstruct the single-shot spectrum (Figure 6.26). These factors, as well as the desire to extend the sensitivity of the x-ray detector to lower energies and reduce the error bars in the region of the spectrum nearest to its peak, together motivated the redesign of the x-ray detector for the 4th round. The switch to an array of K-edge (Ross) filters (Table 5-2), positioned in a packed hexagonal arrangement (Figure 5.20) on a low attenuation polymer mask (Figure 5.18), covered by thin Al foil (Figure 5.22) and integrated into the electron detector, ensured that detection was largely immune to the pointing variability of the x-ray beam (Figure 5.19), the reconstruction of the filtered x-ray profile was much simplified (Figure 5.23), and the drawing of iso-intensity contours followed by sampling

of the filter measurements on those contours (Figure 5.26) became amenable to programmatic treatment (using ImageJ scripts, G.2). The sensitivity of the x-ray spectrometer was also extended to photon energy < 10 keV. The narrowness of the residual sensitivity function in the peak region of the betatron x-ray spectrum (Figure 5.15) ensured that the horizontal (energy) error bars, that are equal to the width of the energy bin for the corresponding function, were minimized compared to the FWHM of the residual sensitivity functions for differential filters that were not K-edge filters. It also became possible to programmatically control the trade-off between the systematic error due to the impact of edge effects on the x-ray data (Figure 5.27) and the statistical error that increased when the edge effect, hence the sample size, was reduced, by specifying the region of the filters used for the sampling of x-ray data. The consequence of this was that the magnitude of the vertical error bars and the denseness of the points on the spectrum could be balanced against one another.

In closing, several enhancements are proposed with the aim of improving the diagnostics and the analysis of data for future runs. In some cases, for example enhancements to the magnetic spectrometer, the improvement is driven by the need to maintain spectrometer resolution at the higher electron energies that are all but certain to be accomplished in the near future. In other cases, these enhancements embody promising ideas that were investigated but not incorporated into the dissertation, due to time constraints.

Enhancement of the Electron Deflection in the Magnetic Spectrometer

As discussed in 3.4 (The Magnetic Spectrometer), a magnet with fringe-free effective magnetic field of 1.48 T over 5 cm was used to produce deflection in the accelerated electrons; 0.005" diameter tungsten fiducial wires placed in the path of the x-rays and electrons produced shadows on the detector positioned 2.46 m downstream from the magnet. Figure 7.1 shows the cumulative deflection of an electron, launched colinear with the diagnostic chamber axis, as a function of its energy, as it arrives on the detector. Despite the parabolic reduction in electron deflection with increasing energy, it was still possible to measure the electron energy with ±5% accuracy at 2 GeV (Figure 3.17). However, it is evident that for electron energies $\gtrsim$ 4 GeV, the deflection curve becomes

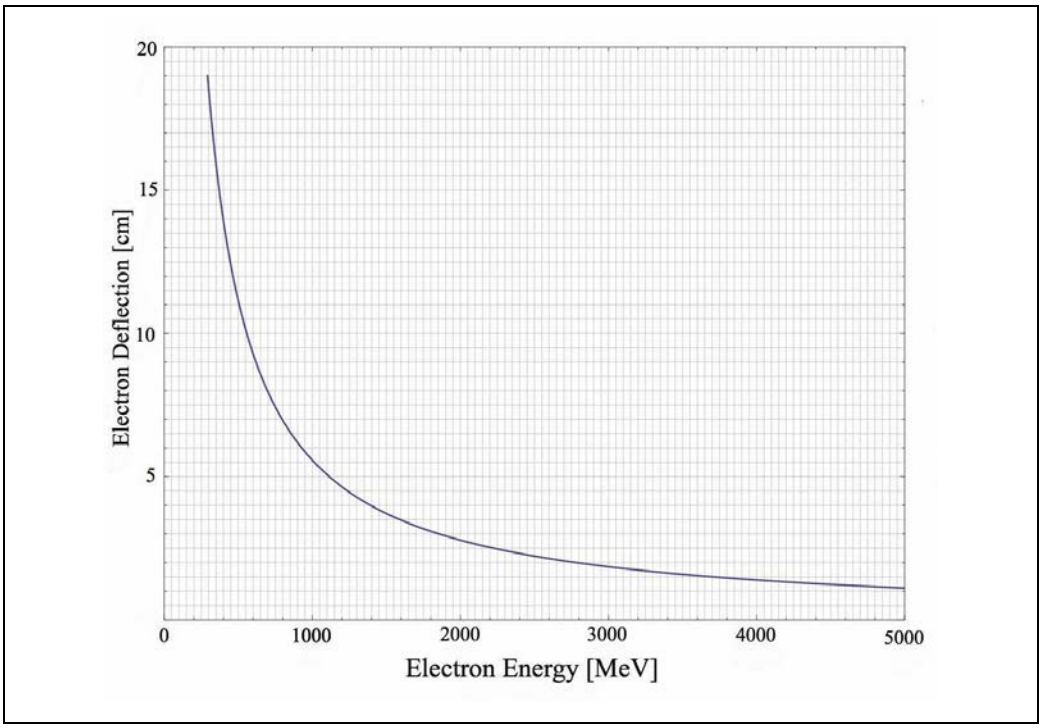

Figure 7.1: The deflection of electrons in the magnetic spectrometer [picture courtesy of Rafal Zgadzaj]

increasingly flat, requiring the use of a stronger magnet. Even at lower energies, a stronger magnet would enhance the electron deflection and reduce the electron background that sometimes interferes with the measurement of the x-ray signal, degrading the profile reconstruction and reducing the signal to noise ratio; this happens whenever the betatron x-ray signal and the high-energy tip of the electron signal overlap. (Figure 6.84 shows one such case.) Similarly, a larger electron deflection at current peak energies will enable a more accurate (i.e., better than ±5% accuracy at 2 GeV) determination of the electron spectrum from fiducial shadows using the triangulation technique (3.4). Note that increasing the drift length of the electrons by increasing the length of the diagnostic chamber is an alternative way to enhance the electron's deflection in the magnetic spectrometer. This may be harder to accomplish due to the space constraints.

Improvements to the Ross Filter Assignment on the Mask

The assignment of filters to positions on the x-ray filter mask (Figure 5.20) gave equal weight to all 7 energy bins. However, the spectrum of the betatron radiation that was subsequently measured indicated a sharp drop in the spectrum at energies $\gtrsim$ 30 keV. This

means that data points from the first 5 bins in the residual sensitivity plot (Figure 5.15) provided the most important information for the 3D reconstruction of the spectrum. Given the limited number of spots available on the polymer mask, an assignment of x-ray filters to positions on the mask that is weighted towards the filters from the first 5 bins would increase the number of data points in the region of the spectrum with the largest variation, in particular on the smallest contours. There is a caveat, however. Since in the wiggler limit the critical energy of betatron radiation scales quadratically with the energy of the accelerated electrons (Eq. 6.9), any increase in the peak electron energy is expected to be accompanied by an increase in the peak x-ray energy.

Maximum Entropy Methods of X-ray Spectrum Deconvolution

Given the filter transmission function, T(E, x), detector response function, R(E), and the transmitted x-ray signal measured by the detector, TS, the convolution integral (Eq. 5.2)

$$TS = \int_0^\infty S(E)T(E,x)R(E)d\,(E)$$

must be solved to determine the x-ray spectrum, S(E). This integral has been tackled in this dissertation using differential and K-edge filters (5.2). Another deconvolution technique that was investigated is the *maximum entropy* method [51]. This method takes as input the combined detector (e.g., imaging plate) and attenuating filter response functions for all filters, the detector measurements corresponding to all filters, and what is referred to as a *default spectrum*, an initial guess for the spectrum (a uniform distribution if such a spectrum does not exist); it then uses Bayesian probability techniques to find the spectrum that would produce the actual detector measurements given the response functions by maximizing the entropy function, $S = -\sum_i p_i \ln(p_i)$, where p_i is the probability obtained from interpreting the spectrum as a probability distribution function. The procedure finds the spectrum that would reproduce the actual detector measurements, given the provided response functions for the detectors (e.g., filters + IP), while minimizing the entropy function. It can be shown [61], that the optimal (in the sense of making the fewest extraneous assumptions) solution to a deconvolution problem is the one that maximizes the entropy, hence the benefit of formulating the spectroscopy of betatron x-rays as an entropy maximization problem.

Depending on the filters chosen and the resulting overlap between the response functions, the number of measurements, and the errors assigned to the measurements, the maximum entropy approach produces a *solution spectrum*, in a closed form as a function of the response functions and the detector measurements, that updates the default spectrum consistent with the provided information, in the energy regions where sufficient information is available. Since the solution is in closed form, sensitivity analysis for the input parameters is straightforward. In addition, it is possible to precisely calculate the spectrum error by propagating the measurement errors.

The maximum entropy technique is very sensitive to the input parameters and the error estimates. This is an advantage when the detector measurement errors are accurately known. However, underestimating the measurement errors can produce biased solution spectra. For the spectroscopy of the betatron radiation, a promising approach would be as follows:

1. Select those iso-intensity contours that intersect at least 4-5 distinct Ross filters;
2. Calculate the x-ray spectrum on the selected iso-intensity contours using the Ross filter deconvolution technique described in 5.7;
3. Produce an accurate estimate of the statistical and systematic measurement errors. (See F.1 for details.)
4. Perform a fit to the spectral data points from the preceding step to produce a spectrum that will then be used as the default (i.e., suggestion) spectrum for maximum entropy analysis;
5. Use the default spectrum from the preceding step, the detector measurements for the individual filters in the Ross filter pairs crossed by the selected iso-intensity contour, estimates of the statistical and systematic measurement errors, and the response functions for those filters, as input to an implementation of the maximum entropy analysis (e.g., MAXED [62]);
6. The solution spectrum from the preceding step is provided as a function of energy, i.e., is already energy-resolved and requires no further fitting. Since it incorporate the response function information, it will be at least as accurate as the fitted contour-specific default spectrum. When solution spectra from a sufficient number of contours

are known, they can be combined using a fitting procedure to produce a 3D spatially resolved spectrum.

Appendix A. Chronology of LPA Experiments at the Texas Petawatt Laser

The LPA experiments driven by the TPW laser were conducted in 5 rounds; the author participated in all but the initial round. In what follows, the chronology and distinguishing features of the experiments are presented:

- Initial or 0^{th} round ("LWFA 1.0"):
  - Dates: 01/2011
  - Shot numbers: There were 20 shots.
  - Major issues:
    1. Only 1 shot produced electrons.
    2. Far-field laser profile had multiple hot spots; this is thought to have prevented self-injection. (Doping of helium with N_2 for ionization-induced injection had not been introduced.)
  - Diagnostics: RCF and ICT were used for electron diagnostics
  - Major outcome [53]:
    Production of a self-injected, collimated (8 mrad divergence), 600 pC bunch of electrons with energies up to 350MeV from a petawatt laser-driven plasma accelerator in a plasma of electron density $n_e = 10^{17} cm^{-3}$, an order of magnitude lower than previous self-injected laser-plasma accelerator.

- 1^{st} round: ("LWFA 1.5")
  - Dates: 11/11/2011-12/02/2011
  - Shot numbers: 2875 to 3053
  - Major changes to the experiment:
    1. Adaptive optics (DFM) introduced and that improved laser pulse profiles
    2. Introduced nitrogen doping of helium for ionization-induced injection; WAKE simulation based on LWFA 1.0 laser parameters indicated relativistic self-focusing at plasma density $n_e = 5 \times 10^{17} cm^{-3}$.
  - Diagnostics changes:

1. Replaced RCF with high sensitivity imaging plates (MS IP) for electron diagnostics
2. Use of EJ-260 (green) plastic scintillator with Basler scA640-70fm (mono) CCD (no Lanex)

- Major outcomes [54]:
  1. Self-injected, dark current-free quasi-monoenergetic ($\Delta E \approx 0.1$ GeV) electrons accelerated to > 1 GeV (1.25 GeV max)
  2. Mismatched propagation led to localized injection
  3. Collimated electron beam (down to 0.25 mrad FWHM divergence, vs. Pollock et al. reported their 0.5 GeV beam was 2.3 mrad)
  4. Pointing stability < 2 mrad
  5. Charge ~ 10 pC
  6. Minimal betatron radiation
- Issues:
  1. Deflector frame was in the path of the high-energy electrons (later corrected via GEANT4 simulations).
  2. The deflector was relatively thick (0.0307" at 23.53° offset to perpendicular, with effective thickness 0.0769" [0.0307"/sin(23.53)] or 1.95 mm) and attenuated the betatron x-rays.
  3. Some shots (e.g., 2931) used a weak magnet (0.175 T) causing low-energy electron to show up as bright dots on the scintillator image.

• 2nd round ("LWFA 2.0"):
  - Dates: 04/17/2012-05/06/2012
  - Shot numbers: 3534 to 3754
  - Major changes to the experiment:
    1. Started with doped helium and later switched to pure helium
    2. The deflector thickness was reduced (from 0.0307" in the previous round, to 0.001" at similar offset, with effective thickness 0.0025" [0.001"/sin(23.529)] or = ~64 μm).
  - Diagnostic changes:

1. More stable and accurate IP frame introduced
2. High resolution IP (SR IP) introduced
3. Improved electron spectrometry by introducing tungsten fiducial arrays optimized by GEANT4 simulation using shot 3033 from previous round
4. It was possible to determine the position of the x-ray source inside the gas cell by triangulation of the x-ray fiducial shadows.
5. Lanex phosphor plate introduced
6. Use of EJ-200 plastic scintillator together with Kodak Lanex Regular and Basler scA1600-14fc (color) CCD. (Initially the plan was to use EJ-212, but it was replaced with EJ-200, for its stronger response to ionizing particles.)

- Major outcomes [32]:
  1. Polyenergetic acceleration of self-injected electrons to > 2 GeV at plasma density n_e ~3-5 × 10^{17} cm^{-3}
  2. Mode-matched propagation led to continuous injection
  3. Small electron divergence (0.5 mrad)
  4. Doping of helium gas by nitrogen was tried and found not to make significant impact.
  5. High charge (> 1 nC)
  6. Strong betatron radiation (filters not used, however)
- Issues:

  IP frame had slight curve

• 3rd round ("LWFA 3.0"):
  - Dates: 01/14/2013-02/15/2013
  - Shot numbers: 5472 to 5870
  - Major changes to the experiment:
    1. Switched to using pure helium (i.e., no nitrogen doping)
    2. For some shots the gas cell length was increased from 7 cm to 9-10 cm.
  - Diagnostic changes:
    1. Introduction of copper and aluminum masks in thicknesses 0.25, 0.5, 1, and 2 mm for x-ray spectroscopy. The lowest x-ray energy that could be measured

was limited by the thickness of the IP protective layer (12 mil Al); this was about 16 keV. Detection of lower-energy x-rays requires a modification of the protective cover. (See LWFA 4.0)

- Major outcomes [32]:
  1. Measured betatron x-ray spectrum
  2. Accelerated electrons > 2 GeV
- Issues:
  1. Uncertainty regarding the measurement of laser far-field focus
  2. IP frame had slight curve
  3. Gas cell pressure sensor calibration changed

- 4th round ("LWFA 4.0"):
  - Dates: 04/28/2014-05/30/2014
  - Shot numbers: 8165 (05/05/2014) to 8398 (05/30/2014)
  - Major changes to the experiment:
    1. The optimization of the midfield profile of the laser pulse
    2. Accurate determination of the laser far-field
    3. Dialing in of hot spots in the far field of the laser profile for “double bubble” shots
    4. Length of the gas cell (i.e., maximum acceleration length) was increased to 9-10 cm.
  - Diagnostic changes:
    1. Introduction of Ross filter array for x-ray spectroscopy in place of differential filters
    2. Design of the x-ray filter pattern with x-ray profile reconstruction in mind
    3. Replacement of the imaging plate frame (to reduce curvature)
    4. Replacement of the 12-mil aluminum IP cover with PEEK IP cover to reduce x-ray attenuation and permit measurement of the lower end of the x-ray spectrum
    5. Not measuring electron energy below 300 MeV (small IP not used)

6. Attempt to measure x-ray source size using copper wires and phase contrast imaging
7. One of the fiducial arrays (the one detecting x-rays and high-energy electrons), needed to be moved closer to the chamber center causing two fiducial shadows (one from each fiducial rack) very close to one another on the x-ray image.

- Major outcomes:
  1. 90% of shots yielded energetic electrons
  2. Enhanced charge (~2 nC) and photon number (10^{10} photons) observed via the "double bubble" mechanism
  3. Signs that there were two x-ray sources (shot 8388)
- Issues:
  1. Some shots have large background, most likely from ablation of the 1.5 mm radius gas cell entrance aperture by the laser pulse
  2. High charge led to heavy IP saturation (repeated scans required); charge with energy < 300 MeV not measured
  3. IP scanner stopped several times during scanning
  4. One of the fiducials was broken during several shots

Appendix B. Algorithm for Reconstruction of Filtered X-Ray Profile

The choice of the reconstruction technique is an important decision in the spatially resolved spectroscopy of betatron radiation. Since iso-intensity contours created on reconstructed x-ray profiles are used to ensure that the two detector measurements used in a differential filter calculation correspond to the same incident x-ray spectrum, the accuracy of image reconstruction determines the accuracy of iso-intensity contours which is one of the factors determining the error in the spectrum. Methods which fit the data by minimizing the squared curvature integrated over the entire surface e.g., cubic splines and biharmonic spline interpolation [47], produce a smooth surface incorporating the data, but have the tendency to produce extraneous inflection points. The latter method, where the interpolating surface is a linear combination of Green's functions of the biharmonic operator centered at each data constraint, has been used in this paper as one of the methods used to reconstruct the spatially-resolved spectra from spectrum data points for different contours; however, it was not found suitable for the reconstruction of the x-ray profile because the large gaps in the profile (typically circular regions with diameter 4.5 mm) can produce artifacts in the reconstructed image which would lead to contour deformity. Even a generalized version of the biharmonic spline interpolation algorithm incorporating a tension parameter as a way to remedy extraneous inflection points and numerical instabilities [63], can still leave behind artifacts in the reconstructed x-ray profile. However the biggest impediment to the use of these algorithm is that the memory requirement scales as N^2, where N is the number of data constraints; for example, for a 600 x 600 pixel image, where $N = 360000$, the algorithm cannot finish on a computer with 16 GB of memory. One suggested solution would be to break up the image into smaller sub-images, reconstruct each separately, and then recombine. This would raise the possibility that contour-deforming edge effects would be present in the recombined image in regions where the sub-images were joined.

The technique developed here, *Interpolated Nearest-Neighbor Moving Average (INNMA)*, is optimized for the reconstruction of filtered x-ray data obtained when a

regular array of x-ray filters is placed in the path of the x-ray photons reaching the detector. It is based on using information available in non-gap regions of the data to determine the value of pixels in the gap region, by taking advantage of the smoothness and the symmetry that exists in an x-ray profile. The method is based on a type of averaging operation applied to both the pixel values as well as their coordinates; therefore it uses less computational resources and avoids memory footprint and instability issues. It has similarities to bilinear interpolation in that it also performs linear interpolation first in one direction, then again in the other direction. However, this algorithm does not merely fill the gaps in the image. It resamples the image data, averages out the noise, and interpolates the resampled x-ray image data, i.e., it replaces the value of all pixels in the image, and in so doing fills the gaps as well as removes the Poisson noise in the x-ray profile.

The algorithm uses a moving *averaging window*, a horizontal or vertical array of pixels large enough to contain N_{NNMA} *source pixels*, possibly interspersed with gaps. (In the case of filtered x-ray data, gaps are created by the removal of pixels affected by the presence of the x-ray filters or fiducials in the path of the x-rays arriving at the IP detector.) The choice for N_{NNMA} is determined by geometry of the image (e.g., the gaps and their separation). The size of the averaging window changes with its location on the image and the presence of gaps, but the window is always chosen large enough to contain N_{NNMA} pixels. (When accumulating N_{NNMA} pixel data, whenever the algorithm encounters gaps in the data, it stretches the window until it finds non-gap pixels.) The technique behaves like a symmetric moving average in that the average pixel value using all source pixels inside an averaging window is assigned to a *target pixel* in the interior of that window; however, instead of choosing the middle pixel as the target pixel, the coordinates of the target pixel are determined by averaging the coordinates of all source pixels inside the averaging window. By using source pixels' coordinates and values to determine the target pixel's coordinates, as well as its value, the algorithm effectively resamples an image with gaps. In the absence of gaps, the value of a target pixel is indeed determined by its nearest neighbors. When there are gaps, a target pixel and its neighboring pixels may be separated by large gaps in the image but the value of a target

pixel will naturally be weighted toward pixels that are closer to it in the averaging window. Using the average source coordinate for the target coordinate has two consequences. First, the average value is automatically assigned to a location with denser set of source pixels, because gap pixels do not contribute to the average coordinate calculation. In the absence of gaps in the data, the algorithm reduces to a symmetric moving average operation where the averaging window is always N_{NNMA}. In the presence of gaps, the algorithm selects a target pixel's location closer to where the source pixels are. This achieves what weighting of the source pixel values would achieve, without using weights. And this is the second consequence of assigning to the target coordinate the average of source coordinates. The averaging operation removes the Poisson noise in the image; this can only happen when all pixels are equally weighted. Therefore, by assigning the averaged pixel value to the average location of all source locations, we get the benefits of weighting by distance without paying the cost of differentially weighing the Poisson noise at different pixels. The nearest neighbor moving average operation is a generalization of the piece-wise linear interpolation to more than two data points, and in the limiting case of an averaging window containing 2 pixels separated by gaps, it can be shown that the NNMA operation, assigns the same value to the target pixel location that a piece-wise linear interpolation would. To demonstrate, Figure B-1 shows the steps in the reconstruction of an x-ray image. The first image (top left) shows the x-ray profile as detected on the IP, with the pixels affected by the presence of filters and fiducials removed. In the next step (top right), NNMA operation has been applied in the vertical direction and with an averaging window size of 7 pixels. (Operation is done in the vertical direction first because, due to the presence of fiducial shadows in the x-ray image, the symmetry of gap regions is broken: more information is available in the image columns than in the image rows. In the case of image with symmetric gaps, the operation can be performed in either direction first.) Following this step, the image has been horizontally resampled: gaps in each column of the image have been partially filled using information from nearby pixels in the column. This image is then linearly interpolated in the vertical direction to produce an image (row 2, left) with some artifacts, as well as vertical gaps from fiducial shadows. The NNMA operation is next applied in the horizontal direction, with an averaging window size of 45 pixels (equal to the diameter of

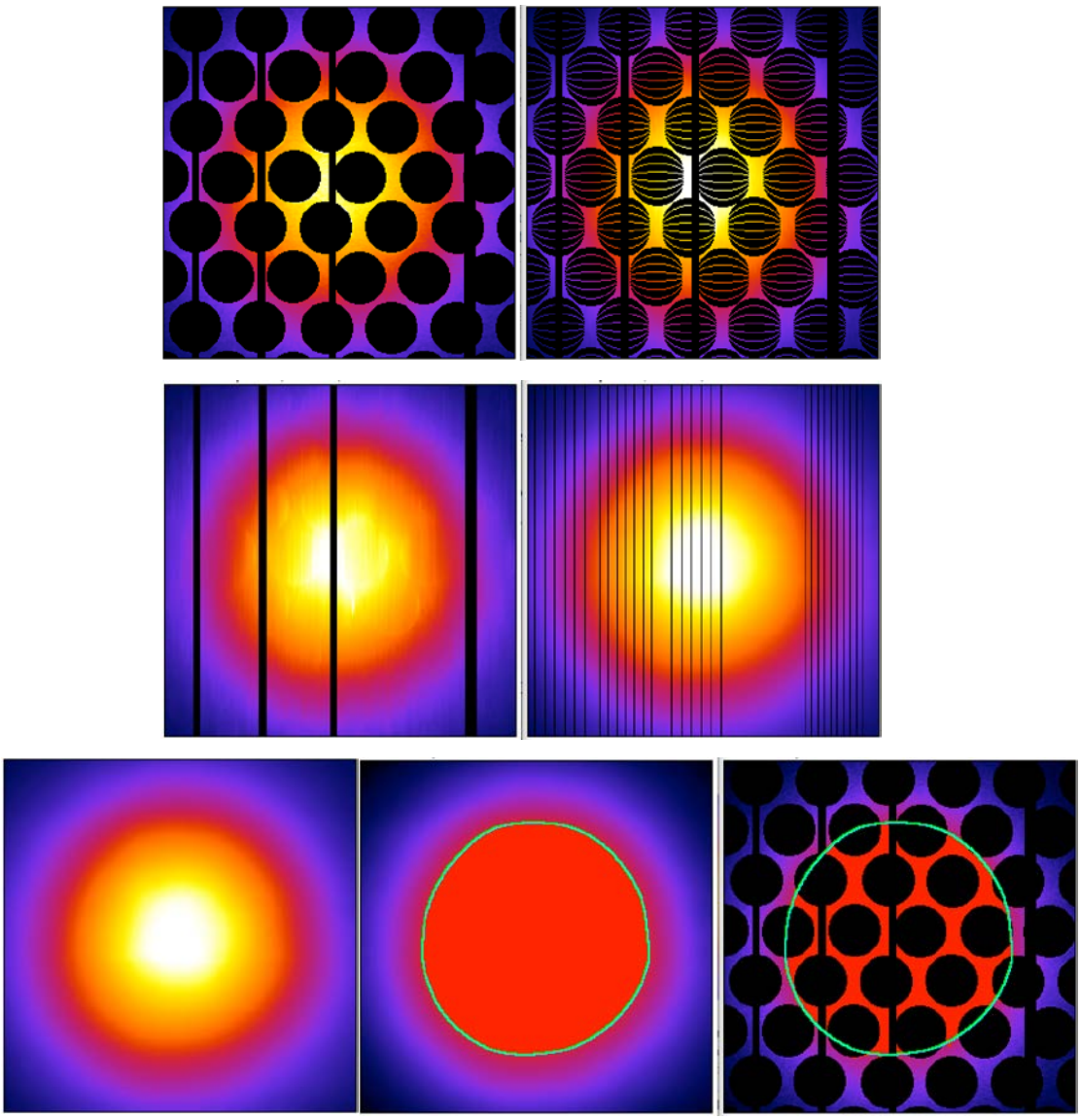

Figure B-1: Image reconstruction steps: 1) Pre-reconstruction image where pixels affected by filters and fiducials have been removed (top left), 2) resampled image following nearest neighbor moving average operation in the vertical direction with averaging window size of 7 pixels (top right), 3) previous image after linear interpolation in the vertical direction (middle left), 4) previous image after resampling using nearest neighbor moving average in the horizontal direction with averaging window size of 45 pixels (middle right), 5) previous image after linear interpolation in the horizontal direction.

the circular gaps in the image). The vertically resampled image produced (row 2, right) has no artifacts and the previously large gaps have been replaced with smaller, but more spaced out, gaps. This image in then linearly interpolated in the horizontal direction to remove the remaining gaps and produce the reconstructed image (row 3). This image has the property that contours drawn around thresholded regions (in this case, down to 50% of the maximum intensity) encompass thresholded pixels in a similarly thresholded (i.e.,

50%) pre-reconstruction image and may therefore be used as iso-intensity contours to sample filter data.

To determine the fidelity of x-ray profile reconstruction, the average pixel value along an iso-intensity contour created on the reconstructed profile was compared with the average pixel value along same contour overlaid on the unreconstructed profile and the averaging restricted to the non-filter pixels. The difference was typically < 1% for same-contour averages calculated on the reconstructed and unreconstructed x-ray profile and similar to the standard deviation of the pixels along the iso-intensity contour created on the reconstructed image. (This error is expected due to the finite resolution of the IP.) This small difference in the average pixel value indicates that the iso-intensity contour created on the reconstructed image, when restored on the raw data image, designates a contour of constant spectrum. Note that since the image reconstruction algorithm replaces all pixels in the image, not just the gap pixels, the difference between the raw image minus filters and the reconstructed image is not expected to be 0 in the areas common to both images; in particular, the Poisson noise in the raw image has been removed in the reconstructed image.

The image reconstruction technique described here takes advantage of the monotonic nature of the x-ray profile. The region in the center of the x-ray profile, where the intensity peaks and monotonicity is broken, is therefore reduced in intensity. The location of the peak intensity pixel, however, is typically preserved to within a few pixels. Since the affected region is small and contains no more than one or two x-ray filters, it usually yields no spectral data points. Iso-intensity contours are always drawn to avoid this region.

Appendix C. Imaging Plates as High-Energy Particle Detectors

C.1 Introduction

Two types of imaging plates (IPs) were used in the laser-wakefield experiments conducted at the TPW laser facility: Fujifilm BAS-MS and BAS-SR, referred to as MS and SR IPs. The MS IP has higher sensitivity (MS stands for *maximum sensitivity*) and has a resolution of 100 μm; the SR IP has a higher high resolution (SR stands for *super resolution*) of 50 μm and has lower sensitivity to ionizing radiation than its MS counterpart. Ionizing particle create metastable transitions in the IP as they pass through the sensitive layer of the detector; these metastable states are then excited by means of a red laser to an upper state from which transitions to the ground state are accompanied by the emission of photons in the blue part of the spectrum. The process is known as *photo-stimulated luminescence (PSL)*. The blue light is then collected (as explained in Appendix D, Fuji-branded scanners may use one of two types for light-collection optics: confocal or light-collecting guide), routed to a PMT, and finally digitized and output in logarithmic format in what is referred to as *quantum levels* (QL). The output is written to files in *Image Save and Carry* or ISAC format, a format developed by the Japanese Industry Radiology Apparatus (JIRA). Used by all Fuji scanners, the ISAC format uses a raw binary data file with name ending in .img, and a text file with name ending in .inf and containing information associated with the image (e.g., the scanner settings used to scan the IP). These files are read by the ImageJ application using the ISAC Manager[12] plugin.

Note that the amount of light collected per IP pixel, also known as the *PSL*, depends on the radiation dose, and the light collection efficiency of the IP and the scanner used to read it; therefore, to convert between PSL and radiation dose (e.g., electron charge or number of x-ray photons), a calibration using a known radiation source and specific to the IP, scanner model, and the resolution knob on the scanner, is required (see Appendix D). The QL values embed the various settings (knobs) on the particular scanner used to

[12] http://rsb.info.nih.gov/ij/plugins/isac.html

scan the IP. To convert between QL and PSL, we need to know how they are related. In the case of Fuji-branded IP scanners, the relationship between the QL and PSL for a pixel is as follows:

$$PSL = \left(\frac{Resolution}{100}\right)^2 \times \left(\frac{4000}{Sensitivity}\right) \times 10^{Latitude\left(\frac{QL}{Gradation} - 0.5\right)} \quad \textbf{Eq. C-1}$$

In this equation,

- *Resolution* on the FLA-7000 scanner can be one of the values 25, 50, 100, and 200. Imaging plates were always read using a scanner resolution that matched the IP resolution, i.e., 100 (μm) for the MS IP and 50 (μm) for the SR IP. It is important to note that calibrations are sometimes provided for different scanner resolutions, e.g., the x-ray calibrations in [44], so keeping track of the scanner resolution is important not only for conversion between QL and PSL using Eq. C-1, but also when converting between PSL and radiation dose.
- *Sensitivity* has one of the values 10000, 4000, or 1000. (In practice, sensitivity parameter was varied with scan. See discussion of scanner sensitivity variation later in this chapter.)
- *Latitude* has possible values of 4 and 5 on the Fuji-branded FLA-7000; the value 5 was used exclusively.
- *Gradation* is an indication of the dynamic range of the output. For the 16-bit output of the FLA-7000, gradation has the numerical value 65535 which is equal to $2^{16} - 1$.
- *QL* is the actual output from the scanner for each pixel and ranges from 0 to 65535 (i.e., the gradation).

C.2 Reconstruction of Saturated Imaging Plate Data

A complication that needs to be addressed when processing imaging plate data is the presence of imaging plate read-out saturation. Imaging plates have a large dynamic range, but the PMT in the read-out system may get saturated during the extraction of the recorded signal. Read-out saturation is more likely to occur in a GeV LPA, as the number of photons radiated by an accelerated electron scales with the square root of the relativistic gamma of the electron (Eq. 5.12). In the presence of saturation, repeated scans of the IP, and the scanner laser-induced fading of the signal, are used to obtain an image

1	*QL (Raw) Image*	Image output by the scanner per IP scan; this is logarithmic data and needs to be linearized before being used for quantitative work.
2	*PSL (Photo-Stimulated Luminescence) Image*	Image created when pixel-wise linearization, using Eq. C-1 and the corresponding scanner settings, is applied to the QL Image. It is suitable for quantitative analysis.
3	*Base PSL Image*	PSL Image corresponding to the first QL Image. It can have saturated pixels for the x-ray, or the x-ray and electron, signal.
4	*Unsaturated PSL Image for X-rays*	PSL Image created from the first QL Image (for scan $N_{unsaturated\ xray}$) on which the x-ray signal is not saturated.
5	*Unsaturated PSL Image for X-rays with Filters Removed*	PSL Image created from Unsaturated PSL Image for X-rays on which a 45-pixel diameter circular region around each filter has been replaced with NaN.
6	*Unsaturated PSL Image for X-rays with Filters and Fiducials Removed*	PSL Image created from Unsaturated PSL Image for X-rays with Filters Removed on which regions corresponding to fiducial shadows have been replaced with NaN.
7	*Unsaturated PSL Image for Electrons*	PSL Image created from the first QL Image (for scan $N_{unsaturated\ electron}$) on which the electron signal is not saturated. It is always the case that $N_{unsaturated\ electron} \geq N_{unsaturated\ xray}$.
8	*Unsaturated Base PSL Image for X-rays*	PSL Image created by applying the x-ray fading factor to the Unsaturated PSL Image for X-rays. When there is no x-ray saturation, Unsaturated Base PSL Image for X-rays is the same as the Base PSL Image.
9	*X-ray Reconstruction Input Image*	PSL Image created from the Unsaturated PSL Image for X-rays from which the pixels corresponding to x-ray filters, fiducial shadows, and high-energy electron peak have been removed by setting them to NaNs.
10	*Reconstructed X-ray Image*	PSL Image created after applying the NNMA reconstruction algorithm to the X-ray Reconstruction Input Image.
11	*Sampling Image*	PSL Image created from the Unsaturated PSL Image for X-rays from which the pixels corresponding to fiducial shadows and high-energy electron peak have been removed by setting them to NaNs.

Table C-1: Terminology for the images used in the processing of the imaging plate data

free of saturated pixels. Then, as described later in this chapter, a *saturation factor* is calculated and used to multiply the measurements obtained from the saturation-free image. (Alternatively, the saturation-free image is divided by a *fading factor*.) It was empirically verified that iso-intensity contours created on an x-ray image scan remain iso-intensity on previous (less faded) scans. Therefore, iso-contours created on the unsaturated image could be used to sample filter data on a saturated scan, provided that the saturation was off-filter. This was frequently the case.

There are a number of different image types involved in the processing of the imaging plate x-ray data; the following terminology (Table C-1) is used to keep track of them: Referring to the terminology just presented, the processing of the x-ray data for each shot, and according to the methodology developed in this dissertation, required the following steps:

1. Creation of the Base PSL Image;
2. Creation of the Unsaturated PSL Image for X-rays;
3. Calculation of the x-ray saturation factor, using the Base PSL Image and the Unsaturated PSL Image for X-rays, following the methodology described in later in this chapter;
4. Creation of the X-ray Reconstruction Input Image;
5. Creation of the Reconstructed X-ray Image following the procedure described in 5.7.1: Reconstruction of the Filtered X-ray Beam Profile ;
6. Determination of the boundaries of the x-ray filters on the Unsaturated PSL Image for X-rays;
7. Creation of iso-intensity contours on the Reconstructed X-ray Image;
8. Restoration (transfer) of iso-intensity contours restored on the Sampling Image;
9. Recording of pixel values on the Sampling Image along iso-intensity contours for all contours and all crossed filters;
10. Determination of Ross pair data (yielding spectrum data points) resulting from sampled pixel values on each contour;
11. Statistical analysis of sampled pixel values for all Ross pair filters to exclude outliers, calculate average PSL, and its standard deviation;

12. Conversion of PSL values from the Unsaturated PSL Image for X-rays to the Unsaturated Base PSL Image for X-rays using the x-ray saturation factor;
13. Application of Eq. 5.11 to Ross pair PSL data for contours; each pair of PSLs yields one point on the spectrum corresponding to that pair of filters.

In what follows, details of some of the steps are described.

Calculation of the Saturation Factor for Imaging Plate Data

As discussed, the output from the reading of the imaging plate stored signal becomes saturated when the IP has been exposed to very high doses of radiation; this is the result of a mismatch between the large dynamic range of the imaging plate detector (5 orders of magnitude), and the smaller dynamic range of the photomultiplier tube used in the IP scanner system (less than 3 at the highest sensitivity setting). In the radiation environment of the laser-wakefield experiments, saturation can be due to very high charge or very high-brightness betatron x-rays. In the case of x-rays, in particular, the radiation dose can change from shot to shot, therefore a reduction in the sensitivity of the scanner to mitigate saturation, while helpful for some shots, would be at the price of weak x-ray signal for others. The maximum scanner sensitivity (10000) was therefore always used and a methodology was developed to recover an unsaturated version of a saturated image from the saturated image. The approach takes advantage of the ability of the scanner system to induce fading in the IP. This scanner-induced fading is the result of photo-stimulated luminescence that takes place when the scanner laser photons (which are in the red part of the spectrum) are absorbed by color (F) centers in the IP phosphor layer, leading to the emission of the blue light collected by the scanner. Although fading is a random process, there is a roughly linear relationship between pixel values before and after a scan. Figure C-1 shows the scatter plots of pixel values, calculated according to Eq. C-1, for the first 4 scans of shot 5862. (The QL values in Eq. C-1 were the output of 4 consecutive scans using a Fuji FLA-7000 imaging plate scanner with resolution setting of 100 μm and

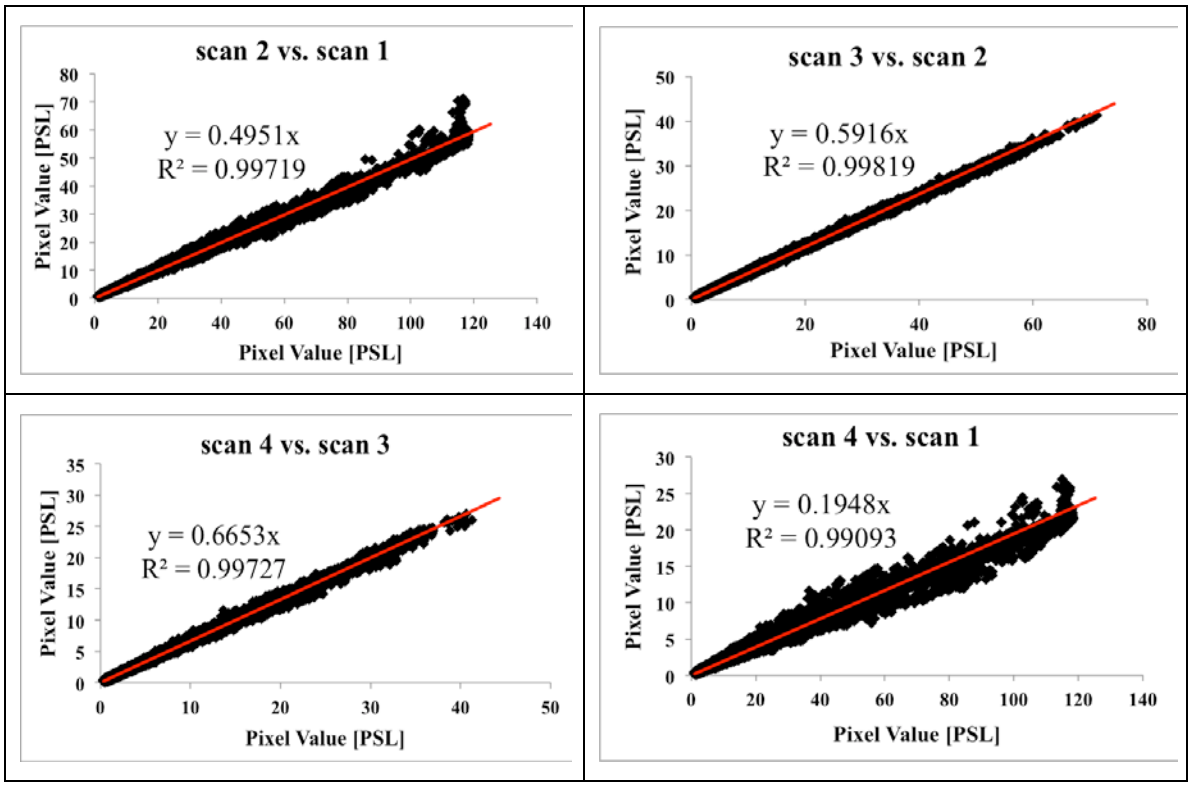

Figure C-1: Scatter plots of pixel values for scans 1 to 4 of shot 5862 from experimental round 3.

sensitivity setting of 10000.) The pixels correspond to a 550 × 550 pixel region of the MS IP detector centered on the betatron x-ray signal. (To prevent bias, pixels that were saturated on scan 1, were excluded from the analysis for all scatter plots.) There is a linear relationship between pixel values from consecutive scans. The slope of the best linear fit to the scatter data, constrained to pass through the origin, is indicative of the average degree of signal fading due to that scan. For example, scan 2 pixel values were on average 49.5% of the scan 1 pixel value; scan 3 pixel values were on average 58.2% of scan 2 pixel values. The following details in these images are worth noting. The pixel fading is characterized by a linear relationship with a random component. The degree of fading depends on the order of the scan and the scanner setting (e.g., sensitivity) and tends to decrease with increasing scan order. The random component may be accompanied by a changing variance in the regression residuals. (For example, the scatter plot for scan 2 vs. scan 1 shows increasing variance at larger pixel values. Statistically, this is known at positive heteroscedasticity). Although the residuals can be relatively small, as in the case for scan 3 vs. scan 2, they are larger for scatter plots of pixel values

from non-consecutive scans, e.g., scan 4 vs. scan 1. Not surprisingly, fading between non-consecutive scans is equal to the product of fading between consecutive intermediate scans, using the slope of the linear regression fit. For example, the product of the slopes from the first 3 fits is 0.1949 (0.4952 × 0.5916 × 0.6653) in good agreement with the slope of the fit of scan 4 vs. scan 1 (0.1948). The presence of a linear relationship makes it possible to define a *fading factor*, as the slope of the line going through the origin and best fitting the scatter data of pixel values before (X axis) and after (Y axis) a scan. When the faded image is divided by this factor, an image is recovered which may be used as proxy for the original image. In the presence of saturated pixels, repeated scans of the saturated image, if necessary at high scanner laser intensity (i.e., at higher scanner sensitivity), can remove the saturation by scanner-induced fading; then the fading factor is calculated between the first (saturated) and last (unsaturated) scan and used to recovered the original image. To justify the use of a single fading factor when the fading itself has a random component, the fading factor should be applied to pixel values where the random component has been averaged out. This is indeed the case. For example, when sampling on an iso-intensity contour drawn on what has been denoted the Unsaturated PSL Image for X-rays (Table C-1), the intersection of a contour with x-ray filters of a given type produces a sample of measurements for that filter type; these are then averaged to remove the noise component, before the fading factor is applied. (As described in Appendix F, the error for the measurement is then determined by the standard deviation of the PSL values for the pixels in the sample, and the sample size, see Eq. F-8.) This approach is equivalent to performing the same sampling on what has been denoted the Unsaturated Base PSL Image for X-rays (Figure C-2); either way, the random component of the pixel values is also averaged out.

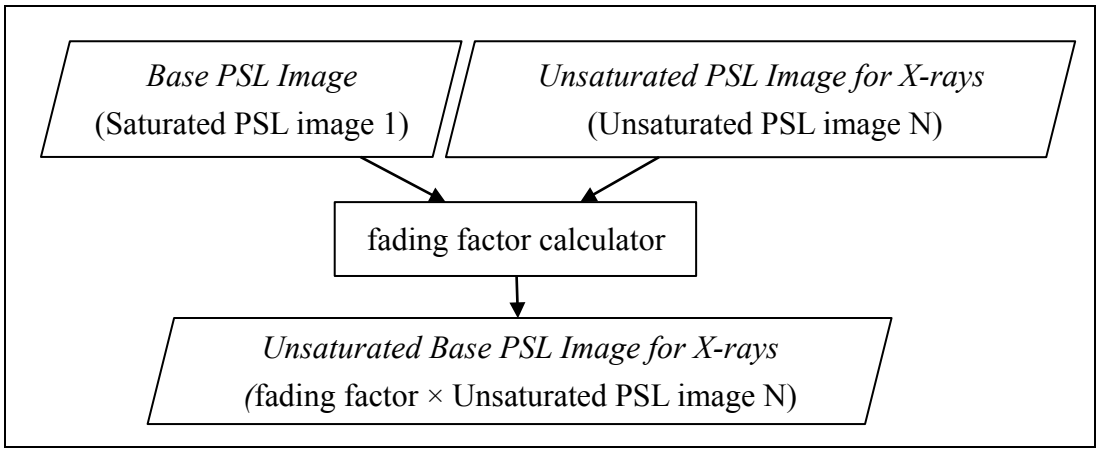

Figure C-2: Procedures for the calculation of an unsaturated image from a saturated image; see **Table C-1** for image terminology

In practice, it was found more convenient to use the inverse of the fading factor, the saturation factor, determined from the distribution of the pixel ratios before and after a scan, and multiply the faded image by that factor to reproduce the original image. The mode of the distribution (the bin of the distribution histogram with the largest number of entries) was found to give the best results; this is because the distribution of the saturation factors is skewed to left (fading factors are skewed to right) and the mode is a better measure of centrality for skewed distributions than mean. (A comparison to the median of the distribution was also performed, however the mode of the saturation was found to be a better global factor for the recovery of the original from a scanned image based on the mean difference for the pixel values in the original and recovered images.) Using the mode of saturation factors also mitigates the issue of heteroscedasticity, which exists in the fading factor calculation using a linear fit. The saturation factor, thus calculated, may be directly applied to a faded image to recover a proxy for the original image. (Alternatively, the inverse of the mode of the distribution of fading factors could be used, but note that the inverse of the mode of a distribution does not necessarily equal the mode of the distribution of the inverse, and by using the distribution of saturation factors, no inversion is necessary.) The mode of the distribution is robust to the existence of saturated pixels in the images; therefore such pixels do not need to be removed. Figure C-3 shows the distribution of saturation factors for the ratio of scan 1 and scan 2 of shot 5862 (experimental round 3). The mode of 1.932 is larger than the mean of 1.873, due to the negative skew of the distribution. The mode can be directly applied to scan 2 to

recover scan 1. Note that 1.932 is within one standard deviation (0.154) of the inverse of the slope of the corresponding fit in Figure C-2 ("scan 2 vs. scan 1"), which is 1/0.4951=2.0198. The latter value is considered less accurate due the increasing variability of the fading factors with increasing pixel value that affects the linear regression procedure.

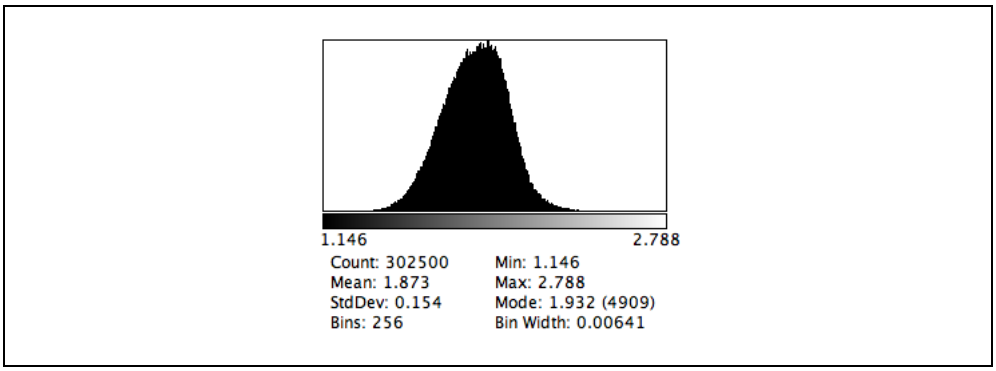

Figure C-3: Saturation factor calculated as the mode of distribution of scan 1 to scan 2 pixel values

The methodology described here referred to the x-rays but is also applicable to imaging plate measurements for electrons in the presence of saturation. The methodology for analyzing saturated images in ImageJ is summarized below. *Region of interest* may be either electrons or x-rays.

I.	*Scan the imaging plate N times until saturation in the region of interest disappears*
II.	*Convert scans 1 and N to from QL to PSL (*Eq. C-1*)*
III.	*Create a **ratio image** by dividing the PSL image from scan 1 by PSL image from scan N ('Process → Image Calculator'... in ImageJ)*
IV.	*Create selection around the region of interest on scan 1*
V.	*Restore the selection created on scan 1 on the ratio image from step III ('Edit → Selection → Restore Selection' in ImageJ)*
VI.	*Create histogram of pixels inside the region of interest on the ratio image (Analyze → Histogram in ImageJ)*
VII.	*Use the **mode** of the histogram distribution as the saturation factor*
VIII.	*Multiply the PSL image from scan N by the saturation factor (Process → Math → Multiply...)*

Appendix D. Imaging Plate Calibration for High-Energy Electrons

D.1 Methodology

The calibration of an imaging plate (IP) is specific to the IP, the scanner, and the ionizing particle for which the IP serves as a detector. In practice, this would require the IP, the scanner, and the particle source to be co-located. It was not possible to transfer the FLA-7000 scanner used for the TPW experiements to an electron source. Instead, all existing imaging plate calibration data for electrons were collected, and reasonable assumptions were made to enable the analysis of the data in order to obtain the sensitivity to relativistic electrons of the imaging plates scanned on a Fuji FLA-7000 IP scanner. The analysis, and the assumptions made, are described in this appendix.

Three sources of IP calibration for electrons in the sensitivity plateau region (> 1 MeV) were available. These were Tanaka el al. [64], Nakanii et al. [65], and Zeil et al. [66]. In all cases, Fujifilm BAS-SR or BAS-MS imaging plates had been exposed to energetic electrons, then scanned using *Fuji-branded* BAS series scanners. This distinction is important; unlike GE-branded ones, Fuji scanners are expected to have similar calibrations; this feature has been exploited to relate the sensitivities obtained using BAS-1800 and BAS-5000 scanners to those for the FLA-7000 scanner. In addition, Zeil et al. determined, using an x-ray source, the relative sensitivities between BAS-1800II and BAS-5000 scanners, for both BAS-MS and BAS-SR imaging plates.

To summarize, this information was available:

- Calibration of SR IP for electrons at 11.5 MeV, 30 MeV, and 100 MeV, using BAS-1800 as scanner;
- Calibration of MS and SR IPs for electrons at 20 MeV using BAS-5000 as scanner;
- Calibration of SR IP for electron at 1 GeV using BAS-1800II as scanner;
- Sensitivity ratios $a^{SR}_{BAS1800II}/a^{SR}_{BAS5000}$ and $a^{MS}_{BAS1800II}/a^{MS}_{BAS5000}$ for SR and MS IPs exposed to x-rays and scanned using BAS-1800II and BAS-5000 scanner

Based on private communication with a representative of GE Healthcare (which overtook the Fuji IP scanner business),

> *"Fuji-branded scanners have a sensitivity adjustment function which adds appropriate voltage to the PMT inside the scanner to make ideal output. This*

function gives almost the same PSL value for all Fuji scanners. For GE-branded scanners the sensitivity function is replaced with direct PMT voltage adjustment by the user and hence each individual instrument has different characteristics. Therefore calibration data from BAS-5000 and BAS-1800II cannot be applied on the FLA-7000 and each instrument has to be calibrated individually."

All the scanners considered are Fuji-branded, justifying the use of BAS-1800 and BAS-5000 calibration data to determine the calibration for FLA-7000. In addition, it was noted that FLA-7000 and BAS-1800 have similar light collection mechanism.

There are two types of light collection mechanisms used in imaging plate scanners. One combines a mechanical scanning system with confocal optics; the other combines an optical scanning system with light collecting guide optics [67]. In confocal systems, better resolution is achieved at the price lower light collection efficiency. This is because only light at given focal plane is collected; to compensate for the lower amount of light, the scanning process is slowed to allow for collection of more light. As a result, scanners using confocal optics are slower. In addition, scanners with confocal optics may use higher quality optical components to compensate for the lower light collection efficiency. The Fuji scanners of interest here have the following light collection mechanisms:

Scanner	*Light Collection Mechanism*
BAS-1800/BAS-1800II	light collecting guide
BAS-5000	confocal
FLA-7000	light collecting guide

Table D-1: Light collection mechanism for different IP scanners

Given the information presented above, the following working assumptions were made:

- No distinction is made between BAS-1800 & BAS-1800II scanners as regards their calibrations. They are jointly referred to as BAS-1800 in the remainder of this analysis;
- The IP sensitivities (in units PSL/e^-) have an exponential dependence [68] on electron energy in the sensitivity plateau (> 1 MeV) region;
- For the same IP scanner model, the calibrations of MS and SR IPs for electrons as a function of energy are related by a constant factor; this factor is determined from the known calibrations at 20 MeV;

- For the same IP type, the calibrations for electrons on different scanner models as a function of energy are related by a constant factor; this factor is the same as the ratio of PSL from that IP type exposed to same dose of x-rays and scanned on different scanner model;
- Fuji-branded scanner models are assumed to same similar calibrations; in particular, scanners models having similar light collection efficiencies (e.g., BAS-1800 and FLA-7000);
- Tanaka et al. provided error bars for the energy measurements, but not for the calibration (PSL/e^-) measurements. Assume the latter error bars have the same magnitude as the energy error bars.

There are 4 calibration data points available for electrons on the BAS-SR IP on the BAS-1800 scanner. In addition, there is calibration of both BAS-SR and BAS-MS IPs on the BAS-5000:

E [MEV]	*IP Type*	*Scanner Model*	*PSL/e-*	*Source*
20	BAS-SR	BAS-5000	0.0207±0.0002	[66]
20	BAS-MS	BAS-5000	0.0534±0.0005	[66]

Table D-2: Calibration data for electrons detected on two IP types scanned on the BAS-5000 scanner

This data may be converted to calibration for electrons on BAS-SR and BAS-MS IPs on the BAS-1800 scanner. This is because in addition to the calibration for electrons of BAS-SR IP on BAS-1800 for electrons, Zeil et al. used an x-ray tube to determine the relative response of BAS-SR and BAS-MS IPs to x-rays as a function of x-ray dose, using both BAS-1800 and BAS-5000 as scanners. As expected, they found a linear relationship between the response of the IPs (PSL) and the x-ray dose (Gy). The slope, *a*, is given below:

Scanner	*a [PSL/mGy]*	
	BAS-SR	*BAS-MS*
BAS-1800	454 ± 3	1890 ± 31
BAS-5000	1163 ± 18	2027 ± 96

Table D-3: Linear response of BAS-SR and BAS-MS IPs to x-rays scanned using Fuji branded BAS-1800II and BAS-5000 IP scanners

This information may be used to convert IP calibrations for electrons, from one scanner to another. Information in Table D-3 yields the following ratios:

$$\frac{a^{SR}_{BAS-5000}}{a^{SR}_{BAS-1800II}} = 2.56 \pm 0.04 \qquad \textbf{Eq. D-1}$$

$$\frac{a^{MS}_{BAS-5000}}{a^{MS}_{BAS-1800II}} = 1.07 \pm 0.05 \qquad \textbf{Eq. D-2}$$

Applying the ratios in Eq. D-1 and Eq. D-2 to data in Table D-2, Zeil et al. obtained the following calibrations for electrons detected on IPs scanned on the BAS-1800 scanner:

E [MEV]	*IP Type*	*Scanner Model*	*PSL/e-*	*Source*
20	BAS-SR	BAS-1800	0.00809±0.00007	[66]
20	BAS-MS	BAS-1800	0.0499±0.0005	[66]

Table D-4: Calibration data for electrons detected on two IP types scanned on the BAS-1800 scanner, obtained by combining the information in **Table D-2** and **Table D-3**

Including the information in Table D-4, there are 5 data points for BAS-SR IP scanned on BAS-1800 scanner model. Table D-5 shows all the available IP calibration data for electrons :

E [MEV]	*IP Type*	*Scanner Model*	*PSL/e-*	*Source*
11.5±5%	BAS-SR	BAS-1800	0.0074±5%	[64]
20	BAS-SR	BAS-1800	0.00809±0.00007	[66]
30±5%	BAS-SR	BAS-1800	0.007±5%	[64]
100±10%	BAS-SR	BAS-1800	0.0064±10%	[64]
1000±0.3%	BAS-SR	BAS-1800	0.0042±11%	[65]

Table D-5: World calibration data for Fujifilm BAS-SR imaging plate

Note that the Zeil et al. data point at 20 MeV in Table D-5 is somewhat at odds with the neighboring data points provided by Tanaka et al., making it necessary to include the error bars when fitting the data.

The following calibration methodology was adopted to determine $calib_e(E; IP, scanner)$, the calibration for electrons as a function of electron energy, for given imaging plate type and scanner model:

Step 1. Perform an error-weighted exponential fit of the 5 calibration data points available at high energies for the BAS-SR IP scanned on the BAS-1800 scanner (Table D-5); this yields $calib_e(E; BAS\text{-}SR, BAS\text{-}1800)$;

Step 2. Determine $calib_e(E; BAS\text{-}MS, BAS\text{-}1800)$ as the product of $calib_e(E; BAS\text{-}SR, BAS\text{-}1800)$ and the ratio of calibrations for different IPs at 20 MeV given in Table D-4;

Step 3. Determine $calib_e(E; BAS\text{-}SR, BAS\text{-}5000)$ as the ratio of $calib_e(E; BAS\text{-}SR, BAS\text{-}1800)$ and the ratio in Eq. D-1;

Step 4. Determine $calib_e(E; BAS\text{-}MS, BAS\text{-}5000)$ as the ratio of $calib_e(E; BAS\text{-}MS, BAS\text{-}1800)$ and the ratio in Eq. D-2.

In Table D-6, data used to perform the fit described in Step 1 above is displayed:

E [GEV]	*PSL/e-*	*Δ(PSL/e⁻)*	$w_i = 1/\Delta_i^2/\Sigma(1/\Delta_i^2)$	*Source*
0.0115	0.0074±5%	0.00037	0.032224861	[64]
0.020	0.00809±0.00007	0.00007	0.900323168	[66]
0.030	0.007±5%	0.00035	0.036012927	[64]
0.1	0.0064±10%	0.00064	0.010770468	[64]
1	0.0042±11%	0.000462	0.020668576	[65]

Table D-6: Errors used to perform error-weighted fit to calibration data for BAS-SR IP on BAS-1800

Using the information in this table, the steps enumerated above were implemented:

Step 1. A weighted exponential fit of the BAS-SR data on BAS-1800 scanner was performed in MATLAB with the following results:

```
General model Power1:
     f(x) = a*x^b
Coefficients (with 95% confidence bounds):
       a =    0.004875  (0.001816, 0.007935)
       b =     -0.1269  (-0.288, 0.03411)
Goodness of fit:
  SSE: 7.454e-08
  R-square: 0.8018
  Adjusted R-square: 0.7357
  RMSE: 0.0001576
```

The fit yields the electron calibration

$calib_e(E; BAS\text{-}SR, BAS\text{-}1800) = 0.004875\ (E[GeV])^{-0.1269}$

Step 2. The ratio of calibrations for different IPs at 20 MeV given in Table D-4 is 0.0499/0.00809=6.168109. Therefore

$calib_e(E; BAS\text{-}MS, BAS\text{-}1800) = 6.168109 \times calib_e(E; BAS\text{-}SR, BAS\text{-}1800) = 0.030070\ (E[GeV])^{-0.1269}$

Step 3. The ratio in Eq. D-1 applied to $calib_e(E; BAS\text{-}SR, BAS\text{-}1800)$ gives

$calib_e(E; BAS\text{-}SR, BAS\text{-}5000) = 2.56 \times 0.004875\ (E[GeV])^{-0.1269} = 0.012480\ (E[GeV])^{-0.1269}$

Step 4. The ratio in Eq. D-2 applied to $calib_e(E; BAS\text{-}1800, BAS\text{-}MS)$ gives

$calib_e(E; BAS\text{-}MS, BAS\text{-}5000) = 1.07 \times 0.030070\ (E[GeV])^{-0.1269} = 0.032175\ (E[GeV])^{-0.1269}$

D.2 Discussion

The weighted nonlinear least square fit to data in Table D-6, using an exponential model of the form $f(E) = a \times E^b$, is shown in Figure D-1:

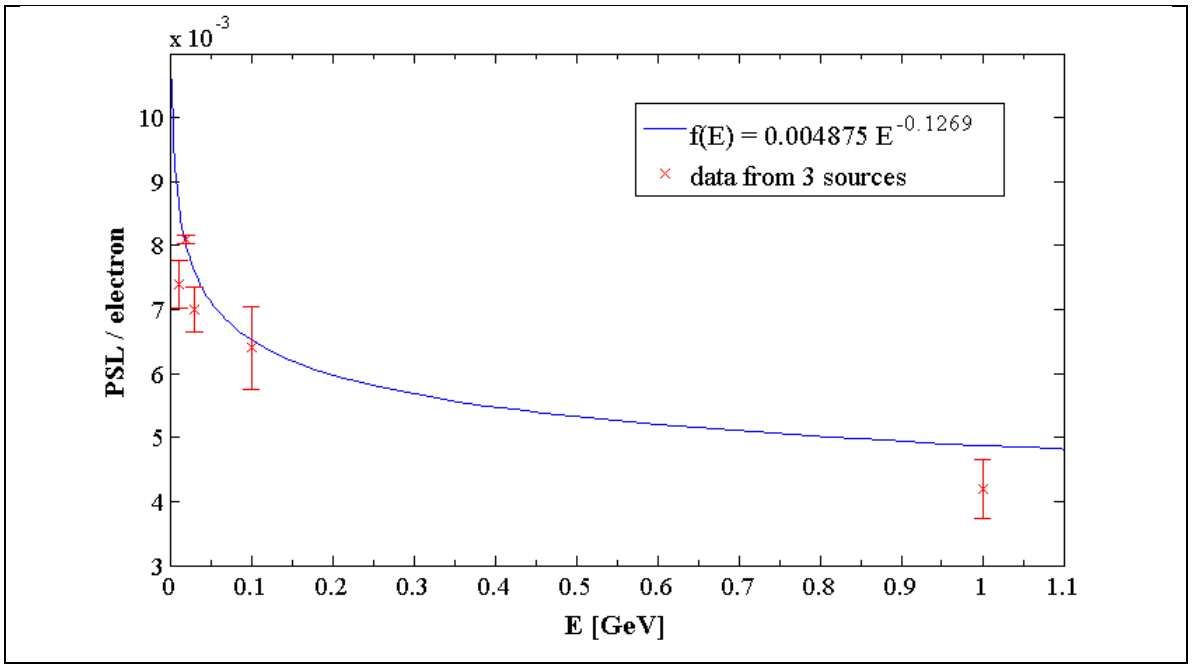

Figure D-1: Weighted exponential fit to data in **Table D-6** for BAS-SR IP on BAS-1800 scanner

The data point at 20 MeV is outside the confidence interval suggested for it by its neighboring data points; however, it has the lowest error, and is allocated a weight of 90% for fitting purposes (Table D-6). The large weight of this data point in the weighted fitting causes the sensitivity curve to shift upwards and fall outside and above the error bar at 1 GeV. This has the consequence that the charge calculated using this fit is more conservative, especially at higher energies, than if weights had not been used. In order to prevent the nonlinear least square algorithm from treating the data point at 20 MeV as an outlier, the robustness feature in MATLAB curve fitting tool was turned off. (Robust fitting excludes data determined to be an outlier.

It is important to note that the x-ray results in Table D-3 have been used only for relating calibrations done on different scanners for the *same* IP exposed to electrons as ionizing particles; this is justified because although different imaging plate types respond differently to the passage of different types of ionizing particles, for the same IP type, the difference between calibrations done using different scanners and a given ionizing particle is only due to the difference in light collection efficiencies between the scanners

and independent of the ionizing particle that the IP was exposed. Therefore the ratios in Eq. D-1 and Eq. D-2, which were obtained using x-rays, should also be applicable to electrons. A summary of the imaging plate calibration analysis is displayed in Table D-7. The calibrations are in units of PSL per electron (PSL/e^-) and are provided as a function of energy (in GeV units):

	BAS-1800	*BAS-5000*
BAS-MS	$0.0301 \times (E[GeV])^{-0.1269}$	$0.0322 \times (E[GeV])^{-0.1269}$
BAS-SR	$0.0049 \times (E[GeV])^{-0.1269}$	$0.0125 \times (E[GeV])^{-0.1269}$

Table D-7: Calibrations of BAS-MS and BAS-SR IPs for electrons on two Fuji-branded scanner models

As previously mentioned, it is expected that the Fuji-branded IP scanners will have similar calibrations for the same IP. The information in suggests that this is the case for the BAS-MS IP but not for the BAS-SR IP, for which BAS-5000 gives a higher sensitivity to electrons. The reason for this is the blue dye used in BAS-SR IPs to reduce the scattering of the laser light and enhance the resolution. A side effect of reduced laser light scattering in the BAS-SR IP is that the light generated from a volume inside the phosphor layer is reduced. Since BAS-5000 are confocal and collect light not from a volume but from the focal plane (having thickness smaller than the volume of phosphor contributing to the photo-stimulated luminescence in the absence of blue dye), they are impacted less by the addition of the blue dye than the BAS-1800 scanner which uses a light collecting guide to collect light from a finite volume inside the phosphor.

Since BAS-SR IPs distinguish between confocal and non-confocal systems, and FLA-7000 is a non-confocal system (see Table D-1), it was therefore decided to use the calibrations in Table D-7 for the (non-confocal) BAS-1800 as proxy for FLA-7000.

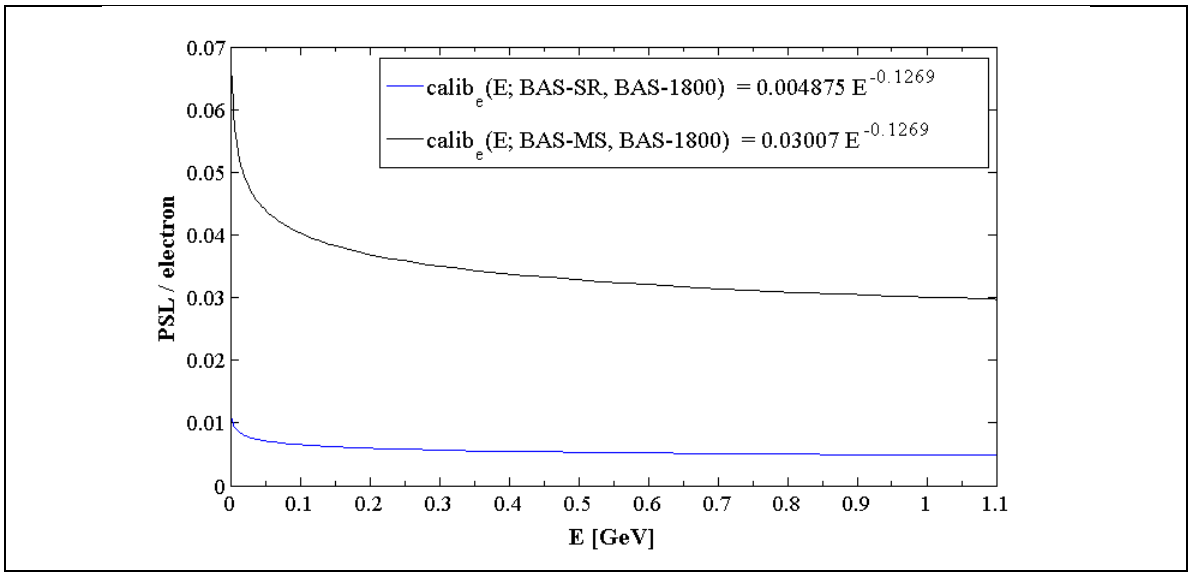

Figure D-2: Calibrations used to convert PSL to electron charge as a function of energy for Fujifilm IPs

D.3 Comparison of charge on different detectors

The values of charge detected using the BAS-MS and BAS-SR IPs, calibrated according to the methodology described here (see Table D-7 for BAS-1800), agree to within a few percent. To demonstrate, the results for a shot from LWFA 4.0 are presented. Table D-8 shows the relevant values required for the calculation of charge for shot 8273.

Shot	*x-ray center [pixel]*	*MS IP saturation factor for electrons (mode of distribution of scan 1 to scan 11 pixel ratios)*	*SR IP saturation factor for electrons (mode of distribution of scan 1 to scan 5 pixel ratios)*
8273	1843	17.070	2.577

Table D-8: Physical parameters used as input for the calculation of charge using the IP detectors

The MS IP saturation factor was calculated as the mode of the distribution of the ratio of pixels between MS IP scan 1 and scan 11 (scan with unsaturated electron signal). Similarly, the SR IP scan saturation factor was calculated as the mode of the distribution of the ratio of pixels between SR IP scan 1 and scan 5 (scan with unsaturated electron signal). In both cases, the region of interest was restricted to the electron signal. (Details are provided in C.2.) The x-ray center was determined by fitting an ellipse to the x-ray profile and finding the X coordinate of its center. (Peak x-ray intensity pixel coordinate could also be used.) Using these values, the following values were obtained for charge at energies > 300 MeV on two different imaging plates calibrated in two different ways:

Detector: MS IP, calibration using fit to available data			
High Energy Tail [pC]	*FWHM [pC]*	*Low Energy Tail [pC]*	*Total Charge [pC]*
4.82	29.58	164.25	198.65

Detector: SR IP, using fit to available calibration data			
High Energy Tail [pC]	*FWHM [pC]*	*Low Energy Tail [pC]*	*Total Charge [pC]*
4.97	29.16	163.37	197.51

Detector: MS IP, using calibration @ 20 MeV			
High Energy Tail [pC]	*FWHM [pC]*	*Low Energy Tail [pC]*	*Total Charge [pC]*
2.69	16.92	104.56	124.16

Detector: SR IP, using calibration @ 20 MeV			
High Energy Tail [pC]	*FWHM [pC]*	*Low Energy Tail [pC]*	*Total Charge [pC]*
2.77	16.58	104.05	123.04

Table D-9: Comparison of charge detected using BAS-MS and BAS-SR imaging plate detector, using fit to calibration data as a function of energy, and at 20 MeV

Table D-9 show the values of charge in different parts of the electron energy spectrum, detected on Fuji BAS-MS and BAS-SR IPs. In all cases where fitting was used, the charge was calculated according to the formula:

$$Q = \sum_{i,j} PSL_{ij} \times saturation\ factor \times \frac{q_e\ [pc]}{calibration_{ij}\ \left[\frac{PSL}{e^-}\right]} \qquad \textbf{Eq. D-3}$$

$calibration_{ij}\left[\frac{PSL}{e^-}\right]$ is from Table D-7 and has the general form of $a\left(E_{ij}[Gev]\right)^b$, where $E_{ij}[Gev]$, the energy of electron arriving at pixel i,j is from Table 4-1 and has the general form $\frac{A}{\Delta x_{ij}\,[pixels]}$; Δx_{ij} is the deflection, in pixels, of electron arriving at pixel i,j after traversing the magnetic spectrometer:

$$Q = \sum_{i,j} PSL_{ij} \times saturation\ factor \times \frac{q_e\ [pc]}{a\left(\frac{A}{\Delta x_{ij}[pixels]}\right)^b\ \left[\frac{PSL}{e^-}\right]} \qquad \textbf{Eq. D-4}$$

For example, for the 4000×2000 pixel BAS-MS IP used for high-energy electron detection in the LWFA 4.0 shot 8273, $calibration\ \left[\frac{PSL}{e^-}\right] = 0.03007\ (E[GeV])^{-0.1269}$ (using BAS-1800 calibration as proxy for FLA-7000) and $E_{e,HEMS}[GeV] \cong \frac{C_{HE,wakefield}}{\Delta x_{HEMS}\,[pixels]}$ with $C_{HE,wakefield} = 561.326$ from Eq. 4.12, and $\Delta x_{HEMS}\ [pixels]$ as the distance between pixel i,j and the x-ray center. The position of the x-ray center and the saturation factor are provided in Table D-8. The constant q_e is the electron charge in units of pC (1.602 E-

7). When fitting was not used, $calibration_{ij}$ $\left[\frac{PSL}{e^-}\right]$ is replaced by the constant calibration value from Table D-4 for the corresponding imaging plate type.

The two types of calibrations that were used to convert PSL to number of electrons (i.e., fit to calibration data for BAS-1800 from Table D-7 and the calibration at 20 MeV [most accurate calibration data point] from Table D-4) yield charge differing by ~60%, due to the fact that the fitting approach incorporates the decreasing sensitivity of the imaging plates at higher energies, whereas the using constant calibration at 20 MeV overestimate the sensitivity at high energies and underestimate the charge. However, in both cases, the charge detected on the BAS-MS and BAS-SR IPs agrees to better than 1%. This is understood as a confirmation of the validity of the assumptions made in this chapter and the correctness of the calibration methodology.

Appendix E. Charge Calculation using the Lanex-Scintillator Detector

In the 2nd and 3rd rounds of the LPA experiments driven by the TPW laser, a combined Lanex-scintillator detector was deployed as an alternative electron charge diagnostic. The Lanex signal enables the calculation of charge using publish calibration data for the Lanex Regular scintillating screen, while the stronger signal from the plastic scintillator ensures a real-time diagnostic for the presence, shape, and approximate peak energy of the electron signal, complementing the weaker Lanex signal. A design (Figure 3.8), calling for the use of a single color CCD, allowed the images from the two detectors to be geometrically commensurate, hence easier to compare, while minimizing the impact of scintillator thickness on the depth of field. In this Appendix, I will discuss how the R, G, and B component signals from the color CCD were extracted from the Bayer pattern output of the CCD, how each undersampled component was reconstructed, develop the relations between the R, G, and B components and the Lanex and scintillator signals, and finally use the Lanex signal to derive an expression for the electron charge in term of the color CCD RGB components, published calibration data for the Lanex Regular screen, and geometrical factors in the experimental setup.

E.1 Reconstruction of the RGB Components in a Color CCD

A color CCD overlays the array of image sensors comprising a mono CCD with a grid of red (R), green (G), and blue (B) filters known as a *color filter array*. An $m \times n$ color CCD image may therefore be decomposed into 3 $m \times n$ component images, or channels, one for each of the colors R, G, and B. There will be gaps in the channels, where the image has been undersampled. A frequently used color filter array, and one used in the Basler scA1600-14fc CCD camera, is the *Bayer pattern* shown in Figure E-1. This is an arrangement in which the red, green, and blue filters alternate between rows and columns. There are 2 types of Bayer patterns used in Basler color CCD cameras: BG and RG. The BG pattern gives higher representation to the G (to match the sensitivity of the human eye) and is the one shown here. (The RG pattern switches the role of B and R.)

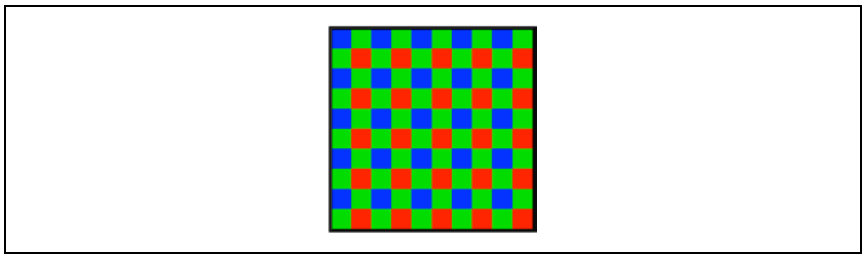

Figure E-1: Bayer pattern for the BG-type filter pattern (used in scA1600-14fc CCD)

Due to the undersampling of R, G, and B channels, interpolation of the image was required. There are many algorithms for this purpose and the one used to reconstruct the Lanex/scintillator images from the LWFA 2.0 and 3.0 experiments is *bilinear interpolation*, demonstrated in the figure below.

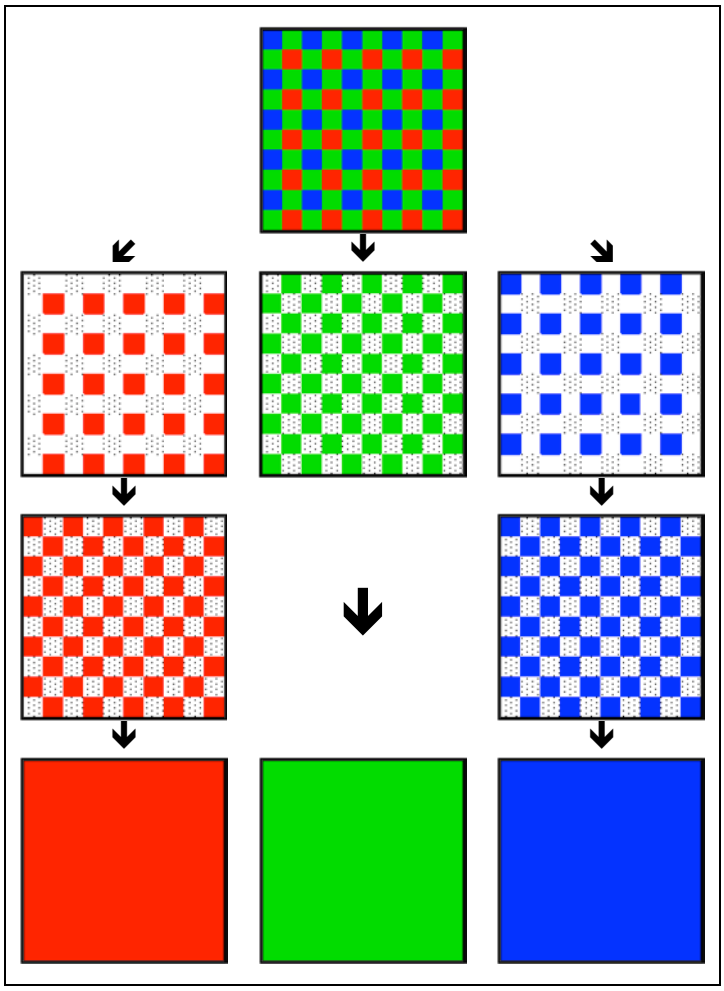

Figure E-2: Steps in the reconstruction of the Bayer pattern

The dotted regions in this figure show the pixels that will be interpolated in each round. The R and B channels are interpolated twice in order to obtain the final image for them.

The G channel requires one round of interpolation. The reconstructed R, G, and B images may be used to recover separate images corresponding to luminescence originating from the Lanex and scintillator. However, before using the R, G, and B images, it is necessary to incorporate the impact of any ND filters used with the CCD camera to prevent saturation. In what follows, R, G, and B will always refer to the reconstructed CCD images with the ND filter correction applied. For example, for a 0.6 ND filter, the reconstructed CCD channel images have been multiplied by $10^{0.6} = 3.98$.

E.2 Recovery of Lanex and Scintillator Signals from RGB Data

A single color CCD was used to detect light emitted by both the Kodak Lanex Regular scintillating screen and the EJ-200 plastic scintillator. As seen in Figure E-3, the Lanex screen emits primarily in the green with a spectrum peaking at ~545 nm, while the scintillator emits in violet and blue with a spectrum peaking at 425 nm:

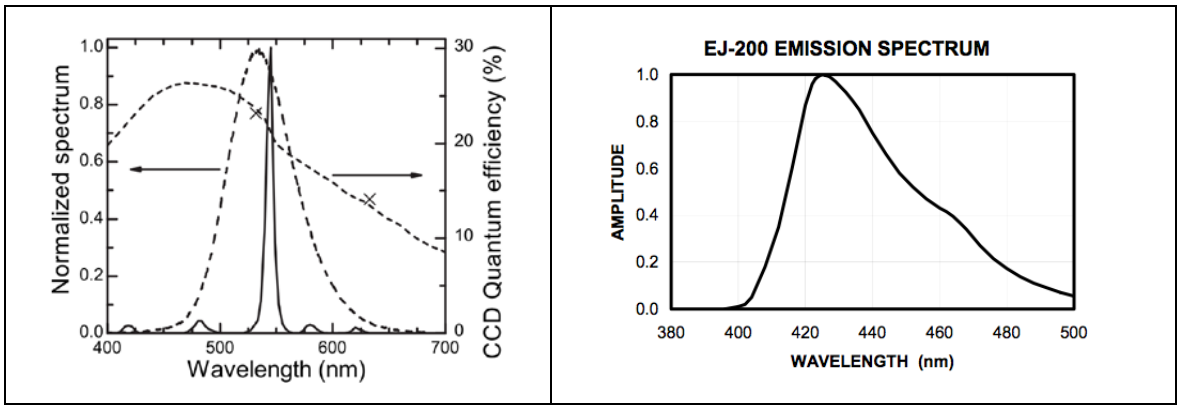

Figure E-3: Emission spectra for the Kodak Lanex Regular (left, solid line) [27], and EJ-200 plastic scintillator (right)

According to the calibration done in [27] for scintillating screens (Figure E-4), the Kodak Lanex Regular produces $(6.95 \pm 0.60) \times 10^{12}$ photons per nC of incident electron charge per unit solid angle. The photon yield is independent of electron energy above 3 MeV (Figure 3.5) and is well approximated by the Lambert's cosine law.

Screen	Absolute calibration (10^9 photons/sr/pC)	$N_{scint}/N_{CLS,20\ ms}/Q$ (pC^{-1})	ρ_{sat} (see Sec. III C) (pC/mm^2)
KODAK Biomax MS	14.8 ± 1.3	5.79 ± 0.26	21.8 ± 5.0
CAWO OG 16	12.4 ± 1.1	4.86 ± 0.21	32.9 ± 6.6
KODAK Biomax Transcreen HE	7.85 ± 0.67	3.02 ± 0.13	47 ± 10
KODAK Lanex Regular	6.95 ± 0.60	2.72 ± 0.12	66 ± 33
KONICA KR	6.58 ± 0.56	2.58 ± 0.11	>100
KODAK Biomax Transcreen LE	1.79 ± 0.15	0.700 ± 0.031	>100
KODAK Lanex Fine	1.75 ± 0.15	0.686 ± 0.030	>100
KONICA KF	1.54 ± 0.13	0.602 ± 0.027	>100

Figure E-4: Calibration data for scintillating screens, including the Kodak Lanex Regular [27]

The value of a CCD image pixel for each channel is attributed to photons arriving at that pixel from both the Lanex and the plastic scintillator and passing through the micro-lens for the corresponding channel. Mathematically this is expressed as

$$L_R + S_R = R, \quad L_G + S_G = G, \quad L_B + S_B = B \qquad \textbf{Eq. E-1}$$

In addition, we can write the following ratios:

$$L_B/L_G = \alpha, \qquad S_B/S_G = \beta, \qquad L_G/L_R = \gamma \qquad \textbf{Eq. E-2}$$

where the parameters α, β, γ may be numerically calculated by noting that the CCD image pixel for each channel for Lanex (scintillator) is proportional to the overlap of the color CCD quantum efficiency curve for that channel and the Lanex (scintillator) emission spectrum. Note, however, that the Basler Corporation does not provide quantum efficiency curves for its color CCDs; instead it provides *Relative Response* curves (Figure E-5).

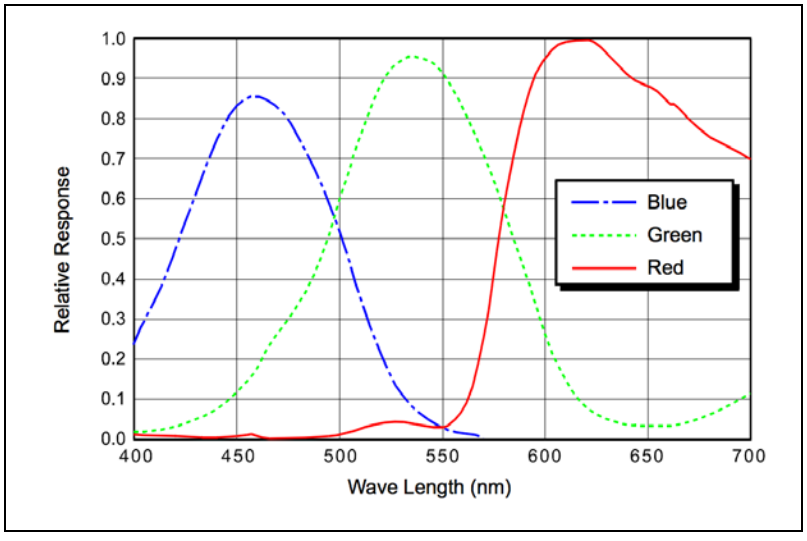

Figure E-5: Relative response of the scA1600-14fc color CCD (source: Basler)

These curves are provided by the Sony Corporation and, according to the documentation for the Sony ICX274AQ CCD image sensor chip, refer to the *spectral sensitivity* for the ICX274AQ chip used in the scA1600-14fm color CCD. One interpretation for these curves is that they represent the relative quantum efficiency of the 3 channels of the color CCD, i.e., they already incorporate the quantum efficiency of the mono CCD (scA1600-14fm) by being the products of the QE of the mono CCD (Figure E-6) and the (unknown) transmission curves of the color filter array used to produce the Bayer pattern, and expressed on a relative scale.

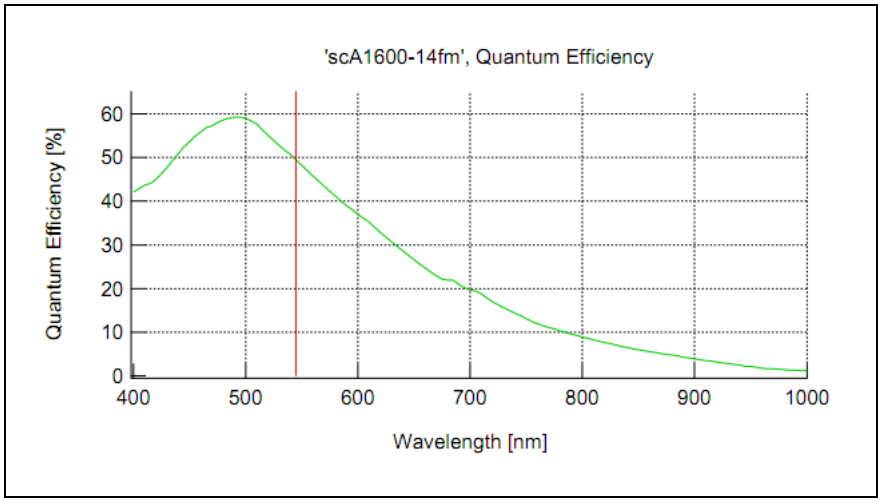

Figure E-6: Quantum efficiency of the scA1600-14fm mono CCD (source: Basler)

An alternative interpretation of the Relative Response curves would be that they only represent the relative transmission curves of the color filter array used in the CCD, in which case the QE of the mono CCD would also need to be incorporated. In communication with the Basler Corporation, it was not possible to determine unambiguously the interpretation for the Relative Response curves, but the Basler representatives believed they represented the relative QE curves. (This interpretation was later supported by comparisons of the charge as determined using the Lanex signal with that from the imaging plate measurements.) In addition, Basler representatives were unable to provide the normalization factor of the curves (to convert relative response to absolute response). Unsuccessful attempts were made to obtain the absolute transmission curves of the color filter array used by the Sony Corporation in the ICX274AQ chip. (This would have made possible an independent calculation of the absolute response curves since the absolute QE of the mono CCD, Figure E-6, the result of the CCD

calibration according to the EMVA Standard 1288, is available from the Basler Corporation.) We were informed that the absolute transmission curves of the color filter array were Sony proprietary information and could not be shared. The decision was therefore made to interpret the Relative Response curves of the color CCD as relative quantum efficiency curves for the channels of the color CCD, and determine the relative to absolute conversion factor (denoted C_{calib}) by a comparison of the Lanex charge to the imaging plate charge for same charge and selected shots. In what follows, the relations required to derive the Lanex and scintillator signal from the color CCD R, G, and B images are derived under this assumption. In addition, to accommodate the small likelihood that the Relative Response curves represent the relative transmission curves of the color filters (in which case the QE of the mono CCD would need to be separately included), the formulas obtained under this scenario are also presented.

The Lanex and plastic scintillator contributions to the CCD image pixel value for each of the 3 color channels may be written using the following 6 equations:

$$L_{R,B,G} = C_L(\Omega, q, C_{calib}) \int \left(QE_{R,B,G} \times NLES\right) d\lambda$$
$$S_{R,B,G} = C_S(\Omega, q, C_{calib}) \int \left(QE_{R,B,G} \times NSES\right) d\lambda \qquad \textbf{Eq. E-3}$$

$QE_{R,B,G}$ refer to the relative quantum efficiency curves for the red, green, and blue pixels of the Basler scA1600-14fc color CCD, in accordance with the reasonable assumption that the Relative Response curves in Figure E-5 represent the relative quantum efficiency curves of the scA1600-14fc color CCD. $C_L(\Omega, q)$ and $C_S(\Omega, q)$ are factors dependent on the geometry, the incident charge on the region of the Lanex and scintillator, respectively, the photons from which are focused onto the CCD pixel; as well as the common factor converting the relative QE curves to absolute curves. Figure E-7 for $QE_{R,B,G}$ is therefore similar to Figure E-5 for the Relative Response. *NLES* and *NSES* are abbreviations for the *normalized Lanex emission spectrum* and *normalized scintillator emission spectrum*, respectively. Each is obtained by normalizing the corresponding emission spectra (Figure E-3) such that they have unit area. (The normalization factor for the Lanex and scintillator are 0.0861 and 0.0222, respectively.) The overlap of $QE_{R,B,G}$ with the

normalized emission spectra for the Lanex (NLES) and the scintillator (NSES) are shown in Figure E-8. As indicated

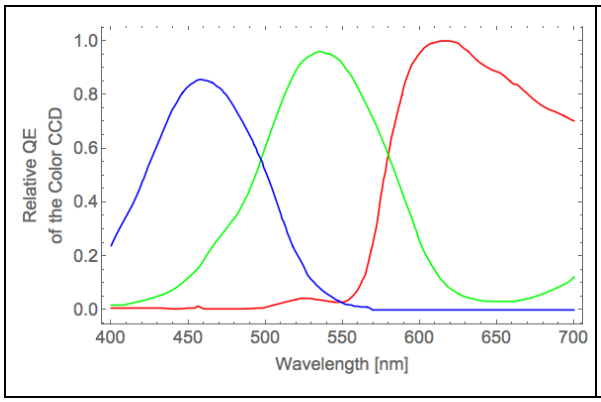

Figure E-7: $QE_{R,G,B}$ or the relative quantum efficiency for the R, G, and B pixels of the Basler scA1600-14fc color CCD.

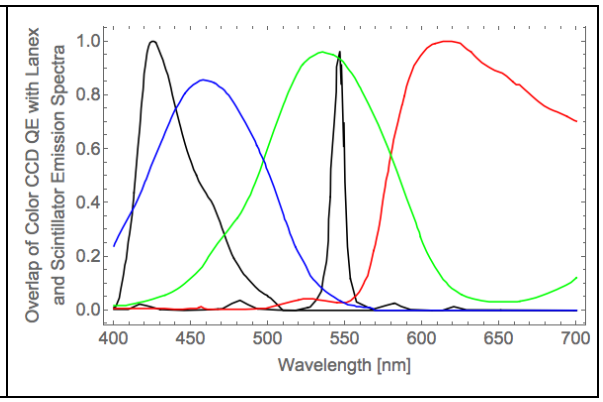

Figure E-8: Overlap of $QE_{R,G,B}$ (**Figure E-7**) and the emission spectra for the Lanex and scintillator (**Figure E-3**).

by the overlap between the normalized emission spectra and QE curves, the Lanex and plastic scintillator emissions are primarily detected by the green and blue CCD channels, respectively.

The integrands in Eq. E-3 are shown in Figure E-9, for the Lanex screen, and in Figure E-10, for the plastic scintillator. For the Lanex detector, the response of the color CCD is primarily in the green, with the red and blue making much smaller contributions. For the scintillator detector, the response of the color CCD is mostly in the blue, with a much smaller green component, and negligible contribution from red.

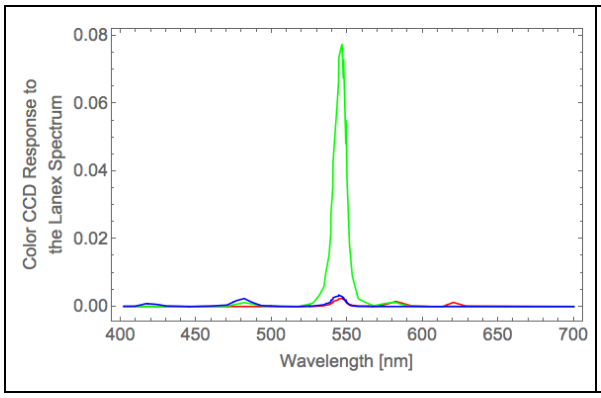

Figure E-9: The product ($QE_{R,G,B}$ × NLES) of $QE_{R,G,B}$ (**Figure E-7**) and the Lanex emission spectrum (**Figure E-3**, left).

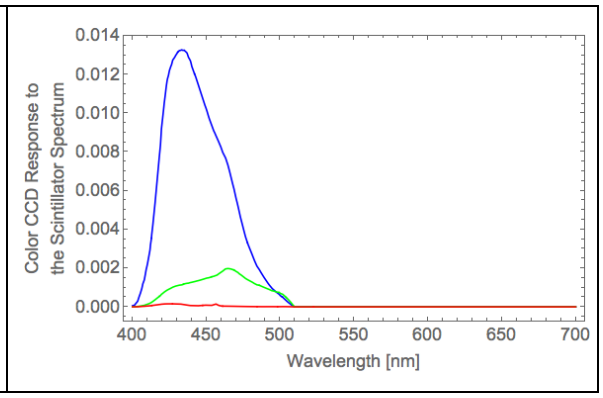

Figure E-10: The product ($QE_{R,G,B}$ × NSES) of $QE_{R,G,B}$ (**Figure E-7**) and the scintillator emission spectrum (**Figure E-3**, right).

The areas under the curves in Figure E-9 and Figure E-10, representing the 6 integrals in Eq. E-3, were numerically calculated as follows:

$\int (QE_R \times NLES)\, d\lambda = 0.063365$	$\int (QE_G \times NLES)\, d\lambda = 0.851315$	$\int (QE_B \times NLES)\, d\lambda = 0.089263$
$\int (QE_R \times NSES)\, d\lambda = 0.006170$	$\int (QE_G \times NSES)\, d\lambda = 0.113104$	$\int (QE_B \times NSES)\, d\lambda = 0.661107$

Table E-1: Overlap integrals for the relative QE of the RGB channels of the color CCD, **Figure E-7**, and the normalized emission spectra for the Lanex (NLES) and the plastic scintillator (NSES), **Figure E-3**.

Using the values in Table E-1, the parameters α, β and γ may then be determined:

$\alpha = \int (QE_B \times NLES)\, d\lambda \Big/ \int (QE_G \times NLES)\, d\lambda = \dfrac{0.089263}{0.851315} = 0.104853$
$\beta = \int (QE_B \times NSES)\, d\lambda \Big/ \int (QE_G \times NSES)\, d\lambda = \dfrac{0.661107}{0.113104} = 5.84512$
$\gamma = \int (QE_G \times NLES)\, d\lambda \Big/ \int (QE_R \times NLES)\, d\lambda = \dfrac{0.851315}{0.063365} = 13.4351$

Eq. E-4

The system of 6 equations in Eq. E-1 and Eq. E-2 with 6 unknowns $(L_R, L_G, L_B, S_R, S_G, S_B)$ has the following solution in terms of R, G, B, α, β, and γ:

$L_R = \dfrac{\beta G - B}{(\beta - \alpha)\gamma}$	$L_G = \dfrac{\beta G - B}{(\beta - \alpha)}$	$L_B = \alpha \dfrac{\beta G - B}{(\beta - \alpha)}$
$S_R = \dfrac{\gamma(\beta - \alpha)R - (\beta G - B)}{(\beta - \alpha)\gamma}$	$S_G = \dfrac{B - \alpha G}{(\beta - \alpha)}$	$S_B = \beta \dfrac{B - \alpha G}{(\beta - \alpha)}$

Eq. E-5

Plugging in the numerical values from Eq. E-4 into Eq. E-5, we get:

$L_R = -0.0130\, B + 0.0758\, G$	$S_R = 0.0130\, (B - 5.8451\, G + 77.1214\, R)$
$L_G = -0.1742\, B + 1.0183\, G$	$S_G = 0.1742\, (B - 0.1049)\, G$
$L_B = -0.0183\, B + 0.1068\, G$	$S_B = 1.0183\, B - 0.1068\, G$

Eq. E-6

The Lanex and scintillator signals may therefore be constructed by combining the interpolated R, G, and B components of the color CCD output:

$$L = L_R + L_G + L_B = \frac{1/\gamma + 1 + \alpha}{\beta - \alpha}(\beta G - B) = -0.2054\, B + 1.2008\, G \qquad \textbf{Eq. E-7}$$

$$S = S_R + S_G + S_B = \frac{1/\gamma(B - \beta G) + (1 + \beta)(B - \alpha G)}{\beta - \alpha} + R = 1.2054\, B - 0.2008\, G + R$$

Note that, as expected, $L + S = R + G + B$, using L and S from Eq. E-7, i.e., the sum of the Lanex and scintillator components of the CCD output equals the sum of the 3 color components.

The overlap between the response function for the R filter and the emission spectrum for both Lanex and plastic scintillator is small ($\int (QE_R \times NLES)\, d\lambda = 0.063365, \int (QE_R \times NSES)\, d\lambda = 0.006170$), the equations involving the R color in Eq. E-5 may be ignored; this yields a system of 4 equations:

$$\begin{aligned} L_G + S_G &= G, & L_B + S_B &= B \\ L_B / L_G &= \alpha, & S_B / S_G &= \beta, \end{aligned} \qquad \textbf{Eq. E-8}$$

The system of equations in Eq. E-8 with the 4 unknowns L_G, L_B, S_G, S_B has the following solution in terms of G, B, α and β:

$$\begin{aligned} L_G &= \frac{\beta G - B}{(\beta - \alpha)} & L_B &= \alpha \frac{\beta G - B}{(\beta - \alpha)} \\ S_G &= \frac{B - \alpha G}{(\beta - \alpha)} & S_B &= \beta \frac{B - \alpha G}{(\beta - \alpha)} \end{aligned} \qquad \textbf{Eq. E-9}$$

Plugging in value for α and β from Eq. E-4, we get:

$$\begin{cases} L_G = -0.1742\ \mathrm{B} + 1.0183\ \mathrm{G} \\ L_B = -0.0183\ \mathrm{B} + 0.1068\ \mathrm{G} \end{cases} \quad \begin{cases} S_G = 0.1742\ \mathrm{B} - 0.0183\ \mathrm{G} \\ S_B = 1.0183\ \mathrm{B} - 0.1068\ \mathrm{G} \end{cases} \qquad \textbf{Eq. E-10}$$

Having ignored the negligible R component of the CCD output, the Lanex and scintillator signals are then constructed by combining the interpolated G and B components of the color CCD output:

$$\begin{aligned} L = L_G + L_B &= \frac{1 + \alpha}{\beta - \alpha}(\beta G - B) = -0.1925\, B + 1.1250\, G \\ S = S_G + S_B &= \frac{1 + \beta}{\beta - \alpha}(B - \alpha G) = 1.1925\, B - 0.1250\, G \end{aligned} \qquad \textbf{Eq. E-11}$$

Once again, $L + S = G + B$, using L and S from Eq. E-11, i.e., the sum of the Lanex and scintillator components of the CCD output equals the sum of the green and blue components.

Note that the R channel of the CCD output does not explicitly appear in the expressions Eq. E-7 (which included the CCD R channel) or Eq. E-11 (excluded the CCD R channel)

for the reconstructed CCD output attributable to the Lanex. The contribution from the R channel appears in the coefficients, which are a function of the overlap integrals but, as mentioned, weakly dependent on the R channel due to the small overlap of the emission spectrum and the CCD response for the red region of the spectrum. The difference between Eq. E-7 and Eq. E-11 for L is therefore $\lesssim 7\%$. In the next section, the electron charge is calculated using the reconstructed Lanex signal given by Eq. E-7.

E.3 Calculation of Charge from Lanex Signal

To calculate the charge for accelerated electrons detected by the Lanex, on the one hand we need to relate the CCD RGB output at each pixel to L, the Lanex component of the CCD output at that pixel; this has been done by the first equation in Eq. E-7 (and Eq. E-11). On the other hand we need to relate the Lanex pixel value to the electron charge incident at that pixel. Eliminating the Lanex pixel value between the two, we are left with a relation between the charge incident at a Lanex pixel and the color CCD RGB output at that pixel. Using the calibration for the Kodak Lanex Regular (Figure E-4), the electron charge incident on a Lanex pixel may be related to the luminescence by the screen, i.e., the number of photons radiated into a given solid angle. This relation is:

$$L = q_{Lanex}(nC) \times LAC(photons\ /\ str\ /\ nC) \times \Omega \times C_{calib}\left(\frac{1}{4}\int (QE_R \times NLES\, d\lambda) + \frac{1}{2}\int (QE_G \times NLES\, d\lambda) + \frac{1}{4}\int (QE_B \times NLES\, d\lambda)\right) \times \frac{2^{12}-1}{CCD\ saturation\ capacity} \qquad \textbf{Eq. E-12}$$

Imaging the light produced by the Lanex onto the surface of a CCD, each pixel on the CCD is represented by a region on the Lanex. Eq. E-12 expresses the Lanex component of the CCD image at a given pixel in terms of the electron charge, $q_{Lanex}(nC)$, incident on the corresponding region on the Lanex and the CCD parameters. The acronym *LAC* stands for the *Lanex Absolute Calibration*; it gives the number of photons (of all wavelengths) emitted by the Lanex per nC of incident charge and per unit solid angle. According to the information in Figure E-4, this is $(6.95 \pm 0.60) \times 10^{12}$ photons/sr/nC. The terms in $\left(\frac{1}{4}\int (QE_R \times NLES\, d\lambda) + \frac{1}{2}\int (QE_G \times NLES\, d\lambda) + \frac{1}{4}\int (QE_B \times NLES\, d\lambda)\right)$ are convolution integrals and incorporate the overlap, shown in Figure E-9, of the CCD relative quantum efficiency curves (for each of the 3 channels) and the normalized Lanex emission spectrum (*NLES*) and are available from Table E-1. (The upfront factors are the

density ratios for the red, green, and blue filters in the BG-type filter pattern used in the color CCD. As seen in Figure E-1, for each red and blue pixel there exist two green pixels.) The factor C_{calib} is a conversion factor between relative and absolute QE curves, and has been determined by a comparison of the same charge calculated by the Lanex screen and the imaging plate (E.4). The color CCD has 12-bit pixel depth and a saturation capacity of (9000 ± 500) electrons at the peak wavelength of 545 nm, therefore the ratio $\frac{2^{12}-1}{CCD\ saturation\ capacity}$, converts the electron yield of the CCD (due to its quantum efficiency) at each CCD pixel to its corresponding the pixel value on the CCD output image. The solid angle Ω is the angle spanned by the focusing lens on the Lanex (Figure 3.8); it is related to the diameter of the CCD objective lens (i.e., focusing aperture) and the distance *L* between the Lanex screen and the lens:

$$\Omega = \frac{\pi(D/2)^2}{L} = \frac{1}{16}\left(\frac{D}{L}\right)^2 \times 4\pi = \frac{\pi}{4} \times \left(\frac{M}{(1+M)^3} \times \frac{1}{f\#}\right)^2 \qquad \textbf{Eq. E-13}$$

where $M = i/o$ is the absolute value of the magnification (for a real image) and $f\#$ is the f-number of the thin lens, characterized by the equation $\frac{1}{f} = \frac{1}{o} + \frac{1}{i}$. (Eq. E-13 is obtained as follows. Use $f = \frac{o \times i}{o+i}$ in $D = \frac{f}{f/D} = \frac{f}{f\#}$ to get $D = \frac{f}{f\#} = \left(\frac{o \times i}{o+i}\right)/f\#$. Then use $o \times M = i$ and write it as $(o \times M) + o = i + o$ to get $o = \frac{i+o}{1+M}$. Use this result, to write $o \times i$ as $o \times i = \frac{i+o}{1+M} \times i = \frac{i+o}{1+M} \times (o \times M) = \frac{i+o}{1+M} \times (\frac{i+o}{1+M} \times M) = \left(\frac{i+o}{1+M}\right)^2 M$. Plugging in this result in $D = \left(\frac{o \times i}{o+i}\right)/f\#$ gives $D = \left(\frac{o \times i}{o+i}\right)/f\# = \frac{(i+o)M}{(1+M)^2}/f\#$. Since the distance from the Lanex screen to the lens is also the object-to-lens distance *o*, we also have $L = o = \frac{i+o}{1+M}$, therefore $\frac{D}{L} = \left(\frac{(i+o)M}{(1+M)^2}/f\#\right)/\left(\frac{i+o}{1+M}\right) = \frac{M}{(1+M)^3} \times \frac{1}{f\#}$. Using this result in the expression for Ω gives Eq. E-13 expressing the solid angle subtended by the CCD objective lens at a point on the Lanex screen in term of the magnification and the f-number of the lens.)

Solving Eq. E-12 for q_{Lanex}, gives:

$$q_{Lanex}(nC) = \frac{CCD\ saturation\ capacity}{2^{12}-1} \times \frac{1}{LAC(photons\ /\ str\ /\ nC) \times \Omega} \times \frac{L}{C_{calib}\left(\frac{1}{4}\int (QE_R \times NLES\ d\lambda) + \frac{1}{2}\int (QE_G \times NLES\ d\lambda) + \frac{1}{4}\int (QE_B \times NLES\ d\lambda)\right)}$$

Eq. E-14

Eliminating L in this equation using the first equation in Eq. E-7 (or Eq. E-11), and replacing Ω using Eq. E-13 yields the charge as a function of the Lanex and CCD parameters:

$$q_{Lanex}(nC) = \frac{CCD\ saturation\ capacity}{2^{12}-1} \times \frac{1}{LAC(photons\ /\ str\ /\ nC) \times \frac{\pi}{4} \times \left(\frac{M}{(1+M)^3} \times \frac{1}{f\#}\right)^2} \times \frac{\frac{1/\gamma + 1 + \alpha}{\beta - \alpha}(\beta G - B)}{C_{calib}\left(\frac{1}{4}\int (QE_R \times NLES\ d\lambda) + \frac{1}{2}\int (QE_G \times NLES\ d\lambda) + \frac{1}{4}\int (QE_B \times NLES\ d\lambda)\right)}$$

Eq. E-15

Using the scA1600-14fc CCD saturation capacity of 9000 electrons, Lanex Absolute Calibration of 6.95×10^{12} photons/sr/nC, magnification of M = 0.107402 (0.1" = 62 pixels, CCD pixel size = 4.4 um), f-number of 2, and replacing $\frac{1/\gamma+1+\alpha}{\beta-\alpha}(\beta G - B)$ using first equation in Eq. E-7, and $\int (QE_i \times NLES\ d\lambda)$ from Table E-1, we get:

$$q_{Lanex\ pixel}(nC) = \frac{9000/4095}{6.95\times10^{12} \times \frac{\pi}{4} \times \left(\frac{0.107402}{(1+0.107402)^3} \times \frac{1}{2}\right)^2} \times \frac{-0.2054\ B + 1.2008\ G}{C_{calib}\left(\frac{1}{4}\times0.063365 + \frac{1}{2}\times0.851315 + \frac{1}{4}\times0.089263\right)}$$

$$\boxed{q_{Lanex\ pixel}(nC) = \frac{5.5518\times10^{-10}}{C_{calib}}(-0.2054\ B + 1.2008\ G)}$$

Eq. E-16

Eq. E-16 gives the charge, in nC, measured by each pixel on the Lanex image as a function of the corresponding pixel value on the B and G channels of the CCD output in the case when all the CCD channels are included. (Note that B and G refer to the reconstructed images from the blue and green CCD channels with the impact of any ND filter to prevent CCD saturation already incorporated via multiplication by 10^{ND}.) C_{calib}, the conversion factor between relative and absolute QE curves, is determined in E.4.

Alternative Interpretation of the Relative Response Curves

If the Relative Response curves in Figure E-5 are interpreted at relative transmission curves of the CCD color filter array, $QE_{R,B,G}$ is then obtained as the product of the quantum efficiency curve of scA1600-14fm mono CCD (Figure E-6) and the relative response curves for the red, blue, and green filters used in the scA1600-14fc color CCD (Figure E-5). This is shown in Figure E-11. The overlap of $QE_{R,B,G}$ and the Lanex and scintillator emission spectra are shown in Figure E-12.

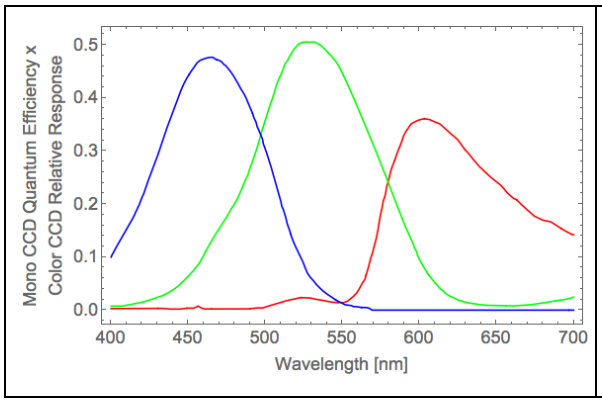

Figure E-11: $QE_{R,G,B}$ or the relative quantum efficiency for the R, G, and B pixels of the Basler scA1600-14fc color CCD (product of plots in **Figure E-6** and **Figure E-5**).

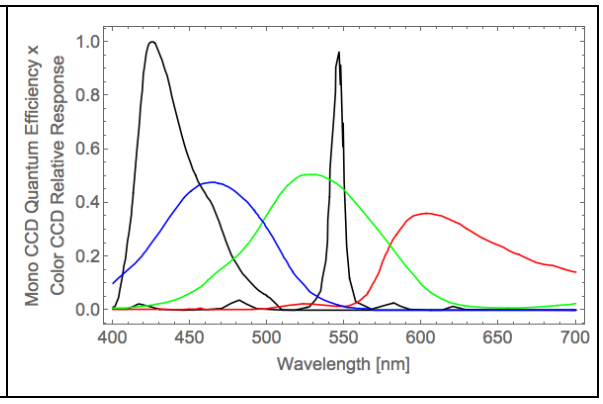

Figure E-12: Overlap of $QE_{R,G,B}$ (**Figure E-11**) and the emission spectra for the Lanex and scintillator (**Figure E-3**).

The integrands in Eq. E-3 are shown in Figure E-13, for the Lanex screen, and in Figure E-14, for the plastic scintillator. Compared to the curves in Figure E-9 and Figure E-10, the CCD response drops by ~50%.

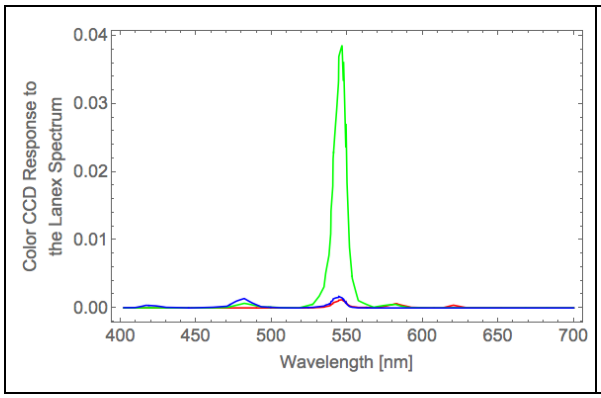

Figure E-13: The product $QE_{R,G,B}$ × NLES) of $QE_{R,G,B}$ (**Figure E-11**) and the Lanex emission spectrum (**Figure E-3**, left).

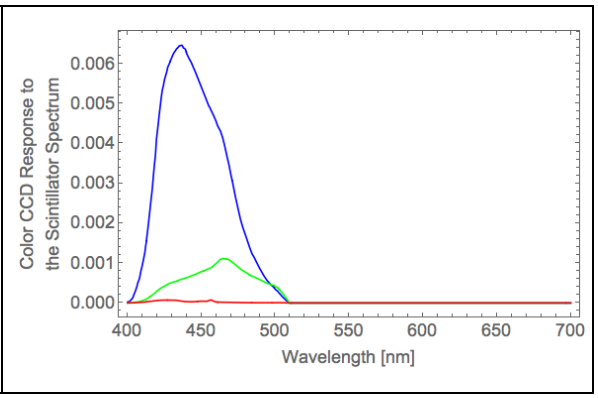

Figure E-14: The product $QE_{R,G,B}$ × NSES of $QE_{R,G,B}$ (**Figure E-11**) and the scintillator emission spectrum (**Figure E-3**, right).

The areas under the curves in Figure E-13 and Figure E-14, representing the 6 integrals in Eq. E-3, were numerically calculated as follows:

$\int (QE_R \times NLES)\, d\lambda = 0.027034$	$\int (QE_G \times NLES)\, d\lambda = 0.425809$	$\int (QE_B \times NLES)\, d\lambda = 0.047245$
$\int (QE_R \times NSES)\, d\lambda = 0.003054$	$\int (QE_G \times NSES)\, d\lambda = 0.061214$	$\int (QE_B \times NSES)\, d\lambda = 0.336366$

Table E-2: Overlap integrals for the relative QE of the RGB channels of the color CCD, **Figure E-11**, and the normalized emission spectra for the Lanex (NLES) and the plastic scintillator (NSES), **Figure E-3**.

Using the values in Table E-2, the parameters α, β and γ may then be determined:

$$\alpha = \int (QE_B \times NLES)\, d\lambda \Big/ \int (QE_G \times NLES)\, d\lambda = \frac{0.047245}{0.425809} = 0.10485$$

$$\beta = \int (QE_B \times NSES)\, d\lambda \Big/ \int (QE_G \times NSES)\, d\lambda = \frac{0.336366}{0.061213} = 5.84512 \qquad \textbf{Eq. E-17}$$

$$\gamma = \int (QE_G \times NLES)\, d\lambda \Big/ \int (QE_R \times NLES)\, d\lambda = \frac{0.425809}{0.027034} = 13.4351$$

Plugging in the numerical values from Eq. E-17 into Eq. E-5, we get:

$L_R = -0.0118\, B + 0.0648\, G$	$S_R = 0.0118\, (B - 5.4950\, G + 84.8035\, R)$
$L_G = -0.1857\, B + 1.0206\, G$	$S_G = 0.1857\, (B - 0.1110\, G)$
$L_B = -0.0206\, B + 0.1132\, G$	$S_B = 1.0206\, B - 0.1132\, G$

Eq. E-18

The Lanex and scintillator signals may therefore be constructed by combining the interpolated R, G, and B components of the color CCD output:

$$L = L_R + L_G + L_B = \frac{1/\gamma + 1 + \alpha}{\beta - \alpha}(\beta G - B) = -0.2181\, B + 1.1986\, G$$
$$S = S_R + S_G + S_B = \frac{1/\gamma(B - \beta G) + (1 + \beta)(B - \alpha G)}{\beta - \alpha} + R = 1.2181\, B - 0.1986\, G + R \quad \textbf{Eq. E-19}$$

The overlap between the response function for the R filter and the emission spectrum for both Lanex and plastic scintillator is small ($\int (QE_R \times NLES)\, d\lambda = 0.027034, \int (QE_R \times NSES)\, d\lambda = 0.003054$), the equations involving the R color in Eq. E-5 may be ignored, yielding the system in Eq. E-8 and the solution in Eq. E-9; plugging in for α and β from Eq. E-17, reconstructs the Lanex and scintillator signals in terms of the interpolated B and G components of the color CCD output:

$$\begin{cases} \mathrm{L}_G = -0.1857\,\mathrm{B} + 1.0206\,\mathrm{G} \\ \mathrm{L}_B = -0.0206\,\mathrm{B} + 0.1132\,\mathrm{G} \end{cases} \quad \begin{cases} \mathrm{S}_G = 0.1857\,\mathrm{B} - 0.0206\,\mathrm{G} \\ \mathrm{S}_B = 1.0206\,\mathrm{B} - 0.1132\,\mathrm{G} \end{cases} \quad \textbf{Eq. E-20}$$

Having ignored the negligible R component of the CCD output, the Lanex and scintillator signals are then constructed by combining the interpolated G and B components of the color CCD output:

$$L = L_G + L_B = \frac{1 + \alpha}{\beta - \alpha}(\beta G - B) = -0.2063\, B + 1.1338\, G$$
$$S = S_G + S_B = \frac{1 + \beta}{\beta - \alpha}(B - \alpha G) = 1.2063\, B - 0.1338\, G \quad \textbf{Eq. E-21}$$

Plugging in from Table E-2 and Eq. E-19 into Eq. E-15 yields

$$q_{Lanex\ pixel}(nC) = \frac{1.1124 \times 10^{-9}}{C_{calib}}(-0.2181\, B + 1.1986\, G) \quad \textbf{Eq. E-22}$$

C_{calib}, the conversion factor between relative and absolute QE curves, is determined in E.4.

E.4 Calibration of the Color CCD

Charge calculation using the Lanex scintillating screen and a color CCD requires the knowledge of the absolute quantum efficiency for the 3 CCD channels. The information that was available for the scA1600-14fc CCD consisted of Relative Response curves (Figure E-5) for the CCD channels; these were interpreted as the relative QE curves for the CCD channels; this interpretation led to the Lanex charge per CCD image pixel, Eq. E-16, as a function of the blue and green channel pixels of the CCD image, and the relative to absolute conversion factor C_{calib}. (The alternative interpretation, that the Relative Response curves represented the relative transmission curves of the color CCD

filter array, produced the formula in Eq. E-22.) To use the Lanex screen as a diagnostic for the measurement of charge, the relative to absolute conversion parameter C_{calib} needs to be determined. This was done by a comparison of the same charge calculated using the MS IP and the Lanex screen as charge detectors.

The Lanex electron measurements from two TPW system shots from the 3rd round of the experiments (LWFA 3.0) were selected for this comparison. The selection criteria were:

1. Absence of saturation in the raw CCD output
2. Large S/N ratio
3. Presence of fiducial shadows in the both the MS IP and Lanex signal

Lanex charge: 4.23 pC	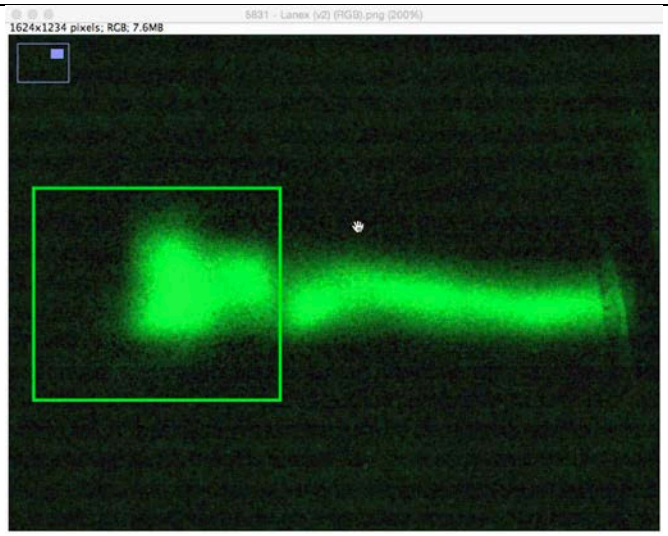
MS IP charge: 7.34 pC (4.40 pC)	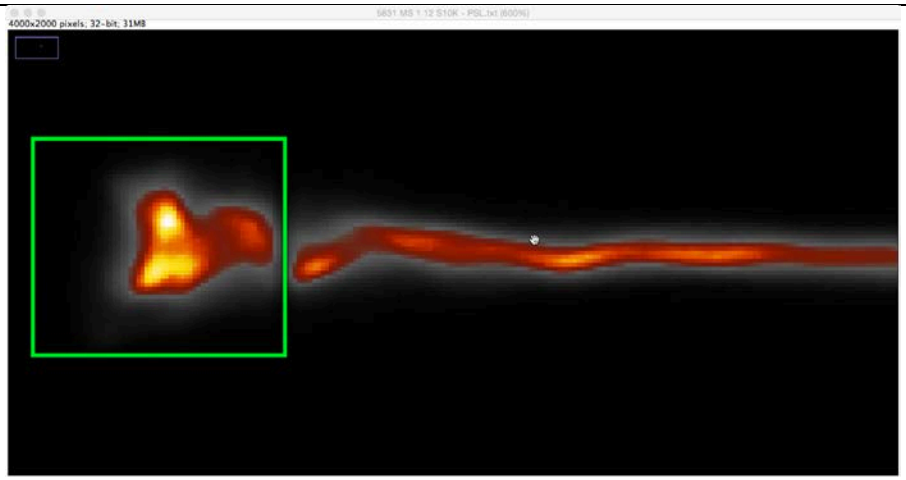
$C_{calib} = 4.23/7.34 = 0.576\ (0.960)$	

Figure E-15: Determination of the relative to absolute conversion factor for the Relative Response curves in **Figure E-5** by a comparison of electron charge (in the high-energy tip of the beam) using the Lanex screen and the MS IP

measurements for shot 5831 (LWFA 3.0). Parenthesis values refer to alternative assumption of constant imaging plate sensitivity to electrons.

The presence of saturated pixels in the CCD output leads to a downward bias in the pixel value for the reconstructed CCD channels; this bias propagates to the final charge calculation, rendering is incorrect. The presence of fiducial shadows is required to ensure that a comparison of detected charge from two diagnostics (Lanex and MS IP) is based on an equivalent dose of incident electrons. Shots 5831 and 5839 (LWFA 3.0) yielded Lanex measurements that were found to satisfy these criteria. In Figure E-15 and Figure E-16, a portion of the electron streak measured for these shots are shown. In each figure, the top panel display the Lanex measurement and the bottom panel the MS IP

Lanex charge: 10.38 pC	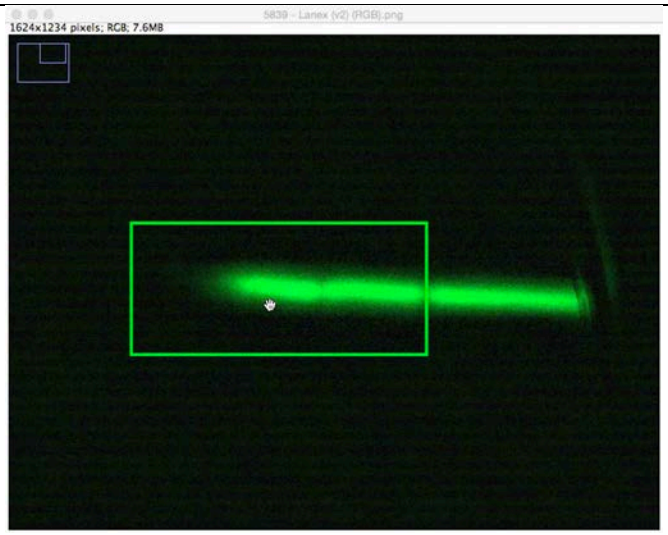
MS IP charge: 15.32 pC (9.24 pC)	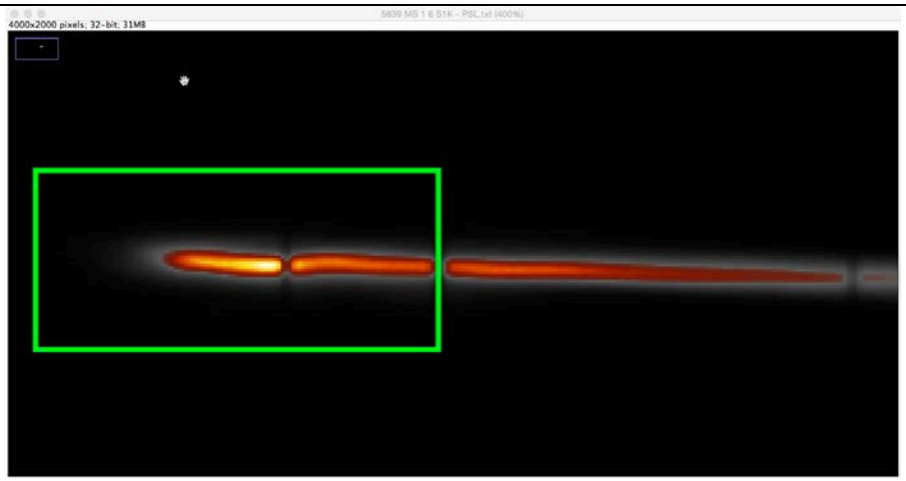
$C_{calib} = 10.38/15.32 = 0.677\ (1.123)$	

Figure E-16: Determination of the relative to absolute conversion factor for the Relative Response curves in **Figure E-5** by a comparison of electron charge (in the high-energy tip of the beam) using the Lanex screen and the MS IP

measurements for shot 5839 (LWFA 3.0). Parenthesis values refer to alternative assumption of constant imaging plate sensitivity to electrons.

measurement. A rectangle having commensurate size for the two images was created to indicate the region of interest. Given the 100 μm resolution of the MS IP, and the 4.4 μm resolution of the scA1600-14fc CCD, and the 0.1074 magnification factor of CCD focusing lens, the rectangular selection was first created on the MS IP, then increased in size by a factor of 2.441 (100 μm / 4.4 μm × magnification) and restored on the Lanex image. Care was taken to position the rectangular selection such that commensurate regions of the electron charge were contained inside the selection on the respective images. The selected shots had a noise to signal ratio of ~10%; this is better than the typical 30-50% level seen in several other shots. Prior to conversion of the reconstructed CCD channel output to an image representation of the Lanex charge according to Eq. E-16, the reconstructed CCD channel output images (R, G, and B) were smoothed and despeckled in ImageJ by removing the bright outliers (*Process ➢ Noise ➢ Remove Outliers...*) using a radius of 5 pixels and a threshold of 50. Following this, the background was subtracted from each of the reconstructed Bayer pattern images (*Process ➢ Noise ➢ Remove Outliers...*) by applying a rolling ball background removal algorithm with radius of 50 pixels and smoothing enabled. (Note that, by default, this technique preprocesses the image by applying a smoothing algorithm prior to the removal of background. This smoothing can lead to the creation of negative pixels in the background-removed image; however the impact is minimal for the main electron signal region. Disabling of smoothing, on the other hand, can lead to a reduction in the amount of background removed and an upward bias in the calculated charge.) The value obtained for the relative to absolute conversion factor (to be applied to Figure E-5 to obtain the absolute QE of the scA1600-14fc CCD) was found to be in the range 0.58–0.68, or $C_{calib} = 0.63 \pm 0.05$. This value is higher than the absolute QE of the mono CCD at ~620 nm of ~33% (Figure E-6). Note that because the peak transmission of the Relative Response for the red channel occurs at 620 nm (Figure E-5) and the absolute transmission for a typical red dichroic filter (a reasonable proxy for the red part of the color filter array used to create the Bayer pattern of the color CCD), is ~90%, it is expected that the combination of the mono CCD quantum efficiency at 620 nm and the transmission rate of

the red color filter at the same wavelength would provide an upper limit for the absolute QE of the color CCD at 620 nm, i.e., C_{calib} is expected to be less than the product 33% × 90% ~ 30%. The measured value of $C_{calib} = 0.63 \pm 0.05$ obtained by using the MS IP sensitivity to electrons using a fit to available calibration data, and assuming a reduction in sensitivity with energy, is higher than this expected threshold. However, note that using an imaging plate charge calculated under the assumption of constant sensitivity of the MS IP to electrons (in parenthesis in Figure E-15 and Figure E-16), yields even larger values for C_{calib} which approach or exceeds the 100% threshold. This suggests that the reduction in the MS IP sensitivity to electron charge with increasing electron energy could be even steeper than provided by the fit. (The high-energy region of the fit relied on one data point at 1 GeV having large error bars. See Figure D-1 and Table D-3.) Therefore, the comparison of the Lanex charge to the MS IP charge, in addition to providing a factor for converting the scA1600-14fc Relative Response curve, Figure E-5, to an absolute one, also supports the assumption of reduced imaging plate sensitivity at higher energies. Figure E-17 shows the absolute QE of the scA1600-14fc color CCD determined by applying $C_{calib} = 0.63$ to the Relative Response curves in Figure E-5.

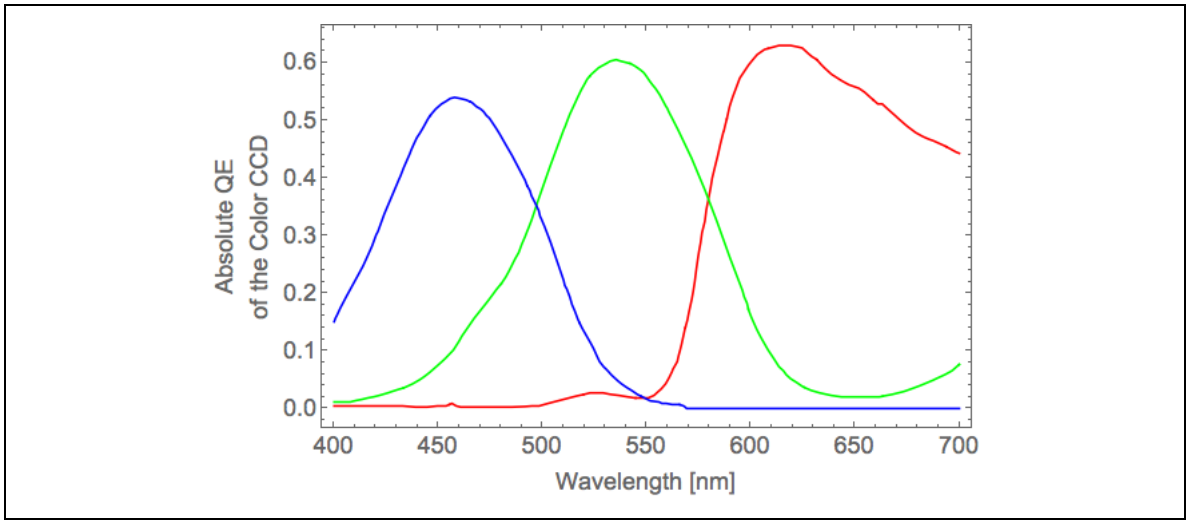

Figure E-17: Absolute response of the scA1600-14fc color CCD calculated by applying $C_{calib} = 0.63$ to **Figure E-5** (assumes Relative Response in **Figure E-5** represents the relative QE of the color CCD channels).

To end this chapter, it is noteworthy that the alternative interpretation of the Relative Response curves in Figure E-5 (as relative transmission curves) produces a relative to absolute conversion factor of $C_{calib} = 1.04 \pm 0.08$. When applied to the peak of the red

curve, this produces a red filter transmission of 104% at 620 nm. This is higher than the expected peak for a red filter (~90% for a red dichroic filter), making the relative transmission curve interpretation of the Relative Response curves less plausible. For completeness, however, the absolute QE under the alternative assumption (the product of $C_{calib} = 1.04$ and Figure E-11) is produced in Figure E-18.

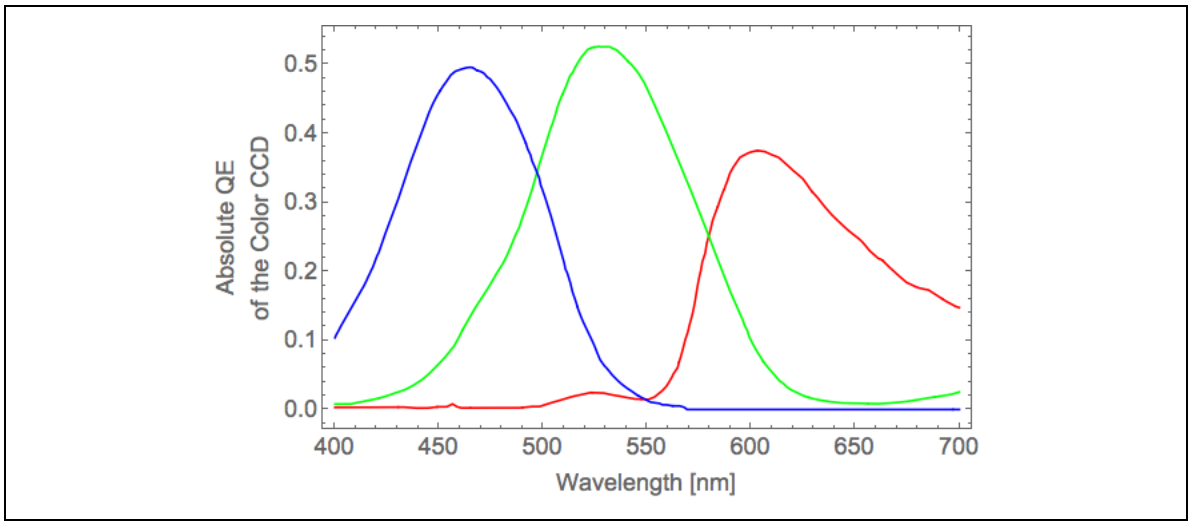

Figure E-18: Absolute response of the scA1600-14fc color CCD calculated by applying C_{calib} = 1.04 to **Figure E-11** (under the unlikely scenario that the Relative Response curves in **Figure E-5** represent the relative transmission of the color filters).

Appendix F. Error Calculations

F.1 Error in the X-ray Spectrum

The error in the x-ray spectrum has 3 components, two of which are statistical, and one is systematic. Each is calculated separately; then they are combined using the sum of the squares rule.

Denoting as $(\Delta N/\Delta E)_k$ the number of photons per unit energy (or per unit bandwidth, see Eq. 5.5 and Eq. 5.9) corresponding to E_k, we can write:

$$(\Delta N/\Delta E)_k = \frac{(\Delta\, TS)_k}{\int ResSen(E)dE} \qquad \textbf{Eq. F-1}$$

$(\Delta\, TS)_k$ is the differential transmitted signal through the x-ray filters *k* and *k+1* at the detector. For an imaging plate

$$(\Delta\, TS)_k = (\Delta\, PSL_{scan\,1})_k = (\Delta\, PSL_{scan\,n})_k \times (Saturation\ Factor)$$

n is the scan at which the x-ray signal is unsaturated, and the *Saturation Factor* (hereafter denoted *Saturation*) is the factor (≥ 1) by which the imaging plate signal is reduced after n consecutive scans (see C.2). Then Eq. F-1 becomes

$$\left(\frac{\Delta N}{\Delta E}\right)_k = \frac{PSL_k - PSL_{k+1}}{\int ResSen(E)dE} \times Saturation = \frac{A}{B} \times C \qquad \textbf{Eq. F-2}$$

where PSL_k (PSL_{k+1}) is average value over the set of pixels that result from the intersection of an iso-intensity contour and filter *k* (*k+1*); $A = PSL_k - PSL_{k+1}$, $B = \int ResSen(E)dE$, and $C = Saturation$. Applying the δ operator to Eq. F-2 yields

$$\delta\left(\frac{\Delta N}{\Delta E}\right)_k = \delta\left(\frac{A}{B}\right) \times C + \frac{A}{B} \times \delta C = \left(\frac{\delta A}{B} - \frac{A\delta B}{B^2}\right) \times C + \frac{A}{B} \times \delta C \qquad \textbf{Eq. F-3}$$

where the general rule for derivatives $\delta\left(\frac{A}{B}\right) = \frac{B\delta A - A\delta B}{B^2} = \frac{\delta A}{B} - \frac{A\delta B}{B^2}$ has been used. The variations $\delta A = \delta(PSL_k - PSL_{k+1})$ and $\delta C = \delta Saturation$ are stochastic in nature, in the first case deriving from the statistical variation of the imaging plate signal on an iso-intensity contour, and in the second case from the distribution of the saturation factors (see C.2). The variations $\delta B = \delta(\int ResSen(E)dE)$, on the other hand, is systematic in nature, deriving from uncertainty in response functions. The two types of statistical errors are uncorrelated with each other and with the systematic error. The square of the error (or the variance) is therefore obtained using the sum of variances:

$$\left(\delta\left(\frac{\Delta N}{\Delta E}\right)_k\right)^2 = \left(\delta\left(\frac{\Delta N}{\Delta E}\right)_{k,stat,1}\right)^2 + \left(\delta\left(\frac{\Delta N}{\Delta E}\right)_{k,stat,2}\right)^2 + \left(\delta\left(\frac{\Delta N}{\Delta E}\right)_{k,syst}\right)^2 \quad \textbf{Eq. F-4}$$

where the terms on the right-hand side are, using notation in Eq. F-2

$$\delta\left(\frac{\Delta N}{\Delta E}\right)_{k,stat,1} = \left(\frac{\delta A}{B}\right) \times C = \frac{\delta(PSL_k - PSL_{k+1})}{\int ResSen(E)dE} \times Saturation \quad \textbf{Eq. F-5}$$

$$\delta\left(\frac{\Delta N}{\Delta E}\right)_{k,stat,2} = \frac{A}{B} \times \delta C = \frac{PSL_k - PSL_{k+1}}{\int ResSen(E)dE} \times \delta Saturation \quad \textbf{Eq. F-6}$$

$$\delta\left(\frac{\Delta N}{\Delta E}\right)_{k,syst} = \left(\frac{A\delta B}{B^2}\right) \times C = \frac{(PSL_k - PSL_{k+1})\ \delta(\int ResSen(E)dE)}{(\int ResSen(E)dE)^2} \times Saturation \quad \textbf{Eq. F-7}$$

The term $\delta(PSL_k - PSL_{k+1}) = \frac{\delta PSL_k}{\sqrt{n_k}} + \frac{\delta PSL_{k+1}}{\sqrt{n_{k+1}}}$ in Eq. F-5 represents the statistical error in the imaging plate signal for filters k and $k+1$. For measurements performed on iso-intensity contours, n_k and δPSL_k represent the number of pixels and the standard deviation of their values, respectively, on the intersection of the contour and filter k. $\delta PSL_k/\sqrt{n_k}$ represents the standard error of the mean for the n_k pixels. Note the use of $\delta PSL_k/\sqrt{n_k}$ in place of δPSL_k. Under very general conditions [69], functions of sample moments (in this case $(\Delta N/\Delta E)_k$ is a function of PSL_k and PSL_{k+1}, both of which are averages) are asymptotically normal, and the variance of such functions is given by the appropriate propagation of error formulas using the sample standard error of the mean.

The term $\delta Saturation$ in Eq. F-6 represents the statistical error in the calculation of the imaging plate saturation factor and is calculated using the standard deviation of the saturation ratios for scans 1 and n, where scan n is the unsaturated scan. ($Saturation = 1$ and $\delta Saturation = 0$ when scan 1 is the unsaturated scan.)

The term $\delta(\int ResSen(E)dE)$ in Eq. F-7 represent the systematic error in the calculation of the residual sensitivity for filters k and $k+1$ and largely derives from the existence of non-vanishing sensitivity in the tail region outside the K-edges (see Figure 5.15 and Table 5-3), and the uncertainty in the thickness specification for the x-ray filters. The uncertainty in the mass attenuations and mass densities used for the filters, and the imaging plate response function for x-rays play a smaller role. $\delta(\int ResSen(E)dE) =$ 10% has been used. Using Eq. F-5, Eq. F-6, and Eq. F-7 in Eq. F-4 yields

$$\delta\left(\frac{\Delta N}{\Delta E}\right) = \sqrt{\left(\frac{\delta PSL_k/\sqrt{n_k} + \delta PSL_{k+1}/\sqrt{n_{k+1}}}{\int ResSen(E)dE} \times Saturation\right)^2 + \left(\frac{PSL_k - PSL_{k+1}}{\int ResSen(E)dE} \times \delta Saturation\right)^2 + \left(\frac{(PSL_k - PSL_{k+1})\,\delta(\int ResSen(E)dE)}{(\int ResSen(E)dE)^2} \times Saturation\right)^2} \quad \textbf{Eq. F-8}$$

F.2 Error in the Calculation of the X-ray Center

The magnetic spectrometer formulas derived in Chapter 4 and summarized in Table 4-1 use as a parameter in the denominator the location of the undeflected electrons on the detector, denoted as x_∞. The center of the betatron x-ray on the same detector has been chosen as a proxy for x_∞. As discussed in Appendix G.1, the center of the x-ray spot may be found either geometrically or using the coordinate of the pixel with the maximum PSL. To determine the error introduced into the energy calculations when these methods produce different results, propagation of error may be applied to formulas in Table 4-1. For example, the formula for the electron energy as a function of its deflection in the magnetic spectrometer, measured on the high-energy (far), high-sensitivity (MS) imaging plate is

$$E_{e,HEMS}[GeV] \cong \frac{C_{HE,wakefield}}{x_{HEMS}\,[pixels] - x_{\infty,MS}[pixel]} \quad \textbf{Eq. F-9}$$

The constant term in the numerator, $C_{HE,wakefield}$, incorporates the parameters of the magnetic spectrometer (see Eq. 4.11) and has been calculated for each of the 4 experimental rounds in Eq. 4.12. An uncertainty $\delta x_{\infty,MS}[pixel]$ in the value of $x_{\infty,MS}[pixel]$ produces the following change in the calculated electron energy:

$$\delta E_{e,HEMS}[GeV] \cong \frac{-C_{HE,wakefield}\,\delta x_{\infty,MS}[pixel]}{\left(x_{HEMS}\,[pixels] - x_{\infty,MS}[pixel]\right)^2} \quad \textbf{Eq. F-10}$$

Using Eq. F-9 in Eq. F-10 gives

$$\delta E_{e,HEMS}[GeV] = \frac{\left(E_{e,HEMS}[GeV]\right)^2}{C_{HE,wakefield}} \times \delta x_{\infty,MS}[pixel] \quad \textbf{Eq. F-11}$$

For example, at 2 GeV, a 1-pixel uncertainty in the location of undeflected electrons on the imaging plate, i.e., $\delta x_{\infty,MS} = 1$, produces an uncertainty in the electron energy of

$\delta E_{e,HEMS}[GeV] = \frac{4 \times 1\,[pixels]}{C_{HE,wakefield}}$. For the 4th experimental round, $C_{HE,4.0}$ = 561.326 GeV per pixel, therefore $\delta E_{e,HEMS}[GeV]$ = 4/561.326 ~ 0.007 or 7 MeV. Therefore the magnetic spectrometer error due to uncertainty in the position of undeflected electrons on the detector is 0.356% per pixel at 2 GeV. A conservative estimate of 5 pixels for $\delta x_{\infty,MS}$ therefore produces an error of ~1.8% at 2 GeV.

Note that he formulas summarized in Table 4-1 assumed a vanishingly small launch angle for the electron. Comparison with electron energies calculated using the more accurate fiducial shadow triangulation technique, which does not make this assumption, indicate an additional 5-10% error in the electron energy as the result of this assumption.

Appendix G. Using ImageJ to Process Imaging Plate Data

G.1 Determination of the Betatron X-ray Center

Accelerated electrons deflect in the magnetic spectrometer. The deflection, as measured on the IP, is with respect to the direction of the electrons before entering the magnetic field. This point on the IP, i.e., the place where undeflected electrons would arrive, was denoted x_∞ in 4.4. One way to find x_∞ is by triangulation of fiducial shadows to determine the electron energy corresponding to each shadow position (3.4). This would yield a set of energy vs. pixel position pairs, one pair for each fiducial. Fitting this set of data to equations in Table 4-1 would yield x_∞.

A less accurate, but also less cumbersome, method is to use the coordinates of the betatron x-ray center, either center of mass or the peak intensity pixel, as a proxy for the position of undeflected electrons on the IP. The center of mass of the betatron x-ray may be found geometrically in ImageJ in one of two ways using the Sampling Image (Table C-1). One way is to set the color map to *Smart* (this color map is particularly suitable for determining intensity boundaries), use the Oval tool to draw an oval around the x-ray signal, tweak the oval to completely encompass the x-ray, then use the *Measurements* tool, to find the x-ray center of mass, XM and YM. XM can then be used as proxy for x_∞. (ImageJ tip: adding the selection to the ROI Manager creates a selection named *stackno-YM-XM*, i.e., the coordinate XM may be extracted from the selection name in the ROI Manager.) The other way is to threshold the image and then do the measurements to find XM and YM.

Finding x_∞ by looking for the geometric center of symmetry however has the drawback that it cannot be applied to x-ray profiles not exhibiting an oval symmetry. This was the case for a number of shots for which there is evidence for the existence of multiple x-ray sources, perhaps originating in two or more accelerating structures. These are the so-called "double bubble" shots. The approach adopted in this dissertation combines relative accuracy with ease of finding x_∞ and can be applied to shots not having a well-defined center of symmetry. It uses the position on the x-ray detector having the highest intensity, in the absence of filters or other attenuating objects, as a proxy for the location of

undeflected electrons. This highest intensity pixel position is expected to correspond with the axis of betatron oscillations for the electrons. Provided that the electron launch angle as it exits the accelerating structure is not too large, the direction of the electrons prior to entering the magnetic spectrometer should therefore be close to the axis of the betatron oscillations. Due to the shadows created by the presence of x-ray filters (and perhaps fiducials) on the x-ray filter, the position of highest intensity pixel on the x-ray detector is often obscured. Several methods were investigated for determining the position of the highest intensity pixel on the x-ray detector. A comparison was made between the position of highest intensity pixel on 1) the X-ray Reconstruction Input Image, 2) the Reconstructed X-ray Image, and 3) the Sampling Image. It was found that the image types (1) and (3) may miss the true pixel position by more than 20 pixels. (This happens when the maximum intensity pixel position coincides with the center of an x-ray filter and is obscured by it.) The Reconstructed X-ray Image did capture the position of the true maximum intensity pixel with reasonable accuracy. This was verified using a shot for which x-ray filters had not been deployed, i.e., where the true maximum intensity pixel could be *a priori* accurately determined on the Unsaturated PSL Image for X-rays. Then circular filters were simulated on the image, the image reconstruction procedures followed, and the position of the maximum intensity pixel on the Reconstructed X-ray Image compared with that on the Unsaturated PSL Image for X-rays. The agreement for the X and Y coordinates between the two images was to within 2-3 pixels.

G.2 Sampling of data on iso-intensity contours

(Optional to do: programmatic aspects of sampling of filters on contours, decisions made in ImageJ scripts. Consider drawing of a flow chart for ImageJ scripts:

- *SampleDetectorOnMultiContours.ijm: see comments at the beginning of the file;*
    - *creates iso-intensity contours, see DiscoverRossPairs.ijm and automated discovery of Ross pairs on contour*
    - *then calls SampleDetectorOnContour.ijm, e.g., how data is selected and averaged when walking on contour, i.e., sampling methods, how NaNs are handled, etc. Discuss this algorithm: there are 2 concentric circles and data is sampled from inside the inner circle. Data from outer circle is not used. Data*

external to both circles for all filters is considered profile pixels and averaged and compared to pixel nominal value.

- *then calls GenerateSpectrumFromRossFilterData.ijm: how data is cleaned (use of safety margins, outlier removal, variance reduction, etc.), statistics are calculated on contour (GetDetectorStatisticsOnContour.ijm), handling of boundary conditions for extrapolation of energy:*

  1) at E=0, spectrum should vanish on all contours;

  2) at some cut-off energy, the spectrum should vanish on all contours; chose E=100 keV.

  3) at all energies, the spectrum should vanish on 0% contour (90-degree angle)

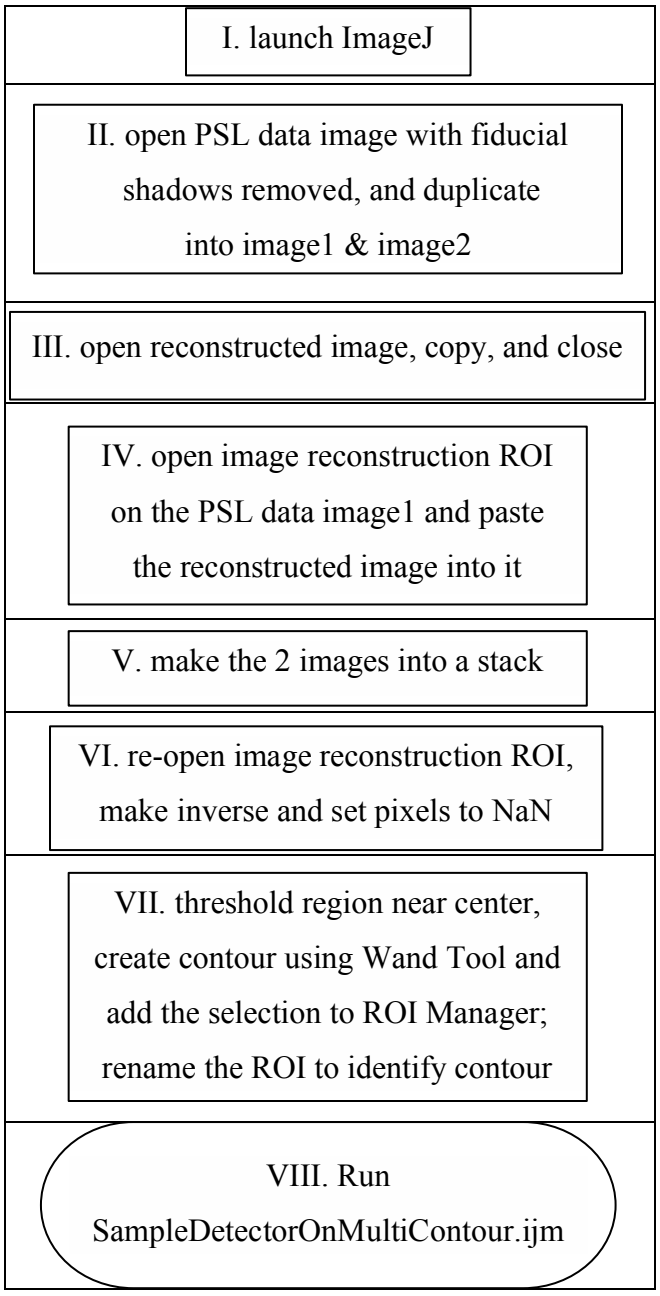
I. launch ImageJ
II. open PSL data image with fiducial shadows removed, and duplicate into image1 & image2
III. open reconstructed image, copy, and close
IV. open image reconstruction ROI on the PSL data image1 and paste the reconstructed image into it
V. make the 2 images into a stack
VI. re-open image reconstruction ROI, make inverse and set pixels to NaN
VII. threshold region near center, create contour using Wand Tool and add the selection to ROI Manager; rename the ROI to identify contour
VIII. Run SampleDetectorOnMultiContour.ijm

Appendix H. Plasma Densities

In this chapter, plasma densities for shots from the 4 rounds of experiments discussed in this dissertation are presented.

- **Round 1 (LWFA 1.5)**

Shot	$n_e[10^{17}\ cm^{-3}]$	Shot	$n_e[10^{17}\ cm^{-3}]$	Shot	$n_e[10^{17}\ cm^{-3}]$	Shot	$n_e[10^{17}\ cm^{-3}]$	Shot	$n_e[10^{17}\ cm^{-3}]$
2875	5.00	**2910**	4.9	**2935**	5.5	**2970**	5.3	**3033**	6.2
2882	3.70	**2912**	5.0	**2937**	4.2	**2976**	4.25	**3035**	4.5
2883	4.80	**2916**	4.7	**2942**	6.6	**2978**	4.20	**3037**	4.5
2887	5.50	**2919**	5.2	**2944**	5.6	**2991**	4.20	**3041**	3.50
2893	0.00	**2921**	6.2	**2946**	6.4	**2993**	6.60	**3043**	4.40
2894	6.00	**2923**	4.8	**2948**	4.7	**2996**	5.75	**3046**	6.65
2899	5.60	**2925**	8.5	**2951**	3.7	**3009**	5.85	**3048**	6
2900	4.30	**2931**	5.5	**2966**	3.0	**3011**	5.32	**3051**	6.45
2908	4.20	**2933**	3.3	**2969**	3.6	**3024**	4.88	**3053**	4.30

Table H-1: Plasma densities for shots from LWFA 1.5 [Courtesy of Rafal Zgadzaj]

- **Round 2 (LWFA 2.0)**

Shot	$n_e[10^{17}\ cm^{-3}]$	Shot	$n_e[10^{17}\ cm^{-3}]$	Shot	$n_e[10^{17}\ cm^{-3}]$	Shot	$n_e[10^{17}\ cm^{-3}]$
3655	5.7	**3725**	4.90	**3732**	2.38	**3748**	4.21
3713	4.76	**3728**	6.41	**3734**	2.65	**3750**	3.44
3723	5.08	**3730**	5.66	**3736**	1.72	**3752**	2.09

Table H-2: Plasma densities for selected shots from LWFA 2.0

- **Round 3 (LWFA 3.0)**

Shot	$n_e[10^{17}\ cm^{-3}]$	Shot	$n_e[10^{17}\ cm^{-3}]$	Shot	$n_e[10^{17}\ cm^{-3}]$	Shot	$n_e[10^{17}\ cm^{-3}]$	Shot	$n_e[10^{17}\ cm^{-3}]$
5472	4.174	**5528**	5.635	**5597**	4.625	**5718**	4.728	**5809**	4.838
5478	4.272	**5530**	4.273	**5599**	4.527	**5722**	4.524	**5812**	5.496
5481	3.945	**5532**	4.336	**5601**	4.352	**5724**	4.441	**5821**	5.381
5483	4.043	**5535**	2.374	**5603**	6.04	**5728**	4.132	**5824**	5.249
5485	3.172	**5543**	4.285	**5605**	4.622	**5735**	5.238	**5831**	4.915
5491	2.291	**5546**	4.088	**5623**	4.064	**5751**	4.865	**5835**	4.016
5493	2.791	**5548**	4.592	**5625**	4.862	**5753**	4.905	**5839**	5.408
5495	3.715	**5551**	4.256	**5629**	4.664	**5762**	5.046	**5841**	4.653
5498	5.049	**5554**	4.191	**5632**	4.948	**5764**	5.359	**5845**	4.289
5504	4.995	**5557**	4.719	**5636**	5.646	**5766**	5.283	**5847**	5.222
5506	5.645	**5559**	4.466	**5642**	4.862	**5769**	5.244	**5858**	4.368
5508	4.79	**5563**	4.012	**5644**	4.885	**5781**	6.225	**5860**	5.332
5510	5.914	**5566**	4.558	**5646**	4.84	**5783**	6.099	**5862**	6.259

5514	4.73	**5568**	5.075	**5671**	4.955	**5785**	5.909	**5866**	6.924
5516	4.512	**5573**	4.905	**5673**	5.085	**5787**	6.083	**5868**	5.485
5518	4.466	**5575**	5.037	**5708**	4.418	**5789**	5.907	**5870**	6.306
5520	4.555	**5577**	4.995	**5710**	4.958	**5791**	5.672		
5522	3.274	**5580**	5.158	**5714**	4.329	**5804**	4.724		
5526	2.88	**5584**	5.109	**5716**	4.467	**5806**	4.724		

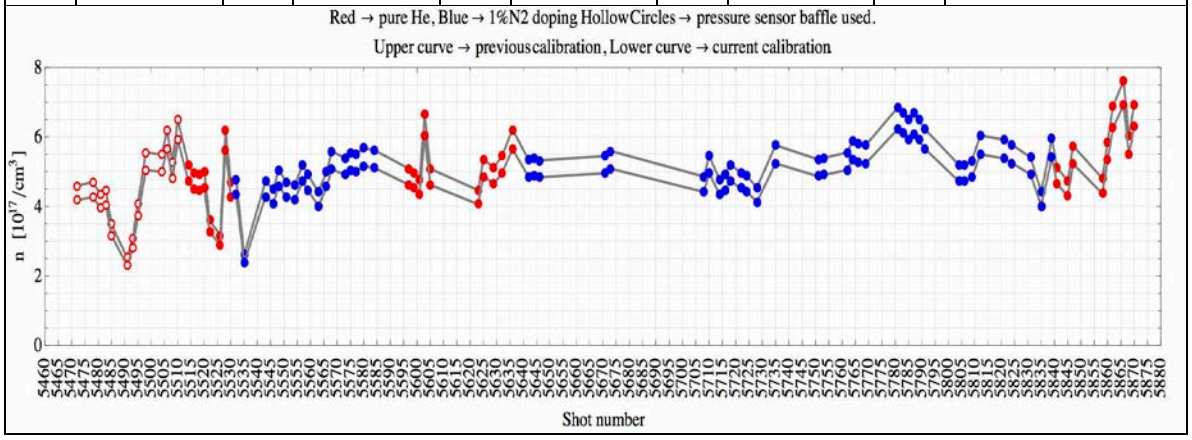

Table H-3: Plasma densities, and nitrogen doping levels, for shots from LWFA 3.0 [Courtesy of Rafal Zgadzaj]

- Round 4 (LWFA 4.0)

Shot	n_e[10^{17} cm^{-3}]	Shot	n_e[10^{17} cm^{-3}]	Shot	n_e[10^{17} cm^{-3}]	Shot	n_e[10^{17} cm^{-3}]	Shot	n_e[10^{17} cm^{-3}]
8165	4.34	**8226**	4.98	**8278**	NA	**8322**	4.07	**8369**	3.09
8169	6.06	**8228**	4.96	**8280**	4.44	**8324**	4.17	**8374**	3.07
8171	6.20	**8230**	4.86	**8282**	4.51	**8326**	4.10	**8376**	4.62
8173	5.90	**8235**	4.52	**8284**	4.34	**8333**	4.49	**8378**	4.47
8175	6.86	**8237**	4.57	**8288**	4.39	**8336**	4.28	**8380**	3.95
8182	4.54	**8239**	4.62	**8290**	4.01	**8338**	4.13	**8382**	3.87
8185	6.45	**8241**	3.99	**8292**	4.30	**8340**	4.57	**8384**	6.05
8187	6.39	**8243**	4.89	**8294**	4.23	**8342**	4.16	**8388**	5.62
8192	5.96	**8247**	4.04	**8296**	3.99	**8344**	3.62	**8390**	5.03
8194	5.97	**8249**	4.69	**8298**	3.35	**8347**	3.04	**8392**	4.77
8196	6.23	**8251**	4.89	**8302**	4.83	**8349**	3.38	**8394**	5.19
8203	5.48	**8253**	4.82	**8304**	4.47	**8351**	3.42	**8396**	5.02
8205	5.34	**8255**	4.93	**8306**	4.27	**8353**	3.48	**8398**	6.14
8207	4.85	**8263**	5.05	**8308**	4.12	**8355**	3.02	**8369**	3.09
8214	4.25	**8265**	5.02	**8310**	3.67	**8359**	2.59	**8374**	3.07
8216	NA	**8267**	4.50	**8312**	4.88	**8361**	2.50	**8376**	4.62
8218	4.72	**8269**	4.72	**8316**	4.32	**8363**	2.43	**8378**	4.47
8222	4.66	**8271**	4.23	**8318**	4.48	**8365**	3.11	**8380**	3.95

Table H-4: Plasma densities for shots from LWFA 4.0 [Courtesy of Rafal Zgadzaj]

Bibliography:

[1] T. Tajima and J. M. Dawson, “Laser Electron Accelerator,” *Phys. Rev. Lett.*, vol. 43, no. 4, p. 4, 1979.

[2] S. Mangles, C. D. Murphy, Z. Najmudin, A. Thomas, J. Collier, a. E. Dangor, E. J. Divall, P. S. Foster, J. G. Gallacher, C. J. Hooker, and others, “Monoenergetic beams of relativistic electrons from intense laser–plasma interactions,” *Nature*, vol. 431, no. 7008, pp. 535–538, 2004.

[3] C. G. R. Geddes, C. Toth, J. Van Tilborg, E. Esarey, C. B. Schroeder, D. L. Bruhwiler, C. Nieter, J. Cary, and W. P. Leemans, “High-quality electron beams from a laser wakefield accelerator using plasma-channel guiding,” *Nature*, vol. 431, no. 7008, pp. 538–541, 2004.

[4] J. Faure, Y. Glinec, A. Pukhov, S. Kiselev, S. Gordienko, E. Lefebvre, J.-P. Rousseau, F. Burgy, and V. Malka, “A laser–plasma accelerator producing monoenergetic electron beams,” *Nature*, vol. 431, no. 7008, pp. 541–544, 2004.

[5] C. E. Clayton, J. E. Ralph, F. Albert, R. Fonseca, S. H. Glenzer, C. Joshi, W. Lu, K. Marsh, S. Martins, W. B. Mori, A. Pak, F. Tsung, B. Pollock, J. S. Ross, L. O. Silva, and D. H. Froula, “Self-Guided Laser Wakefield Acceleration beyond 1 GeV Using Ionization-Induced Injection,” *Phys. Rev. Lett.*, vol. 105, no. 10, pp. 3–6, Sep. 2010.

[6] J. Liu, C. Xia, W. Wang, H. Lu, C. Wang, A. Deng, W. Li, H. Zhang, X. Liang, Y. Leng, X. Lu, C. Wang, J. Wang, K. Nakajima, R. Li, and Z. Xu, “All-Optical Cascaded Laser Wakefield Accelerator Using Ionization-Induced Injection,” *Phys. Rev. Lett.*, vol. 107, no. 3, pp. 2–5, Jul. 2011.

[7] W. P. Leemans, B. Nagler, A. Gonsalves, C. Tóth, K. Nakamura, C. G. R. Geddes, E. Esarey, C. B. Schroeder, and S. M. Hooker, “GeV electron beams from a centimetre-scale accelerator,” *Nat. Phys.*, vol. 2, no. 10, pp. 696–699, Sep. 2006.

[8] D. H. Froula, C. E. Clayton, T. Döppner, K. Marsh, C. P. J. Barty, L. Divol, R. Fonseca, S. H. Glenzer, C. Joshi, W. Lu, S. F. Martins, P. Michel, W. B. Mori, J. P. Palastro, B. Pollock, A. Pak, J. E. Ralph, J. S. Ross, C. W. Siders, L. O. Silva, and T. Wang, "Measurements of the Critical Power for Self-Injection of Electrons in a Laser Wakefield Accelerator," *Phys. Rev. Lett.*, vol. 103, no. 21, pp. 1–4, Nov. 2009.

[9] S. Kneip, S. Nagel, S. Martins, S. Mangles, C. Bellei, O. Chekhlov, R. J. Clarke, N. Delerue, E. J. Divall, G. Doucas, K. Ertel, F. Fiuza, R. Fonseca, P. S. Foster, S. Hawkes, C. Hooker, K. M. Krushelnick, W. Mori, C. Palmer, K. Ta Phuoc, P. Rajeev, J. Schreiber, M. Streeter, D. Urner, J. Vieira, L. Silva, and Z. Najmudin, "Near-GeV Acceleration of Electrons by a Nonlinear Plasma Wave Driven by a Self-Guided Laser Pulse," *Phys. Rev. Lett.*, vol. 103, no. 3, p. 035002, Jul. 2009.

[10] B. Pollock, C. E. Clayton, J. E. Ralph, F. Albert, a. Davidson, L. Divol, C. Filip, S. H. Glenzer, K. Herpoldt, W. Lu, K. Marsh, J. Meinecke, W. B. Mori, A. Pak, T. Rensink, J. S. Ross, J. Shaw, G. Tynan, C. Joshi, and D. H. Froula, "Demonstration of a Narrow Energy Spread, ~0.5 GeV Electron Beam from a Two-Stage Laser Wakefield Accelerator," *Phys. Rev. Lett.*, vol. 107, no. 4, pp. 1–4, Jul. 2011.

[11] R. Boyd, *Nonlinear Optics, Third Edition*. Burlington, MA: Academic Press, 2008.

[12] J. D. Jackson, *Classical electrodynamics*. New York: Wiley, 1999.

[13] A. Pukhov and J. Meyer-ter-Vehn, "Laser wake field acceleration: the highly non-linear broken-wave regime," *Appl. Phys. B Lasers Opt.*, vol. 74, no. 4–5, pp. 355–361, Apr. 2002.

[14] W. Lu, M. Tzoufras, C. Joshi, F. Tsung, W. B. Mori, J. Vieira, R. Fonseca, and L. O. Silva, "Generating multi-GeV electron bunches using single stage laser wakefield acceleration in a 3D nonlinear regime," *Phys. Rev. Spec. Top. - Accel. Beams*, vol. 10, no. 6, pp. 1–12, Jun. 2007.

[15] J. Rosenzweig, B. Breizman, T. Katsouleas, and J. Su, "Acceleration and focusing of electrons in two-dimensional nonlinear plasma wake fields," *Phys. Rev. A*, vol. 44, no. 10, pp. R6189–R6192, Nov. 1991.

[16] P. Gibbon, *Short Pulse Laser Interactions with Matter Part: An Introduction*. 2007.

[17] S. Kalmykov, S. A. Yi, V. Khudik, and G. Shvets, "Electron Self-Injection and Trapping into an Evolving Plasma Bubble," *Phys. Rev. Lett.*, vol. 103, no. 13, pp. 1–4, Sep. 2009.

[18] S. Kalmykov, S. A. Yi, a. Beck, a F. Lifschitz, X. Davoine, E. Lefebvre, V. Khudik, G. Shvets, and M. C. Downer, "Dark-current-free petawatt laser-driven wakefield accelerator based on electron self-injection into an expanding plasma bubble," *Plasma Phys. Control. Fusion*, vol. 53, no. 1, p. 014006, Jan. 2011.

[19] C. D. Decker, W. B. Mori, K.-C. Tzeng, and T. Katsouleas, "The evolution of ultra-intense, short-pulse lasers in underdense plasmas," *Phys. Plasmas*, vol. 3, no. 1996, p. 2047, 1996.

[20] S. Kalmykov, S. A. Yi, A. Beck, A. F. Lifschitz, X. Davoine, E. Lefebvre, A. Pukhov, V. Khudik, G. Shvets, S. Reed, P. Dong, X. Wang, D. Du, S. Bedacht, R. Zgadzaj, W. Henderson, A. Bernstein, G. Dyer, M. Martinez, E. Gaul, T. Ditmire, and M. C. Downer, "Numerical modelling of a 10-cm-long multi-GeV laser wakefield accelerator driven by a self-guided petawatt pulse," *New J. Phys.*, vol. 12, no. 4, p. 045019, Apr. 2010.

[21] P. Sprangle, E. Esarey, and A. Ting, "Nonlinear theory of intense laser-plasma interactions," *Phys. Rev. Lett.*, vol. 64, no. 17, pp. 2011–2014, 1990.

[22] S. G. Gales and C. D. Bentley, "Image plates as x-ray detectors in plasma physics experiments," *Rev. Sci. Instrum.*, vol. 75, no. 10, p. 4001, 2004.

[23] D. Dowsett, P. Kenny, and R. E. Johnston, *The physics of Diagnostic Imaging*, 2nd ed. London New York: Hodder Arnold Distributed in the USA by Oxford University Press, 2006.

[24] Y. Amemiya, "Imaging plates for use with synchrotron radiation.," *J. Synchrotron Radiat.*, vol. 2, no. Pt 1, pp. 13–21, Jan. 1995.

[25] K. Takahashi, "Progress in science and technology on photostimulable BaFX:Eu2+ (X = Cl, Br , I) and imaging plates," *J. Lumin.*, vol. 100, pp. 307–315, 2002.

[26] A. E. S. von Wittenau, C. M. Logan, M. B. Aufderheide, and D. M. Slone, "Blurring artifacts in megavoltage radiography with a flat-panel imaging system: Comparison of Monte Carlo simulations with measurements," *Med. Phys.*, vol. 29, no. 11, p. 2559, 2002.

[27] A. Buck, K. Zeil, a Popp, K. Schmid, A. Jochmann, S. D. Kraft, B. Hidding, T. Kudyakov, C. M. S. Sears, L. Veisz, S. Karsch, J. Pawelke, R. Sauerbrey, T. Cowan, F. Krausz, and U. Schramm, "Absolute charge calibration of scintillating screens for relativistic electron detection.," *Rev. Sci. Instrum.*, vol. 81, no. 3, p. 033301, Mar. 2010.

[28] Y. Glinec, J. Faure, a. Guemnie-Tafo, V. Malka, H. Monard, J. P. Larbre, V. De Waele, J. L. Marignier, and M. Mostafavi, "Absolute calibration for a broad range single shot electron spectrometer," *Rev. Sci. Instrum.*, vol. 77, no. 10, p. 103301, 2006.

[29] J. B. Birks, *The Theory and Practice of Scintillation Counting: International Series of Monographs in Electronics and Instrumentation*. New York: Pergamon Press, 1964.

[30] K. Schmid, "Laser Wakefield Electron Acceleration: A Novel Approach Employing Supersonic Microjets and Few-Cycle Laser Pulses," Springer, 2011.

[31] B. Pollock, J. S. Ross, G. R. Tynan, L. Divol, S. H. Glenzer, V. Leurent, J. P. Palastro, J. E. Ralph, D. H. Froula, C. E. Clayton, K. A. Marsh, A. E. Pak, T. L. Wang, and C. Joshi, "Two-screen method for determining electron beam energy and deflection from laser wakefield acceleration," *Proceedings of the 2009 Particle Accelerator Conference*. Vancouver, 2009.

[32] X. Wang, R. Zgadzaj, N. Fazel, Z. Li, S. A. Yi, X. Zhang, W. Henderson, Y.-Y. Chang, R. Korzekwa, H.-E. Tsai, C.-H. Pai, H. Quevedo, G. Dyer, E. Gaul, M. Martinez, a. C. Bernstein, T. Borger, M. Spinks, M. Donovan, V. Khudik, G. Shvets, T. Ditmire, and M. C. Downer, "Quasi-monoenergetic laser-plasma acceleration of electrons to 2 GeV," *Nat. Commun.*, vol. 4, no. May, Jun. 2013.

[33] G. R. Plateau, C. G. R. Geddes, D. Thorn, M. Chen, C. Benedetti, E. Esarey, A. Gonsalves, N. Matlis, K. Nakamura, C. Schroeder, S. Shiraishi, T. Sokollik, J. van Tilborg, C. Toth, S. Trotsenko, T. Kim, M. Battaglia, T. Stöhlker, and W. P. Leemans, "Low-Emittance Electron Bunches from a Laser-Plasma Accelerator Measured using Single-Shot X-Ray Spectroscopy," *Phys. Rev. Lett.*, vol. 109, no. 6, p. 064802, Aug. 2012.

[34] C. Thaury, E. Guillaume, S. Corde, R. Lehe, M. Le Bouteiller, K. Ta Phuoc, X. Davoine, J. M. Rax, A. Rousse, and V. Malka, "Angular-Momentum Evolution in Laser-Plasma Accelerators," *Phys. Rev. Lett.*, vol. 111, no. 13, p. 135002, Sep. 2013.

[35] E. Esarey, B. Shadwick, P. Catravas, and W. P. Leemans, "Synchrotron radiation from electron beams in plasma-focusing channels," *Phys. Rev. E*, vol. 65, no. 5, pp. 1–15, May 2002.

[36] L. Silberstein, "Determination of the spectral composition of x-ray radiation from filtration data," *J. Opt. Soc. Am.*, vol. 22, no. 491, pp. 265–278, 1932.

[37] H. Kramer and H. von Seggern, “The Determination of X-ray Spectra From Attenuation Data, Part I: The potentials of various methods,” *Nucl. Instruments Methods Phys. ...*, vol. 213, pp. 373–380, 1983.

[38] H. Kramer, “The Determination of X-ray Spectra From Attenuation Data, Part II: Experimental results,” *Nucl. Instruments Methods Phys. Res.*, vol. 214, pp. 445–450, 1983.

[39] A. L. Meadowcroft, C. D. Bentley, and E. N. Stott, “Evaluation of the sensitivity and fading characteristics of an image plate system for x-ray diagnostics.,” *Rev. Sci. Instrum.*, vol. 79, no. 11, p. 113102, Nov. 2008.

[40] A. Rousse, K. Ta Phuoc, R. Shah, A. Pukhov, E. Lefebvre, V. Malka, S. Kiselev, F. Burgy, J.-P. Rousseau, D. Umstadter, and D. Hulin, “Production of a keV X-Ray Beam from Synchrotron Radiation in Relativistic Laser-Plasma Interaction,” *Phys. Rev. Lett.*, vol. 93, no. 13, pp. 1–4, Sep. 2004.

[41] S. Kneip, C. McGuffey, J. L. Martins, S. F. Martins, C. Bellei, V. Chvykov, F. J. Dollar, R. Fonseca, C. Huntington, G. Kalintchenko, a. Maksimchuk, S. P. D. Mangles, T. Matsuoka, S. R. Nagel, C. a. J. Palmer, J. Schreiber, K. Ta Phuoc, A. Thomas, V. Yanovsky, L. O. Silva, K. M. Krushelnick, and Z. Najmudin, “Bright spatially coherent synchrotron X-rays from a table-top source,” *Nat. Phys.*, vol. 6, no. 12, pp. 980–983, Oct. 2010.

[42] D. Thorn, C. G. R. Geddes, N. H. Matlis, G. R. Plateau, E. Esarey, M. Battaglia, C. B. Schroeder, S. Shiraishi, T. Stöhlker, C. Tóth, and W. P. Leemans, “Spectroscopy of betatron radiation emitted from laser-produced wakefield accelerated electrons.,” *Rev. Sci. Instrum.*, vol. 81, no. 10, p. 10E325, Oct. 2010.

[43] N. D. Powers, I. Ghebregziabher, G. Golovin, C. Liu, S. Chen, S. Banerjee, J. Zhang, and D. Umstadter, “Quasi-monoenergetic and tunable X-rays from a laser-driven Compton light source,” *Nat. Photonics*, vol. 8, no. 1, pp. 28–31, Nov. 2013.

[44] B. R. Maddox, H. S. Park, B. a Remington, N. Izumi, S. Chen, C. Chen, G. Kimminau, Z. Ali, M. J. Haugh, and Q. Ma, "High-energy x-ray backlighter spectrum measurements using calibrated image plates.," *Rev. Sci. Instrum.*, vol. 82, no. 2, p. 023111, Feb. 2011.

[45] S. Corde, K. Ta Phuoc, G. Lambert, R. Fitour, V. Malka, A. Rousse, a. Beck, and E. Lefebvre, "Femtosecond x rays from laser-plasma accelerators," *Rev. Mod. Phys.*, vol. 85, no. 1, pp. 1–48, Jan. 2013.

[46] F. Albert, B. Pollock, J. Shaw, K. Marsh, J. E. Ralph, Y.-H. Chen, D. Alessi, a. Pak, C. E. Clayton, S. H. Glenzer, and C. Joshi, "Angular Dependence of Betatron X-Ray Spectra from a Laser-Wakefield Accelerator," *Phys. Rev. Lett.*, vol. 111, no. 23, p. 235004, Dec. 2013.

[47] D. Sandwell, "Biharmonic spline interpolation of GEOS-3 and SEASAT altimeter data," *Geophys. Res. Lett.*, vol. 14, no. 2, pp. 139–142, 1987.

[48] R. Franke, "Scattered data interpolation: tests of some methods," *Math. Comput.*, vol. 38, no. 157, pp. 181–181, Jan. 1982.

[49] W. Thompson, "On a Criterion for the Rejection of Observations and the Distribution of the Ratio of Deviation to Sample Standard Deviation," *Ann. Math. Stat.*, vol. 6, no. 4, pp. 214–219, 1935.

[50] E. Gaul, M. Martinez, J. Blakeney, A. Jochmann, M. Ringuette, D. Hammond, T. Borger, R. Escamilla, S. Douglas, W. Henderson, and others, "Demonstration of a 1.1 petawatt laser based on a hybrid optical parametric chirped pulse amplification/mixed Nd: glass amplifier," *Appl. Opt.*, vol. 49, no. 9, pp. 1676–1681, 2010.

[51] S. Pressé, K. Ghosh, J. Lee, and K. A. Dill, "Principles of maximum entropy and maximum caliber in statistical physics," *Rev. Mod. Phys.*, vol. 85, no. 3, pp. 1115–1141, Jul. 2013.

[52] I. V. Khutoretsky, “Design of an optimal Ross filter system for x-ray spectra measurements in the range of 8.98–88 keV,” *Rev. Sci. Instrum.*, vol. 66, no. 1, p. 773, 1995.

[53] X. Wang, R. Zgadzaj, S. A. Yi, V. Khudik, W. Henderson, N. Fazel, Y.-Y. Chang, R. Korzekwa, H.-E. Tsai, C.-H. Pai, Z. Li, E. Gaul, M. Martinez, G. Dyer, H. Quevedo, A. Bernstein, M. Donovan, G. Shvets, T. Ditmire, and M. C. Downer, “Self-injected petawatt laser-driven plasma electron acceleration in 10^{17} cm^{-3},” *J. Plasma Phys.*, vol. 78, no. 04, pp. 413–419, Apr. 2012.

[54] X. Wang, R. Zgadzaj, W. Henderson, and N. Fazel, “Generation of dark-current-free quasi-monoenergetic 1.25 GeV electrons by laser wakefield acceleration,” in *Proceedings of CLEO QELS 2012*, 2012, pp. 11–12.

[55] A. Pak, K. Marsh, S. Martins, W. Lu, W. Mori, and C. Joshi, “Injection and trapping of tunnel-ionized electrons into laser-produced wakes,” *Phys. Rev. Lett.*, vol. 104, no. 2, pp. 1–4, Jan. 2010.

[56] S. Agostinelli, “GEANT4—a simulation toolkit,” *Nucl. Instruments Methods Phys. Res. Sect. A Accel. Spectrometers, Detect. Assoc. Equip.*, vol. 506, no. 3, pp. 250–303, Jul. 2003.

[57] M. Wen, B. Shen, X. Zhang, and L. Ji, “Generation of high charged energetic electrons by using multiparallel laser pulses,” *Phys. Plasmas*, vol. 103113, no. May 2014, pp. 1–6, 2010.

[58] A. Rousse, K. Ta Phuoc, R. Shah, R. Fitour, and F. Albert, “Scaling of betatron X-ray radiation,” *Eur. Phys. J. D*, vol. 45, no. 2, pp. 391–398, Aug. 2007.

[59] H. Wiedemann, *Synchrotron Radiation*. Springer, 2003.

[60] S. Fourmaux, S. Corde, K. Ta Phuoc, P. M. Leguay, S. Payeur, P. Lassonde, S. Gnedyuk, G. Lebrun, C. Fourment, V. Malka, S. Sebban, A. Rousse, and J. C.

Kieffer, “Demonstration of the synchrotron-type spectrum of laser-produced Betatron radiation,” *New J. Phys.*, vol. 13, no. 3, p. 033017, Mar. 2011.

[61] J. Shore and R. Johnson, “Axiomatic Derivation of the Principle of Maximum Entropy and the Principle of M inimum Cross-Entropy,” *IEEE Trans. Inf. Theory*, vol. IT-26, no. 1, pp. 26–37, 1980.

[62] M. Reginatto, P. Goldhagen, and S. Neumann, “Spectrum unfolding, sensitivity analysis and propagation of uncertainties with the maximum entropy deconvolution code MAXED,” *Nucl. Instruments Methods Phys. Res. Sect. A Accel. Spectrometers, Detect. Assoc. Equip.*, vol. 476, no. 1–2, pp. 242–246, Jan. 2002.

[63] P. Wessel and D. Bercovici, “Interpolation with Splines in Tension : A Green’s Function Approach,” *Math. Geol.*, vol. 30, no. 1, pp. 77–93, 1998.

[64] K. A. Tanaka, T. Yabuuchi, T. Sato, R. Kodama, Y. Kitagawa, T. Takahashi, T. Ikeda, Y. Honda, and S. Okuda, “Calibration of imaging plate for high energy electron spectrometer,” *Rev. Sci. Instrum.*, vol. 76, no. 1, p. 013507, 2005.

[65] N. Nakanii, K. Kondo, T. Yabuuchi, K. Tsuji, K. a. Tanaka, S. Suzuki, T. Asaka, K. Yanagida, H. Hanaki, T. Kobayashi, K. Makino, T. Yamane, S. Miyamoto, and K. Horikawa, “Absolute calibration of imaging plate for GeV electrons.,” *Rev. Sci. Instrum.*, vol. 79, no. 6, p. 066102, Jun. 2008.

[66] K. Zeil, S. D. Kraft, A. Jochmann, F. Kroll, W. Jahr, U. Schramm, L. Karsch, J. Pawelke, B. Hidding, and G. Pretzler, “Absolute response of Fuji imaging plate detectors to picosecond-electron bunches.,” *Rev. Sci. Instrum.*, vol. 81, no. 1, p. 013307, Jan. 2010.

[67] K. Miura, “Imaging and detection technologies for image analysis in electrophoresis.,” *Electrophoresis*, vol. 22, no. 5, pp. 801–13, Mar. 2001.

[68] A. Mancić, J. Fuchs, P. Antici, S. A. Gaillard, and P. Audebert, “Absolute calibration of photostimulable image plate detectors used as (0.5-20 MeV) high-energy proton detectors.,” *Rev. Sci. Instrum.*, vol. 79, no. 7, p. 073301, Jul. 2008.

[69] H. H. Ku, “Notes on the use of propagation of error formulas,” *J. Res. Natl. Bur. Stand. (Engineering Intrumentation)*, vol. 70C, no. 4, pp. 263–273, 1966.